Adaptive Aggregation and Chirality Recognition

of Neuroactive Substances and their Building Blocks:

A Vibrational Spectroscopic and Microscopic Study

Dissertation

for the award of the degree

"Doctor rerum naturalium"

of the Georg-August-Universität Göttingen

submitted by

Marija Nedić

from Hamburg

Göttingen 2012

Prof. Dr. Martin A. Suhm (Referee)

Georg-August-Universität Göttingen/ Institute of Physical Chemistry

Prof. Dr. Sarah Köster (Co-Referee)

Georg-August-Universität Göttingen/ Institute for X-Ray Physics

Prof. Dr. Philipp Vana

Georg-August-Universität Göttingen/ Institute of Physical Chemistry

I (Marija Nedić), hereby confirm that I completed my dissertation independently and without any unauthorized support.

Göttingen,

Acknowledgments

I would like to give my sincere thanks to all the people who contributed to this dissertation in any professional or personal way. Your help and support were invaluable to the success of this work.

I would like to thank my advisor Prof. Dr. Martin A. Suhm for the interesting project and time for discussions. I would also like to thank Prof. Dr. Sarah Köster and Prof. Dr. Philipp Vana for being members of my thesis committee.

I would like to thank the mechanical workshop of the Institute of Physical Chemistry for constructing the sublimation cell. I would also like to thank the electric and glass workshops as well as Milo W. Noack for their helpfulness. I would also like to thank Birger Dittrich from the Institute of Inorganic Chemistry for solving the crystal structures of the three methyl mandelate forms, Ralf Tonner from Philipps-University Marburg for crystal calculations on methyl mandelate (still in progress), and Reinhard Machinek from the Institute of Inorganic Chemistry for recording the NMR data of methyl-d_3 mandelate.

I would like to thank the GGNB for their financial support (GGNB bridging fund, DFG Grant GSC 226/1) and the opportunity to take part in various seminars, excursions, and conferences. I would also like to thank the Graduiertenkolleg 782 for the chance to participate as a guest student.

I would like to say thank-you to the entire Suhm Group for creating an enjoyable working atmosphere, their interest and advice, as well as the small distractions during and after work. Special thanks also go to Tobias N. Wassermann who contributed to the alcohol-water project, to Alexandra Domanskaya who gave the decisive hint for the methyl mandelate project, and to Fabian Ziegler who wrote his Bachelor thesis on sublimated methylxanthines.

I would like to thank Amy Henslin, Nils Lüttschwager, Alexandra Domanskaya, and Julia Zischang for proofreading.

Finally, I would especially like to thank my parents, my brother, my boyfriend, and my extended family for their personal support over the years: Danke, Kiitos, and Hvala!

Contents

1. Introduction

The effectiveness of neuroactive substances, the activity of drugs as well as our ol-
factory sense are based on the chirality and conformation of the receptor and the
molecules themselves [1]. The molecular recognition of such complexes is also
known as the lock-and-key principle [2]. The discrimination between two enan-
tiomeric molecules which differ like image and mirror image is called chirality
recognition [3–6]. The receptors in the human body are chiral and are thus open
for chirality recognition phenomena. The conformation of a molecule describes
its spatial arrangement and influences its energy. The energetical order of confor-
mations is determined by intramolecular interactions but also by interactions with
the surrounding e.g., intra- and intermolecular hydrogen bonds, respectively [7–9].
The change of the preferred monomer conformation as a response to the surround-
ing may be called adaptive aggregation [10–12]. In this work chirality recognition
phenomena and adaptive aggregation in hydrogen bonded crystals are investigated.
Their high degree of long-range three-dimensional internal order of the molecules
leads to more complexity than in molecular complexes, but also opens powerful
options for the characterization [13]. Small hydrogen bonded clusters, which are
also investigated within this work, serve as a model case for adaptive aggrega-
tion [11, 14].

There is a variety of methods to characterize molecular crystals [15]. Diffrac-
tion methods such as single-crystal X-ray or neutron diffraction are frequently used
to solve the structure of crystals [13]. Vibrational spectroscopy provides informa-
tion on the local interactions and couplings between the molecules [16], as well
as on the driving forces for conformational rearrangements during crystal packing
which can lead to polymorphism as a function of crystal preparation. Though Ra-
man microspectroscopy has the advantage of a better spatial resolution due to a
lower diffraction limit [17], IR microspectroscopy can be the method of choice.
IR microspectroscopy provides a better signal-to-noise ratio and can be used for
imaging purposes, while only stepwise mapping is possible with Raman microspec-

troscopy [17]. Anisotropic media such as crystals are available for polarization studies which provide information about the direction of the vibrational transition dipole vector.

Sublimation is a rather rare technique used in the crystallization process. Nevertheless, it is the conceptually cleanest way of crystal preparation since no solvent or further sample treatment is required [18, 19]. Here, adaptive aggregation and chirality recognition effects depend on the inherent interactions between equal molecules and not on molecule-solvent interactions. The crystal habit is only determined by the fastest growth directions [20] and reveals information about the relative strengths of the interactions present in the crystal. Comparison with gas phase measurements and quantum-chemical calculations are feasible. Kinetic control allows for the sublimation of sub-millimeter-sized crystals which are suitable for infrared measurements in transmission mode without further preparation. Measurement of different faces is possible by rotating the crystal on the substrate.

There is an enhanced propensity for complex crystal structures in sublimated crystals. The percentage of organic molecules in the Cambridge Structural Database (CSD) with more than one molecule in the asymmetric unit ($Z'>1$) increases from 11% to 17% for sublimated crystals [21, 22]. A tendency to form complex crystal structures was also found for chiral molecules or molecules having directional intermolecular interactions, e.g., hydrogen bonds [23]. FTIR spectra of crystals, and especially of sublimated chiral crystals, are expected to show complex inphase and antiphase coupling patterns for many molecular vibrations (factor group splittings) [16]. Additionally, quantitative differences in the molecular structures building the asymmetric unit may lead to further spectral splittings [24]. However, the increased complexity of crystal spectra compared to gas phase spectra may be turned into an assignment advantage by exploring crystal rotation, IR polarization, and monomer calculations. The facial and polarization dependence of vibrational bands gives information about the direction of the vibrational transition dipole vector within the macroscopic crystal.

FTIR polarization microscopy has been applied in the infrared before [25–27], mostly in reflection mode. Also, oriented single crystals and oriented films were investigated by polarized THz transmission spectroscopy [28–31]. Furthermore, polarized Raman spectroscopy has been used to assign molecular and phonon modes of single crystals [32, 33].

In the present work, polarized Fourier transform infrared (FTIR) microspectroscopy in transmission mode is primarily applied to the characterization of sublimated crystals. All investigated substances are chiral and are open for hydrogen bonding. Rotated crystal measurements support the assignment of spectra to different faces. In order to unravel the molecular orientation within the crystals a version of the oriented gas model approach [25, 34, 35] is adopted. Monomer calculations are used to simulate the intensities of fundamental modes according to the molecular orientation within the crystal and the applied polarization. Published crystal structures, if available, are used for the assignment of the molecular orientation based on the assumption that the same polymorph is present in the sublimated microcrystals. Crystal phase calculations of the vibrational spectra would be highly desirable, but meet formidable challenges due to the size of the molecules and of the unit cells. A cooperation was started with R. Tonner [36].

In Chapter 2, elementary aspects of the vibrational transition dipole vector are elucidated and the limits of the oriented gas model approach for the modeling of crystal IR spectra based on monomer calculations in the gas phase are explored. It is shown that the oriented gas model approach exhibits deficiencies in predicting red shifts and intensifications which are due to hydrogen bonds. Nonetheless, it is useful to predict the polarization behavior of a crystal.

The sublimation cell constructed for the vacuum sublimation and measurement of microcrystals is characterized in Chapter 3. The experimental and theoretical methods are described there as well.

Adaptive aggregation is investigated in Chapter 4 for the elementary case of small alcohol-water clusters in jet-expansions [11, 14]. It is shown that water acts as the proton donor in mixed dimers and that ethanol exhibits the less stable gauche conformation in the ethanol-water dimer. This serves as a model case for conformational switching in the more complex crystals.

Methyl mandelate was chosen as the test substance for the polarized transmission FTIR microspectroscopic studies on sublimated crystals because of its structural similarity to some neurotransmitters [37]. Results including the change of conformation and chirality recognition of a 1:1 and a 3:1 racemic crystal [38] are presented in Chapter 5. Quantum-chemical calculations, ATR-IR spectra, and isotope labeling are used for the vibrational assignment. The molecular orientation within the crystals is inferred through a comparison of experimental with oriented gas model spectra.

3

The polarized transmission FTIR microspectroscopic method is applied to mandelic acid [37] in Chapter 6 and to the neuroactive phenylpropanolamines norephedrine, pseudonorephedrine, ephedrine, and pseudoephedrine in Chapter 7. Chirality recognition effects are presented for norephedrine and pseudoephedrine. In the case of ephedrine a hydrate and an anhydrate are crystallized. The spectroscopic crystal studies are supported by quantum chemical calculations, ATR spectra, and deuteration experiments. Vibrational assignments are performed and the molecular orientation within the crystals are determined. Tentative molecular orientations are proposed for enantiopure norephedrine and racemic pseudoephedrine. In the case of the phenylpropanolamines the influence of hydrogen bonds and of the molecular conformation on the N-H stretching positions is investigated.

A summary of the results and an outlook are given in Chapter 8.

2. Basics

IR spectroscopy is a powerful tool standardly used for the investigation of vibrational modes and the analysis of hydrogen bonds [16, 39, 40]. It is based on the interaction of the electric vector of infrared radiation with a molecular dipole moment oscillating with the same frequency. In order for a vibrational mode to be IR active it needs to change its dipole moment. Thus, a permanent dipole moment is not needed, but a transition dipole moment. The transition dipole moment $\vec{\mu}_{nm}$ is a vector quantity given by:

$$\vec{\mu}_{nm} = \int \Psi_n^* \vec{\mu} \Psi_m \mathrm{d}\tau \tag{2.1}$$

with respect to the energy eigenfunctions $\Psi_{n,m}$ of the states n, m involved in the transition and $\mathrm{d}\tau$ being the volume element $\mathrm{d}x\mathrm{d}y\mathrm{d}z$ [39, 41, 42]. $\vec{\mu}$ is the electric dipole moment vector obtained by summing over the product of all charges q_i multiplied by their position vectors $\vec{r}_i$ [39, 42]:

$$\vec{\mu} = \sum_i q_i \vec{r}_i. \tag{2.2}$$

Whether a transition is allowed or forbidden depends on the properties of the wavefunctions, the orientation of the dipole moment, and the direction and polarization of the incident radiation [41]. For a heteronuclear diatomic molecule the electric dipole moment usually varies with the displacement of the internuclear distance from equilibrium $Q = r - r_e$. The resulting variation of the transition dipole moment can be expressed in a Taylor series as [39, 43]:

$$\vec{\mu}_{nm} = \vec{\mu}_e \int \Psi_n^* \Psi_m \mathrm{d}Q + \left(\frac{\mathrm{d}\vec{\mu}}{\mathrm{d}Q}\right)_e \int \Psi_n^* Q \Psi_m \mathrm{d}Q + ... \tag{2.3}$$

The wavefunctions are eigenfunctions of the same hamiltonian and therefore orthogonal. Equation 2.3 becomes:
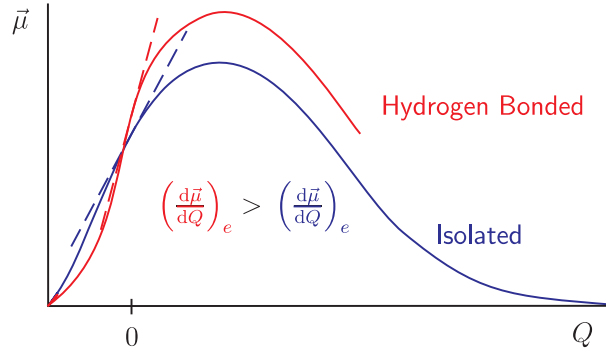
Figure 2.1.: Variation of the dipole moment $\vec{\mu}$ with the displacement of the internuclear distance Q. The blue curve corresponds to an isolated vibrational mode and the red curve to a hydrogen bonded mode.

$$\vec{\mu}_{nm} = \left(\frac{\mathrm{d}\vec{\mu}}{\mathrm{d}Q}\right)_e \int \Psi_n^* Q \Psi_m \mathrm{d}Q + ... \qquad (2.4)$$

The IR intensity I is proportional to the square of the transition dipole moment $\vec{\mu}_{nm}$ [39, 42, 44]:

$$I \propto |\vec{\mu}_{nm}|^2 \qquad (2.5)$$

and according to Equations 2.4 and 2.5 also to the squared derivative of the dipole moment $\vec{\mu}$ with respect to the displacement Q [39, 42]:

$$I \propto \left(\frac{\mathrm{d}\vec{\mu}}{\mathrm{d}Q}\right)_e^2. \qquad (2.6)$$

A schematic curve of the relation $\vec{\mu}$ versus Q is shown in Fig. 2.1 for an isolated and a hydrogen bonded mode [39]. The slope $\left(\frac{d\vec{\mu}}{dQ}\right)$ at $Q=0$ (internuclear distance at equilibrium) is steeper for the hydrogen bonded vibrational mode. Therefore, the vibrational transition dipole moment (Equation 2.4) and the IR intensity (Equation 2.5) are larger for a hydrogen bonded than for an isolated vibrational mode [45, 46].

The dipole moment operator $\vec{\mu}$ has components along the cartesian axes. Accordingly, the transition dipole vector also has components in x, y, and z direction [39]:

$$|\vec{\mu}_{nm}|^2 = (\mu_{nm,x})^2 + (\mu_{nm,y})^2 + (\mu_{nm,z})^2 \qquad (2.7)$$

Therefore, in an anisotropic environment such as a crystal being illuminated from
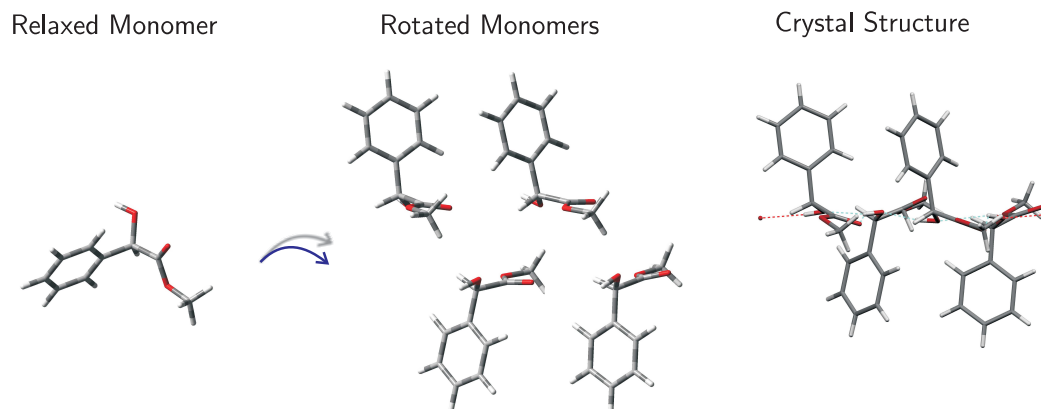
Figure 2.2.: Rotation of a relaxed monomer unit (here, methyl mandelate) into the desired orientation within the asymmetric unit of the crystal structure solved by X-ray analysis.

one direction, the x, y, and z components may have varying contributions to the intensity [47]. The observed IR intensity depends on the orientation of the crystal and on the polarization of the incident radiation. Crystal IR spectra can be modeled based on monomer calculations using the oriented gas model approach [25, 34, 35]. In this approach intermolecular interactions are neglected. This is not true for several modes in hydrogen bonded crystals.

Within this work a variation of the oriented gas model approach was developed. Spectra corresponding to the different crystal faces as well as for different polarizations are simulated for a better comparison between experiment and prediction. Monomers taken from the crystal structure are geometrically optimized to the nearest isolated minimum structure by quantum chemical calculations. The relaxed monomers are then rotated into the orientation of the molecules within the crystal (see Fig. 2.2). This yields a rotation matrix which is applied to the calculated dipole derivatives $\vec{\mu}'$ of a given vibration. Intensities of the different faces are approximated by summing up the squares of the x- and y-components of the dipole derivatives, if z is the direction of the incident light:

$$I \sim \mu_x'^2 + \mu_y'^2. \tag{2.8}$$

In the case of polarization measurements, the intensity corresponds to the square of the x-component ($I \sim \mu_x'^2$) and to the square of the y-component ($I \sim \mu_y'^2$) of the dipole derivatives. The dipole derivatives of the different molecules within the
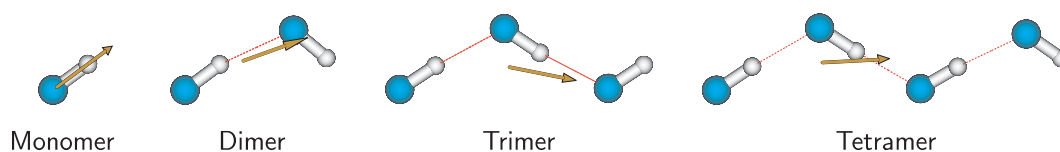
Figure 2.3.: The direction of the vibrational transition dipole vectors (yellow, unit length) of the symmetric F-H stretching mode for small HF clusters ($n = 1$–4, B3LYP/6-31+G(d) level). The trimer and tetramer do not represent minimum structures.

asymmetric unit are first squared and then added. Thus, the oriented gas model spectra do not account for couplings within the crystal, but rather correspond to the center of the coupling patterns. A Matlab script [48] was written to rotate the relaxed monomer units from a view along the crystallographic *c*-axis into views along the crystallographic *a*- and *b*-axes of the monomer units within the crystal structure and to calculate nonpolarized and polarized intensities of the different crystals' faces (see Supplement A). In the following, the limits of this approach will be explored on the basis of HF.

HF crystallizes in the space group *Bmmb* with one molecule in the asymmetric unit (Z'=1) and six molecules in the unit cell (Z=6). It forms disordered infinite F-H· · ·F hydrogen bonded zigzag chains along the crystallographic *b* axis (ICSF REF Code: 14121) [49, 50]. Fragments of the zigzag chain are shown for small optimized HF clusters in Fig. 2.3. Note that the dimer [51] but not the trimer [52,53] and tetramer [54] correspond to a minimum structure. The dipole derivatives of the imaginary frequencies are perpendicular to the molecular plane. Fig. 2.3 shows the influence of cluster size (*n*=1–4) on the direction of the vibrational transition dipole vector of the symmetric F-H stretching mode. In the case of the monomer, the vibrational transition dipole vector points along the F-H axis. The direction changes upon hydrogen bonding. It points roughly along the hydrogen bond axis in the dimer. In the presence of a hydrogen bonded chain the vibrational transition dipole vector shows more or less along the HF chain. This alignment improves with increasing cluster size largely due to symmetry reasons. It is therefore perfect in the case of an infinite chain which is realized in the crystal.

In Fig. 2.4 the limits of the oriented gas model approach are displayed for the hydrogen bonded HF dimer. The polarized spectra of two HF monomer units and of the HF dimer in the F-H stretching region are compared. The monomer units and the dimer are rotated in the molecular plane in the upper part of Fig. 2.4 compared

to the lower part. The black curves correspond to the nonpolarized spectra and are the same for the upper and lower part of Fig. 2.4. They already exhibit deficiencies of the oriented gas model approach. The calculation of the monomer cannot account for the red shift and intensification of the dimer modes which result from the hydrogen bond. The infinite hydrogen bonded chain in the HF crystal can be expected to lead to even larger red shifts and intensifications.

In Fig. 2.4 the polarized spectra are displayed in red for a horizontal polarization and in blue for a vertical polarization. Since the molecules of the lower part are rotated in comparison to the upper part, the polarization spectra differ. In the upper part the intensities are almost equal for both polarizations. In the lower part the intensity of the asymmetric stretching when applying a vertical polarization is almost as high as in the nonpolarized spectrum. The opposite is true for the symmetric stretching. Here, the intensity of the horizontally polarized spectrum is nearly as high as the nonpolarized. The opposite behavior results from nearly perpendicular vibrational transition dipole vectors which are aligned along the *x* and *y* axes. In the case of the monomer mode, the horizontal polarization leads to a 1.5 times higher intensity than the vertical polarization. This reflects the properties of the symmetric stretching with some contributions from the less perfectly aligned asymmetric mode.

An increased stabilization energy per hydrogen bond, strong red shifts of the F-H stretching frequency, and significantly enhanced IR intensities were found for HF_{1-19} chains investigated by SCF calculations asymptotically approaching the solid properties [55, 56]. Monomer calculations cannot account for the intensification and wavenumber shifts in hydrogen bonded systems. Nevertheless, the relative intensity change upon different directions of polarization can be simulated by the oriented gas model approach. In the case of nonbonded modes, scaled monomer predictions are reasonable and suitable for wavenumber, intensity, and polarization simulations.
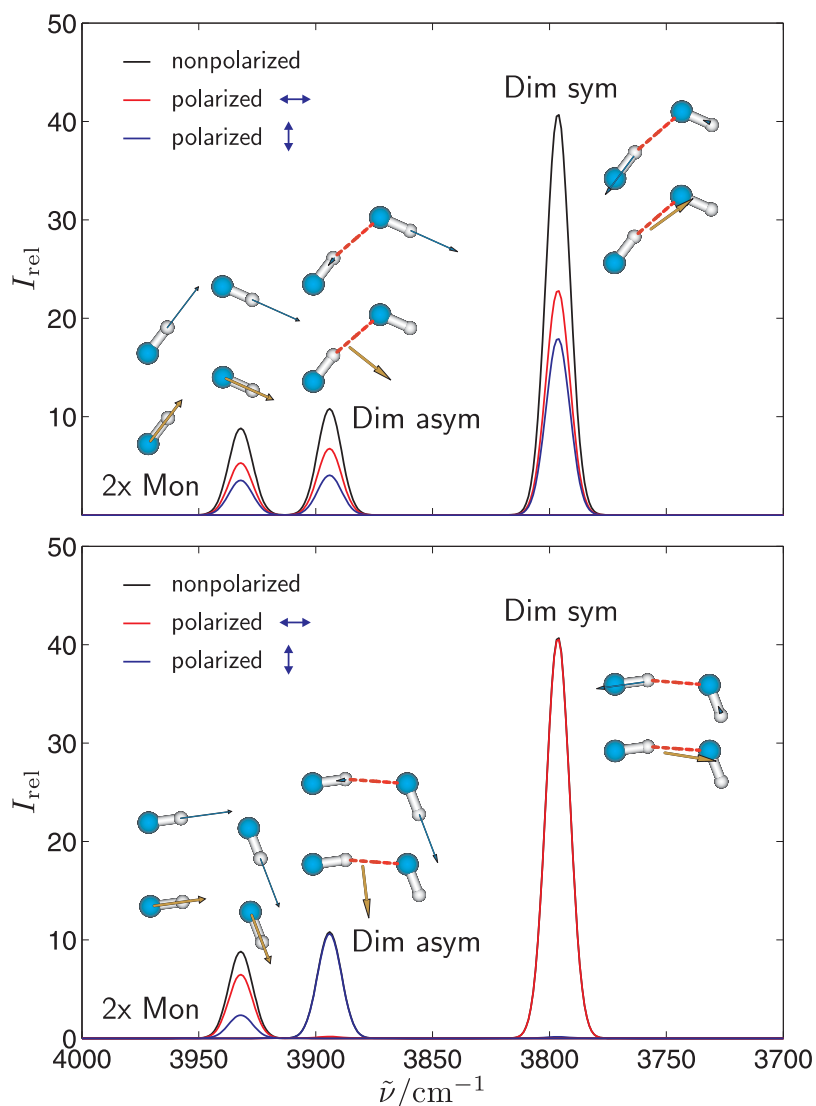
Figure 2.4.: Oriented gas model polarization spectra (B3LYP/6-31+G(d) level) of the HF dimer's (Dim) asymmetric (asym) and symmetric (sym) F-H stretching mode as well as the F-H stretching mode of two HF monomer units (2x Mon). The black curve corresponds to the nonpolarized, the red curve to the horizontally polarized, and the blue curve to the vertically polarized spectra. The direction of the vibrational transition dipole vectors (yellow, unit length) as well as the displacement vectors of each mode (blue) are indicated. The monomer and dimer units are rotated in the molecular plane in the upper in comparison to the lower part.

3. Methods

The results of this work were obtained using both experimental and theoretical approaches. The focus was on experimental investigations. Quantum chemical calculations supported their interpretation. In Sect. 3.1 the preparation of samples will be elucidated. The experimental methods will be illustrated in Sect. 3.2. The theoretical approaches will be described in Sect. 3.3.

3.1. Sample Preparation

3.1.1. Substances

Compounds used within the framework of the presented projects are listed in Supplement B. The chemical formulas, CAS-numbers, suppliers, and purity are also provided there. The synthesis of methyl-d$_3$ mandelate and the crystallization of racemic and deuterated compounds will be described in the following Section.

Synthesis of Methyl-D$_3$ Mandelate

CD$_3$-deuterated methyl mandelate (methyl-d$_3$ mandelate) was not commercially available. The synthesis of mandelates according to Refs. [57, 58] was modified to obtain methyl-d$_3$ mandelate [37]. 0.458 g R-mandelic acid (0.0030 mol) was dissolved in 3 mL methanol-d$_3$ (0.0742 mol, 25-fold molar excess). One droplet of concentrated sulfuric acid was added. The mixture was refluxed at 72°C for 3.5 hours. Afterwards, excess methanol-d$_3$ was removed using a rotary evaporator. The crude methyl-d$_3$ mandelate was dissolved in ether and washed twice with aqueous potassium carbonate followed by saturated aqueous sodium chloride solution. Finally, the organic layer was dried over anhydrous sodium sulfate, filtered, and distilled with the rotary evaporator. The yield of methyl-d$_3$ mandelate was 63 % (0.319 g). The chemical purity determined in cooperation with R. Machinek by [1]H
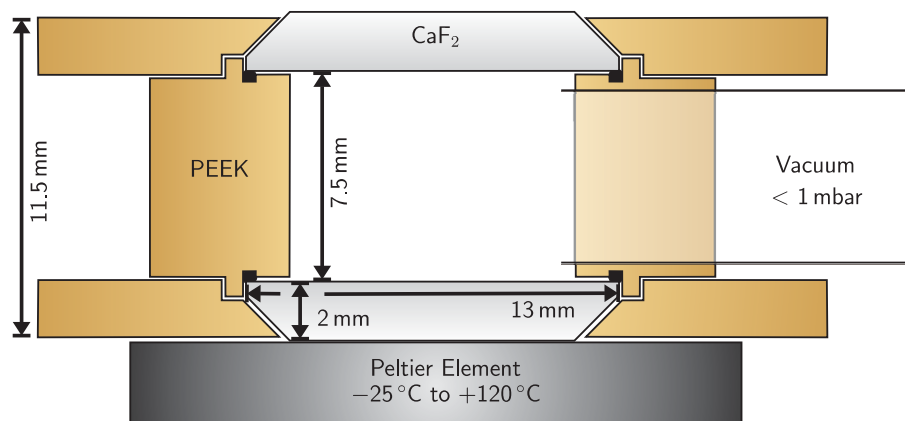
Figure 3.1.: Cross section of the sublimation cell with CaF$_2$ windows mounted on a Peltier element.

NMR ((300 MHz, CDCl$_3$): δ 3.5 (s, 1H) 5.2 (s, 1H) 7.3–7.4 (m, 5H)) was $\geq$90 %. It can be assumed that the purity increased upon sublimation and resublimation.

3.1.2. Crystallization via Sublimation

A sublimation cell for the crystallization via sublimation and resublimation was built and tested within the framework of the present study. The cell is constructed to optimize the crystallization process by lowering the pressure and by applying a temperature gradient. The powdery substance sublimates at the bottom and resublimates in the form of microcrystals (10–500 μm) at the top. Hereafter, the process of sublimation and resublimation will be referred to as sublimation only. By changing the pressure and temperature, the crystallization growth can be controlled and microcrystals suitable for transmission spectroscopy can be obtained. A scheme of the sublimation cell is depicted in Fig. 3.1.

The sublimation cell consists of two CaF$_2$ windows (Korth Kristalle GmbH) which transmit light in the range of 0.13–12 μm ($\approx$77000–830 cm^{-1}). The windows have a diameter of 13$\pm$0.1 mm, a thickness of 2$\pm$0.1 mm, and a bevel of 1.5 mm $\times$ 45°. A 6 mrad wedge on the planar face and the optical polish reduce interference and light scattering. The anisotropic CaF$_2$ crystals are randomly oriented within the windows. The CaF$_2$ plates are held together by a PEEK (polyether ether ketone) holder which is temperature resistant (up to 300°C). The PEEK holder and the CaF$_2$ windows are sealed by using either perbunan$^{®}$ (up to 60°C) or viton$^{®}$ o-rings of 10 $\times$ 1.0 mm (up to 300°C). Two versions of the sublimation cell had been

constructed and tested. The first version was equipped with a PEEK olive which was connected to a plastic hose. For the second version a flexible steel hose with a flange is glued to the PEEK holder. With the second version low pressures are obtained faster and can be maintained longer. The sublimation cell can be connected to a turbomolecular pump (Pfeiffer Vacuum TSH 071 and MVP 015-2) and evacuated down to a pressure of less than 1 mbar (minimal pressure limited by leakage of the sublimation cell, see below). The pressure was measured with a baratron pressure gauge in the range of 0.001–10 mbar (MKS baratron type 626). The speed of the evacuation process can be controlled by using a needle valve (HOKE Milli-Mite 13335G6Y). The standard position for the evacuation of the sublimation cell was 8 μm. The sublimation cell can be mounted on a Peltier element (Linkam PE94). Thus, it is possible to regulate the temperature at the bottom of the cell in a range of $-25°$C to $+120°$C.

Generally, the sublimation process was performed in a pressure region of 0.1–10 mbar with a closed needle valve (0 μm). For crystallizations that took longer than one day, the needle valve remained open (8 μm) to compensate the leakage of the cell. The temperature was set at 20°C and increased in steps of 5°C in order to determine the approximate sublimation temperature for a given sample. The crystallization growth could be stopped by lowering the temperature at the bottom of the cell below the sublimation temperature. Occasionally, sublimation temperatures below room temperature were necessary. In these cases, either the air conditioner was used or the windows were opened during winter. By doing this, room temperatures as low as 10°C were obtained.

Crystallization via sublimation is optimized by applying a temperature gradient. Ideally, there is a perfect heat transfer from the Peltier element to the bottom of the cell but no heat transfer to the top. Temperature tests with the sublimation cell were performed in order to test the heat transfer from the Peltier element to the cell and the temperature gradient of the sublimation cell. Measured melting temperatures of several substances were compared with literature data. Also, the set temperature of the Peltier element was compared to the temperature measured with a thermocouple device.

The melting temperatures of different substances ((*R*)-alanine ethyl ester hydrochloride, (*R*)-methyl mandelate, (*RS*)-methyl mandelate, (*RS*)-menthol, ethyl ac-
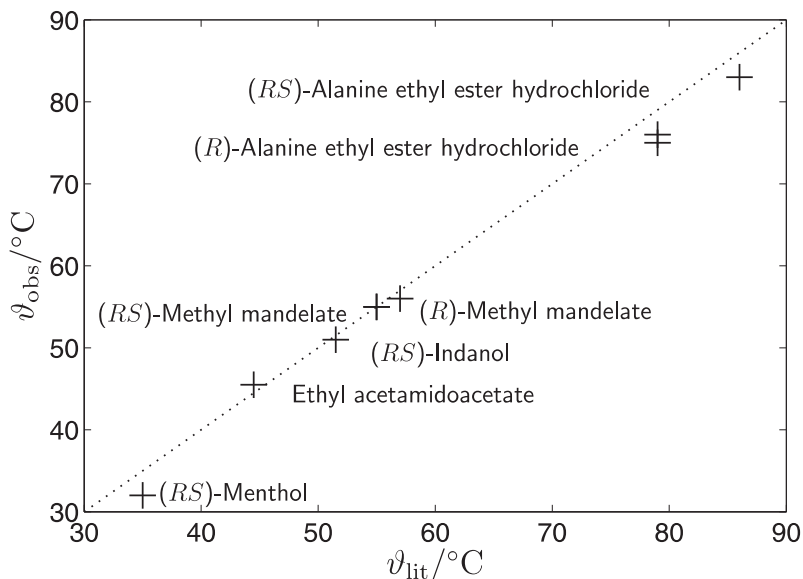
Figure 3.2.: Comparison of observed melting temperatures at the bottom of the sublimation cell (ϑ_{obs}) and melting temperatures provided by the supplier (ϑ_{lit}) in °C of different substances. The dotted line marks negligible deviation.

etamidoacetate, (*RS*)-indanol, and (*RS*)-alanine ethyl ester hydrochloride) provided by the supplier were compared with the temperature in the sublimation cell determined with the Peltier element. In Fig. 3.2 the melting temperatures provided by the supplier ϑ_{lit} are plotted versus the observed temperatures ϑ_{obs} (see also Tab. 3.1).

Fig. 3.2 shows a good agreement between literature and observed melting temperatures of the substances. A tendency of measuring slightly lower melting temperatures in the sublimation cell can be noticed. The deviation of less than 1°C can be explained by the loss of heat between the Peltier element and the bottom of the cell. An alternative explanation for the deviation of the melting temperature is the deviation between the set and actual temperature of the Peltier element. Nevertheless, the deviation in temperature is negligible for the sublimation experiments.

The heat transfer was also monitored by using a thermocouple device (Peak Tech, digital multimeter 2010). In order to account for deviations in the room temperature, the difference of the temperature set at the Peltier element and the room temperature was plotted against the difference between the measured temperature and room temperature in Fig. 3.3. The black line shows a perfect heat transfer ($\Delta\vartheta_{thermo}$/°C=$\Delta\vartheta_{PE}$/°C, not observed). The brown curve is the calibration curve

Table 3.1.: Literature ϑ_{lit} (information provided by supplier) and observed standard melting temperatures ϑ_{obs} of various substances used for the sublimation cell temperature test.

Substance	$\vartheta_{\text{lit}}/°C$	$\vartheta_{\text{obs}}/°C$
(*RS*)-Menthol	34–36	32
Ethyl acetamidoacetate	43–46	45.5
(*RS*)-Indanol	50–53	51
(*RS*)-Methyl mandelate	54–56	55/55
(*R*)-Methyl mandelate	56–58	56
(*R*)-Alanine ethyl ester hydrochloride	78–80	76/75
(*RS*)-Alanine ethyl ester hydrochloride	85–87	83

of the thermocouple and shows the deviation of the thermocouple reading with an ice-water mixture ($\vartheta_{\text{PE}}=0°C$) and boiling water ($\vartheta_{\text{PE}}=100°C$, $\Delta\vartheta_{\text{thermo}}/°C=0.96 \cdot \Delta\vartheta_{\text{PE}}/°C+1.2$). The temperature measured at the heating plate of the Peltier element (blue) already shows a deviation to lower temperatures above approximately room temperature and to higher temperatures below approximately room temperature ($\Delta\vartheta_{\text{thermo}}/°C=0.83 \cdot \Delta\vartheta_{\text{PE}}/°C-0.57$). The deviation at the bottom of the cell (reddish) was found to be roughly twice as high as the one at the heating plate at temperatures above approximately room temperature ($\Delta\vartheta_{\text{thermo}}/°C=0.75 \cdot \Delta\vartheta_{\text{PE}}/°C-0.85$). Below approximately room temperature the deviation is almost the same as at the heating plate.

The temperature measured at the inner part of the CaF_2 window without direct contact to the heating plate (hole for the beam, red) was approximately the same as at the outer part with direct contact (pink). The behavior for heating (circles) was approximately the same as for cooling (points), i.e. no hysteresis was observed. A much larger deviation was found at the top of the cell (green), being slightly larger when venting the sublimation cell (light green, $\Delta\vartheta_{\text{thermo}}/°C=0.25 \cdot \Delta\vartheta_{\text{PE}}/°C+0.52$), as compared to the evacuated cell (dark green, $\Delta\vartheta_{\text{thermo}}/°C=0.30 \cdot \Delta\vartheta_{\text{PE}}/°C+0.59$). The temperature steps were arbitrarily chosen. It should be noted that it was not possible to measure the temperature at the top of the cell from the inside. The temperature inside the cell can be estimated to have a slightly higher deviation from room temperature than the temperature outside.

Summing up, Fig. 3.3 shows that there is a good heat transfer from the Peltier
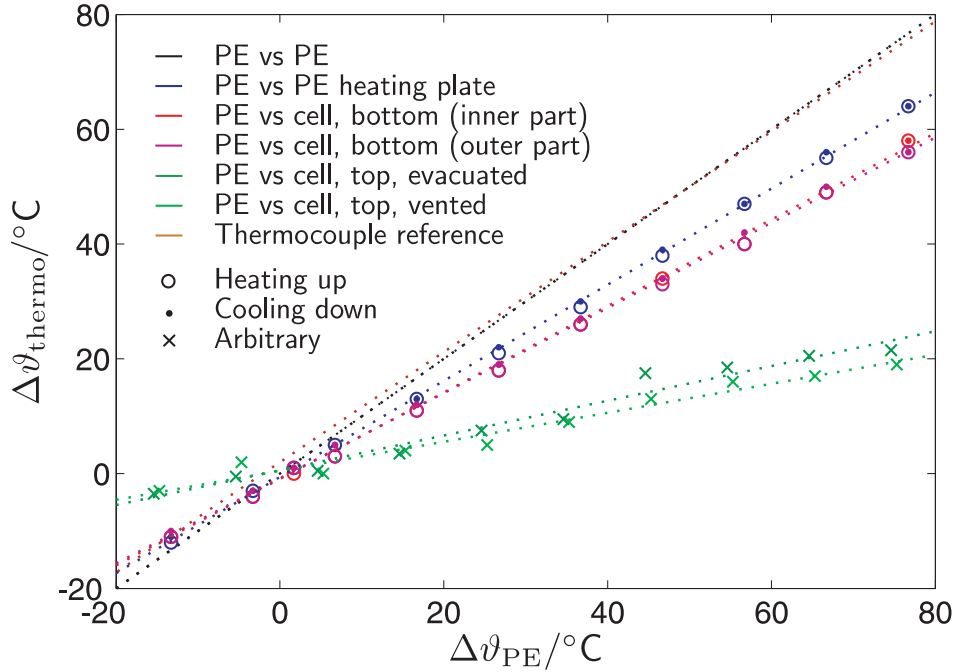
Figure 3.3.: Deviation of the temperature set at the Peltier element and the temperature measured with a thermocouple device at the heating plate of the Peltier element (PE vs PE heating plate, blue), at the bottom (PE vs cell, bottom, reddish) and the top of the sublimation cell (PE vs cell, top, greenish). Also, an ideal curve (PE vs PE, black, not observed) and the deviation of the thermocouple device from 0°C of frozen and 100°C of boiling water (thermocouple reference, brown) are shown.

element to the bottom of the cell and a good isolation of the top of the cell. Thus, an acceptable temperature gradient within the sublimation cell for crystallization can be obtained.

Low pressures assist the crystallization via sublimation in addition to a temperature gradient. It is possible to obtain pressures down to 0.01 mbar with the second version of the sublimation cell during evacuation. The leak tightness after closing the needle valve (and thus stopping the evacuation process) was tested. In Fig. 3.4 a typical leakage test with and without the sublimation cell is shown.

The setup was evacuated with a needle valve position of $8\,\mu$m until the pressure remained stable (± 0.001 mbar) for 10 seconds. Then the needle valve was closed. The pressure was measured with a baratron over a time period of 600 seconds (period of crystallization for most substances in this work) in order to observe the

sublimation cell's degree of leakage in comparison to the setup without sublimation cell. O-rings with two different cross sections (1.5 mm and 1.0 mm) were also tested. The upper green curve corresponds to the sublimation cell with a 1.5 mm o-ring connected to a T-piece. The centered curves correspond to measurements with the sublimation cell and a 1.0 mm o-ring connected to the T-piece (red) as well as to the T-piece covered with a blind flange instead of using the sublimation cell (blue). The lowest curve shows the pressure without using the T-piece nor the sublimation cell (black). The initial pressure of the setup without the T-piece or sublimation cell is the lowest (0.09 mbar and 0.06 mbar). When using the sublimation cell with the 1.0 mm o-ring the starting pressure was the same as using a blind flange on the T-piece (0.11 mbar and 0.10 mbar). The highest initial pressure was observed for the T-piece connected to the sublimation cell with a 1.5 mm o-ring (0.12 mbar and 0.11 mbar). However, initial pressures rather reflect differences in time and efficiency of pumping than tightness. The slope of all four curves is nearly equal (0.01 mbar per 100 sec) for a pressure range of 0.10–0.25 mbar, showing that the leakage rate is determined by the needle valve or the construction between needle valve and pump. It also shows that the leakage of the sublimation cell is minor in comparison to the whole construction.

A leakage test was also performed with the old version of the sublimation cell (olive + fabric tube for evacuation) (not shown). The pressure increased by a factor of 40 within the first 200 seconds (from ca. 5 mbar to ca. 200 mbar) reaching a saturation after a few minutes in the range of 1–5 mbar.

The leakage test shows a reasonable leak tightness of the sublimation cell for the crystallization via sublimation. Generally, an increase of pressure over 10 mbar was observed no earlier than 1 hour after closing the needle valve. Occasionally, a pressure less than 10 mbar was maintained for 24 hours.

Crystallization of Racemic and Deuterated Substances

Racemic compounds of methyl mandelate, norephedrine, and pseudoephedrine were crystallized by using an equal amount of both enantiomers. The enantiomers were pestled and put either in a glass tube or into the sublimation cell. Then, the glass tube or the sublimation cell was evacuated. Samples prepared in the glass tube were stored for one to ten weeks and regularly evacuated.

In order to obtain OD- or ND/OD-deuterated crystals, the pestled sample was
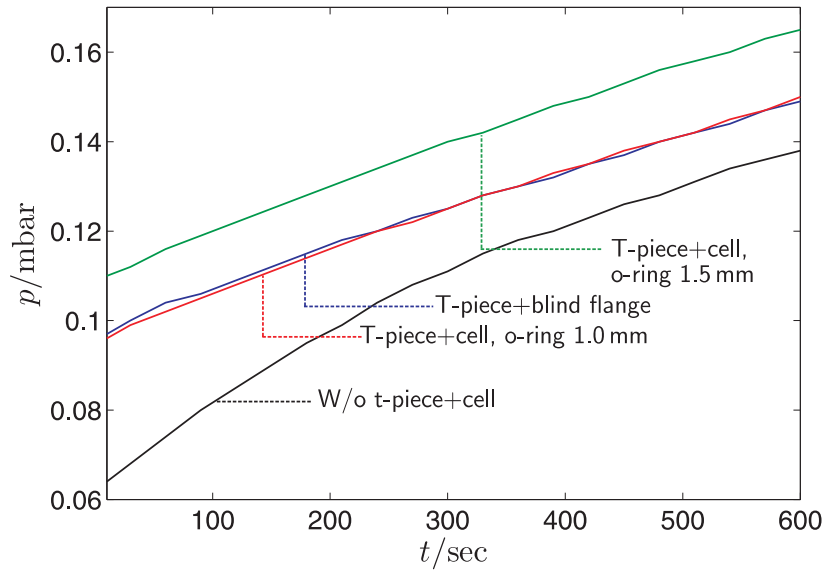
Figure 3.4.: Leakage test of the sublimation cell with a 1.5 mm and a 1.0 mm o-ring connected to a T-piece. The leakage of the T-piece with a blind flange and the leakage without the T-piece are also shown. The pressure p in mbar was recorded over a time interval t of 600 sec.

dissolved in a few drops of D_2O directly in the sublimation cell. Then, the cell was evacuated. Afterwards, the obtained amorphous or crystalline OD- or ND/OD-deuterated sample was sublimated. In these cases, the needle valve was not closed to prevent an exchange of deuterium with hydrogen from moist air and spectra were only measured directly in the sublimation cell.

3.2. Experimental Methods

A variety of spectrometric techniques was used within the framework of the present study. In order to investigate the molecular conformation and orientation of sublimated microcrystals polarization FTIR microspectroscopy was applied. Pestled solid samples without preferred orientations were recorded by FTIR-ATR spectroscopy for comparison. The relative vapor pressures of enantiopure and racemic compounds were investigated by mass spectrometry to assist the study of chirality recognition phenomena. The conformation and aggregation of small clusters were observed by using FTIR-jet and Raman-jet spectroscopy. In the following sections these setups will be described.

3.2.1. FTIR Microspectroscopy

Polarized FTIR microspectroscopy [17] was applied to investigate the molecular conformation and orientation of sublimated microcrystals (Chapters 5, 6, and 7), see also Refs. [27, 59]. The setup consists of a Vertex 70v FTIR spectrometer (Bruker Optics) and a Hyperion3000 microscope (Bruker Optics). For the sublimation of crystals a sublimation cell was constructed (Sect. 3.1). For rotation and polarization measurements a rotation device and a polarizer were available.

The Vertex 70v is an evacuable FTIR spectrometer with a cube-corner interferometer. For all microspectroscopic measurements a 12 V Globar mid infrared source and a KBr beamsplitter were used.

The optical pathway of the FTIR microscope is shown in Fig. 3.5. The microscope can be used in IR, visual (halogen light sources), and in a combined IR/Vis mode. For the measurements presented here, only the IR or the visual mode were used since the combination mode reduces the spectral quality. Three different objectives were available. A $4\times$ visual objective (glass), a $15\times$ IR/Vis objective, and a $20\times$ ATR-IR/Vis objective. The $4\times$ objective was used to get an overview, while the $15\times$ objective was used for IR measurements and for the visual pictures shown in this dissertation. The photos were taken with a color CCD camera (Sony ExwaveHAD SSC-DC80P) attached to the microscope. For the IR detection two MCT (mercury cadmium telluride) detectors were applied, which will be described in detail below. Additional options include an IR or a visual polarizer as well as an analyzer that can be placed in the optical pathway. The microscope is purged with
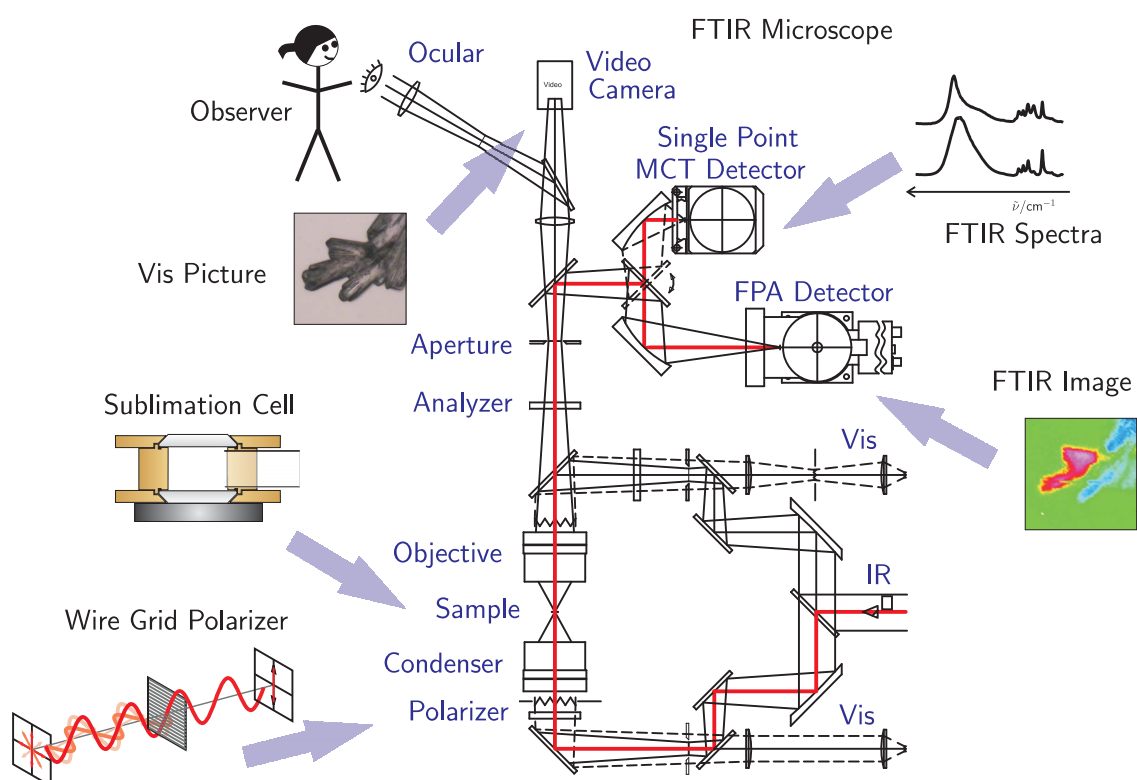
Figure 3.5.: Optical pathway and accessories of the FTIR microscope (Hyperion 3000). The original figure of the microscope provided by Bruker Optics is modified. The picture of the wire grid polarizer was taken from Ref. [60] and is slightly modified.

dry air.

For regular measurements the single element MCT detector (4000–1000 cm^{-1} with a recording area of 0.25×0.25 mm^2 and the $15\times$ IR/Vis objective were applied. The standard experiment Hyperion_transmittance.xpm (provided by Opus 6.5 [61]) with a spectral resolution of 4 cm^{-1} and an aperture of 2 mm was used. Additionally, a cutting aperture was applied to confine the area of interest. Normally, 32 or 50 scans were recorded. For a better signal-to-noise ratio 100 or 200 scans were occasionally taken.

In order to obtain chemical IR images a focal plane array (FPA) detector [62, 63] was available. The FPA detector with 64×64 elements has a recording area of 2.56×2.56 mm^2 which corresponds to a sample area of 0.170×0.170 mm^2 when applying the $15\times$ IR/Vis objective. It is a multiple MCT detector and thus covers the mid infrared region from 4000 to 1000 cm^{-1}. It can be used to obtain spatially resolved vibrational information of the sample. For measurements with the FPA detector a low pass filter and an attenuator were used. The standard experiment Hyperion_3000_FPA.xpm was applied. The aperture was set to 8 mm and 500 scans with a resolution of 8 cm^{-1} were recorded. The frame rate was set to 3773 Hz and an integration time of 0.15 ms was chosen. An offset of 230 and a gain of 1 were applied.

Crystal samples were directly measured in the closed sublimation cell or on the CaF$_2$ substrate after removing it from the sublimation cell. Occasionally, a rotation device was applied in order to measure the different faces of the crystals. Due to the small size of the sublimated crystals (10–500 μm) it was possible to record all spectra in transmission mode. A comparison of a transmission and a reflection spectrum of a sublimated (*R*)-methyl mandelate crystal is shown in Fig. 3.6. The signal-to-noise ratio is acceptable for both modes. However, the spectrum measured in transmission mode shows a superior spectral quality. In reflectance mode intense bands are attenuated.

Rotation Experiments

The microcrystals investigated in this work grow on one or two preferred faces. In order to record FTIR spectra from other faces, a rotation device was used (see Fig. 3.7). It consists of a 360° microrotation stage (Standa 7R128, 1° accuracy) and a rod of 5 cm in length and 0.5 cm in diameter. The CaF$_2$ window with a crystal
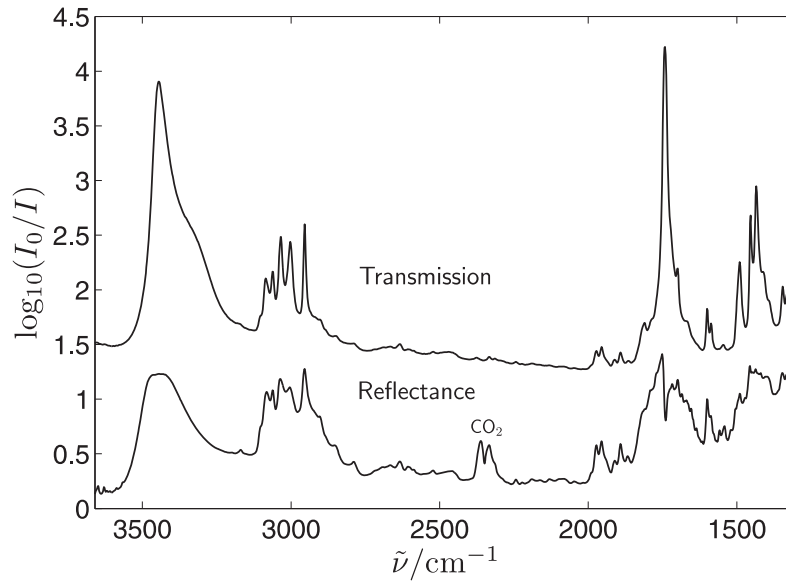
Figure 3.6.: Transmission (top) and reflectance (bottom) FTIR spectra of an (*R*)-methyl mandelate crystal on CaF$_2$ substrate. In reflection mode strong bands are attenuated.

can be glued with general purpose glue on top of the rod. The rotation device with the window can be screwed onto the *xy* stage of the microscope to prevent misalignment.

For rotation experiments, one microcrystal needs to be chosen and all others grown on the CaF$_2$ substrate need to be removed. Otherwise, there is the risk of several crystals appearing in the beam-pathway. For cleaning, a cotton bud of 2 mm diameter was used (NeoLab, 2-1022). No solvent was employed since it affects the crystal of interest. Occasionally, brushes (da Vinci Forte Basic 5/0, 135 or da Vinci Nova Synthetics 10/0, 245) were also used to remove bigger amounts of crystals.

In Fig. 3.8 visual pictures of a rotated crystal are shown. The rotated crystals exhibit a mirror image on the CaF$_2$ substrate. The right half shows the crystal, whereas the left part corresponds to its mirror image. In the following, the mirror image will not be shown.

Rotation spectra (especially along the long crystal axis, face C) exhibit large absorbances. Spectra a–g in Fig. 3.8 show the dependence of the spectral quality from the position of measurement indicated by the gray box. As expected there is no absorbance when the measured region includes the background (a and g) due to scattered light. The absorbance rises from spectrum a to c since less scattered light
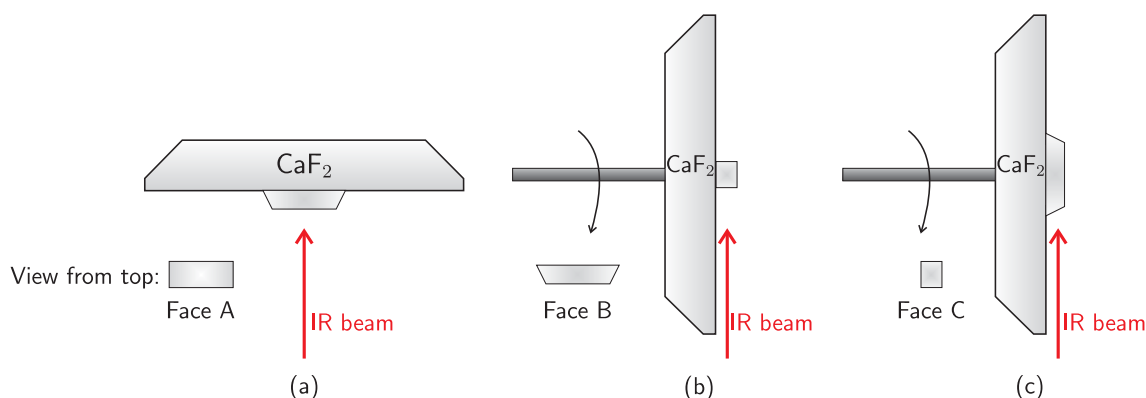
Figure 3.7.: Scheme of a CaF$_2$ window with a crystal showing face A as implemented in the sublimation cell (a) and two rotated CaF$_2$ windows with a crystal showing face B (b) and face C (c). The crystal faces at the bottom correspond to a view along the IR beam.

hits the detector. The absorbance then falls when the mirror image is also measured (d and e), although less so than expected. In spectrum f the absorbance rises again even though only the mirror image is measured. In order to explain this unusual behavior further measurements are needed.

Polarizer

FTIR polarization studies were carried out to gain information about the spatial orientation of the molecules within the crystals. For polarization measurements a ZnSe holographic wire grid polarizer (Medway Optics Ltd) was used. It is 2 mm thick and has a diameter of 25 mm (unmounted). The clear aperture is 22.5 mm in diameter. The transmitted wavelength is 1–16 μm (10000–625 cm^{-1}). A wire grid polarizer transmits light with an electric vector perpendicular to the wires. The principal transmittances of a polarizer are the transmission efficiency (K_1) and the unwanted transmission (K_2). K_1 is the optical power transmitted by the polarizer with grid lines parallel and K_2 with grid lines perpendicular to the electric vector of a polarized source. In the case of a perfect polarizer K_2 equals 0. Properties which can be derived from K_1 and K_2 are the contrast ratio (r_{contr})

$$r_{contr} = \frac{K_1}{K_2},$$ (3.1)

the extinction ratio (r_{ext}),
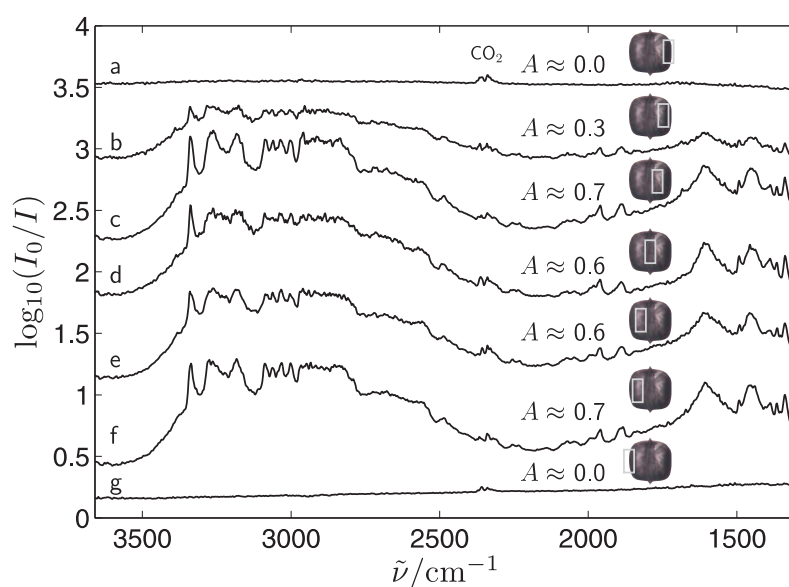
Figure 3.8.: FTIR spectra recorded at different positions of a rotated (1*S*,2*R*)-norephedrine crystal. The visual pictures show the crystal itself (right part) and its mirror image (left part). The gray box marks the spectroscopically investigated region. The absorbance *A* (maximum) of every spectrum is indicated.

Table 3.2.: The transmission efficiency (K_1), the unwanted transmission (K_2), the contrast ratio (r_{contr}), the extinction ratio (r_{ext}), and the degree of polarization (d_{pol}) of the ZnSe polarizer at $3\,\mu$m ($3333\,\text{cm}^{-1}$) and at $10\,\mu$m ($1000\,\text{cm}^{-1}$) are listed.

λ/μm	$\tilde{v}/\text{cm}^{-1}$	K_1	K_2	r_{contr}	r_{ext}	d_{pol}
3	3333	0.69	0.007	98:1	49:1	0.980
10	1000	0.72	0.002	360:1	180:1	0.994

$$r_{ext} = \frac{K_1}{2K_2} \tag{3.2}$$

and the degree of polarization (d_{pol}) [64]

$$d_{pol} = \frac{K_1 - K_2}{K_1 + K_2}. \tag{3.3}$$

Values for the used polarizer at $3\,\mu$m ($3333\,\text{cm}^{-1}$) and at $10\,\mu$m ($1000\,\text{cm}^{-1}$) can be found in Tab. 3.2. Small deviations between a nonpolarized spectrum and an average spectrum of two perpendicular polarized spectra were found to be erratic (not shown).

3.2.2. FTIR-ATR Spectroscopy

FTIR-ATR (attenuated total reflection) measurements of the substances used for microspectroscopic analysis were performed for comparison. ATR spectroscopy is based on an evanescent wave which penetrates the surface of the sample. The pestled samples used for the FTIR-ATR measurements represent a more or less perfect average over all orientations.

The FTIR-ATR measurements were performed in the sample compartment of the Vertex 70v FTIR spectrometer. The pestled sample was applied onto a diamond ATR unit (Harrick, MVP Pro-Star). For mid infrared measurements (4000–$400\,\text{cm}^{-1}$) a 12 V Globar source, a KBr beamsplitter, and a DTGS detector (deuterated triglycine sulfate) were used. The resolution was set at $4\,\text{cm}^{-1}$, the aperture at 6 mm, and the scanning velocity at 10 Hz in the standard experiment MVP-Pro_ATR_Diamond.xpm. In the cases of methyl mandelate, mandelic acid, and methyl lactate (Chapters 5 and 6) a total number of 200 scans (2·100) were recorded
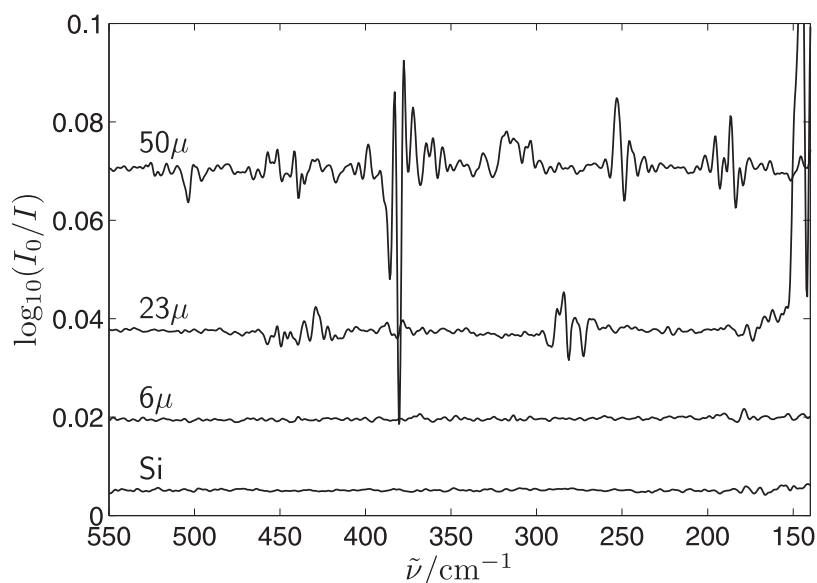
Figure 3.9.: FTIR spectra showing signal-to-noise ratios of three mylar (50μ, 23μ, and 6μ) and a massive silicon beamsplitter (Si).

whereas in the case of the phenylpropanolamines 50 scans were taken (Chapter 7).

Far infrared (FIR) measurements in combination with the diamond ATR unit were also recorded. They were performed using a 12 V or a 24 V Globar source with a massive silicon beamsplitter and a liquid helium cooled silicon bolometer (IRLab, Inc. HDL-5) in the range of $30\,\mathrm{cm}^{-1}$ to $470\,\mathrm{cm}^{-1}$. The standard experiment used was FIR-DTGS(FIRSI).xpm. The resolution was $2\,\mathrm{cm}^{-1}$ with an aperture of 8 mm and a scanning velocity of 60 kHz. A total number of 400 scans ($4\cdot100$) were averaged.

In Fig. 3.9 the performance of the massive silicon beamsplitter is compared to different mylar beamsplitters ($6\,\mu$m, $12\,\mu$m, and $50\,\mu$m multilayer). The FTIR spectra are shown in the spectral range of 550–$140\,\mathrm{cm}^{-1}$ and were measured using an FIR-DTGS detector for 100 s (16 scans). The aperture was set to 6 mm and the scan velocity to 2.5 kHz. It can be seen that the signal-to-noise ratios of the 50μ and the 23μ mylar beamsplitters are rather low and have specific minima. The signal-to-noise ratio of the 6μ beamsplitter is comparable to the ratio of the silicon beamsplitter, but the ratio is slightly worse. Furthermore, this beamsplitter is very difficult to align. All in all, the massive silicon beamsplitter shows a reasonable signal-to-noise ratio which is more or less constant in the shown spectral range.
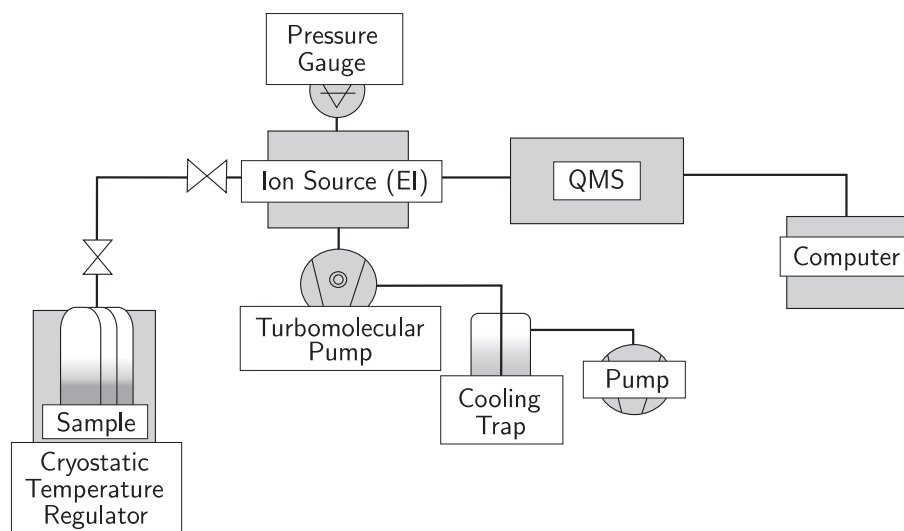
Figure 3.10.: Schematic layout of the mass spectrometer used to determine relative vapor pressures.

3.2.3. Mass Spectrometry

Mass spectrometry was employed in order to determine the relative vapor pressure of substances showing chirality recognition phenomena [38,65,66]. A layout of the setup is depicted in Fig. 3.10. It consists of a quadrupole mass spectrometer (QMS, Stanford Research Systems RGA 200). Its vacuum chamber can be evacuated by a rotary vane pump (Vacuubrand RS-4) and a turbomolecular pump (Leybold Turbovac 50) down to a pressure of 10^{-5} to 10^{-6} mbar. Solid pestled samples placed into three tubes can be temperature regulated in a bath cryostat (Haake CH/F3). The amount of vapor flowing into the mass spectrometer is regulated by a precision needle valve (HOKE Milli-Mite 13335G6Y).

The vapor is ionized in an electron impact ionizer. A Faraday cup detector measures the ion currents at an electron energy of 70 eV. It covers a range of 10^{-7} to 10^{-15} A for both positive and negative values with the same accuracy and resolution. Measurements can be performed in a range of 1 to 300 amu. The relative intensities of characteristic ion fragments were used to determine relative vapor pressures.

A specific amount of substance (usually 100 mg) was evacuated in one of the three glass tubes. Mass spectra of the intensity versus the m/z value were recorded every five minutes for about six hours. The software rga3.05 [67] which allows for scheduled measurements was used. The intensities of selected fragments were
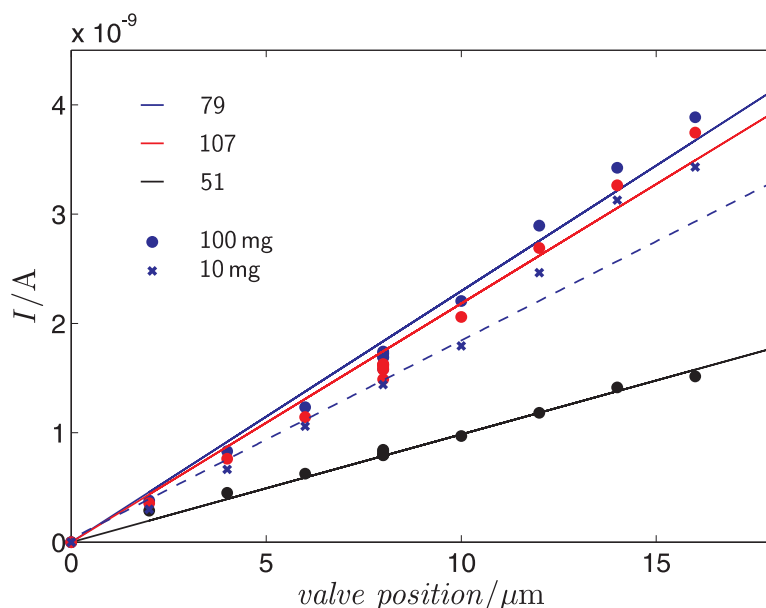
Figure 3.11.: Intensities of m/z values for different valve positions and different amounts of substance (here, racemic methyl mandelate).

automatically read and averaged with a script written in Matlab R2009b [48]. An example script can be found in Supplement C.

The optimal valve position for a stable dynamical equilibrium of leakage into the chamber and pumping-off was determined by performing a series of measurements with different valve positions. 100 mg and 10 mg of the test substance (racemic methyl mandelate) were thermostated at 20°C. Mass spectra were recorded at different valve positions every two minutes for 30 minutes. The average intensity of the peaks at an m/z value of 51, 79, and 107 are plotted against the setting of the needle valve in Fig. 3.11. The intensity increases linearly for larger openings of the valve. This shows that the stream of vapor is thermodynamically controlled. In the case of a kinetically controlled process, a leveling off of the intensities would be expected. To verify the results, measurements were also performed at a temperature of 5°C leading to the same results (not shown). A stable dynamical equilibrium of leakage was obtained after an induction period of a few minutes. Fig. 3.11 also shows that an amount of 10 mg leads to a bigger divergence of the linear fit. Furthermore, the intensity breaks down at a valve position of 18 μm.
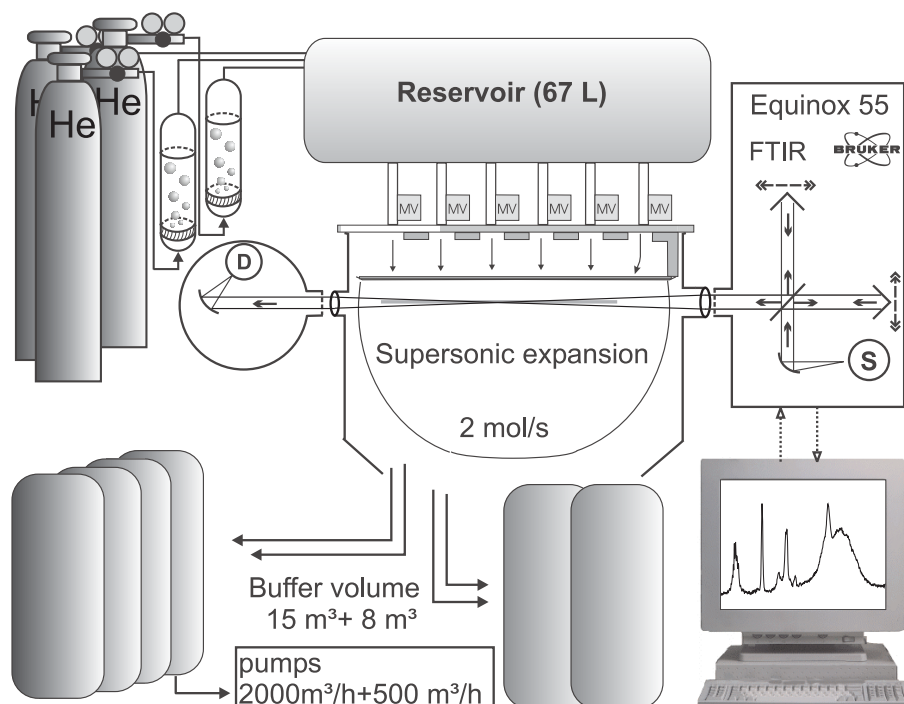
Figure 3.12.: Schematic layout of the filet-jet taken from Ref. [71], modified.

3.2.4. Jet Spectroscopy

Jet spectroscopy is used for the spectroscopic investigation of isolated monomers and small clusters [68–70]. The adiabatic expansion from a higher to a lower pressure region causes the temperature to lower significantly. Especially, the translational and rotational temperatures are lowered and the Doppler broadening is reduced. The use of a noble gas (here helium and argon in helium) allows for a more efficient cooling. Vibrational spectra are simplified and can be more easily compared to quantum chemical calculations.

Two jet setups were used in the framework of the present work. One is based on FTIR and the other on Raman spectroscopy. Both setups will be briefly explained below.

FTIR-Jet Spectroscopy

FTIR-jet spectroscopic measurements were performed using the filet-jet (**fi**ne but **le**ngthy, a description of the nozzle). A scheme of the setup is shown in Fig. 3.12. Detailed descriptions of the setup can be found in Refs. [71–74].

The substances of interest can be heated in two saturators which are purged with a carrier gas (helium). The gaseous mixture is then filled into a reservoir of 67 L volume using magnetic valves. The concentration was lowered by a third stream of the carrier gas to traces of up to 0.6%. Relative concentrations were roughly estimated based on relative intensities, vapor pressures, and mixing ratios. After reaching the stagnation pressure of 1 bar, the gas mixture is directed over six magnetic valves into a prechamber ensuring a homogeneous expansion. The mixture is then expanded through a high-throughput slit nozzle of 600 mm length and a width of 0.2 mm into the jet chamber (stainless steel, 776 mm length, 400 mm diameter). The jet chamber is connected to a buffer volume of 23 m^3 which keeps the background pressure at less than a few mbar. After evacuating the jet chamber (2500 m$^3 \cdot$h^{-1}) the magnetic valves are opened again and another expansion is induced.

FTIR scans were performed with an Equinox 55 FTIR spectrometer (Bruker Optics). In the meantime, this spectrometer has been replaced by the evacuable IFS66v/S which shows a better signal-to-noise ratio. The beam is aligned perpendicular to the direction of propagation to attain a long distance of absorption. For every pulse, a total of 25 scans are recorded. The first 20 scans are carried out before every gas pulse and averaged into one background spectrum. Two scans before and two after every gas pulse are used for control measurements. 150–200 pulse scans were averaged to improve the signal-to-noise ratio. Further parameters are listed in Supplement D.

Raman-Jet Spectroscopy

Raman-jet measurements were performed with the curry-jet (**c**lassical **un**restricted **R**aman spectroscop**y**). Four variants of the curry-jet were used within the present studies. Detailed parameters of the variants are listed in Supplement D. A schematic layout of the curry-jet is shown in Fig. 3.13.

A gaseous mixture is produced by running a carrier gas (helium or argon) through two temperature controlled saturators filled with the substances of interest. The pressure was set at 1.5 bar, but decreased during measurements to 1.0–1.1 bar. The expansion takes place through a 4.0 × 0.15 mm^2 slit nozzle into a jet chamber. The jet chamber is evacuated by a 250 m$^3 \cdot$h^{-1} roots pump backed up by a 100 m$^3 \cdot$h^{-1} rotary vane pump. In the newest version of the curry-jet a 500 m$^3 \cdot$h^{-1} roots pump has been added to increase the pumping capacity.
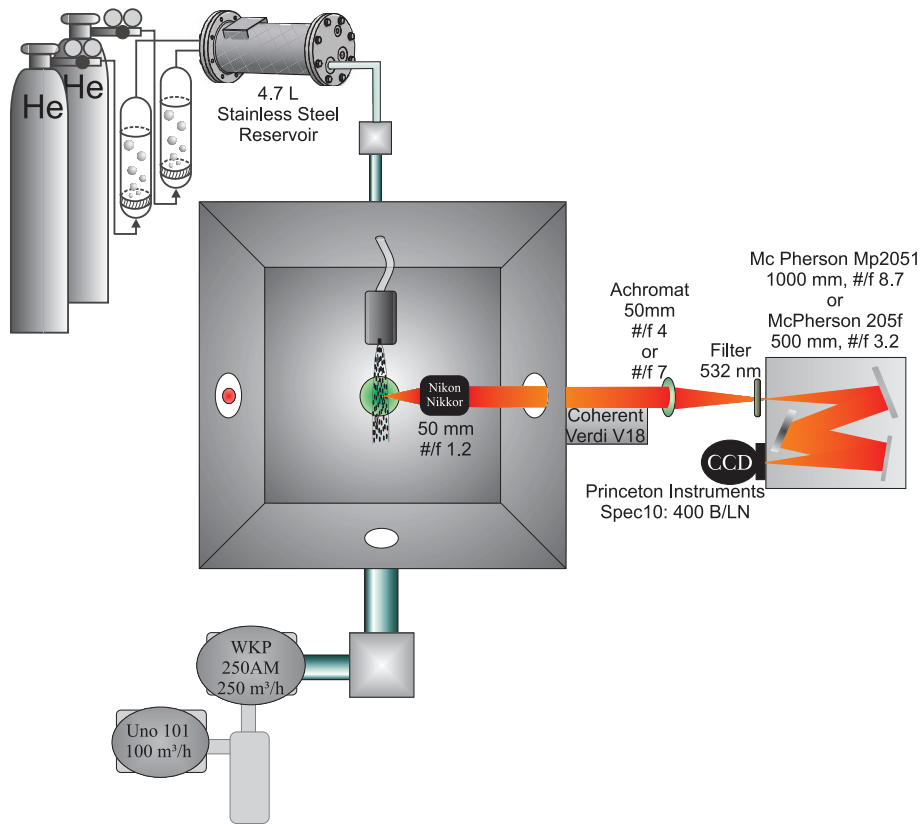
Figure 3.13.: Schematic layout of the curry-jet taken from Ref. [75], modified.

An 18 W 532 nm Nd:YVO$_4$ laser source is focused by a planoconvex lens on the jet expansion. A McPherson Inc. Model 2051 monochromator or a McPherson 205f spectrograph disperses the scattered radiation onto a Princeton Instruments Spec-10:400B/LN CCD camera. Wavelength calibrations were carried out with Ne atomic fluorescence lines. The absolute wavenumber scale is expected to be accurate within 1–2 cm^{-1}. An average of four to twelve independent acquisitions with an integration time of 200–600 s was smoothed to gain the final spectra. For a more detailed description see Refs. [11, 14, 75–80].

3.3. Theoretical Methods

Theoretical methods were applied to assist the vibrational interpretation. In the following, the performed quantum chemical calculations will be described. Data treatment to obtain FTIR images will also be illustrated. All spectra recorded with the single element MCT detector and with the ATR device are shown without any postprocessing. For the treatment of the Raman-jet spectra see Refs. [75, 81].

3.3.1. Quantum Chemical Calculations

Quantum chemical calculations were performed to assist the assignment of experimental bands to different vibrational modes and to different clusters. The calculations provide information on the energy of a given conformation or cluster, their vibrational modes and frequencies, as well as the *x*-, *y*-, and *z*-components of the dipole derivatives. Quantum chemical calculations were performed for the sublimated crystals investigated by FTIR-microspectroscopy and for mixed alcohol-water clusters investigated by Raman- and FTIR-jet spectroscopy.

Sublimated Crystals

For the FTIR-microspectroscopic studies frequency calculations including dipole derivatives were performed on geometrically optimized (fully relaxed) structures of the most stable monomer conformations in the gas phase (structure provided by Refs. [38, 82–87]) as well as on conformations taken from the crystal structures [38, 88–92]. Harmonic calculations were performed with the Gaussian03 program suite [93] employing B3LYP with the 6-311++G(3df,2p) basis set and the MP2 level with the 6-311+G(2d,p) basis (not employed in the case of the phenylpropanolamines). The calculated harmonic wavenumbers are scaled by a universal best fit factor of 0.966 which accounts for neglected anharmonicity in X-H stretching fundamentals and deficiencies of the B3LYP method.

In the case of methyl mandelate partly optimized structures (1–5 optimization steps) taken from the crystal structure [38] were also used. The conformations of these partly optimized structures are closer to the conformation of the frozen monomer than the fully relaxed monomers. For the partly optimized methyl mandelate monomers with 1–5 optimization steps no reasonable partial convergence was found. The O-H stretching wavenumbers listed in Tab. 3.3 show an erratic con-

Table 3.3.: Predicted harmonic wavenumbers of the O-H stretching mode ω(O-H) in cm^{-1} and energy differences without and with zero point energies (ΔE and ΔE_0) in kJ·mol^{-1} of the frozen monomer, monomer optimized in 1–5 steps as well as the fully relaxed monomer taken from the crystal structure of enantiopure methyl mandelate and the most stable monomer [38].

	Frozen	Step 1	Step 2	Step 3	Step 4	Step 5	Fully relaxed	Most stable
ω(O-H)	5934	4931	3764	3803	3836	3858	3835	3723
ΔE	366.6	132.2	23.4	20.9	20.7	18.4	15.4	0.0
ΔE_0	370.9	131.6	21.4	19.6	19.8	17.0	14.6	0.0

vergence. As a result, only frequencies from fully relaxed structures are used in this work.

Alcohol-Water Cluster

Conformational Raman and IR frequency calculations were performed on small water-alcohol cluster with the Gaussian03 program suite [93]. The levels of harmonic calculations employed in this work (with their abbreviations given in parenthesis) include B3LYP/6-311+G(d) (B3-S), MP2/6-311+G(d) (MP2-S), MP2/6-311++G(2d,p) (MP2-M), and MP2/6-311++G(3df,2p) (MP2-L). S, M, and L indicate small, medium, and large basissets, respectively.

To compensate empirically for some deficiencies in the electronic structure treatment and other effects, the average of the corresponding harmonic O-H stretching wavenumbers ω(th,n) calculated at the MP2-S and MP2-M levels was used. This ad hoc choice should be viewed as a pragmatic interpolation approach in the absence of more rigorous systematic calculations, including larger clusters.

The average harmonic dimer and trimer O-H stretching wavenumbers ω(th,n) were shifted by the difference between the experimental water dimer donor wavenumber $\tilde{v}_{\mathbf{ww}}$(exp) (3602 cm^{-1} for $(H_2O)_2$ in the IR and Raman case, 2632 cm^{-1} for $(D_2O)_2$) and the corresponding harmonic wavenumber prediction $\omega_{\mathbf{ww}}$(th) (see Supplement E):

$$\tilde{v}(\text{th},n) = \omega(\text{th},n) + \tilde{v}_{\mathbf{ww}}(\text{exp}) - \omega_{\mathbf{ww}}(\text{th}) \qquad (3.4)$$

Zero point energy corrections to binding energies were estimated in the harmonic approximation. This may not be a satisfactory approximation for the large ampli-

tude torsions and for intermolecular degrees of freedom [94].

IR intensities *I* were calculated as integrated band strenghts in units of km·mol^{-1}. Raman intensities depend on the wavenumber of the used laser $\tilde{v}_0$. Differential scattering cross sections σ' in units of m^{2}sr^{-1} can be calculated using the calculated scattering activities A_{Raman} [75]:

$$\sigma' = \frac{2\pi^2 h}{45c\tilde{v}_k} \cdot \frac{(\tilde{v}_0 - \tilde{v}_k)^3 \tilde{v}_0}{1 - e^{\frac{-hc\tilde{v}_k}{kT}}} \cdot g_k A_{\text{Raman,k}} \tag{3.5}$$

Since the investigated vibrational energies are much higher than the thermal excitation in the jet, $hc\tilde{v}_k >> kT$ was assumed.

3.3.2. FTIR Images

To obtain the FPA-FTIR chemical images shown in this work two wavenumber regions were integrated using the baseline corrected integration method of OPUS 6.5 [61] and then subtracted using a prefactor to maximize the contrast between the two wavenumber regions. The integrated areas are chosen according to spectral differences of the substances.

In the case of methyl mandelate the regions of 3018–2982 cm^{-1} (H for high) and 2972–2934 cm^{-1} (L for low) were integrated. Twice the integral absorption of region H was subtracted from the integral of region L (L−2·H). Blue colors show a higher intensity of bands in the 3018–2982 cm^{-1} region, whereas red colors refer to a higher intensity in the 2972–2934 cm^{-1} region. Absorption free regions and regions with balanced intensities in the 3018–2982 cm^{-1} and 2972–2934 cm^{-1} windows are shown in green (BG).

In order to obtain chemical images of mandelic acid, the regions 3120–3100 cm^{-1} (H) and 3100–3080 cm^{-1} (L) were integrated. Three times the integral of region H was subtracted from the integral of L (L−3·H). Blue colors show a higher band intensity in the 3120–3100 cm^{-1} region, while red colors correspond to a higher intensity in the 3100–3080 cm^{-1} region.

The chemical images of pseudoephedrine were obtained by subtracting the integrated region of 3335–3310 cm^{-1} (Enant) from the integrated region of 3310–3290 cm^{-1} (Rac, Rac−Enant). Thus, higher band intensities in the region of 3335–3310 cm^{-1} are shown in blue and in the region of 3310–3290 cm^{-1} in red colors.

4. Alcohol-Water Clusters

Ethanol is the smallest organic molecule which shows conformational isomerism. There are three stable conformers, a trans conformer and two less stable gauche conformers, gauche+ and gauche− (see Fig. 4.1). This conformational preference is partially modified in the crystal which contains one trans and one gauche− ethanol conformation in the asymmetric unit [95]. The molecule adopts to its environment. Small ethanol clusters [10, 80] and ethanol-water [11, 14] clusters are elementary model cases to study such an adaptive aggregation.

Alcohol-water mixtures show some anomalies on the macroscopic scale [96], such as volume contraction [97, 98] and asymmetric heats of mixing [99, 100]. The anomalies are expected to emerge at a nanoscopic scale, at the level of hydrogen bonded clusters [101]. Alcohol-water mixtures are of great importance for industrial purposes and in daily life. Especially, ethanol-water mixtures are widely known for their neuroactive effects.

So far, remarkably little is known about the conformations and interactions within the smallest building blocks of aqueous solutions of the two simplest alcohols, methanol and ethanol. The structure of the methanol-water dimer was unravelled by microwave spectroscopy [102]. The methanol-water dimer and larger clusters were investigated by matrix isolation infrared spectroscopy [103]. Vacuum isolation studies, which lend themselves better to direct comparison between theory and
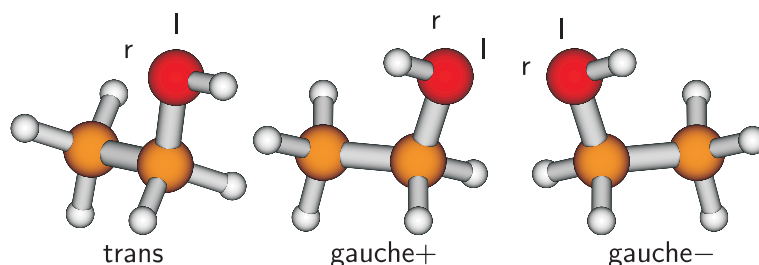
Figure 4.1.: Illustration of trans, gauche+, and gauche− ethanol conformations and the right (r) and left (l) lone pairs.

experiment, were started in the framework of the author's *Hausarbeit im Rahmen der Ersten Staatsprüfung für das Lehramt an Gymnasien* [81] and continued within the present project [11, 14, 75]. The sparsity of experimental data results from the absence of a suitable UV chromophore which would allow for sensitive double-resonance spectroscopy approaches. VUV double resonance techniques might be feasible but are still in their infancy [104] and do not always provide faithful infrared spectra [105].

In the following, the conformational preferences during adaptive aggregation of small methanol-water and ethanol-water clusters investigated by Raman- and FTIR-jet spectroscopy in the O-H stretching region will be analyzed. Concentration and relaxation studies as well as measurements of isotope labeled mixtures will be shown. Quantum chemical calculations of mixed methanol- and ethanol-water dimers to tetramers for structural investigations and for the assistance of the vibrational assignments will be presented.

The main results of this chapter are published in Refs. [11, 14]. Verbatim citations are used with permission of all co-authors. Results on relative donor/acceptor strengths, weak secondary hydrogen bonds, tunneling processes in acceptor lone pair switching, and thermodynamic anomalies are elucidated in Refs. [11, 14] and will not be repeated in this chapter.

4.1. Preliminary Considerations

Water and the alcohols methanol and ethanol possess a hydroxy group which can simultaneously act as a proton donor and acceptor for hydrogen bonding. In the case of water two hydroxy groups are present and therefore, hydrogen bonded networks can be established [106]. In the following, the hydrogen bond donor within a dimer will be named first and the acceptor second. The abbreviations **a** for alcohol, **m** for methanol, **e** for ethanol, and **w** for water will be used. Thus, **wm** names a dimer in which water takes the role of the proton donor and methanol the acceptor. The sequence of letters is irrelevant for higher cyclic clusters. In the case of ethanol the trans, gauche+, and gauche− conformations need to be considered. The abbreviations $\mathbf{e}_t$, $\mathbf{e}_{g+}$, and $\mathbf{e}_{g-}$ are used. There are two free electron pairs of each acceptor oxygen atom differentiated as right (r) and left (l) lone pairs (see Fig. 4.1). In case of cyclic structures, the molecules may point up (*u*) and down (*d*) with respect to
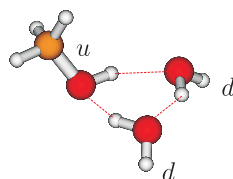
Figure 4.2.: Illustration of a methanol molecule pointing up (*u*) and two water molecules pointing down (*d*) the ring's plane.

the ring's plane (Fig. 4.2). The formation of hydrogen bonds, the presence of iso-merism, and the arrangement of molecules influence the conformation of the mixed clusters and also the position of the O-H stretching band. The latter can be used to unravel the conformation of the clusters.

There are numerous quantum-chemical calculations for methanol, ethanol and their complexes with water available in the literature. Results for methanol-water dimers can be found in Refs. [94, 107–115], among others. Data for higher clusters are summarized in Refs. [110, 113, 116], whereas simulations on aqueous methanol mixtures are described in Refs. [117, 118]. Calculations for mixed ethanol-water dimers are presented in Refs. [107, 108, 112, 115, 119, 120]. Others also per-formed studies on higher ethanol-water clusters (e.g. see Refs. [116, 121–123]). In the present work, some of these calculations had to be repeated and com-plemented in order to obtain all the information relevant for this study. E.g. in Refs. [107, 115, 120, 121] conformational isomerism of ethanol is not considered. Refs. [108, 112] distinguish between trans and gauche ethanol but do not take into account the gauche+ and gauche− variants which are spectroscopically distinguish-able in mixed dimers. Additionally, Raman intensities were rarely calculated or a given level of approximation was not available for both alcohols.

To identify trends between methanol and ethanol in this work, reliable compar-isons are indispensable. Calculations were carried out for all conceivable dimer structures (**aw** and **wa** including torsional variants). In the case of ethanol, the dif-ferent conformers were considered. For mixed cyclic trimers (**aaw** and **aww**) no systematic calculations on all possible conformers were carried out due to expected and experimentally confirmed spectral overlap. Only clusters with the right electron pair being the hydrogen bond acceptor are considered since they are spectroscopi-cally indistinguishable from their mirror images involving the left electron pair in the hydrogen bond. For further details on the selection of calculated structures see

Ref. [81]. Predicted harmonic wavenumbers are summarized in Supplement E.

Predicted intensities were modified taking into account the approximate alcohol mole fraction $x_\mathbf{a}$ as well as the number of possible conformers. The probability p for a given cluster type was estimated by a binominal distribution, leading to the following equations for dimers:

$$
\begin{aligned}
p_{\mathbf{ww}} &= (1-x_\mathbf{a})^2 \\
p_{\mathbf{wa}} &= (1-x_\mathbf{a}) \cdot x_\mathbf{a} \\
p_{\mathbf{aw}} &= x_\mathbf{a} \cdot (1-x_\mathbf{a}) \\
p_{\mathbf{aa}} &= (x_\mathbf{a})^2
\end{aligned}
\tag{4.1}
$$

and trimers:

$$
\begin{aligned}
p_{\mathbf{www}} &= (1-x_\mathbf{a})^3 \\
p_{\mathbf{aww}} &= 3 \cdot x_\mathbf{a} \cdot (1-x_\mathbf{a})^2 \\
p_{\mathbf{aaw}} &= 3 \cdot (x_\mathbf{a})^2 \cdot (1-x_\mathbf{a}) \\
p_{\mathbf{aaa}} &= (x_\mathbf{a})^3
\end{aligned}
\tag{4.2}
$$

To account for the lower abundance of trimers relative to dimers in the supersonic expansions, empirical intensity scaling factors are applied for the simulated spectra. For the methanol-water trimers, intensity scaling factors of $\frac{1}{2}$ and $\frac{1}{4}$ are applied for the simulated Raman and IR spectra, respectively. For the ethanol-water trimers, an intensity scaling factor of $\frac{1}{4}$ is applied for both the simulated spectra. Furthermore, the average intensities predicted by the MP2-S and MP2-M levels were used for the simulated spectra (see Figs. 4.5, 4.7, and 4.10 later on), based on the relative intensity information σ_{rel} and I_{rel} gathered in Supplement E.

4.2. Methanol-Water

Fig. 4.3 provides an overview of the O-H stretching region of the mixed methanol-water system comparing Raman- and FTIR-jet spectra with assignments of the corresponding clusters. Bands appearing in the spectra of the mixed system but not in the pure ones are assigned to mixed clusters. A list of assigned bands can be found
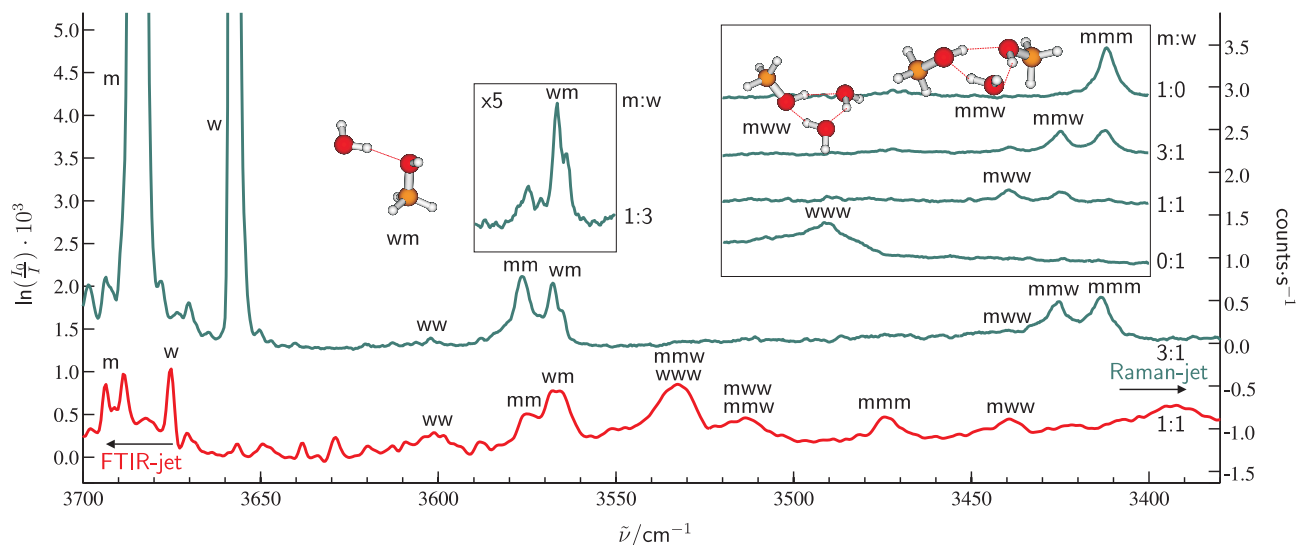
Figure 4.3.: Raman- and FTIR-jet spectra of the mixed methanol-water system in the O-H stretching region. Absorbance magnification factors are shown in the insets, which share the wavenumber scale of the main spectra. The left inset shows the effect of reduced methanol concentration, helping in the mixed dimer assignment. The right inset shows the evolution of mixed trimers with increasing methanol-to-water ratio.

in Tab. 4.1. Small IR/Raman differences of band positions are within the Raman calibration accuracy.

The mixed band near 3567 cm^{-1} appears in Raman- and FTIR-jet spectra, consistent with a dimer origin. It corresponds to the band at 3508 cm^{-1} observed in size selected ternary benzene-methanol-water trimers [125]. Two dimers **mw** and **wm** are found at all levels of calculation (see Fig. 4.4). For a better comparison between experimental and calculated spectra, the harmonic predictions of both dimers (see Supplement E) are shown in Fig. 4.5. On top an experimental Raman-jet spectrum and at the bottom the experimental FTIR-jet spectrum from Fig. 4.3 is repeated. In between, relative Raman scattering powers σ_{rel} and IR band strengths I_{rel} of mixed and pure clusters are plotted as stick spectra (for the scaling procedures see Sect. 3.3). The O-H stretching band of **mw** is predicted at higher wavenumber than **ww** where no band is observed, whereas the predicted red shift of **wm** matches the new band emerging in the mixed system. The associated intensity transfer from the relaxation of **mw** into **wm** is indicated by dotted arrows and lines in Fig. 4.5c. This conformational preference is in agreement with most quantum chemical calculations [94, 107, 109, 120, 126, 127] (but not at the B3-S and MP2-S levels) as well as

Table 4.1.: Experimental FTIR- and Raman-jet O-H stretching band positions $\tilde{\nu}$ in cm^{-1} together with proposed assignments for pure and mixed methanol-water dimers, trimers, and tetramers as well as for pure and mixed deuterated methanol-deuterium oxide dimers and trimers.

Assignment	$\tilde{\nu}_{FTIR}$	$\tilde{\nu}_{Raman}$
ww	3602	3602
mm	3575	3577
wm	3567	3568
wm (shoulder)		3565.5
www, mmw	3533	
mww, mmw	3514	
www		3491
mmm	3475	
mww	3439	3440
mmw		3425
mmm		3414
w_4	3400[a]	
w_4		3341[b]
m_4	3294	
m_3w (?)		3239
m_4		3212
w_5	3355[a]	
w_5		3311[c]
m_4w (?)		3191
m_5		3167
mm (deuterated)		2637
ww (deuterated)		2632
wm (deuterated)		2611
www (deuterated)		2557[b]
mmm (deuterated)		2530
mww (deuterated)		2526
mmw (deuterated)		2526

[a]See also Ref. [124]
[b]Average of two components at 3334 and 3347 cm^{-1} [77]
[c]Tentative assignment [77]
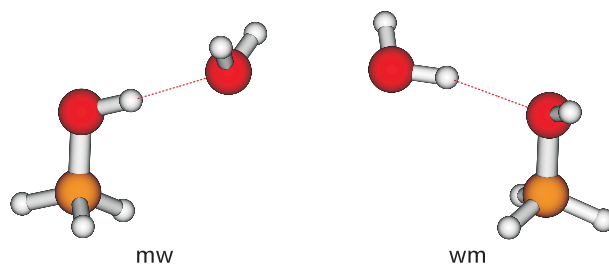
Figure 4.4.: Structures of the **mw** and **wm** dimer configurations at MP2-L level.

microwave spectroscopic investigations [102]. In cryogenic argon matrices, **wm** is also found to be the most stable dimer isomer [103, 126], whereas nitrogen matrices change this donor/acceptor preference [103, 128]. Diffusion Monte Carlo simulations for **wm** and **mw** have shown that the stability of the mixed dimers also depends on the zero point energy for the hindered internal rotation of the monomers [94]. The methanol hydroxy group is engaged in the hydrogen bond in **mw**. Thus, its torsion mode is more restricted than in **wm** and blue shifted. Its contribution to the zero point energy is thus strongly augmented, which contributes to the reduced stability of **mw** compared to **wm**.

In the central part of Fig. 4.3 the **wm** dimer region from a Raman measurement with relative concentration of **m:w**≈1:3 (magnified by a factor of five) is also shown. The **wm** band persists, whereas the **mm** band decreases compared to the spectrum with a **m:w** ratio of 3:1. By taking a closer look at the **wm** band a hardly resolved splitting of approximately $2.5\,\mathrm{cm}^{-1}$ between a more intense band at $3568.0\,\mathrm{cm}^{-1}$ and a less intense one at $3565.5\,\mathrm{cm}^{-1}$ can be noticed. This splitting is not resolved in the corresponding IR spectrum due to more extensive rotational contours. Since the splitting cannot be traced back to conformational or donor-acceptor isomerism (see Refs. [14, 75]), a tunneling process is the probable cause. To further investigate this hypothesis, measurements with OD-deuterated methanol and deuterium oxide were carried out. Raman jet spectra of the O-D stretching region are shown in Fig. 4.6. The theoretical prediction shown in Fig. 4.7 is again unambiguous in terms of the donor/acceptor preference. The corresponding **wm** band was observed at $2611\,\mathrm{cm}^{-1}$. No splitting can be resolved in the O-D stretching spectra. Therefore, a mass-independent cause for the splitting in the O-H stretching region can be excluded. The most likely reason for the splitting seems to be an exchange of the water donor between the methanol acceptor lone pairs (see Refs. [14, 75]).
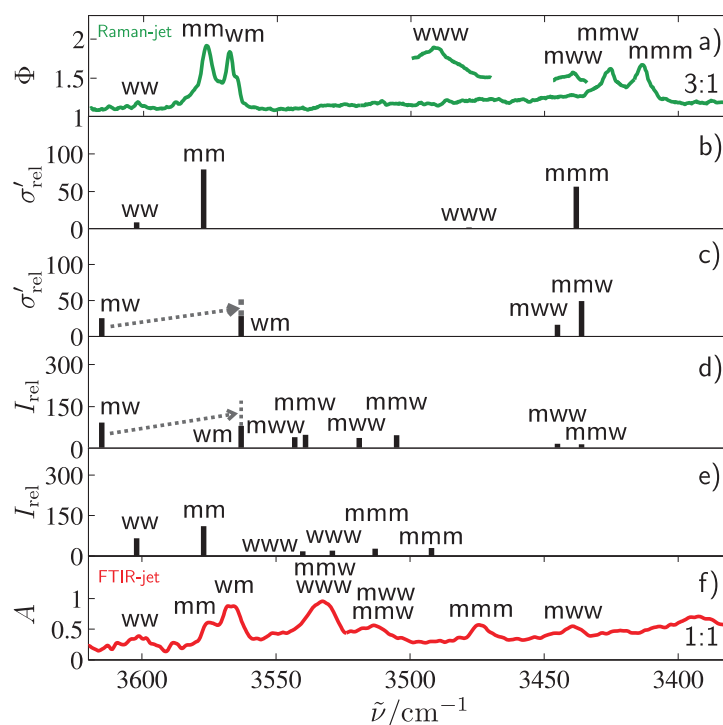
Figure 4.5.: Comparison of calculated (MP2-S/MP2-M average) and experimental Raman and FTIR spectra of pure and mixed dimers and trimers of the methanol-water system: a) Raman-jet (Φ in counts·s^{-1}), b) Raman prediction for pure clusters (σ'_{rel} in 10^{-36}·m^2·sr^{-1}), c) Raman prediction for mixed clusters (σ'_{rel} in 10^{-36}·m^2·sr^{-1}), d) IR prediction for mixed clusters (I_{rel} in km·mol^{-1}), e) IR prediction for pure clusters (I_{rel} in km·mol^{-1}), f) FTIR-jet ($A=\ln(\frac{I_0}{I}) \cdot 10^3$). For the scaling procedure, see Sect. 3.3. In the trimer case, the most stable MP2-M structure with two equal molecules pointing into the same direction (Fig. 4.2) is used for the stick spectra.
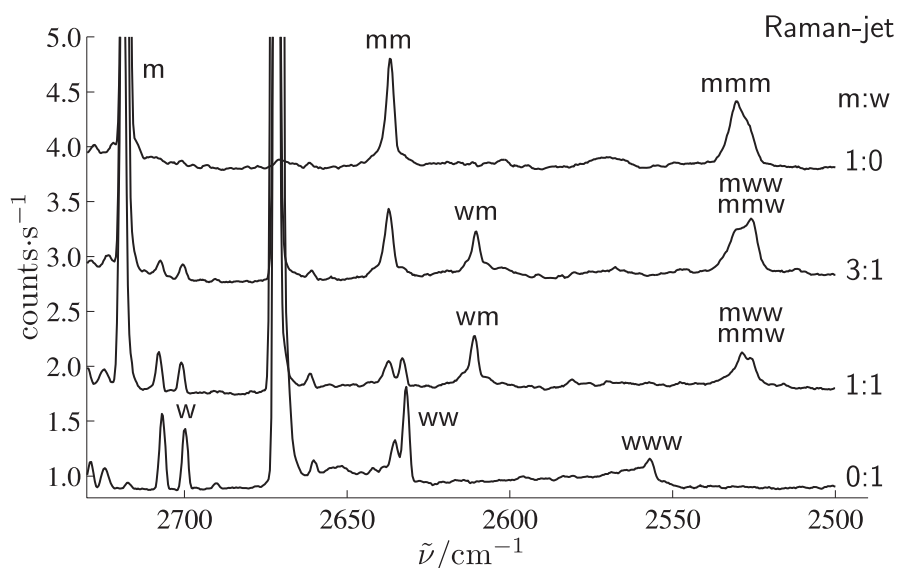
Figure 4.6.: Raman-jet spectra of the mixed deuterated methanol-deuterium oxide system in the O-D stretching region.
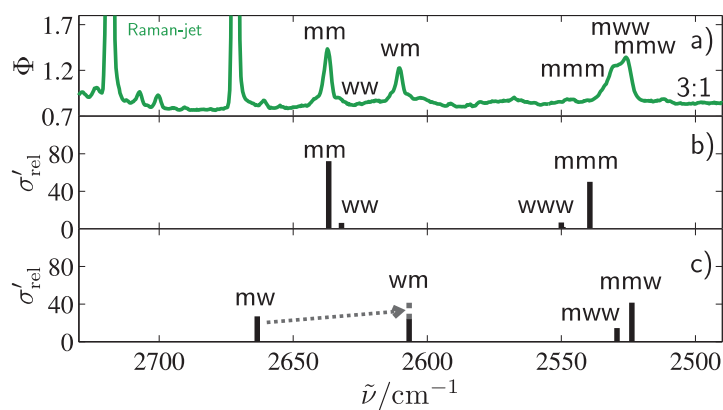
Figure 4.7.: Comparison of calculated (MP2-S/MP2-M average) and experimental Raman spectra of pure and mixed dimers and trimers of the deuterated methanol-deuterium oxide system: a) Raman-jet (Φ in counts·s^{-1}), b) Raman prediction for pure clusters (σ'_{rel} in 10^{-36}·m^2·sr^{-1}), c) Raman prediction for mixed clusters (σ'_{rel} in 10^{-36}·m^2·sr^{-1}). For the scaling procedure, see Sect. 3.3.

The more challenging trimer signatures are shifted further to low frequency. Due to their cyclic, quasisymmetric nature, largely different Raman and IR intensities for the individual O-H stretching bands can be expected. Concerted stretching [78] leads to the lowest frequency band with a large change in polarizability. The IR intensity profits from out-of-phase vibration of the three coupled oscillators. There is no obvious localization of the vibrational amplitude on either water or methanol. To discriminate among trimers of different compositions, Raman-jet results for different ratios of water and methanol are shown in the box in the upper-right corner of Fig. 4.3. Adding small amounts of water to methanol leads to the appearance of a band at $3425\,\text{cm}^{-1}$ (**mmw**). With more water, a mixed trimer band at $3440\,\text{cm}^{-1}$ is observed (**mww**). This **mww** feature can also be found in the FTIR-jet spectra at $3439\,\text{cm}^{-1}$, together with at least two new trimer bands which require quantum chemical predictions for a tentative assignment.

There is considerable isomerism expected for mixed methanol-water trimers despite the complete absence of competitive non-cyclic structures, as inferred experimentally from the analogous methanol case [129] and theoretically in many studies [107, 110, 111, 113]. This is somewhat different when a benzene chromophore is attached. In all cases, one unit (arbitrarily) points above the hydrogen bonded ring (*u*) and two below (*d*) in the most stable structure (Fig. 4.2). At B3LYP level, the two *d* units preferentially belong to different species, whereas MP2 calculations predict the two *d* units to be the same in the most stable variant (see Tab. 4.2). However, the differences are only on the order of 0.1 to $0.3\,\text{kJ·mol}^{-1}$ and therefore, emphasis will be given on the MP2 preference in the following. The full set of trimer results is summarized in Supplement E. There is a systematic increase of the trimer dissociation energy with increasing methanol content as expected based on dispersion energy contributions and also the trend in the dimers. Note, that the B3-S approach almost fails in reproducing this trend (Tab. 4.2).

The quality of the harmonic wavenumber predictions can be tested for the Raman active bands, which are straightforward to assign based on the experimental data. There, a large wavenumber shift from **www** to **mww** followed by smaller shifts in the same direction for **mmw** and **mmm** can be found. This is not fully reflected in the MP2 prediction shown in Fig. 4.5, where **mmw** even overshoots **mmm** slightly. However, the predicted shifts are within $20–30\,\text{cm}^{-1}$ of experiment, which is reasonable at this elementary level of theory.

As shown in traces d) and e) of Fig. 4.5, the IR situation is considerably more

Table 4.2.: Differences of zero point corrected dissociation energies of pure and mixed methanol-water trimers ΔD_0 in kJ·mol^{-1}. Numbers in parentheses refer to the OD-deuterated clusters.

	$w_d w_d w_u$	$m_d w_d w_u$	$m_u w_d w_d$	$m_d m_u w_d$	$m_d m_d w_u$	$m_d m_d m_u$
B3-S	0.00	-1.03	-0.88	-1.48	-1.30	-1.82
		(-0.29)	(-0.50)	(-1.18)	(-1.25)	(-2.08)
MP2-S	0.00	-2.27	-2.59	-4.83	-4.92	-7.26
		(-1.26)	(-1.48)	(-2.48)	(-2.69)	(-3.72)
MP2-M	0.00	-4.16	-4.39	-8.41	-8.58	-12.85
		(-3.06)	(-3.20)	(-6.09)	(-6.31)	(-9.44)
MP2-L	0.00	-5.24	-5.48	-10.68	-10.81	-16.21
		(-4.26)	(-4.30)	(-8.54)	(-8.73)	(-13.09)

congested with up to 8 new trimer transitions expected, due to the lifting of the C_3 symmetry degeneracy. A comparison of traces e) and f) shows that the calculations overestimate this degeneracy lifting. For **mmm**, the predicted splitting of 21 cm^{-1} is to be compared to the experimental one of 5 cm^{-1} [129]. With this and the general error bar of $\approx$20–30 cm^{-1} in mind, some mixed assignments of the three trimer bands which fall in the region between the dimer absorption and the Raman active trimer bands may be proposed (see Tab. 4.1). The band at 3533 cm^{-1} is expected to have **www** contributions [130], but may derive most of its intensity from **mmw**. The band at 3514 cm^{-1} is likely to have contributions from both mixed trimers. However, one can clearly see that the Raman active bands are less ambiguous.

In the case of OD-deuterated methanol co-expanded with deuterium oxide only one new band is present in the trimer region of the Raman-jet measurements (see Fig. 4.6). No other band appears when the ratio of deuterated methanol and deuterium oxide is changed. A comparison of experimental and calculated spectra is shown in Fig. 4.7. It can be seen that the mixed trimers (**mww** and **mmw**) are predicted near the turning point of the **www** $\rightarrow$ **mmm** sequence, lower in wavenumber than **mmm** and closely neighboured. Therefore, the mixed band at 2536 cm^{-1} can tentatively be assigned to overlapping mixed trimers. The overshooting red shift of mixed clusters, which was already predicted at some levels for non-deuterated mixtures (see Supplement E) but not observed in the experiment, is fully developed after deuteration in both experiment and theory. This points at substantial excess effects in the mixtures, which are discussed in Refs. [11, 14].

A Raman-jet concentration study performed in order to investigate higher clusters
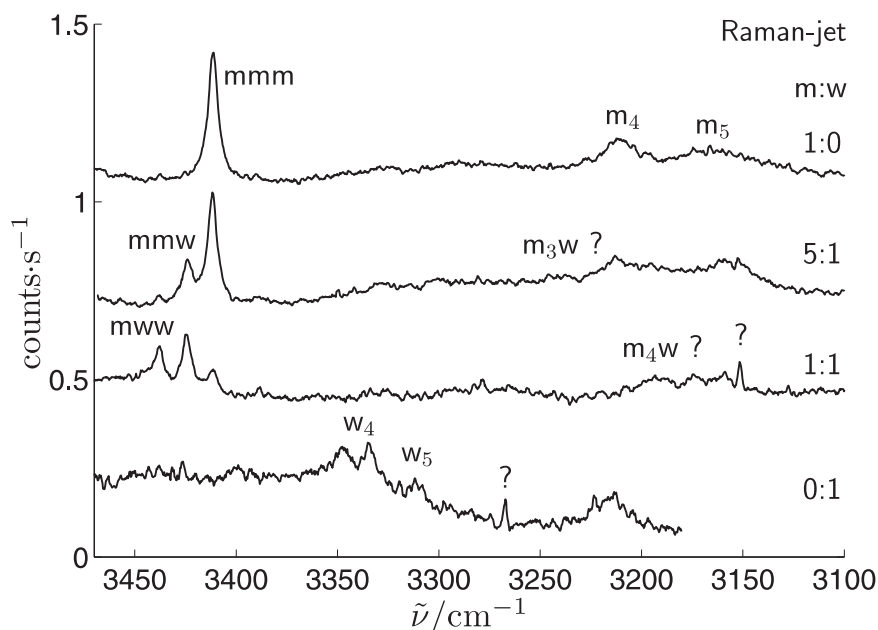
Figure 4.8.: Raman-jet spectra of the mixed methanol-water system in the O-H stretching region of higher clusters. The pure water spectrum at the bottom was taken from Fig. 6.1 in Ref. [77].

is shown in Fig. 4.8. By adding water to the pure methanol-water system, two bands at slightly higher wavenumbers than the pure methanol tetramer and pentamer arise. A mixed methanol-water tetramer **m$_3$w** at 3239 cm^{-1} and a mixed methanol-water pentamer **m$_4$w** 3191 cm^{-1} can tentatively be assigned. A better signal-to-noise ratio and comparison with quantum chemical calculations would be needed to support the assignments.
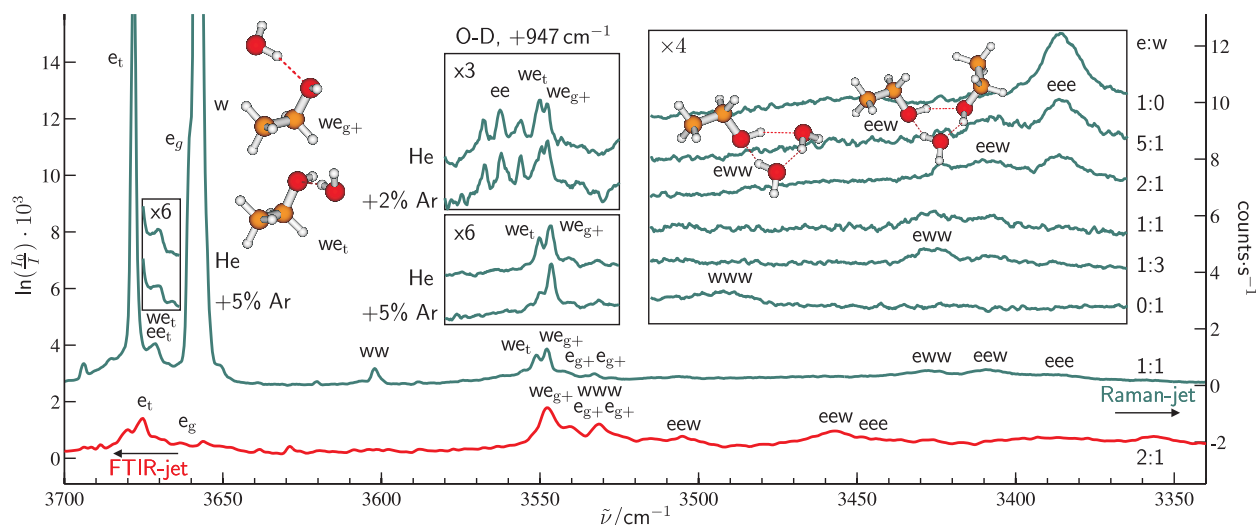
Figure 4.9.: Raman- and FTIR-jet spectra of the mixed ethanol-water system in the O-H (and O-D) stretching region. Absorbance magnification factors are shown in the insets, which share the wavenumber scale of the main spectra. The bottom centered inset shows relaxation of we_t to we_{g+} by adding Ar. The top centered inset shows the analog relaxation in the O-D region (shifted in wavenumber to match the we_{g+} O-H spectrum). The right inset shows the evolution of mixed trimers with increasing ethanol-to-water ratio.

4.3. Ethanol-Water

Fig. 4.9 displays a survey of the Raman- as well as the FTIR-jet spectrum of the mixed ethanol-water system. The Raman-jet spectrum was recorded at an estimated ethanol:water concentration ratio of 1:1, whereas the ethanol:water ratio in the FTIR-jet spectrum is approximately 2:1. Assignments of the observed bands are summarized in Tab. 4.3.

In analogy to the methanol-water system, mixed dimer bands are present in the Raman and FTIR-jet spectra. However, while the Raman spectrum shows two peaks at 3551 and 3548 cm^{-1}, the former is only a weak shoulder in the FTIR spectrum. It is caused by a metastable conformation, which is relaxed into the more stable conformation due to the larger average nozzle distance and therefore colder expansion in the FTIR experiment. The mixed dimer band at lower wavenumber is due to a gauche ethanol acceptor subunit, whereas the band at higher wavenumbers is assigned to a trans acceptor. The left inset in Fig. 4.9 shows the acceptor region of

Table 4.3.: Experimental FTIR- and Raman-jet band positions $\tilde{v}$ in cm^{-1} together with proposed assignments for pure and mixed ethanol-water dimers and trimers as well as for pure and mixed deuterated ethanol-deuterium oxide dimers. *A* labels the acceptor mode. All other modes refer to vibrations of the donor.

Assignment	$\tilde{v}_{\text{FTIR}}$	$\tilde{v}_{\text{Raman}}$
we$_{t,A}$, ee$_{t,A}$		3671
ww		3602
we$_t$		3551
we$_{g+}$	3548	3548
e$_{g-}$e$_t$	3547[a]	3548[b]
ee	3541	3544
e$_{g+}$e$_{g+}$	3531[a]	3532[b]
www	3531	
eew	3505	
www		3491
eew	3457	
eee	3449	
eww		3427
eew		3409
eee		3386
ww (deuterated)		2632
e$_{g-}$e$_t$ (deuterated)		2621[b]
ee (deuterated)		2615[b]
e$_{g+}$e$_{g+}$ (deuterated)		2609[b]
we$_t$ (deuterated)		2602
we$_{g+}$ (deuterated)		2601

[a]Taken from Ref. [10]
[b]See also Ref. [75]

trans ethanol for Raman measurements without (top) and with (bottom) 5% argon. In the lower central inset of Fig. 4.9 the hydrogen bonded O-H stretching bands are shown. The intensity of the **we**$_t$ band at $3551\,\mathrm{cm}^{-1}$ decreases along with the acceptor band of trans ethanol when the heavier collider argon is added, showing that **we**$_{g+}$ is more stable. Assuming a conservative lower limit of the effective conformational temperature in the argon doped expansion of $10\,\mathrm{K}$ and at most 10% remaining **we**$_t$ fraction, a lower limit for the energy difference between **we**$_t$ and **we**$_{g+}$ of $0.2\,\mathrm{kJ\cdot mol}^{-1}$ from the Boltzmann population can be derived. These assignments are also supported by quantum chemical calculations (see Fig. 4.10 and Supplement E). At all levels of calculation five mixed ethanol-water dimer configurations can be optimized. Relative stabilities and local minimum structures are illustrated in Fig. 4.11. In the three most stable structures, water acts as the hydrogen bond donor. In these cases, not only the conformation of ethanol (trans or gauche) is relevant, but also the choice of the acceptor lone pair (see Sect. 4.1). As illustrated in Fig. 4.11, **we**$_{g+}$ (with a hydrogen bond to the right lone pair of ethanol) is predicted to be the most stable and most compact mixed dimer at MP2-L level. In contrast to **we**$_{g-}$ it is stabilized by a secondary hydrogen bond-like interaction between a C-H group and the water oxygen [131]. It bends the primary hydrogen bond slightly further away from the linear arrangement. The enhanced stability of **e**$_g$ in this complex parallels the stabilization observed for ethanol dimers [10,75,78], as does the enhanced red shift. The donor/acceptor roles of ethanol and water in a matrix are analogous to those of methanol and water, with **we** being the more stable one in argon and **ew** in nitrogen [103]. In the jet, **ew** dimers are expected to relax into the more stable structures, as implied by the intensity shifts postulated in Fig. 4.10 by the dotted lines. The **we**-splitting shrinks by a factor less than 2 upon OD-deuteration of both ethanol and water (see Fig. 4.9). Theory predicts this factor to be 1.3 (MP2-L). Furthermore, the relaxation behavior is analogous to that of the nondeuterated dimer, although less pronounced because a smaller amount of argon is added. Therefore, it is clear that the **we**-splitting is not due to tunneling, as in **wm**, but rather to conformational isomerism.

To assign the trimer bands in the Raman-jet spectra, concentration variation was applied (see the rightmost box in Fig. 4.9 with relative concentration estimates). In analogy to the mixed methanol-water trimer bands, the intensity of the band at higher wavenumber ($3427\,\mathrm{cm}^{-1}$) increases with an increasing content of water,
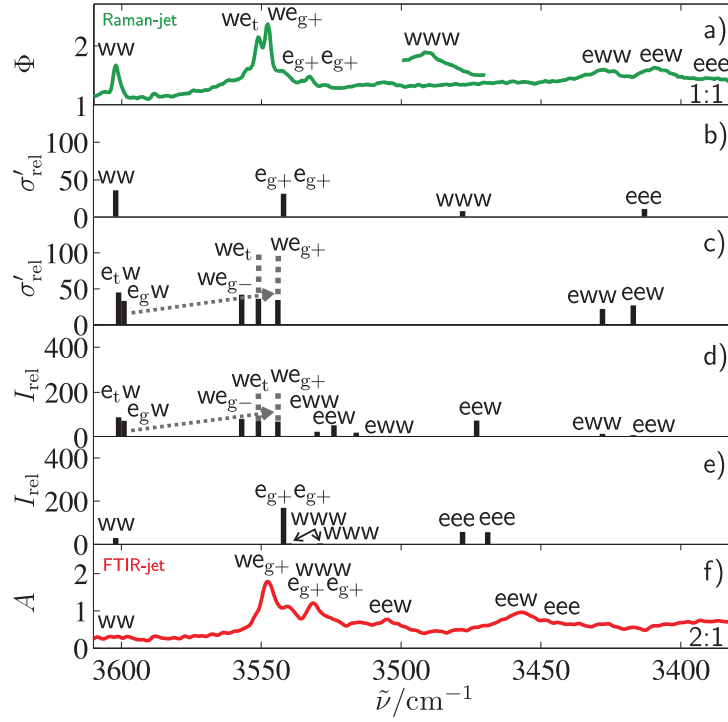
Figure 4.10.: Comparison of calculated (MP2-S/MP2-M average) and experimental Raman and FTIR spectra of pure and mixed dimers and trimers of the ethanol-water system: a) Raman-jet (Φ in counts$\cdot$s^{-1}), b) Raman prediction for pure clusters (σ'_{rel} in $10^{-36}\cdot$m$^2\cdot$sr^{-1}), c) Raman prediction for mixed clusters (σ'_{rel} in $10^{-36}\cdot$m$^2\cdot$sr^{-1}), d) IR prediction for mixed clusters (I_{rel} in km$\cdot$mol^{-1}), e) IR prediction for pure clusters (I_{rel} in km$\cdot$mol^{-1}), f) FTIR-jet (A=ln($\frac{I_0}{I}$) $\cdot 10^3$). For the scaling procedure, see Sect. 3.3.

Figure 4.11.: Structures and relative stabilities of **we/ew** dimer isomers at MP2-L level. Secondary hydrogen bond-like C-H$\cdots$O contacts and hydrogen bond lengths as well as the O-H$\cdots$O angles are indicated.

while the more red shifted band at $3409\,cm^{-1}$ increases with the relative ethanol content. As supported by the calculations in Fig. 4.10 (and Supplement E), the band at $3427\,cm^{-1}$ can be assigned to **eww**, while the band at $3409\,cm^{-1}$ corresponds to **eew**. Isomerism does not scramble the coarse-grained sequence from **www** over **eww** and **eew** to **eee** in the spectrum. The stability of the trimers (Tab. 4.4) increases with an increasing alcohol content (except for the B3-S level), see also Ref. [111]. Again, the most stable configurations appear to be those with equivalent molecules pointing in the same direction relative to the ring plane, but the preference is weak. Trimers containing trans ethanol tend to be more stable than those containing the gauche conformation, however no systematic exploration was attempted. At the MP2-M and MP2-L levels only trimers containing trans ethanol with two equal molecules pointing into the same direction were calculated and plotted (Fig. 4.10). Unlike in the methanol-water case, the prediction of the trimer sequence matches the experimental one in its qualitative behavior. There is no overshooting of the red shift as a function of alcohol content, before the pure alcohol value is reached. However, the size of the shifts is underestimated towards high ethanol content.

As Fig. 4.10 illustrates, the IR absorption of the Raman active trimer bands involving synchronous O-H stretching motion is too low to make them detectable. Instead, there are a few stronger bands predicted at higher wavenumbers e.g., the

Table 4.4.: Differences of zero point corrected dissociation energies of pure and mixed ethanol-water trimers ΔD_0 in kJ·mol^{-1}.

	$w_dw_dw_u$	$e_{g,d}w_dw_u$	$e_{t,d}w_uw_d$	$e_{g,u}w_dw_d$	$e_{t,u}w_dw_d$	
B3-S	0.00	+0.75	+0.29	+0.60	−0.42	
MP2-S	0.00	−1.65	−1.69	−2.41	−2.79	
MP2-M	0.00				−5.32	
MP2-L	0.00				−6.65	

	$e_{g,u}e_{g,d}w_d$	$e_{g,d}e_{g,u}w_d$	$e_{g,d}e_{t,u}w_d$	$e_{t,d}e_{t,u}w_d$	$e_{t,d}e_{t,d}w_u$	$e_{t,d}e_{t,d}e_{t,u}$
B3-S	+0.96	+0.87	−0.15	−0.06	+0.08	+0.30
MP2-S	−4.83	−4.85	−5.20	−5.30	−5.60	−8.09
MP2-M					−11.02	−16.91
MP2-L					−13.59	

band at 3457 cm^{-1} may correspond to **eew**, as may the band at 3505 cm^{-1}. Overall, the IR spectra are more ambiguous to assign due to the higher congestion. More reliable quantum chemical predictions would be helpful.

4.4. Conclusions

Dimers and trimers composed of water and either methanol or ethanol were studied by Raman and FTIR spectroscopy in supersonic jets, complemented by harmonic quantum chemical calculations to explore their limitations in reproducing the O-H (O-D) stretching manifold. In mixed alcohol-water dimers water was found to assume the role of the hydrogen bond donor. A simple case of adaptive aggregation is the water-ethanol dimer. Here, water forces ethanol into its less stable gauche conformation upon dimerization. This dimer conformation profits from the interaction with a C-H hydrogen bond of the methyl group. For mixed alcohol-water clusters a cyclic structure can be assumed. A tentative assignment was made for a mixed methanol-water tetramer and a pentamer.

The study of higher alcohols with water would be interesting in order to investigate how an increased aliphatic chain [132] affects the hydrogen bond and also the structures by introducing competing dispersion interactions. The study of highly polar fluorinated alcohols [133] in combination with water [134] is also of interest.

The investigated ethanol-water dimer represents one of the simplest model cases of what happens when a molecule being capable of hydrogen bond interactions is embedded into a crystal. It will typically rearrange its functional groups in order to

optimize intermolecular interactions. The conformational preferences of more complex hydrogen bond formers within a crystal and their interactions will be discussed in the following Chapters.

5. Methyl Mandelate

Methyl mandelate is a chiral α-hydroxycarboxylic acid ester with an ester, a hydroxy, and a phenyl group (see Fig. 5.1). Due to its numerous functional groups it is a good model system to explore the competition between a variety of interactions [38] e.g., inter- and strained intramolecular O-H···O=C hydrogen bonds, which are important for the structure and function of biomolecules. Furthermore, methyl mandelate is suitable to study the competition between dispersion forces and hydrogen bond interactions. The aromatic ring is a weak acceptor for free OH groups and is also responsive to π–π- and CH–π interactions [135, 136]. Since its functional groups are close to the chiral center (marked with an asterisk (*) in Fig. 5.1) aggregation might be influenced by effects of chirality recognition [3]. Furthermore, it shows structural similarities to mandelic acid and some neurotransmitters which will be discussed later on in Chapters 6 and 7.

Monomers and small clusters of methyl mandelate were extensively studied by FTIR-jet spectroscopy and double-resonance IR/UV spectroscopy [38, 137, 138]. IR and vibrational circular dichroism studies were performed on methyl mandelate in solution [139–141]. KBr pellet and ATR-IR spectra are reported for the solid state [38]. X-ray structure analysis and polarization FTIR microspectroscopic measurements were initiated within the present framework and are reported

(S) (R)
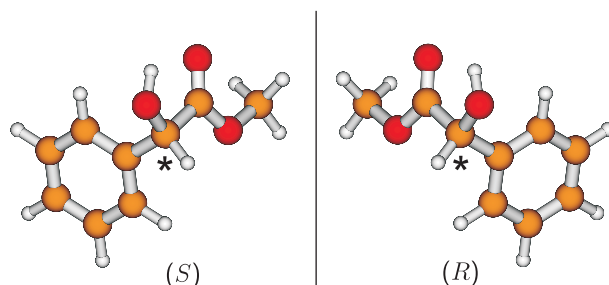
Figure 5.1.: (S)- and (R)-methyl mandelate monomers. The center of chirality is marked with an asterisk (*).

in Refs. [37, 38]. The relative vapor pressure of enantiopure and racemic methyl mandelate was also determined [38, 142, 143].

In this chapter the aggregation of methyl mandelate and chirality recognition phenomena will be discussed. First, the results of the X-ray structure analysis [38] will be described and compared to FTIR-ATR spectroscopic [143] and relative vapor pressure measurements [38, 142, 143]. Based on this, the monomer conformation within the crystal structures and the most stable monomer in the gas phase will be compared. Preliminary spectral considerations will be made before discussing FTIR microspectroscopic results of sublimated methyl mandelate crystals. Emphasis will be put on preferred growth directions, the assignment of the CH chromophores, and the deduction of the molecular orientation from the spectra of the different crystal faces. The vibrational assignment of the C-H stretching modes will be performed by comparing the FTIR microspectra to quantum chemical calculations, FTIR-ATR spectra of related compounds, and isotope labeling. Vibrational transition dipole vectors will be deduced from crystal rotation and polarization experiments. The direction of these vectors will be used to constrain the absolute orientation of the molecules within the crystal and for the assignment of further vibrational bands. In doing this, it will be shown that the polarization FTIR microspectroscopic method is suitable for determining the molecular orientation and for the assignment of vibrational modes.

The (*S*)- and (*R*)-enantiomers of methyl mandelate show equivalent FTIR spectra (not shown). All spectra of enantiopure methyl mandelate depicted in this work were measured using the (*R*)-form. Nevertheless, the (*S*)-enantiomer is consistently used in all figures since it matches the configuration of the enantiopure crystal solved by the X-ray structure analysis.

Parts of this chapter are published in Refs. [37,38]. Verbatim citations of Ref. [37] are used with the consent of the co-author.

5.1. Crystal Structures

Since no crystal structure of methyl mandelate had been published before, the structure analysis was carried out within this study and is published in Ref. [38]. Two crystallization techniques were employed. Slow solvent evaporation of methyl mandelate solutions in water, methanol, ethanol, and toluene was performed and subli-

mation in evacuated glass tubes (ca. 10 mbar) at room temperature was carried out. The X-ray structure analysis was carried out by B. Dittrich. Details on refinement data can be found in Ref. [38].

(*S*)-methyl mandelate crystals were obtained by cooling of an oversaturated aqueous solution. Sublimation also led to large single crystals. In both cases, the enantiopure crystals showed a needle-like habit. Enantiopure methyl mandelate crystallizes in the monoclinic space group $P2_1$ (see Fig. 5.16 later on). Attempts to obtain racemic crystals by sublimation of racemic methyl mandelate were unsuccessful. However, needle-like crystals with an (*RRRS*) pattern were obtained (see Fig. 5.21 later on). The quality of these crystals was poor, but after several attempts a small untwinned specimen was obtained. The formation of non-racemic, non-enantiomeric crystals is rarely observed [144, 145]. Like enantiopure methyl mandelate, the (*RRRS*) compound also crystallizes in the monoclinic space group $P2_1$. The racemic compound was finally obtained from a solution of the racemate in toluene. It also shows a rather rare (*RRRS − SSSR*) pattern [146] similar to the mixed pattern of the (*RRRS*) crystal (see Fig. 5.20 later on). Racemic methyl mandelate crystallizes in the triclinic space group $P\bar{1}$.

The three stereoisomeric crystal structures of methyl mandelate have common features. Each compound has eight molecules in the unit cell (*Z*=8) and four molecules in the asymmetric unit (*Z'*=4). In one dimension there are infinite zigzag chains of bifurcated O-H$\cdots$O=C and O-H$\cdots$O-H hydrogen bonds with different distances and angles (see Fig. 5.2 for enantiopure methyl mandelate and Tab. 5.1). Orthogonal to the hydrogen bonds, the aromatic rings interlock with each other by π-π-interactions. These two layers are held together by van der Waals interactions of the methyl ester groups and aromatic rings in a third dimension. Besides the configurations and patterns, a major difference is the orientation of the aromatic ring. In the enantiopure compound the aromatic rings alternatingly point up and down with regard to the hydrogen bond chain. In the mixed (*RRRS*) and the racemic crystals, every fourth monomer is enantiomeric to the others and does not follow the alternating up/down pattern observed in the enantiopure crystal. Therefore, the stapling of π-π interlocked hydrogen bonded chains is less efficient than in the case of the enantiopure compound. In the case of the racemic crystal, (*RRRS*) and (*SSSR*) layers alternate.

The monomers within the unit cell of all three crystals have the same qualitative conformation (see Fig. 5.5 later on) but differ in their interactions. Stronger and
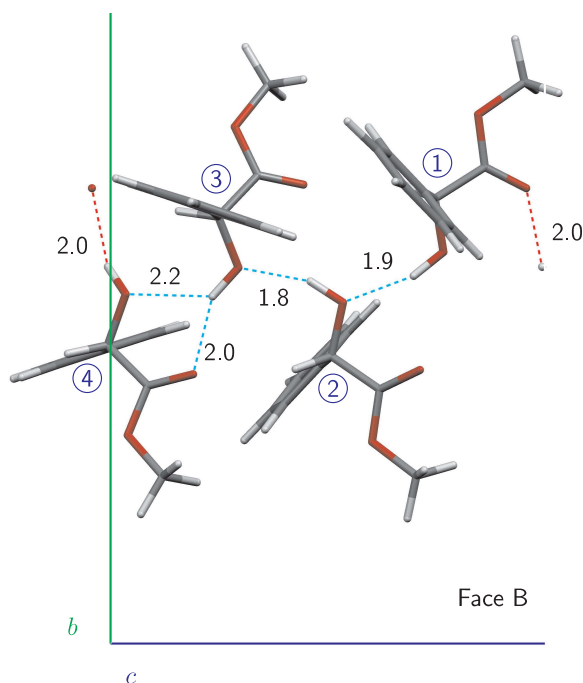
Figure 5.2.: Hydrogen bonded network of (*S*)-methyl mandelate showing four different hydrogen bonded OH groups [38]. Hydrogen bond distances are given in Å. Circled numbers enumerate the monomer units. Note that only hydrogen bonds with a maximum H-X distance of 2.5 Å and a minimum angle of 130° are shown.

weaker hydrogen bonds alternate (see Fig. 5.2 for enantiopure methyl mandelate, Tab. 5.1). The average H···O distance of the bifurcated O-H···O=C and O-H···O-H hydrogen bonds falls in the range of 2.0–2.2 Å. Either a strong and a weak or two intermediate contacts are formed. The average between both hydrogen bond angles varies from 139–144°. The only exception is the monomer unit 4 of enantiopure methyl mandelate which has an average angle of 131°.

The formation of three different crystal structures was verified by FTIR-ATR spectroscopy and by mass spectrometric measurements of the relative vapor pressures. Mid infrared ATR spectra of enantiopure, 3:1 mixed, and racemic methyl mandelate are shown in Fig. 5.3. The spectra exhibit differences regarding the shape and position of several bands of the enantiopure compound compared to the 3:1 and the racemic crystal. Most bands of the enantiopure substance appear blue shifted relative to the other compounds. No significant differences are observed for the mixed (*RRRS*) and the racemic crystal in the mid infrared region.

Table 5.1.: Types, distances d in Å ($d_{\text{H}-\text{X}}$ and $d_{\text{Y}-\text{X}}$), and angles α in $^\circ$ of hydrogen bonds Y-H$\cdots$X found in the crystal structures of enantiopure (S)-, mixed ($RRRS$)-, and racemic ($RRRS - SSSR$)-methyl mandelate.

	O-H$\cdots$O=C			O-H$\cdots$O-H		
Monomer	$d_{\text{H}-\text{X}}$	$d_{\text{Y}-\text{X}}$	α	$d_{\text{H}-\text{X}}$	$d_{\text{Y}-\text{X}}$	α
(S)-Methyl mandelate						
1	2.5	3.1	126	1.9	2.8	162
2	2.5	3.1	126	1.8	2.7	158
3	2.0	2.9	152	2.2	2.9	130
4	2.0	2.8	143	2.5	3.1	119
($RRRS$)-Methyl mandelate						
1	2.4	3.1	135	2.0	2.9	150
2	2.0	2.8	135	2.1	3.0	143
3	2.3	3.0	132	2.0	2.9	152
4	2.1	2.9	132	2.0	2.9	150
($RRRS - SSSR$)-Methyl mandelate						
1	2.1	2.9	133	2.1	2.9	147
2	2.2	3.0	135	2.0	2.9	150
3	2.0	2.8	137	2.1	3.0	143
4	2.3	3.1	134	2.0	2.9	151
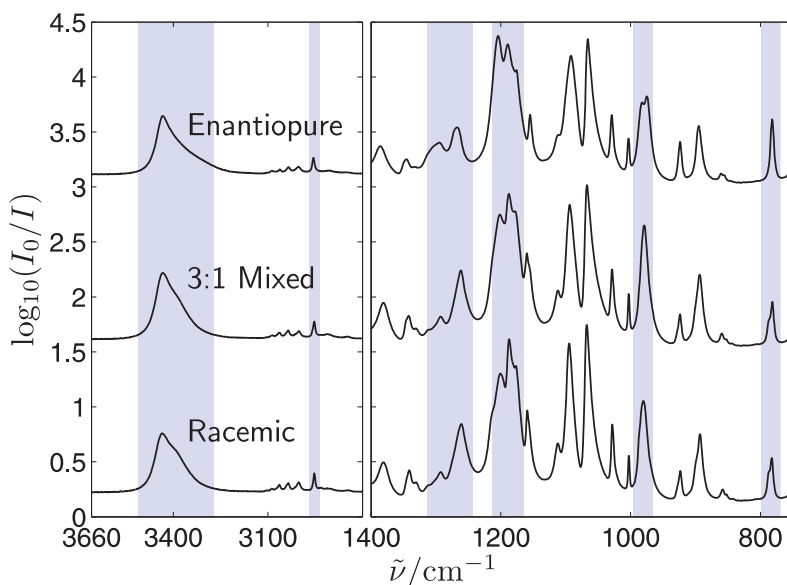
Figure 5.3.: FTIR-ATR spectra of enantiopure (*S*), mixed (*RRRS*), and racemic (*RRRS* − *SSSR*) methyl mandelate recorded in the mid infrared region (3660–$2800\,\mathrm{cm}^{-1}$, 1400–$750\,\mathrm{cm}^{-1}$). The blue bars mark regions of spectral differences.

The far infrared FTIR-ATR spectra of enantiopure, 3:1 mixed, and racemic methyl mandelate (Fig. 5.4) show substantial differences experienced by lattice vibrations. The relative differences of the enantiopure compound on one hand and 3:1 and racemic methyl mandelate on the other hand are more pronounced in this spectral region. Especially, the appearance of a new peak at $340\,\mathrm{cm}^{-1}$, the intensity gain and sharpening at $220\,\mathrm{cm}^{-1}$, and the shifts at 170 and $60\,\mathrm{cm}^{-1}$ should be noted. The spectra of the mixed (*RRRS*) and the racemic crystal also show differences in the far infrared region. One difference is the band at $165\,\mathrm{cm}^{-1}$ which appears intermediate in the spectra of the 3:1 crystal showing that the spectrum of the mixed (*RRRS*) crystal cannot be represented by a superposition of the enantiopure and the racemic crystal. This supports the formation of a third crystal structure next to the enantiopure and the racemic crystal.

Relative vapor pressures of the three different methyl mandelate compounds were determined by quadrupole mass spectrometry. The relative vapor pressures of enantiopure and racemic methyl mandelate already had been measured by L. Schrader and J. Zischang [38, 142, 143]. Within the scope of this work, the results were verified and the relative vapor pressure of the mixed (*RRRS*) compound was measured
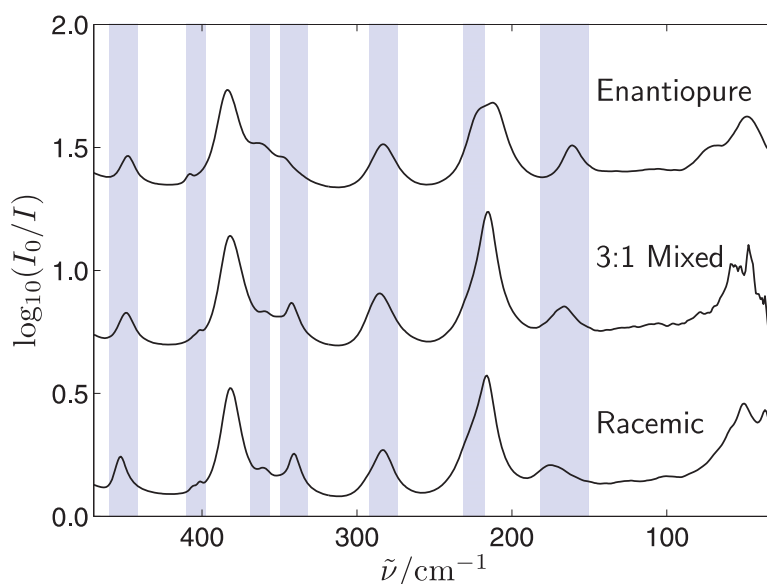
Figure 5.4.: FTIR-ATR spectra of enantiopure (*S*), mixed (*RRRS*), and racemic (*RRRS − SSSR*) methyl mandelate recorded in the far infrared region (470–30 cm^{-1}). The blue bars mark regions of spectral differences.

newly. Based on the mass peaks 79 and 107, the relative vapor pressure of the enantiopure and the racemic compound is determined as (19±5)% and the relative vapor pressure of the 3:1 mixed compound and the racemic methyl mandelate is determined as (35±10)% at 293.0±0.5 K. Thus, although the FTIR-ATR spectra only show subtle differences, the vapor pressures are considerably different as a result of intermolecular diastereoisomerism.

5.2. Monomer Conformations

To characterize the conformation of methyl mandelate monomers a three-letter nomenclature was employed [138]. It describes the syn (S,s), cis (C), skew (sk), gauche (G), and anti (A) conformations of the H-O-C-C, the O-C-C=O, and the O=C-O-CH$_3$ dihedral angles.

The monomer units of enantiopure, 3:1 mixed, and racemic methyl mandelate do not differ qualitatively within the unit cell but also not for the different crystals. The energies and predicted wavenumbers are thus the same for relaxed (geometrically optimized) enantiopure, 3:1 mixed, and racemic methyl mandelate monomer units.

Frozen monomer unit
from the crystal structure

Relaxed monomer unit
from the crystal structure

Most stable
monomer
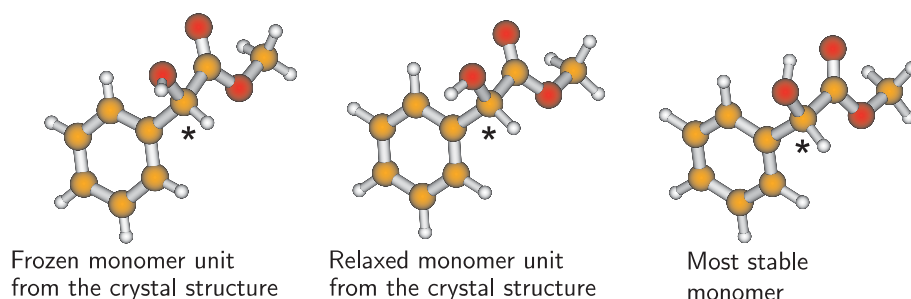
Figure 5.5.: Frozen and relaxed monomer units ((*S*)-enantiomer) taken from the crystal structure of enantiopure methyl mandelate [38] as well as the most stable monomer [138] (B3LYP/6-311++G(3df,2p) level).

Therefore, only the enantiopure crystal's monomer unit is shown in Fig. 5.5 and will be considered in the remainder. It exhibits an AsC conformation. No intramolecular hydrogen bond is formed in this conformation.

The most stable monomer conformation was determined by IR/UV double resonance and resonant two-photon ionization spectroscopy in combination with quantum chemical calculations on the MP2/6-31G(d,p) and DFT levels of approximation [138]. Two stable monomers were found, the more stable monomer having an SsC and the other a GskC structure. The results were confirmed by FTIR-jet spectroscopy [38, 137]. Both conformations form an intramolecular O-H$\cdots$O hydrogen bond. In the case of the SsC structure the O=C is the hydrogen bond acceptor, whereas in the GskC monomer the O-CH$_3$ group takes on this role. The structure and frequencies of the SsC conformation were recalculated on the B3LYP/6-311++G(3df,2p) and MP2/6-311+G(2d,p) levels of theory within the current framework. The most stable monomer calculated on the B3LYP method is depicted in Fig. 5.5.

The energy differences without and with zero point energies between the relaxed monomer unit from the crystal structure and the most stable monomer conformation as well as the distance and angle of the intramolecular O-H$\cdots$O hydrogen bond of the most stable monomer are summarized in Tab. 5.5. The energy difference with and without zero point energies of 13–15 kJ$\cdot$mol^{-1} (B3LYP and MP2 levels) results from the establishment of a hydrogen bond within the most stable monomer. Nevertheless, the energetically unfavorable monomer unit is present in the crystal structure since it is capable of stronger intermolecular hydrogen bonds than the most stable monomer unit. Thus, the energy difference of the monomer units reflects the

Table 5.2.: Distances d in Å ($d_{\text{H}-\text{O}}$ and $d_{\text{O}-\text{O}}$) and angle α in ° of the O-H···O hydrogen bond in the most stable monomer as well as energy differences without and with zero point energies (ΔE and ΔE_0) of the relaxed monomer unit from the crystal structure [38] and the most stable monomer [138] of methyl mandelate in kJ·mol^{-1} on the B3LYP/6-311++G(3df,2p) and MP2/6-311+G(2d,p) levels of theory. No imaginary frequencies are observed.

	$d_{\text{H}-\text{O}}$	$d_{\text{O}-\text{O}}$	α	ΔE	ΔE_0
B3LYP/6-311++G(3df,2p)	2.1	2.7	119	-15.4	-14.6
MP2/6-311+G(2d,p)	2.1	2.7	120	-13.6	-12.9

benefit of intermolecular over intramolecular hydrogen bonds.

5.3. Preliminary Spectral Considerations

Methyl mandelate possesses a hydroxy group, a phenyl ring, and an ester functional group (see Fig. 5.5 above). Therefore, a variety of fundamental bands can be expected in the mid infrared region. There will be an O-H stretching fundamental, several C-H stretching bands (aromatic, methyl, and α-acidic), a C=O stretching band, C-C stretching modes, and several combination bands. Predicted wavenumbers are listed in Supplement F.

The position and intensity of the O-H stretching band strongly depend on the nature and strengths of the hydrogen bonds [147, 148]. The stronger the hydrogen bond the more red shifted and intensified the band is e.g., the position of the theoretically localized O-H stretching band of the water monomer ($\frac{\text{sym}+\text{asym}}{2}$) red shifts from $3707\,\text{cm}^{-1}$ to $3602\,\text{cm}^{-1}$ in the water dimer and to $3567\,\text{cm}^{-1}$ in the mixed water-methanol dimer (see Chapter 4) [14, 81]. The O-H stretching band of the methyl mandelate monomer was found to appear at $3549\,\text{cm}^{-1}$ and $3552\,\text{cm}^{-1}$ by FTIR-jet and IR/UV depletion spectroscopy, respectively [38, 138]. Several dimer bands were observed 10–$35\,\text{cm}^{-1}$ red shifted to the monomer. Only one dimer band is blue shifted by $7\,\text{cm}^{-1}$. The trimer and a higher cluster's O-H stretching band are red shifted by $88\,\text{cm}^{-1}$ and $248\,\text{cm}^{-1}$ as shown by FTIR-jet spectroscopy [38]. The small shifts of the dimer O-H stretching bands result from the isolated character of the hydrogen bonds and the competition from intramolecular hydrogen bonding in

the monomer. Within the crystal the monomers form hydrogen bonded chains (see Sect. 5.1). Therefore, larger red shifts can be expected.

Methyl mandelate has three different types of CH groups. There are the aromatic CH groups, the ester methyl group, and one α-acidic CH. The aromatic C-H stretch may show a multiplet of up to five bands in the $3100\,cm^{-1}$ to $3000\,cm^{-1}$ region [148]. The aliphatic ROC-H_3 stretching bands appear in the 2995–$2865\,cm^{-1}$ spectral region with the asymmetric stretchings at higher wavenumber than the symmetric [148]. C-H stretching bands of methyl mandelate monomers were found at $3101\,cm^{-1}$, $3076\,cm^{-1}$, $3043\,cm^{-1}$, $3009\,cm^{-1}$, $2964\,cm^{-1}$, and $2804\,cm^{-1}$ by FTIR-jet spectroscopy [38]. Only slightly different positions ($3105\,cm^{-1}$, $3080\,cm^{-1}$, $3045\,cm^{-1}$, $3009\,cm^{-1}$, $2963\,cm^{-1}$, and $2900\,cm^{-1}$) were observed using IR/UV depletion spectroscopy [38, 138]. The bands at higher wavenumbers are assigned to aromatic C-H stretching modes, while the bands at $3009\,cm^{-1}$, $2964\,cm^{-1}$, and $2900\,cm^{-1}$ are assigned to aliphatic C-H stretchings [138].

The C=O stretching mode appears as a strong band in the region of 1800–$1650\,cm^{-1}$ [148]. The C=O stretching band of the methyl mandelate monomer was detected at $1752\,cm^{-1}$ by FTIR-jet spectroscopy [38]. Dimer bands were found to be shifted by $-17\,cm^{-1}$ to $+11\,cm^{-1}$. C-C stretching bands appear around $1600\,cm^{-1}$. The modes show a lifted degeneracy and may appear as a quadruplet [147, 148]. In benzene these modes are doubly degenerate. The substitution of the benzene ring destroys the high symmetry of the ring.

Complex in-phase and antiphase coupling patterns for many molecular vibrations (factor group splittings) can be expected [16]. Further spectral splittings may result from quantitative differences in the molecular structures discussed in Sect. 5.1.

5.4. FTIR Microspectroscopy

5.4.1. Enantiopure Methyl Mandelate

In the following section, results on sublimated microcrystals of enantiopure methyl mandelate studied by polarized FTIR microspectroscopy which are published in Ref. [37] will be presented. Enantiopure methyl mandelate is a white powder with a melting point of 56–$58°C$ under ambient conditions (according to the supplier). There is no evidence that it is hygroscopic.

The sublimation of enantiopure methyl mandelate led to microcrystals with two
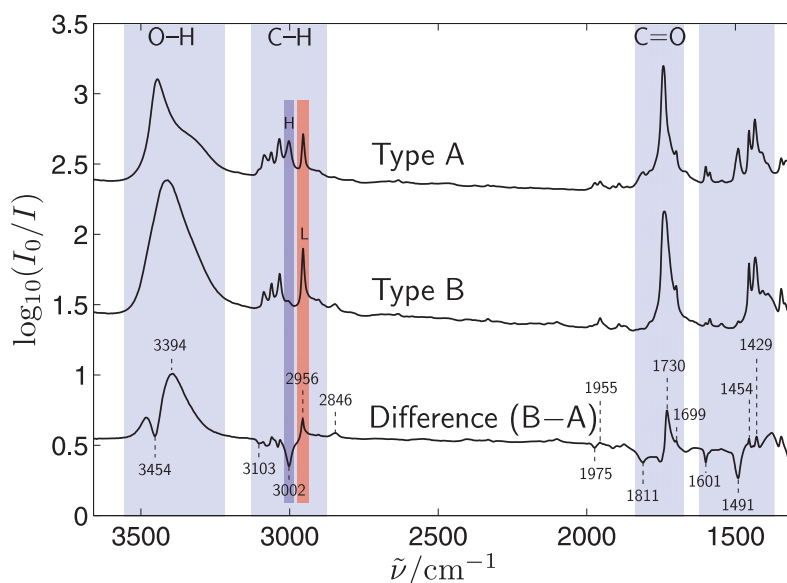
Figure 5.6.: Type A and B FTIR spectra of enantiopure methyl mandelate crystals as well as the difference spectrum of type A subtracted from type B (B−A). Wavenumbers for selected bands in the difference spectrum are given in cm^{-1}. They may differ slightly from those of the band maxima in the raw spectra. Regions H and L used for integration are marked in blue and red, respectively.

different habits. Liquid droplets which often formed above +35 °C crystallized into dendritic carpets. Tabular crystals were directly obtained by sublimation in a temperature range of +28 °C and +40 °C. After nucleation the methyl mandelate crystals grew to a size of 10 μm and larger within seconds.

The sublimated methyl mandelate crystals (dendritic carpets as well as tabular crystals) show two different types of spectra which are denoted as type A and type B in Fig. 5.6. The spectra differ in relative intensities (e.g., in the C-C stretching or C-H bending region), in band shape (e.g., the O-H stretching band), and in wavenumber (e.g., the C=O stretching band). Different spectral types may result from polymorphism, solvent content, or different crystal faces. The appearance of a crystal hydrate appears to be rather unlikely since none was observed by X-ray structure analysis (see Sect. 5.1). Furthermore, the crystallization was performed via sublimation which minimizes the presence of solvents. A difference spectrum of type A subtracted from type B (B−A) emphasizes the spectral differences (Fig. 5.6). Wavenumbers of maxima and minima in the difference spectrum are given in cm^{-1}.

67
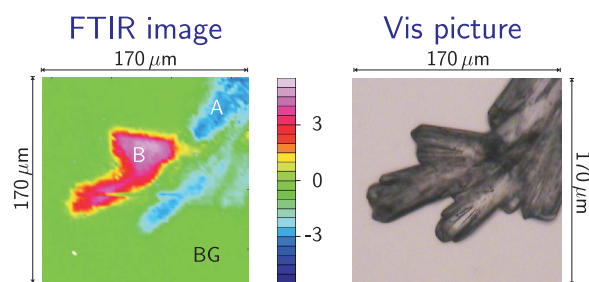
Figure 5.7.: FTIR image of an enantiopure methyl mandelate polycrystal showing that type A and B spectra can coexist in a sample.

FTIR images were recorded in order to determine if both types of spectra can coexist and whether a single crystal only shows one spectral type. The images shown in Figs. 5.7 and 5.8 were obtained by integrating the regions 3018–2982 cm^{-1} (H) and 2972–2934 cm^{-1} (L) with the OPUS 6.5 [61] baseline corrected integration method (see Chapter 3). Twice the integral absorption of region H was subtracted from the integral of region L (L$-$2·H) to maximize the contrast between the two C-H stretching sections. Blue colors show a higher intensity of bands in the region of 3018–2982 cm^{-1}, whereas red colors refer to a higher intensity in the region of 2972–2934 cm^{-1}. Absorption free regions and regions with balanced intensities in the 3018–2982 cm^{-1} and 2972–2934 cm^{-1} windows are shown in green (BG).

The FTIR image of a dendritic crystal shows that the two types of spectra can coexist in a sample (Fig. 5.7). The images of two single crystals (Fig. 5.8) exhibit that the crystals either show type A (top) or type B spectra (bottom). The visual pictures next to the images show that the type A crystals' shape is rectangular, whereas type B spectra result when the shorter edge of the crystal is not orthogonal to the long edge. This correlation was also observed for other single methyl mandelate crystals not shown here. A 1:1 ratio for the occurrence of crystals showing type A and B spectra was noticed as well.

Rotation experiments around the long crystal axis revealed that type A and type B spectra can be interchanged (Fig. 5.9). This shows that the spectral differences cannot be attributed to polymorphism or solvation, but to different faces the crystals are growing on and therefore to the molecular orientation. Since the distribution of both spectral types was found to be balanced, the growth direction of the crystals on the CaF$_2$ substrate appears to be largely statistical with respect to these short axes [149]. In the following, crystal faces showing type A spectra are named face
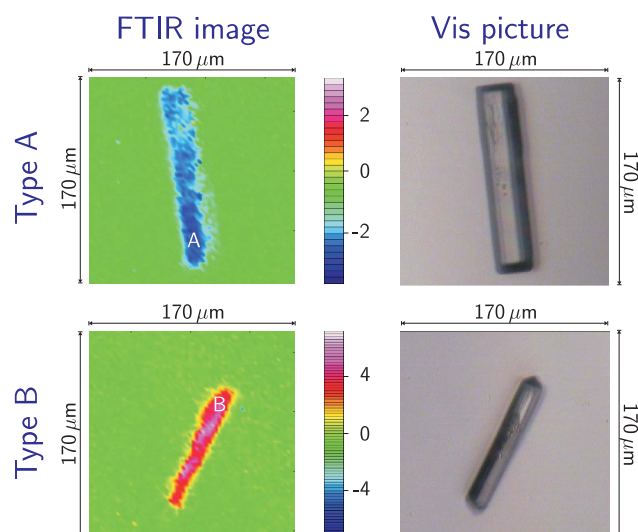
Figure 5.8.: FTIR images of enantiopure methyl mandelate crystals showing only one type of spectra for single crystals.

A and crystals showing type B spectra face B.

Also, enantiomerically mixed (unknown ratio), OD-deuterated enantiopure, and CD_3-deuterated enantiopure methyl mandelate crystals grow on two faces. The spectra are analog to the two spectral types observed in the enantiopure case as shown for enantiomerically mixed methyl mandelate in Fig. 5.10. A comparison of the difference spectra (Fig. 5.11) exhibits the similarities which result from similar interactions within the crystal structures (see Sect. 5.1) and their directions of growth. The polarization microspectra of the enantiomerically mixed methyl mandelate crystals will be shortly discussed in Sect. 5.4.2.

There are strong differences in the region of the C-H stretching bands of face A and B spectra. Especially, the intensities of the bands at $3003\,cm^{-1}$ and $2954\,cm^{-1}$ differ. FTIR-ATR spectra of methyl mandelate were compared to those of the structurally similar molecules mandelic acid (MA), methyl lactate (ML), and methyl-d_3 mandelate (Fig. 5.12) for the assignment of the C-H stretching bands to the aromatic and aliphatic groups.

The C-H stretching bands in the $3100–3020\,cm^{-1}$ region appear in the spectra of methyl mandelate, mandelic acid, and methyl-d_3 mandelate but not in the spectrum of methyl lactate. Thus, the bands in this region can be assigned to aromatic C-H stretching modes (see Tab. 5.3). While the spectra of mandelic acid and methyl-
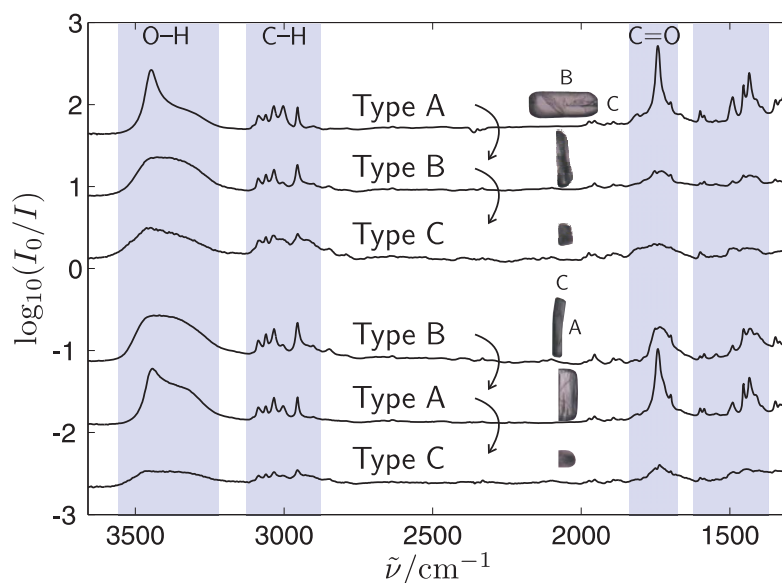
Figure 5.9.: FTIR spectra obtained after rotation of methyl mandelate microcrystals showing type A and type B spectra. Rotating the crystal interconverts the spectral types A and B and exhibits a spectrum of type C.
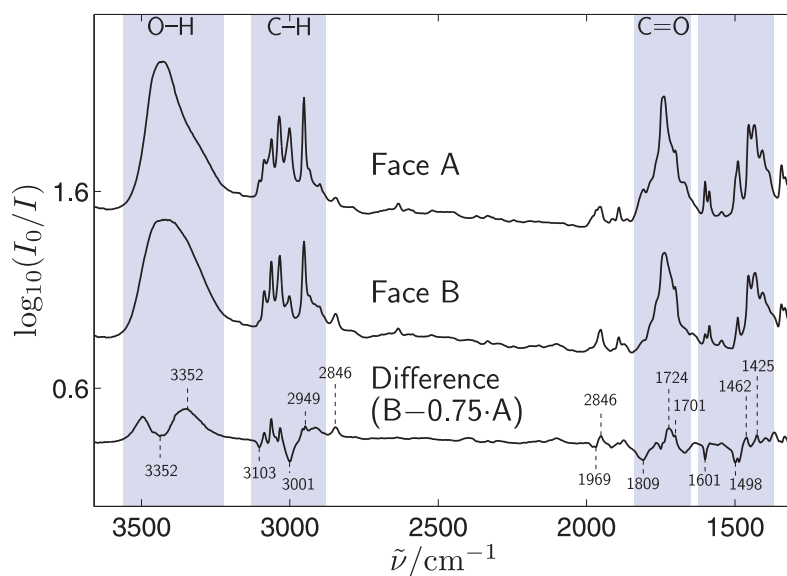
Figure 5.10.: Type A and B FTIR spectra of enantiomerically mixed methyl mandelate crystals of unknown ratio as well as the difference spectrum of type A times 0.75 subtracted from type B (B−0.75·A). Wavenumbers for selected bands in the difference spectrum are given in cm^{-1}. They may differ slightly from those of the band maxima in the raw spectra.
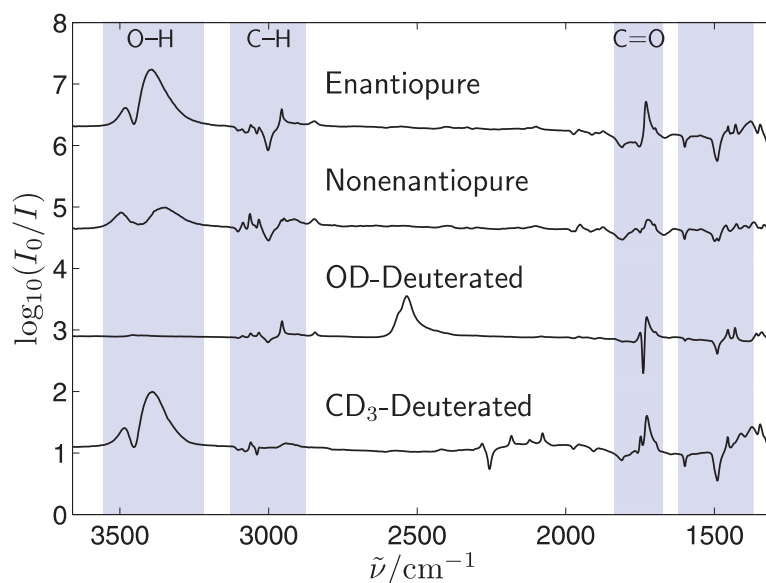
Figure 5.11.: FTIR difference spectra of type A subtracted from type B of non-deuterated enantiopure, nondeuterated enantiomerically mixed (unknown ratio, nonenantiopure), OD-deuterated enantiopure, and D$_3$-deuterated enantiopure methyl mandelate crystals.
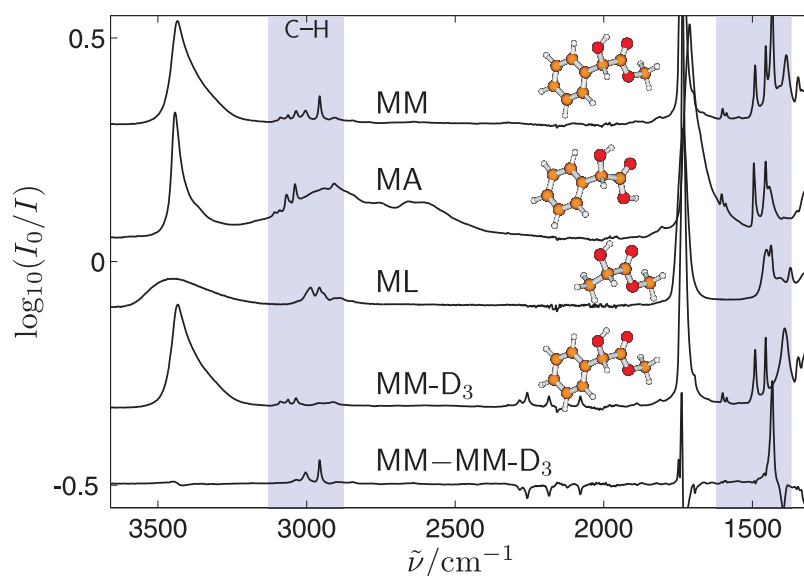
Figure 5.12.: FTIR-ATR spectra of methyl mandelate (MM), mandelic acid (MA), methyl lactate (ML), methyl-d$_3$ mandelate (MM-D$_3$), and a difference spectrum of nondeuterated and methyl-d$_3$ mandelate (MM−MM-D$_3$).

d_3 mandelate do not show bands around $3003\,\text{cm}^{-1}$ and $2954\,\text{cm}^{-1}$, the spectra of methyl mandelate and methyl lactate do. Accordingly, the two bands must be due to C-H stretchings of the methyl groups. This matches the assignments of the C-H stretching signals observed in FTIR-jet and IR/UV depletion spectra at $3009\,\text{cm}^{-1}$ and $2964\,\text{cm}^{-1}$ [38, 138] (see Sect. 5.3). The weak band at $2903\,\text{cm}^{-1}$ can be assigned to the stretching vibration of the α-acidic CH in agreement with an aliphatic C-H stretching band appearing at $2904\,\text{cm}^{-1}$ in the FTIR-jet and at $2900\,\text{cm}^{-1}$ IR/UV depletion spectra [38, 138]. The difference spectrum of methyl-d_3 mandelate subtracted from methyl mandelate (MM$-$MM-D$_3$) exhibits a weak band of a third methyl C-H stretching mode at $3035\,\text{cm}^{-1}$. It is hidden underneath the aromatic C-H stretching bands in the nondeuterated methyl mandelate spectrum. This methyl C-H stretching mode may also contribute to the band at $3043\,\text{cm}^{-1}$ in the FITR-jet spectrum [38]. It was not assigned in the IR/UV depletion spectrum, because of its low intensity and its overlap with aromatic signals [138].

The bands at $1973\,\text{cm}^{-1}$, $1956\,\text{cm}^{-1}$, $1600\,\text{cm}^{-1}$, $1587\,\text{cm}^{-1}$, $1454\,\text{cm}^{-1}$, and $1491\,\text{cm}^{-1}$ (see Fig. 5.6) do not appear in the methyl lactate spectrum but they do appear in the spectra of the aromatic compounds. These bands are due to aromatic fundamental modes with C-H bending and C-C stretching character. In particular the two doublets near $1600\,\text{cm}^{-1}$ and below $1500\,\text{cm}^{-1}$ are robust signatures of the phenyl group as discussed in Sect. 5.3 [147]. The bands at $2850/2848\,\text{cm}^{-1}$ and $1436/1433\,\text{cm}^{-1}$ do not appear in methyl-d_3 mandelate and can be assigned to bending vibrations of the methyl group.

Fig. 5.13 shows a comparison of the experimental FTIR-ATR and quantum-chemically predicted methyl mandelate spectra. It can be seen that the scaled harmonic predictions for isolated molecules (universal best fit factor 0.966) largely agree with the experimental assignments, although some intensities are distorted and the splitting between symmetric and asymmetric C-H$_3$ modes is exaggerated. Based on these predictions, it is possible to assign the methyl vibration bands at $3035\,\text{cm}^{-1}$ and $3003\,\text{cm}^{-1}$ to the asymmetric methyl stretching modes, while the band at $2954\,\text{cm}^{-1}$ corresponds to the symmetric stretching of the methyl group. In contrast to the methyl vibrations, the aromatic C-H stretching bands are predicted too close together for a detailed assignment based on theoretical band positions. However, comparison to the mandelic acid case (see Chapter 6) and information on the vibrational transition dipole vectors allow for the tentative assignment given in Tab. 5.3.
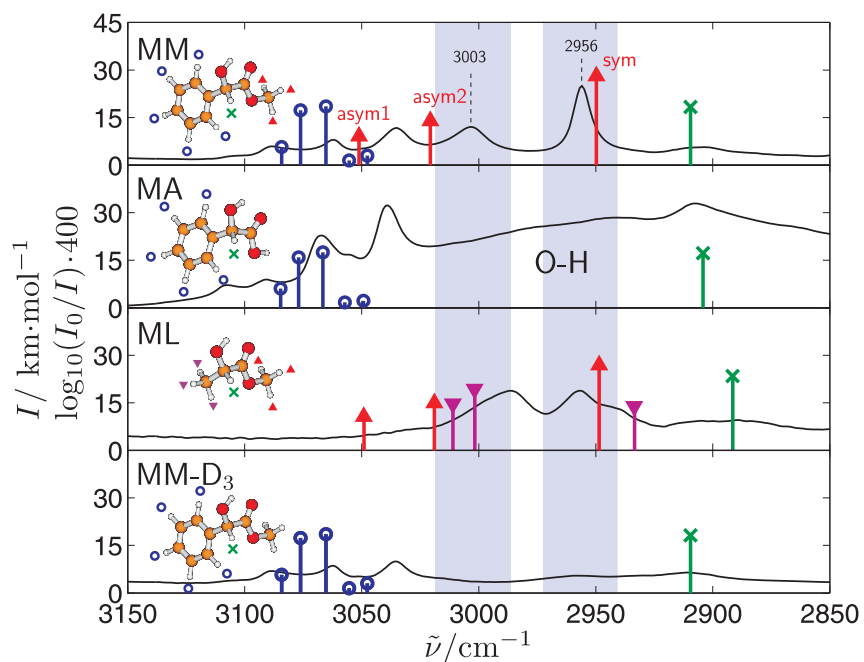
Figure 5.13.: Comparison between calculated spectra on the B3LYP/6-311++G(3df,2p) level and experimental FTIR-ATR spectra of methyl mandelate (MM), mandelic acid (MA), methyl lactate (ML), and methyl-d$_3$ mandelate (MM-D$_3$) in the C-H stretching region. Calculated spectra are scaled by a factor of 0.966 to roughly match the experimental spectrum despite a neglect of anharmonic effects. Aromatic positions are marked with a circle (∘, blue), methyl bands are marked with a triangle (△, red), pointing downward (▽, pink) in the case of the second methyl group of ML, and the position of the α-acidic group is marked with a cross (×, green).

Table 5.3.: Assignments of experimental band maxima in the FTIR microscopic spectra of enantiopure methyl mandelate of face A, face B, FTIR-ATR spectra, FTIR spectra of the melt as well as calculations of a monomer unit relaxed from the crystal structure ($Mon_{crystal}$) and of the most stable monomer (Mon_{stable}) on the B3LYP/6-311++G(3df,2p) level. All wavenumbers are given in cm^{-1}. The stretching and bending vibrations are indicated as ν and δ and the symmetric and asymmetric vibrations with sym and asym.

Assignment	Face A	Face B	ATR	Melt	$Mon_{crystal}$	Mon_{stable}
ν(O-H)	3450	3420	3434	3487	3835	3723
ν(C-H$_{aromatic,sym}$)	3103		3103		3190	3193
ν(C-H$_{aromatic,2}$)	3085	3087	3088	3088	3184	3184
ν(C-H$_{aromatic,3}$)	3062	3060	3062	3064	3174	3173
ν(C-H$_{aromatic,4}$)			3049		3164	3163
ν(C-H$_{aromatic,5}$)	3035	3035	3035	3033	3156	3155
ν(C-H$_{3,asym1}$)	3035	3035	3033		3152	3159
ν(C-H$_{3,asym2}$)	3003	3003	3003	3008	3121	3127
ν(C-H$_{3,sym}$)	2954	2954	2956	2954	3050	3054
ν(C-H$_\alpha$)	2902	2901	2904	2903	3019	3012
2δ(C-H$_3$)	2850	2848	2848	2849		
aromatic combination	1973	1973				
aromatic combination	1956	1956		1955		
ν(C=O)	1811		1811			
ν(C=O)	1740	1739	1736	1738	1817	1777
ν(C=O)	1699	1699	1698			
ν(C=O)	1671		1669			
ν(C-C$_{aromatic,1}$)	1600	1600	1600	1601	1640	1641
ν(C-C$_{aromatic,2}$)	1587	1587	1586	1587	1624	1626
ν(C-C$_{aromatic,3}$)	1491	1491	1491	1495	1527	1528
ν(C-C$_{aromatic,4}$)	1454	1454	1455	1454	1488	1488
δ(C-H$_3$)	1436	1433	1433	1439		
δ(C-H$_3$)$_{shoulder}$	1411	1409				
δ(C-H$_{3,asym1}$)					1501	1499
δ(C-H$_{3,asym2}$)					1488	1488
δ(C-H$_{3,sym}$)					1476	1478
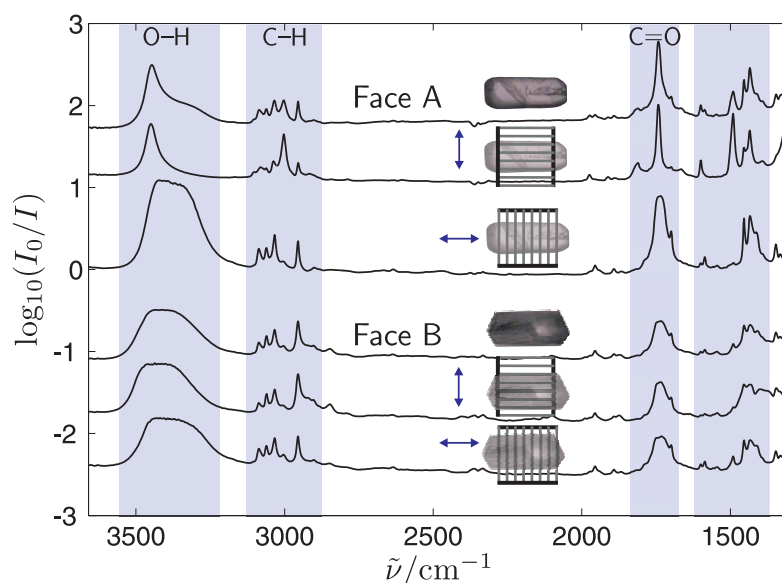
Figure 5.14.: Polarized FTIR spectra through face A and B of enantiopure methyl mandelate. The double arrows show the direction of the electric vector of the radiation which passes the polarizer and can excite corresponding vibrational transition dipole vector components.

The spectral differences of the faces A and B provide information about the direction of the vibrational transition dipole vector. The intensity of the band at $3003\,\text{cm}^{-1}$ ($\nu(\text{C-H}_{3,\text{asym2}})$) decreases significantly when turning the crystal from face A to B. This suggests that its vibrational transition dipole is more or less perpendicular to face B. In order to confirm its orientation within face A, polarization experiments were carried out. In Fig. 5.14 the direction of the electric vector (double arrow) and the corresponding spectra measured through face A and B are shown. Clearly, the vibrational transition dipole has a negligible component along the long crystal axis consistent with the vanishing band for face B. Fig. 5.15 shows the polarization spectra through face A including the direction of the vibrational transition dipole vector for several other bands. It can be noticed that the vibrational transition dipole vectors of several closely spaced pairs of bands point in different directions. In many cases, this is caused by in-phase and antiphase vibrations of the same molecular mode within the crystal, i.e. factor group splitting.

In the weakly interacting C-H$_3$ stretching case, this splitting is not spectrally resolved, thus allowing for a direct statement about the average molecular orientation in the crystal. E.g., when looking at face A the vibrational transition dipole vec-
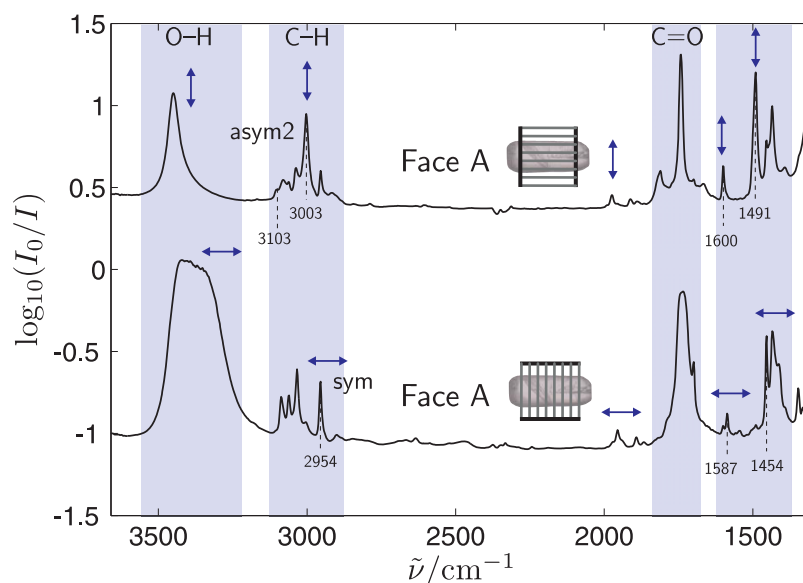
Figure 5.15.: Polarized FTIR spectra of a methyl mandelate crystal showing face A.
Several neighboring bands show vibrational transition dipole vectors
in two directions as indicted by the arrows.

tor of the band at $3003\,\mathrm{cm}^{-1}$ (ν(C-H$_{3,\mathrm{asym2}}$)) points in the short direction of the
crystal, while the one of the band at $2954\,\mathrm{cm}^{-1}$ (ν(C-H$_{3,\mathrm{sym}}$)) points more in the
long direction. However, its largest component is perpendicular to face A. This is
consistent with the orientation of the molecules for the three crystal faces shown
in Fig. 5.16. Thus, face A largely corresponds to a view along the crystallographic
b axis, whereas face B corresponds to a view along the *a* axis. Beyond this spa-
tial orientation, which can also be obtained from pure X-ray studies, the polarized
spectra show that the band at $3003\,\mathrm{cm}^{-1}$ corresponds to the asymmetric component
perpendicular to the plane of the ester group. This is in agreement with the quantum
chemical predictions for the isolated molecule (see Supplement F).

Intermolecularly coupled oscillators such as the O-H stretching modes can also be
used to check or determine the absolute molecular orientation in the microcrystals.
The preferential orientation of the hydrogen bonded chains along the long crystal
axis is confirmed by the appearance of the lower frequency O-H stretching mode
for IR polarization along this direction, because the symmetric mode in a hydrogen
bonded zigzag chain is always the one with the lower frequency due to the coop-
erative nature of such hydrogen bonds. However, the underlying hydrogen bonds
themselves differ quite substantially (see Fig. 5.2 and Tab. 5.1 in Sect. 5.1), super-
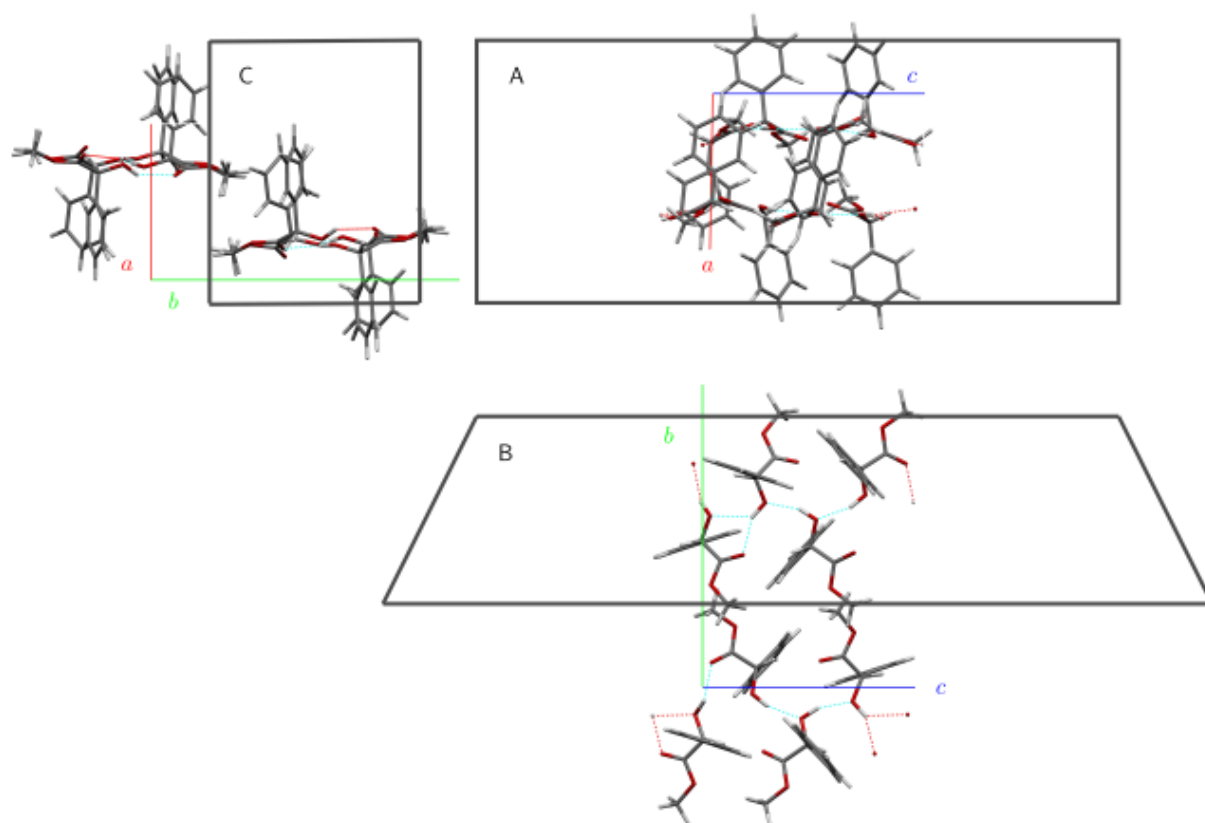
Figure 5.16.: Molecular orientation of (*S*)-methyl mandelate along the three crystal faces. The crystal structure was taken from Ref. [38] (see Sect. 5.1).
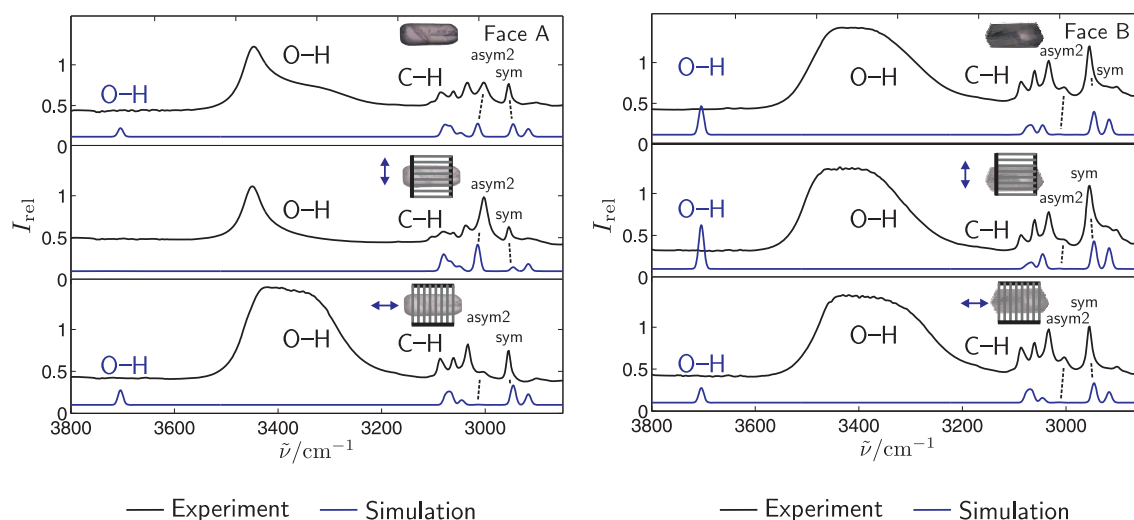
Figure 5.17.: Comparison of experimental (top, black) and oriented gas model (bottom, blue) polarization spectra (B3LYP/6-311++G(3df,2p) level) for face A and B in the O-H and C-H stretching region of enantiopure methyl mandelate. Wavenumbers of the oriented gas model spectra are scaled by a factor of 0.966 and the theoretical intensity scale is matched qualitatively to the C-H stretching region.

imposing the coupling pattern in a complex way. Pronounced couplings can also be found for the C=O stretching band due to its large transition dipole moment [150], rendering a detailed assignment difficult.

In Fig. 5.17 a comparison of experimental and oriented gas model spectra for nonpolarized and polarized spectra of face A and B is made. The polarization and face dependence of the asymmetric and symmetric methyl stretching bands are reproduced satisfactorily. The broadening, intensification, and low-frequency shift of the O-H stretching bands in the hydrogen bonded crystal are beyond the reach of the oriented gas model as hydrogen bonds are neglected (Chapter 2). Nevertheless, predicted intensity ratios of the different faces and polarizations are in reasonable agreement with the experiment. The molecular orientation of the different faces is confirmed. Crystal phase calculations of the vibrational spectra were started in cooperation with R. Tonner [36]. The preliminary results are encouraging.

Further bands can be assigned by comparing the experimental and oriented gas model polarization spectra. The bands at $3103\,\mathrm{cm}^{-1}$, $1600\,\mathrm{cm}^{-1}$, $1587\,\mathrm{cm}^{-1}$, $1491\,\mathrm{cm}^{-1}$, and $1454\,\mathrm{cm}^{-1}$ (see Fig. 5.15) are caused by aromatic groups. The experimental and calculated vibrational transition dipole vectors of the symmetric

aromatic C-H stretching mode at $3103\,cm^{-1}$ as well as the aromatic C-C stretching modes at $1600\,cm^{-1}$ and $1491\,cm^{-1}$ [147] point in a similar direction as the ones of the asymmetric methyl C-H stretching band at $3003\,cm^{-1}$, while the directions of the vibrational transition dipole vectors of the aromatic stretching modes at $1587\,cm^{-1}$ and $1454\,cm^{-1}$ are more in agreement with the symmetric methyl C-H stretching band at $2954\,cm^{-1}$. The band assignments can be found in Tab. 5.3. The corresponding vibrations are depicted in Supplement F. Thus, there is no need to invoke a factor group splitting for their assignment.

The methyl bending bands at $1435\,cm^{-1}$ and $1411\,cm^{-1}$ are too congested for an individual assignment, but the persistence of structure in the molten phase (Fig. 5.18) suggests that factor group splitting is not the only explanation for their appearance. The bands at $2850/2848\,cm^{-1}$, $1973\,cm^{-1}$, and $1956\,cm^{-1}$ are caused by overtone or combination vibrations. The methyl band at $2850/2848\,cm^{-1}$ can be assigned to a bending overtone with the fundamental mode at 1409–$1436\,cm^{-1}$.

In summary, large couplings between different molecules in the unit cell can be found for ν(O-H) and for ν(C=O). For methyl and C-C stretching vibrations, the coupling is negligible. In both cases, the polarization experiments provide information on the molecular orientation in the crystal, whereas intermediate couplings are not easily interpreted in terms of molecular orientation for such a complex crystal structure with eight molecules in the unit cell.

5.4.2. Enantiomerically Mixed Methyl Mandelate

Racemic methyl mandelate melts at a slightly lower temperature than enantiopure methyl mandelate. According to the supplier the melting temperature is 54–56 °C under ambient conditions. Racemic methyl mandelate is a white powder. There is no evidence that it is hygroscopic.

The racemic compound as it was provided by the supplier and not a mixture of both enantiomers was chosen for the sublimation experiments. Several sublimation attempts at ambient temperatures were needed to obtain single crystals suitable for the X-ray structure analysis as described in Sect. 5.1. For the microspectroscopic analysis a temperature range of 30–40 °C was applied at the bottom of the sublimation cell. Polycrystals consisting of needle-like to tabular single crystals were obtained with this method.

As in the enantiopure case, two types of spectra were obtained which are shown
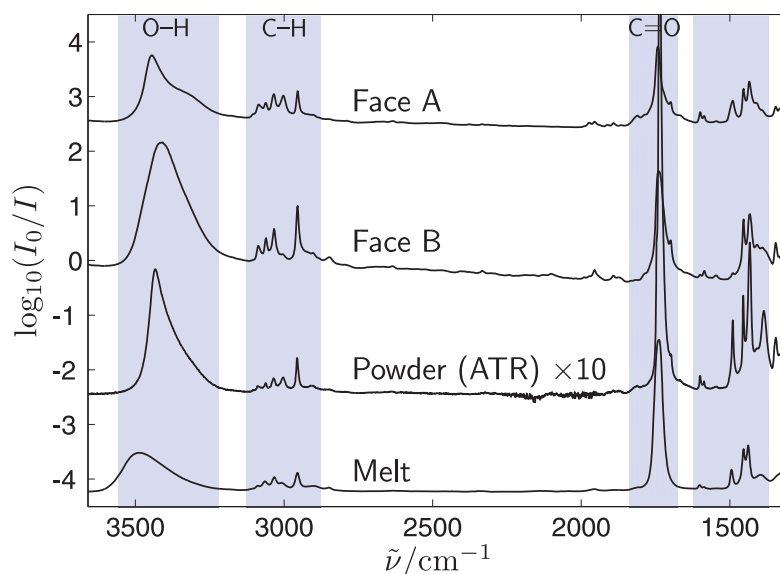
Figure 5.18.: FTIR spectra of enantiopure methyl mandelate crystals (face A and B), FTIR-ATR spectrum of the powder multiplied by a factor of ten and FTIR spectrum of molten enantiopure methyl mandelate.

in Fig. 5.19. The spectral types are similar to type A and B spectra of enantiopure methyl mandelate. The spectral differences of type A subtracted from type B spectra for enantiopure and enantiomerically mixed methyl mandelate of unknown ratio are compared in Fig. 5.11 above. The spectral behavior upon polarization is analogous as well. Band positions are summarized in Tab. 5.4. Also, the habits of the crystal faces are similar (face A: rectangular, face B: shorter edge not orthogonal to the long edge) although not as well defined as in the enantiopure case. Similar crystal structures can be assumed on the basis of the spectral and facial similarities. As discussed in Sect. 5.1, the crystal structures of enantiopure, mixed (*RRRS*), and racemic (*RRRS* − *SSSR*) methyl mandelate do indeed show the same patterns. Along the three crystal axes comparable interactions take place within the three crystal structures.

The sublimation of a racemic mixture at ambient temperatures leads to mixed (*RRRS*) and not to a racemic crystal (see Sect. 5.1). Therefore, the sublimation of the racemate in the sublimation cell is likely to have also led to the mixed (*RRRS*) crystal and not the racemate. As discussed, the mid infrared ATR spectra of racemic and 3:1 mixed methyl mandelate (Fig. 5.3) are not distinguishable. Therefore, by comparing mid infrared spectra it is not possible to decide whether a racemic or a 3:1 crystal is
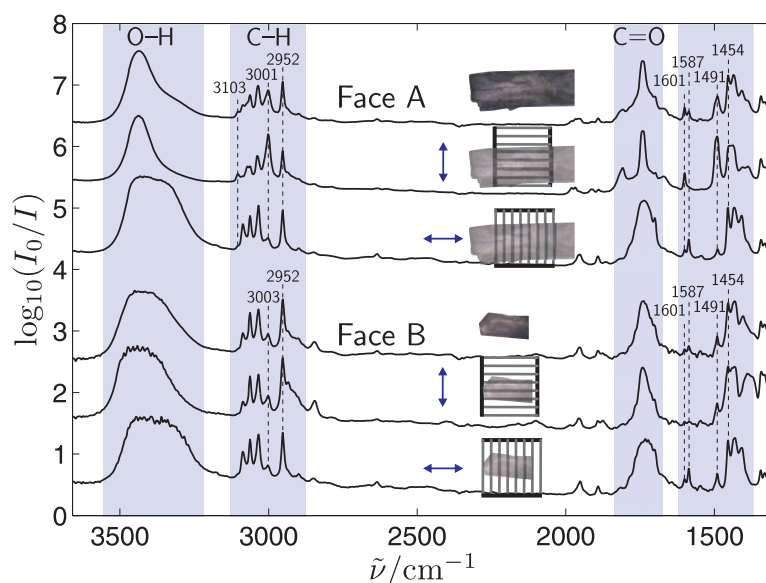
Figure 5.19.: Polarized FTIR spectra through face A and B of enantiomerically mixed methyl mandelate of unknown ratio. The double arrows show the direction of the electric vector of the radiation which passes the polarizer and can excite corresponding vibrational transition dipole vector components.

present. Additionally, the comparison of polarized spectra and vibrational transition dipole vectors do not lead to a decisive conclusion since the molecular conformation and their average arrangement are the same. Deviations between experimental and oriented gas model polarization spectra are larger than the differences between the oriented gas model spectra of the different crystals. Therefore, no oriented gas model spectra were prepared for racemic and 3:1 methyl mandelate.

Figs. 5.20 and 5.21 show the molecular orientation along the crystal axes assuming a racemic and a mixed (*RRRS*) crystal, respectively. If racemic crystals are present, face A corresponds to a view along the crystallographic *c* axis and face B corresponds to a view along the *a* axis. Assuming the presence of mixed (*RRRS*) crystals, face A corresponds to a view along the *c* axis and face B corresponds to a view along the *b* axis. An assignment to either the racemic or the 3:1 crystal needs further investigations.

Table 5.4.: Assignments of experimental band maxima in the FTIR microscopic spectra of enantiomerically mixed methyl mandelate of face A, face B, and FTIR-ATR spectra. All wavenumbers are given in cm^{-1}. The stretching and bending vibrations are indicated as ν and δ and the symmetric and asymmetric vibrations with sym and asym.

Assignment	Face A	Face B	ATR
ν(O-H)	3435	3425	3436
ν(C-H$_{aromatic,sym}$)	3103		3104
ν(C-H$_{aromatic,2}$)	3087	3087	3089
ν(C-H$_{aromatic,3}$)	3062	3062	3064
ν(C-H$_{aromatic,5}$)	3035	3033	3036
ν(C-H$_{3,asym1}$)	3035	3033	3036
ν(C-H$_{3,asym2}$)	3001	3003	3002
ν(C-H$_{3,sym}$)	2952	2952	2953
ν(C-H$_\alpha$)	2898		2902
2δ(C-H$_3$)	2846	2846	2846
aromatic combination		1986	
aromatic combination		1953	
ν(C=O)	1808	1807	1810
ν(C=O)	1740	1739	1736
ν(C=O)	1701	1703	1701
ν(C=O)	1672		1672
ν(C-C$_{aromatic,1}$)	1601	1601	1602
ν(C-C$_{aromatic,2}$)	1587	1587	1587
ν(C-C$_{aromatic,3}$)	1491	1491	1491
ν(C-C$_{aromatic,4}$)	1454	1454	1456
δ(C-H$_3$)	1435	1432	1432
δ(C-H$_3$)$_{shoulder}$	1408	1404	1408
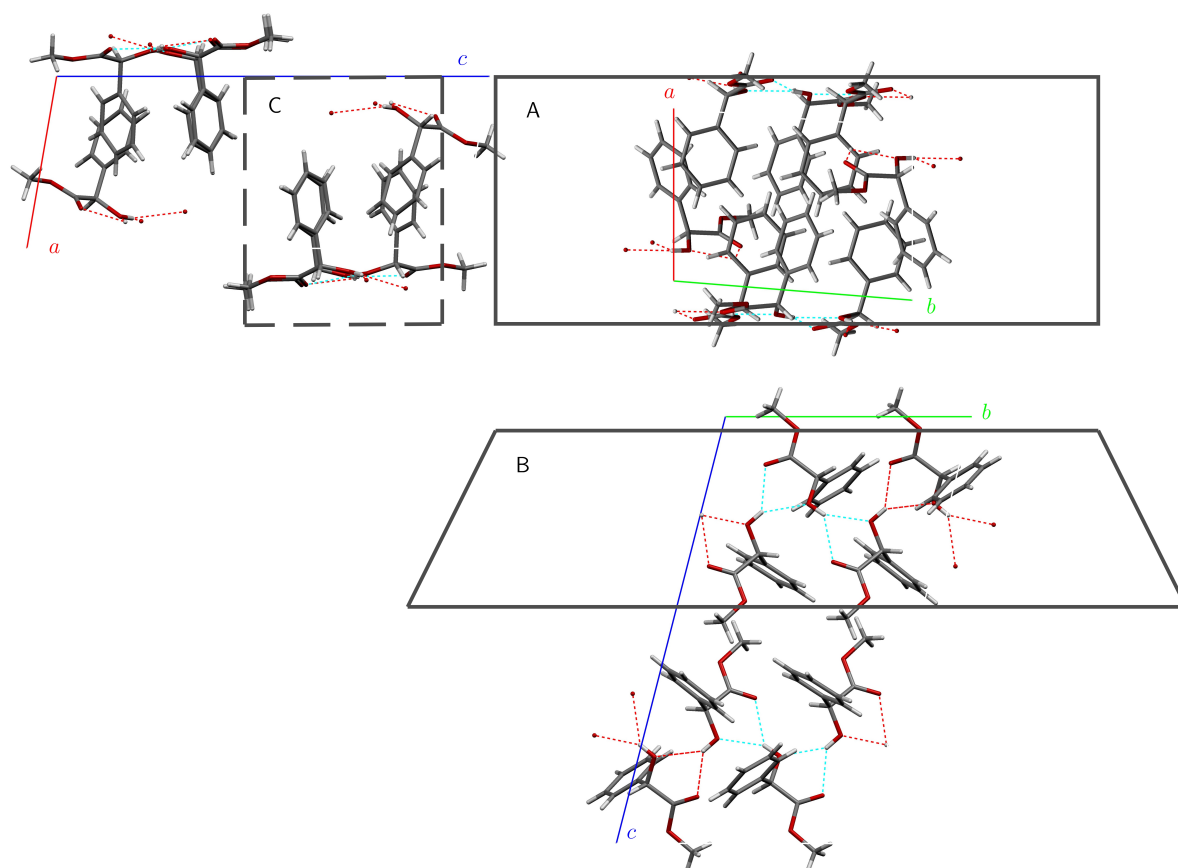
Figure 5.20.: Molecular orientation of racemic methyl mandelate along the three crystal faces. The crystal structure was taken from Ref. [38] (see Sect. 5.1). The continuous frames mark the observed faces, whereas the unobserved face is dash-framed.
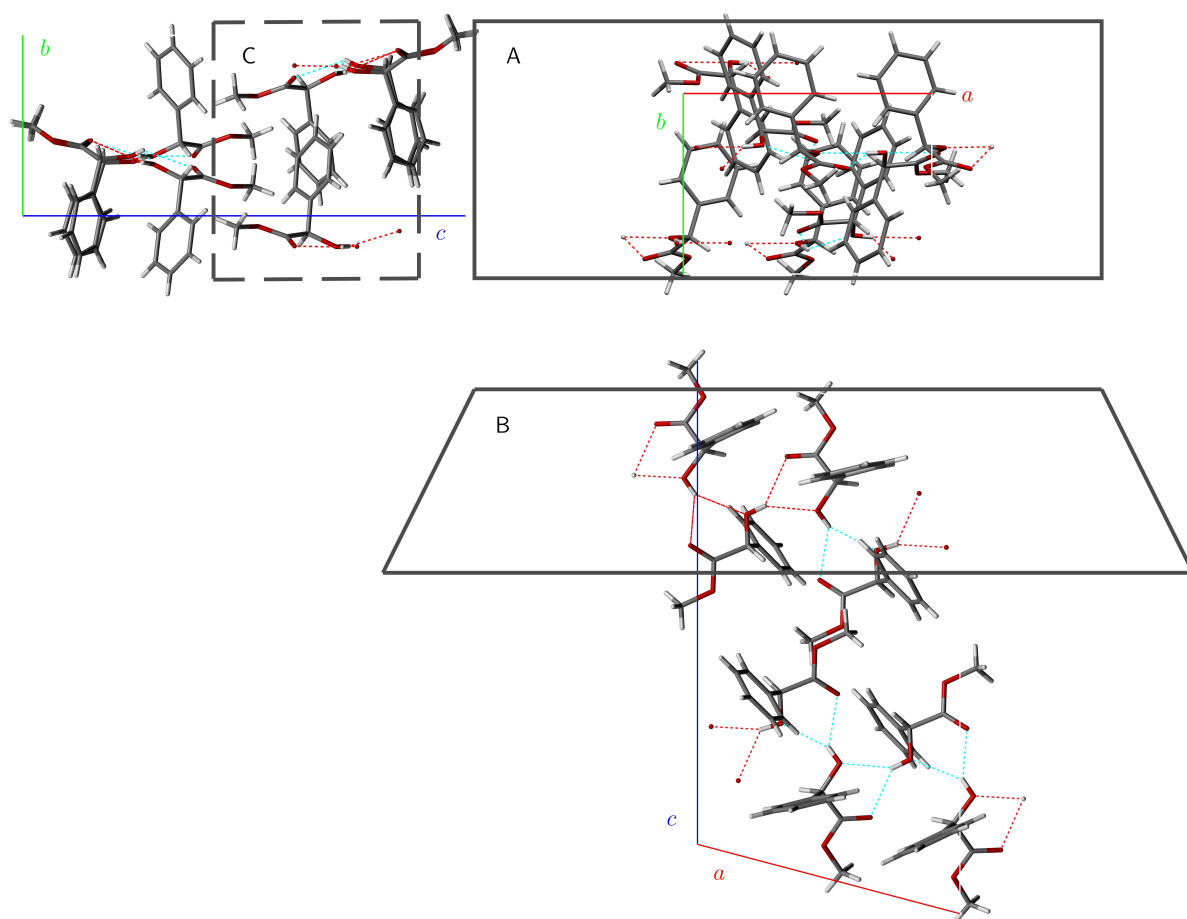
Figure 5.21.: Molecular orientation of mixed (*RRRS*)-methyl mandelate along the three crystal faces. The crystal structure was taken from Ref. [38] (see Sect. 5.1). The continuous frames mark the observed faces, whereas the unobserved face is dash-framed.

5.5. Conclusions

The FTIR microspectroscopic method of sublimated crystals investigated in transmission mode was tested using methyl mandelate [37]. Prior to this, the crystal structures were determined and FTIR-ATR spectra and relative vapor pressures were measured. It was found that methyl mandelate crystals grow on two faces on the CaF_2 substrate of the sublimation cell exhibiting two types of spectra. Spectral differences of nonpolarized and polarized measurements were used to infer the molecular orientation of the crystals. The orientation of the hydrogen bonded chains and of the methyl group along the long axis were confirmed. Detailed assignment of closely spaced normal modes was possible by comparison of experimental methyl mandelate spectra with structurally similar substances, partial deuteration, as well as a comparison of experimental and oriented gas model polarization spectra. The increased complexity of the crystal compared to gas phase spectra was turned into an advantage by applying crystal rotation, IR polarization, and monomer calculations. The FTIR microspectroscopic method will also be applied for mandelic acid in Chapter 6 and for some phenylpropanolamines in Chapter 7. It was also applied to the methylxanthines caffeine, theophylline, and theobromine [151,152], but these results are not presented here. Assignments made in this Chapter will be used for the spectral interpretation of mandelic acid and the phenylpropanolamines.

6. Mandelic Acid

Mandelic acid is an aromatic α-hydroxycarboxylic acid with one center of chirality (marked with an asterisk (*) in Fig. 6.1). It is the corresponding acid to the ester methyl mandelate which was discussed in Chapter 5. Like methyl mandelate it contains a phenyl group, an α-acidic CH, and a carbonyl group. In contrast to methyl mandelate it possesses two OH groups which are chemically very different. The alcoholic hydroxy group is also present in methyl mandelate but not the acidic carboxyl group. Therefore, there is a larger variety of hydrogen bond interactions.

Due to is chirality, mandelic acid is used in the field of enantioselective chemistry for the separation of racemates, with important applications in the pharmaceutical industry [145, 153–156]. A variety of phase diagrams are determined [157, 158]. The enantiomeric purity in solutions can be measured by simultaneous dual circular dichroism and UV spectroscopy [159]. Solutions of mandelic acid were also investigated by IR spectroscopy [140, 160–163]. FTIR-ATR spectra of solid mandelic acid were measured as well [20, 163–165]. The crystal structures of enantiopure and racemic mandelic acid were solved by means of X-ray structure analysis [88, 166–168].

In the following, the crystal structures of enantiopure and racemic mandelic acid will be described. Then, the monomer units within the crystal structures which ex-
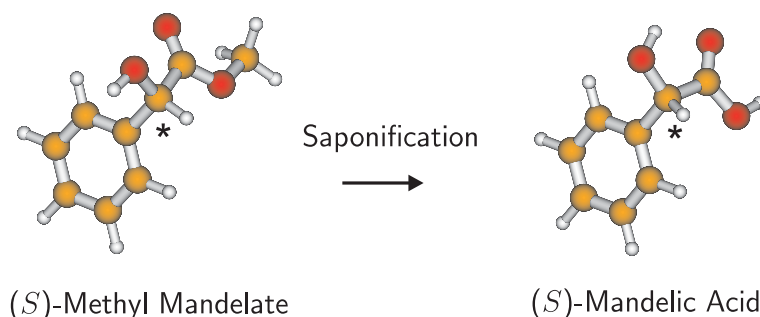
Figure 6.1.: (S)-enantiomers of methyl mandelate and mandelic acid. Centers of chirality are marked with an asterisk (*).

hibit the same conformation as the most stable monomer will be discussed. Based on the crystal structure of enantiopure mandelic acid and the monomer conformation preliminary spectral considerations will be made. Experimental and oriented gas model spectra of enantiopure mandelic acid will be compared. Vibrational transition dipole vectors will be deduced from crystal rotation and polarization experiments. The molecular orientation and a spectral assignment of several fundamental modes will be inferred by a comparison of polarization spectra, deduced vibrational transition dipole vectors, oriented gas model spectra, the crystal structure of enantiopure mandelic acid, and the results gained for methyl mandelate in Chapter 5.

The (*S*)- and (*R*)-enantiomers of mandelic acid exhibit the same FTIR-spectra [164]. All mandelic acid spectra depicted in the present work were measured using the (*R*)-enantiomer. Nevertheless, the (*S*)-form is consistently used in all figures since it matches the configuration of the enantiopure crystal characterized by X-ray crystallography [88]. No spectra of the racemic compound were recorded.

The content of this chapter is published in Ref. [37]. Verbatim citations are used with permission of the co-author.

6.1. Crystal Structures

In the case of mandelic acid the crystal structures of both the enantiopure and the racemic compound were solved by X-ray structure analysis [88, 166–168]. (*S*)-mandelic acid crystallizes in the monoclinic space group $P2_1$ (CSD REF Code: FEGHAA) [88]. It contains four molecules in the unit cell (*Z*=4) and two molecules in the asymmetric unit (*Z'*=2). Patil et al. report a hexagonal, platy habit for enantiopure mandelic acid when crystallized from chloroform or from a 9:1 ethanol-methylene chloride mixture [88]. However, the sublimation at 110–112°C under atmospheric pressure led to very thin needles. The molecules form corrugated chains with $\cdot[\cdot\cdot OH\cdots O=C-OH\cdot]\cdots$ repeat units, where three intermolecular hydrogen bonds link the alcoholic OH and the C=O group of an individual molecule (see Fig. 6.2 and Fig. 6.7 later on). There are no hydrogen bonds connecting two corrugated chains. The alcoholic and the acidic OH groups are nearly orthogonal to each other. The angle between two neighbored hydrogen bonds H···O are 86° or 87°, whereas the O-O-O angles are 102° for both chains.

Two polymorphs of racemic mandelic acid are known, one thermodynamically
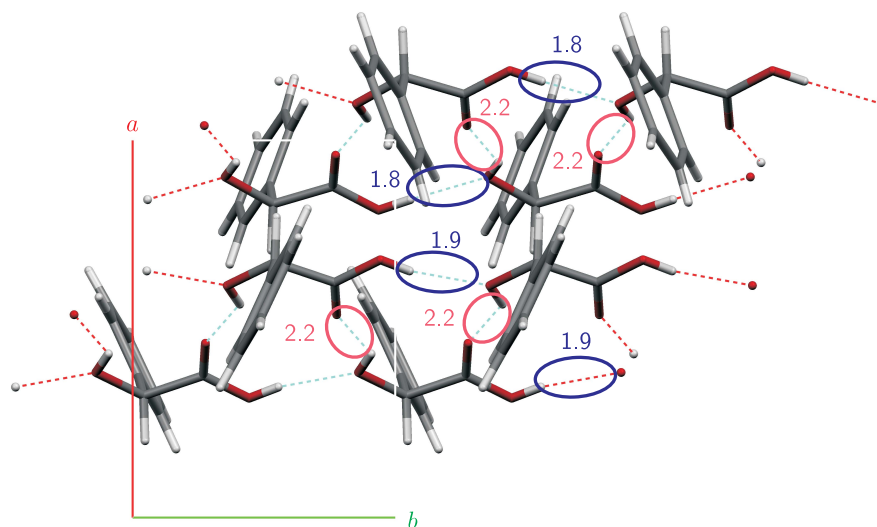
Figure 6.2.: Crystal structure of (*S*)-mandelic acid [88] along the crystallographic *c*-axis. Two different types of O-H···O hydrogen bonds nearly orthogonal to each other are shown. H-O hydrogen bond distances are given in Å.

stable (I) and one metastable form (II) [166, 167, 169]. The stable form crystallizes in the orthorhombic space group *Pbca* (CSD REF Codes: DLMAND01, DLMAND03) [167, 168]. It contains 8 molecules in the unit cell (*Z*=8) and one molecule in the asymmetric unit (*Z*'=1). The molecules form a two-dimensional hydrogen bonded network along the crystallographic *a* and *c* axes (not depicted). Molecules of the same enantiomer are connected by O=C-OH···OH hydrogen bonds along the *c* axis. In addition, every molecule forms OH···O=C-OH hydrogen bonded dimeric units with the opposite enantiomers along the *a* axis. The dimeric units are alternatingly oriented. The formation of solid racemate I from a 1:1 mixture of powdered (*R*)- and (*S*)-enantiomers in Nujol mull at ambient temperature is reported to occur within 2 hours [165].

The metastable form was obtained from an undersaturated aqueous solution by slow evaporation at room temperature in the dark (CSD REF Code: DLMAND02) [166]. It crystallizes in the monoclinic space group *P*2$_1$/*c* with eight molecules in the unit cell (*Z*=8) and two molecules in the asymmetric unit (*Z*'=2). The metastable racemic mandelic acid forms O=C-OH···OH hydrogen bonded strings of enantiomeric molecules running along the crystallographic *a* axis (not depicted). Two strings are connected by dimeric units of opposite enantiomers held together by two OH···O=C-OH hydrogen bonds along the *b*/*c* bisector. There are two parallel
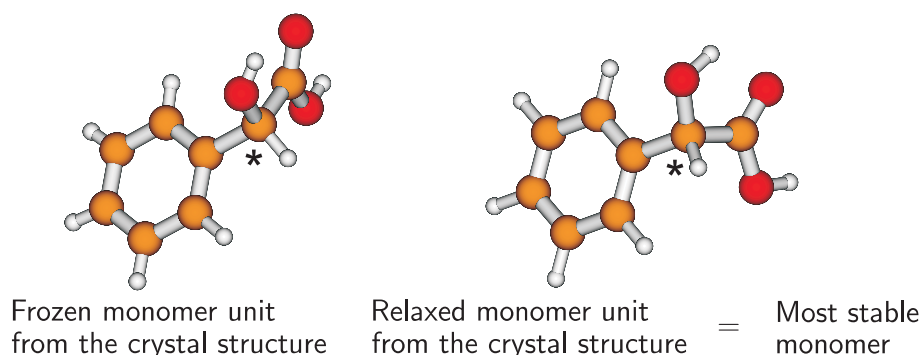
Figure 6.3.: Frozen and relaxed monomer units ((*S*)-enantiomer) taken from the crystal structure of enantiopure mandelic acid [88] as well as the most stable monomer (B3LYP/6-311++G(3df,2p) level). The conformations of the relaxed monomer from the crystal structure and the most stable monomer are the same.

chains which contain different monomer units. The units differ by the orientation of the phenyl group. The two chains are held together by π-stacking along the crystallographic a/c bisector. The crystal structure of racemate II exhibits similarities to the crystal structure of enantiopure mandelic acid. Both structures consist of two symmetry independent double chains made up of only one kind of molecule. In contrast, the crystal structure of racemate I differs significantly from enantiopure and racemate II mandelic acid by forming two-dimensional networks.

6.2. Monomer Conformations

Mandelic acid monomers can be described by a two-letter nomenclature in analogy to the nomenclature used for methyl mandelate (see Chapter 5) [138]. It describes the syn (Ss), cis (C), skew (sk), gauche (G), and anti (A) conformations of the H-O-C-C and O-C-C=O dihedral angles.

The monomer conformations within the crystal structures of enantiopure and racemic (stable and metastable) do not differ qualitatively. Therefore, the energies and wavenumbers of the relaxed monomer units are also the same by means of quantum chemical optimization. In the following, only the monomer of (*S*)-mandelic acid will be considered. An Ss conformation is exhibited which contains an intramolecular O-H$\cdots$O=C hydrogen bond (see Fig. 6.3). Note, that a rotation of the phenyl group by about 45° takes place during structure optimization.

There are no studies reported on the most stable monomer conformation of mandelic acid. It can be assumed that isolated mandelic acid exhibits an Ss conformation in analogy to the most stable monomer of methyl mandelate which was found to have an SsC conformation (see Chapter 5). The Ss form is the same conformation found in the crystal structures of mandelic acid. Structure and frequency calculations of this mandelic acid monomer were performed on the B3LYP/6-311++G(3df,2p) and MP2/6-311+G(2d,p) levels within the current framework.

The H-O distance of the intramolecular O-H···O=C hydrogen bond is 2.1 Å, the O-O distance 2.7 Å, and the angle 118° on the B3LYP/6-311++G(3df,2p) level. A slightly different angle of 119° is predicted on the MP2/6-311+G(2d,p) level. The distances and the angle of the intramolecular hydrogen bond are nearly the same as calculated for the most stable conformer of methyl mandelate (see Chapter 5).

6.3. Preliminary Spectral Considerations

Several vibrational modes of mandelic acid can be expected to appear at similar spectral positions with similar vibrational transition dipole vectors as in the case of methyl mandelate. Tab. 6.1 summarizes the wavenumbers of fundamental modes found in the ATR spectra of methyl mandelate (see Chapter 5 as well). The absence of the methyl group in mandelic acid enables a less ambiguous assignment of the aromatic C-H modes in the mandelic acid spectra. The carboxylic acid group itself introduces a very strong intermolecular binding motif. Predicted wavenumbers and intensities are listed in the Supplement F. Vibrational modes and transition dipole vectors can also be found there.

Two O-H stretching bands, one of the alcoholic and one of the acidic OH group, can be expected for mandelic acid. The spectral position of an O-H stretching mode strongly depends on its hydrogen bond environment as discussed in Chapter 5. Also, the nature of the OH group itself is important. Within a hydrogen bond, the acidic O-H stretching mode is generally more red shifted and broadened than the O-H stretching of the alcoholic O-H group [148]. Since the two OH groups are nearly orthogonal to each other the corresponding modes will show opposite polarization behavior, if the electric vector of the IR radiation does not bisect the vibrational transition dipole vectors.

The C-H stretching region as well as the region below $1600\,\text{cm}^{-1}$ are less con-

Table 6.1.: Wavenumbers $\tilde{\nu}$ in cm^{-1} of experimentally observed reference bands in the ATR spectra of methyl mandelate (see Chapter 5).

Assignment	Methyl Mandelate
ν(O-H)$_{alcoholic}$	3434
ν(C-H$_{aromatic,sym}$)	3103
ν(C-H$_{aromatic,2}$)	3088
ν(C-H$_{aromatic,3}$)	3062
ν(C-H$_{aromatic,4}$)	3049
ν(C-H$_{aromatic,5}$)	3035
ν(C-H$_\alpha$)	2904
ν(C=O)	1811
ν(C=O)	1736
ν(C=O)	1698
ν(C=O)	1669
ν(C-C$_{aromatic,1}$)	1600
ν(C-C$_{aromatic,2}$)	1586
ν(C-C$_{aromatic,3}$)	1491
ν(C-C$_{aromatic,4}$)	1455

gested compared to methyl mandelate due to the absence of the methyl group. This enables a less ambiguous assignment of the aromatic C-H and C-C stretching modes and supports the assignment made for methyl mandelate in Chapter 5.

The monomer units of the mandelic acid crystal are qualitatively the same and undergo the same interactions unlike in the case of methyl mandelate (see Sect. 6.1 and Chapter 5). Nevertheless, complex in-phase and antiphase coupling patterns (factor group splittings) can also be expected for many molecular vibrations [16] due to the complexity of the unit cell.

6.4. FTIR Microspectroscopy

In the following section, results on sublimated microcrystals of enantiopure mandelic acid studied by polarized FTIR microspectroscopy which are published in Ref. [37] will be presented.

(*R*)-mandelic acid is a white powder. There is no evidence that it is hygroscopic. Its melting point under ambient pressure is 130–134°C (according to the supplier). (*R*)-mandelic acid crystallizes at temperatures between +38°C and +45°C in the
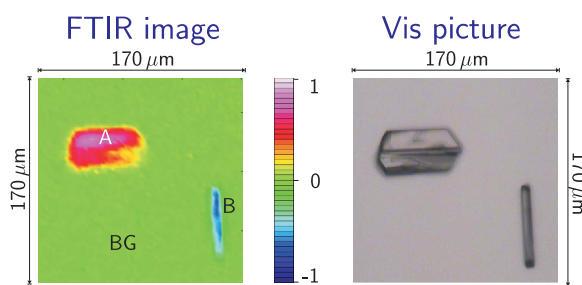
Figure 6.4.: FTIR image of enantiopure mandelic acid crystals grown on two faces A ($\approx$ 95% abundance) and B ($\approx$ 5% abundance).

sublimation cell. The sublimated crystals have a platy (oblate) habit. They can grow on two faces, A and B as shown in Fig. 6.4. Face A is about 20 times more abundant. However, this likely reflects a preferred position of the final crystals due to their platy (oblate) shape and gravitation, rather than a preference emerging at the nucleation stage.

Rotation experiments were carried out in order to verify that type A and B spectra actually correspond to different faces of a given mandelic acid crystal. Fig. 6.5 shows that rotation of a crystal exhibiting a type A spectrum leads to a type B spectrum. Due to oversaturation, it was not possible to record suitable face C spectra (through the long crystal axis). The aromatic C-H stretching band at the highest wavenumber (3107 cm^{-1}, H) only appears for face B, whereas the next C-H stretching band at 3089 cm^{-1} (L) is only present in type A spectra.

Polarized FTIR spectra of face A of mandelic acid exhibit large differences regarding the relative intensities of the alcoholic (3454 cm^{-1}) and acidic (3230–2370 cm^{-1}) O-H stretching bands as well as the aromatic C-H stretching bands (Fig. 6.6). Further differences can be found for the C=O stretching band as well as in the C-C stretching and C-H bending region. The nearly complementary intensity pattern for the alcoholic and acidic O-H stretching bands with rotation of the polarizer can be explained by almost perpendicular O-H vibrational transition dipole moment projections, which are aligned with the microcrystal axes (see Sects. 6.1 and 6.2). The aromatic C-H stretching bands all follow the behavior of the alcoholic O-H stretching band. Thus, the aromatic CH group projections are also perpendicular to the acidic OH group transition moment.

Face B exhibits similar polarization behavior, although the intensity pattern changes somewhat. Again, the alcoholic O-H stretching and the C-H stretching
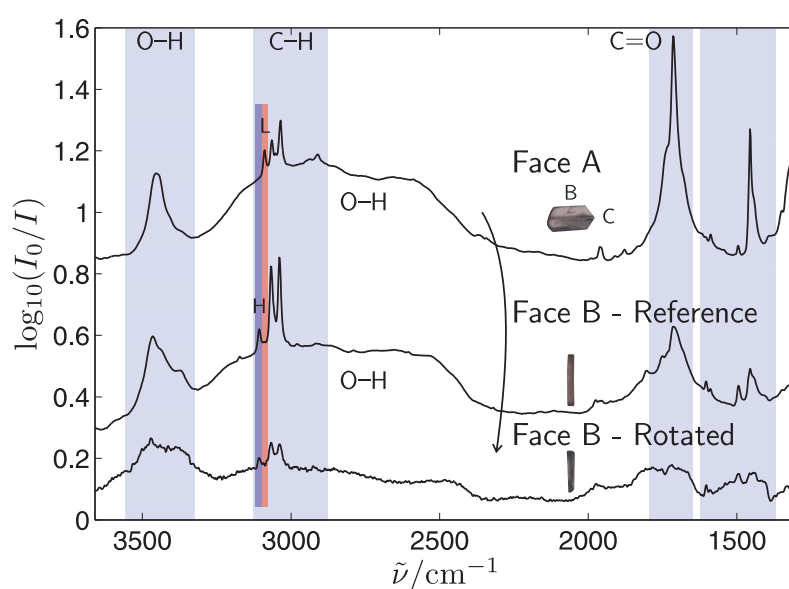
Figure 6.5.: FTIR spectra of enantiopure mandelic acid obtained after rotation of crystals growing on face A (top) to face B (bottom, strong peaks attenuated by stray light) as well as a reference spectrum of face B (center). Regions H and L used for integration are marked in blue and red, respectively.
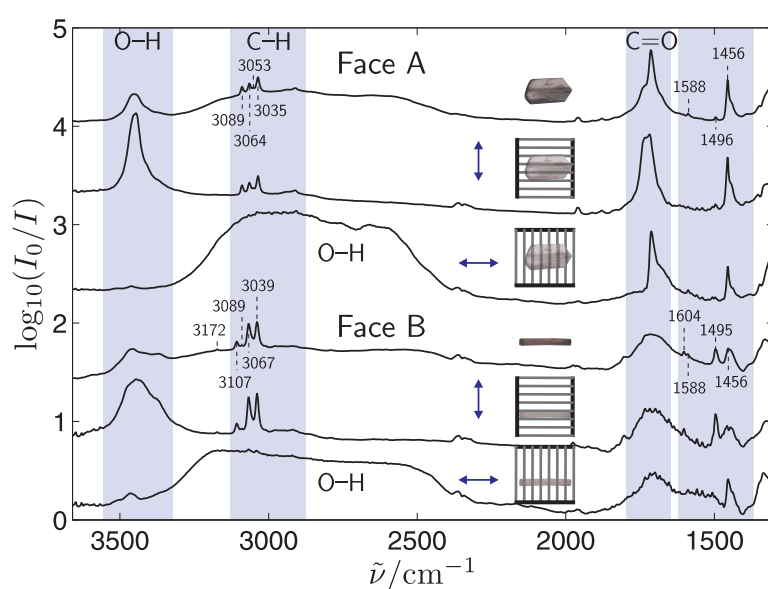
Figure 6.6.: Polarized FTIR spectra of enantiopure mandelic acid through face A and B. The double arrows show the direction of the electric vector of the radiation which passes the polarizer and can excite corresponding vibrational transition dipole vector components. Wavenumbers for selected bands in the difference spectrum are given in cm^{-1}.

bands are anti-correlated with the acidic O-H stretching band. The two findings can be reconciled by positioning the common plane of the alcoholic OH and the phenyl groups more or less parallel to face C, with most vibrational transition moments pointing between the faces A and B. Assuming only weak deviations between bond and transition moment vectors, structural information about the molecules in the crystal can thus already be extracted from the polarization behavior in the crystal.

Fig. 6.7 shows the postulated orientation of the mandelic acid unit cell along the three microcrystal faces assuming the same modification in the sublimation and X-ray experiments [88]. The orientation along the crystallographic axes *a* and *c* reflects the structural results obtained by the polarization experiments. The alcoholic and acidic OH groups are almost perpendicular to each other, and the plane of the phenyl group is perpendicular to the acidic OH group. The OH groups do not align with the *ab* or *bc* cell planes, consistent with the polarization measurements for the microcrystal's A and B faces. Like in the methyl mandelate case, the strong hydrogen bonded chain direction is the preferred growth direction in the sublimation process.

A comparison of experimental and oriented gas model polarization spectra of face A and B in Fig. 6.8 confirms that the alcoholic O-H stretching band gains in intensity, while the acidic O-H stretching band decreases and vice versa. Thus, the experimental O-H stretching bands can be easily assigned due to their opposite polarization behavior (Tab. 6.2) despite the dramatic shortcomings of the oriented gas model for the acidic O-H stretching shift. The latter correlates with a shorter hydrogen bond length (see Fig. 6.2). There is also good agreement between experimental and oriented gas model spectra of the aromatic C-H stretching bands. For both faces the intensities increase with a polarization along the short crystal axis. The detailed directions of the calculated transition moments of the two highest frequency transitions are not as complementary as in the experiment (Fig. 6.6). This may be due to the relatively large distortion of the phenyl ring orientation in the crystal compared to the relaxed monomer conformation (see Fig. 6.3) and invites a crystal calculation. The assignment of the aromatic C-H stretching bands is thus based mostly on the sequence of the predicted modes.

The mandelic acid bands at $1604 \, \text{cm}^{-1}$, $1588/1589 \, \text{cm}^{-1}$, $1496/1495 \, \text{cm}^{-1}$, and $1456 \, \text{cm}^{-1}$ (see Fig. 6.6) are very close to those of methyl mandelate ($1600 \, \text{cm}^{-1}$, $1587 \, \text{cm}^{-1}$, $1491 \, \text{cm}^{-1}$, and $1454 \, \text{cm}^{-1}$) and can be assigned to the same vibrational modes. An overview of the band assignments is given in Tab. 6.2. The corre-
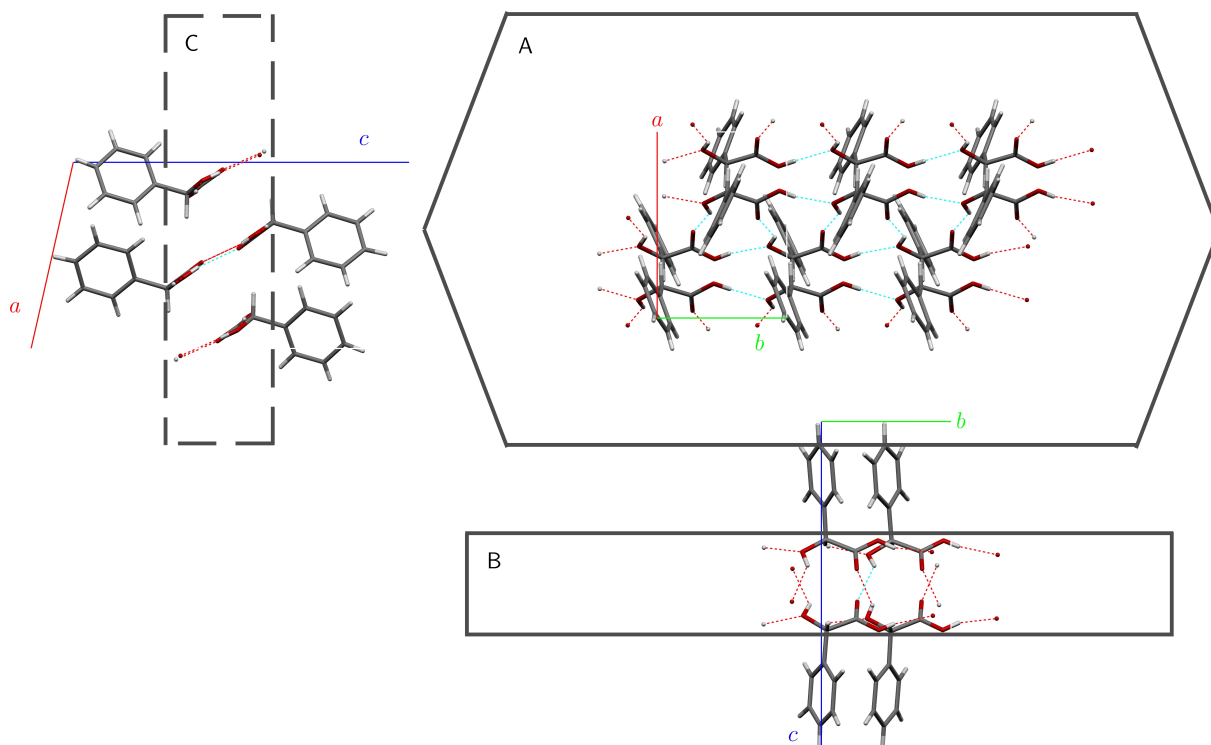
Figure 6.7.: Molecular orientation of (*S*)-mandelic acid along the three crystal faces. The crystal structure was taken from Ref. [88]. The continuous frames mark the observed faces, whereas the unobserved face is dash-framed.
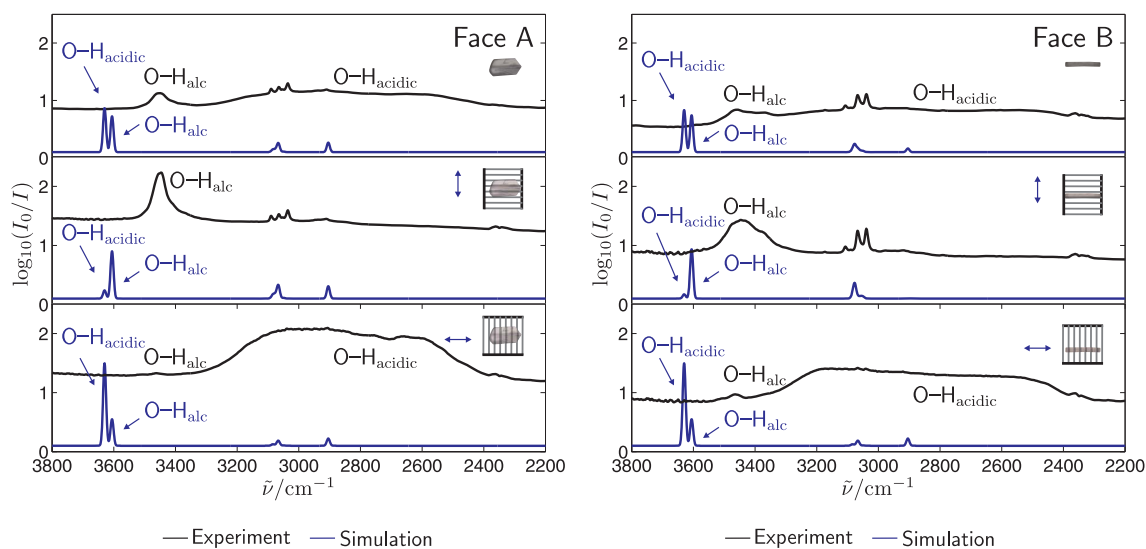
Figure 6.8.: Comparison of experimental (top, black) and oriented gas model (bottom, blue) polarization spectra (B3LYP/6-311++G(3df,2p) level) of face A (left) and face B (right) of enantiopure mandelic acid.

Table 6.2.: Assignments of experimental band maxima in the FTIR microscopic spectra of mandelic acid of face A, face B, FTIR-ATR spectra (without ATR correction) as well as calculations of the relaxed monomer unit taken from the crystal structure (Mon$_{crystal}$) on the B3LYP/6-311++G(3df,2p) level. All wavenumbers are given in cm^{-1}. The stretching and bending vibrations are indicated as ν and δ and the symmetric and asymmetric vibrations with sym and asym.

Assignment	Face A	Face B	ATR	Mon$_{crystal}$
ν(O-H)$_{alcoholic}$	3454	3465	3443	3732
ν(O-H)$_{acidic}$	3230–2370	3230–2370	3230–2370	3757
		3172		
ν(C-H$_{aromatic,sym}$)		3107	3108	3193
ν(C-H$_{aromatic,2}$)	3089	3089	3091	3185
ν(C-H$_{aromatic,3}$)	3064	3067	3068	3174
ν(C-H$_{aromatic,4}$)	3053			3165
ν(C-H$_{aromatic,5}$)	3035	3039	3039	3156
ν(C-H$_\alpha$)	2910		2908	3006
aromatic		1975		
aromatic	1961	1963		
ν(C=O)		1803	1803	
ν(C=O)		1750		
ν(C=O)	1738			1799
ν(C=O)	1714	1714	1712	1799
ν(C-C$_{aromatic,1}$)		1604	1604	1641
ν(C-C$_{aromatic,2}$)	1588	1589	1589	1626
ν(C-C$_{aromatic,3}$)	1496	1495	1495	1528
ν(C-C$_{aromatic,4}$)	1456	1456	1455	1487

sponding modes are visualized in the Supplement F. The band at $1456\,\text{cm}^{-1}$ (ν(C-$C_{\text{aromatic},4}$)) has a higher intensity in face A than in face B spectra, suggesting the orientation of face A to be perpendicular to the *c* axis. The aromatic C-C stretching bands at $1604\,\text{cm}^{-1}$ and $1496/1495\,\text{cm}^{-1}$ (ν(C-$C_{\text{aromatic},1}$) and ν(C-$C_{\text{aromatic},3}$)) are weak or absent in face A spectra. The vibrational transition dipole vectors of both point more or less along the C-C bond between the phenyl group and the substituent. Therefore, they are not excited when looking along the *c* axis. This confirms the assignment of the crystallographic *c* axis perpendicular to face A or else provides a detailed normal mode assignment of these aromatic bands. All four C-C stretching bands appear in face B spectra. Polarization spectra (Fig. 6.6) show that the vibrational transition dipole vectors of ν(C-$C_{\text{aromatic},1}$) and ν(C-$C_{\text{aromatic},3}$) are oriented along the short axis of face B. This again suggests that face B includes the crystallographic *c* axis as shown in Fig. 6.7 and it shows that the predicted sequence and shape of the C-C stretching modes (Supplement F) is consistent with the one found in the microcrystals.

6.5. Conclusions

Polarization FTIR microspectra of sublimated mandelic acid crystals were recorded and vibrational transition dipole vectors inferred. Experimental and predicted results were compared and the molecular orientation within the crystal structure determined. An assignment of several vibrational modes was performed which supports the vibrational assignment made for methyl mandelate in Chapter 5. Overall, the performance of the polarization FTIR microspectroscopic method of sublimated crystals was shown on another substance.

So far, only the enantiopure compound of mandelic acid was investigated. It might be worthwhile to also investigate the racemic compound. As reported, the stable racemate shows spectral differences compared to the enantiopure compound in the mid infrared region [20, 164, 165]. A comparison of enantiopure and racemic mandelic acid polarization spectra might support the assignment of vibrational bands appearing in the region of 1400–$1000\,\text{cm}^{-1}$. Further light may also be shed on the polymorphism observed in the racemate [166–168, 170].

7. Phenylpropanolamines

The 1-phenylpropan-1-ol-2-amines (1*R*,2*S*)-norephedrine (NE), (1*S*,2*S*)-pseudonorephedrine (PNE), (1*R*,2*S*)-ephedrine (E), and (1*S*,2*S*)-pseudoephedrine (PE) can be found in the Ephedra species of plants [171]. They are biologically active and act on the sympathetic nervous system by altering the natural neurotransmission process. E.g., (1*R*,2*S*)-norephedrine is used as an appetite suppressant, (1*R*,2*S*)-ephedrine for broncho dilatation, and (1*S*,2*S*)-pseudoephedrine in flu medication [171].

Norephedrine, pseudonorephedrine, ephedrine, and pseudoephedrine are structurally similar chiral substances (see Fig. 7.1). Norephedrine and pseudonorephedrine are diasteroisomers (C_6H_5–CHOH–CHNH(CH_3)–CH_3), as are ephedrine and pseudoephedrine (C_6H_5–CHOH–$CHNH_2$–CH_3). All possess a phenyl, a hydroxy, and an amino group next to two acidic C-H groups (α and β) and at least one methyl group. The phenylpropanolamines of interest have two chiral carbon atoms (marked with an asterisk (*) in Fig. 7.1, (1): CHORR', (2): CHNRR') and are open for chirality recognition. They are available for hydrogen bonding at the oxygen and the nitrogen functionalities as well as for aromatic interactions. An overview of their FTIR-ATR spectra (Fig. 7.2) exhibits spectral similarities. Furthermore, they also show structural similarity to methyl mandelate and mandelic acid which have been extensively studied within the framework of the present work (see Chapters 5 and 6). Their melting points, sublimation and condensation temperatures are listed in Tab. 7.1.

In this chapter, the aggregation of sublimated microcrystals of (1*S*,2*R*)-norephedrine, (1*R*,2*R*)-pseudonorephedrine, (1*R*,2*S*)-ephedrine, and (1*S*,2*S*)-pseudoephedrine as well as mixtures of both enantiomers of norephedrine as well as pseudoephedrine will be analyzed. Molecular recognition phenomena will be investigated in the case of norephedrine and pseudoephedrine. In the case of ephedrine an anhydrate and a hydrate will be observed. Polarization FTIR spectra of the above mentioned microcrystals will be presented. The molecular conformation of

Table 7.1.: Standard melting temperature (information provided by supplier and Ref. [173]) (ϑ_m°) as well as observed sublimation (ϑ_{Subl}) and liquid condensation temperatures (ϑ_{Cond}) of the investigated phenylpropanolamines set at the bottom of the sublimation cell.

Substance	ϑ_m°/°C	ϑ_{Subl}/°C	ϑ_{Cond}/°C
Norephedrine, enant (NE, enant)	51–53	18–20	28
Norephedrine, rac (NE, rac)	102	40	-
Pseudonorephedrine (PNE)	76	30–40	-
Ephedrine Anhydrate (E-AH)	37–39	30(?)[a]	18
Ephedrine Hemihydrate (E-H)	39–43	-	-
Pseudoephedrine, enant (PE, enant)	116–120	30–45	-
Pseudoephedrine, rac (PE, rac)	119	35–50	-

[a]see Sect. 7.6

the molecules within the crystals [89–92, 172] will be derived by a comparison of experimental and oriented gas model spectra, by comparison with the results gained from methyl mandelate and mandelic acid (Chapters 5 and 6), and by comparison of the crystal habit and the interactions. It will be shown, that an assignment of the molecular conformation is possible. Tentative molecular orientations will be derived for enantiopure and racemic pseudoephedrine. Also, an assignment of several vibrational bands will be carried out. The crystal structures, the conformations within the published crystal structures [89–92, 172] and those of the most stable monomers [82–87] as well as preliminary considerations concerning expected vibrational bands will be discussed beforehand. A variety of N-H modes will be analyzed in Sect. 7.8.

Note, that the configuration of pseudonorephedrine investigated within the present work (1*R*,2*R*) differs from the configuration in the published crystal structure (1*S*,2*S*) [90]. Both enantiomers show equivalent spectra (verified in the methyl mandelate case [37], see Chapter 5). If not stated otherwise, the form found in the crystal structure (1*S*,2*S*) is depicted in all figures.

7.1. Crystal Structures

The crystal structures of a variety of phenylpropanolamines and their salts have already been determined [89–92, 172]. The molecular conformations in the crystal structures provided by the Cambridge Structural Database (CSD) (see Ref. [174])
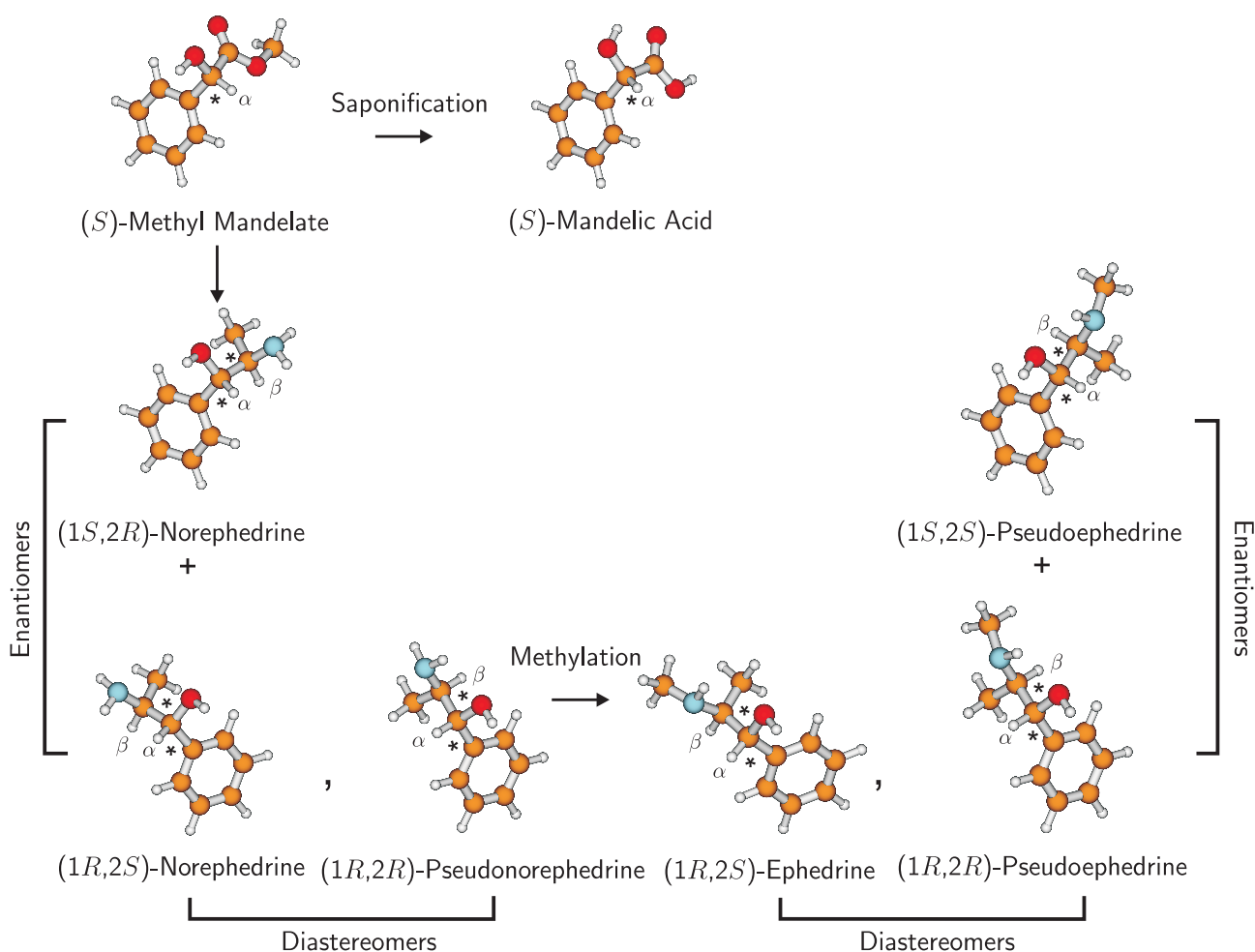
Figure 7.1.: Phenylpropanolamines investigated by polarization FTIR microspec-
troscopic sublimation experiments. The figure exhibits structural simi-
larities of the phenylpropanolamines among each other and with regard
to methyl mandelate and mandelic acid. Centers of chirality are marked
by an asterisk (*). The shown configurations are those investigated in
the solid state.
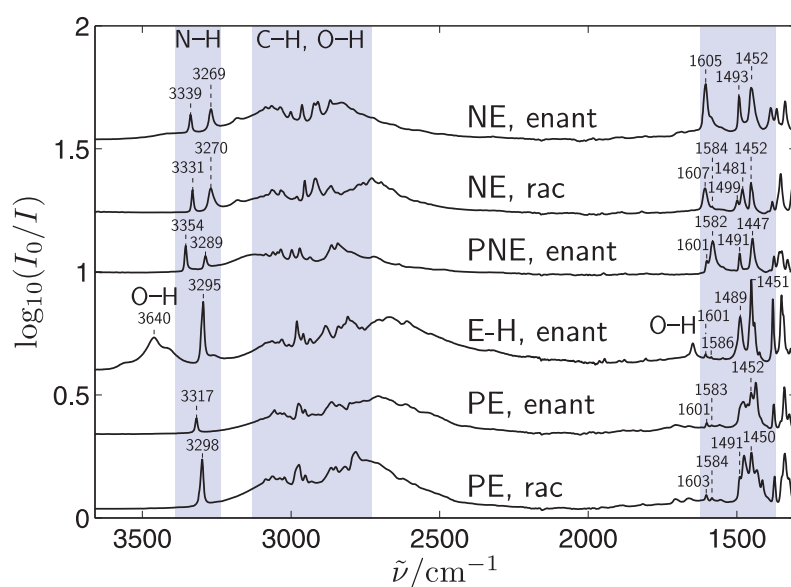
Figure 7.2.: FTIR-ATR spectra of enantiopure norephedrine (NE, enant), racemic norephedrine (NE, rac), enantiopure pseudonorephedrine (PNE, enant), enantiopure ephedrine hemihydrate (E-H, enant), enantiopure pseudoephedrine (PE, enant), and racemic pseudoephedrine (PE, rac). Band positions are given in cm^{-1}.

Table 7.2.: Types, distances d in Å (d_{H-X} and d_{Y-X}), and angles α in $^\circ$ of Y-H$\cdots$X hydrogen bonds appearing in the crystal structures of the investigated phenylpropanolamines [89–92].

	O-H$\cdots$N			N-H$\cdots$O			C-H$\cdots$O			O-H$\cdots$O		
	d_{H-X}	d_{Y-X}	α	d_{H-X}	d_{Y-X}	α	d_{H-X}	d_{Y-X}	α	d_{H-X}	d_{Y-X}	α
NE, rac	1.89	2.78	176	2.28	3.07	139	-	-	-	-	-	-
PNE, enant	2.02	2.84	171	2.47	3.27	154	-	-	-	-	-	-
E-AH, enant	1.96	2.78	173	(2.57)	(2.87)	(101)	2.72	3.51	131	-	-	-
E-H, enant	1.94	2.74	168	2.23	3.09	167	-	-	-	2.00	2.86	170
PE, rac	1.88	2.74	174	(2.24)	(2.68)	(108)	2.22	3.34	162	-	-	-

are used for quantum chemical calculations and the simulation of spectra (see Chapter 3). The crystal structures and the interactions which affect the habit of the sublimated microcrystals will be analyzed in the corresponding Sections. No polymorphism has been reported for any of the investigated phenylpropanolamines. There is an anhydrous and a hydrous form in the case of ephedrine.

Similar patterns of interactions are present in the crystal structures of all investigated phenylpropanolamines. Tab. 7.2 summarizes the types of hydrogen bonds, their distances and angles. In one direction there are infinite chains of O-H$\cdots$N hydrogen bonds with a distance of 1.9–2.0 Å. These infinite strands are held together by weaker N-H$\cdots$O and C-H$\cdots$O hydrogen bonds with a distance of 2.2–2.5 Å. The resulting layers are held together by van der Waals interactions.

7.2. Monomer Conformations

The conformation of monomers within a crystal depends on the possibility of forming intra- as well as intermolecular interactions. The conformation can vary within the unit cell of a given crystal (conformational isomorphism, e.g., *trans*-1,4-cyclohexanediol [175]), for different polymorphs (conformational polymorphism, e.g., vitamin A acid [176–178]) or for solvates (e.g., ephedrine anhydrate and ephedrine hemihydrate [91], see below). A crystal's monomer conformation may vary from the most stable conformation under vacuum-isolated conditions. In the following, the conformations and energy differences of fully relaxed crystal and most stable monomer structures will be compared.

Butz et al. introduced an A/G notation for the different conformations of norephedrine, ephedrine, pseudoephedrine, and hydrated clusters of ephedrine and pseudoephedrine [82–84]. The notation describes the anti (A) and gauche (G) arrangements of the CCCN and OCCN groups. In the published crystal structure of norephedrine the monomer units adopt a GG conformation [89]. In contrast, pseudonorephedrine, ephedrine (anhydrate as well as hemihydrate) and pseudoephedrine were found to have an AG conformation also in the crystal structures [90–92]. The amino groups of ephedrine anhydrate on one hand and ephedrine hemihydrate and pseudoephedrine on the other hand are enantiomeric to each other. To account for this, the structure of ephedrine anhydrate is named AG(a) and the ones of ephedrine hemihydrate and pseudoephedrine are named AG(b) [82–84]. The monomer conformations found in the crystal structures of the investigated phenylpropanolamines are depicted in Fig. 7.3. It should be noted, that hydrogen atoms are weak X-ray diffractors and the position is often geometrically calculated and then refined [13, 179]. It is possible that not the AG(a) but the AG(b) conformations and vice versa are present in the crystal structures. Nevertheless, the positioning of the hydrogens is in agreement with the establishment of hydrogen bonds within the crystals. In the following, the correctness of the hydrogen position will be assumed.

The most stable monomer conformations of norephedrine, ephedrine, and pseudoephedrine as well as of 1:1 and 1:2 ephedrine water clusters were determined by combining resonant two-photon ionization, laser induced fluorescence, and resonant ion-dip infrared jet-spectroscopy in combination with ab initio calculations (HF/6-31G(d), B3LYP/6-31+G(d), MP2/6-311+G(d,p)) by Butz et al. [82–84]. The conformations of ephedrine (calculated on the MP2/6-311++G(d,p) level) and pseudoephedrine (calculated on the CC/aug-cc-pVDZ level) were confirmed by Karaminkov et al. who also carried out low- and high-resolution resonantly enhanced two-photon ionization spectroscopic studies with mass selection of jet cooled molecules [85, 86]. A mixed ephedrine-water dimer as well as two conformations of ephedrine were observed with the same technique [180]. Further conformations of norephedrine, ephedrine, and pseudoephedrine were found by Alonso et al. using gas phase molecular beam Fourier transform microwave spectroscopy in combination with MP2/6-311++G(d,p) level calculations [87]. The most stable monomer and some other conformations of ephedrine were also found in FTIR-jet spectroscopic studies [181].
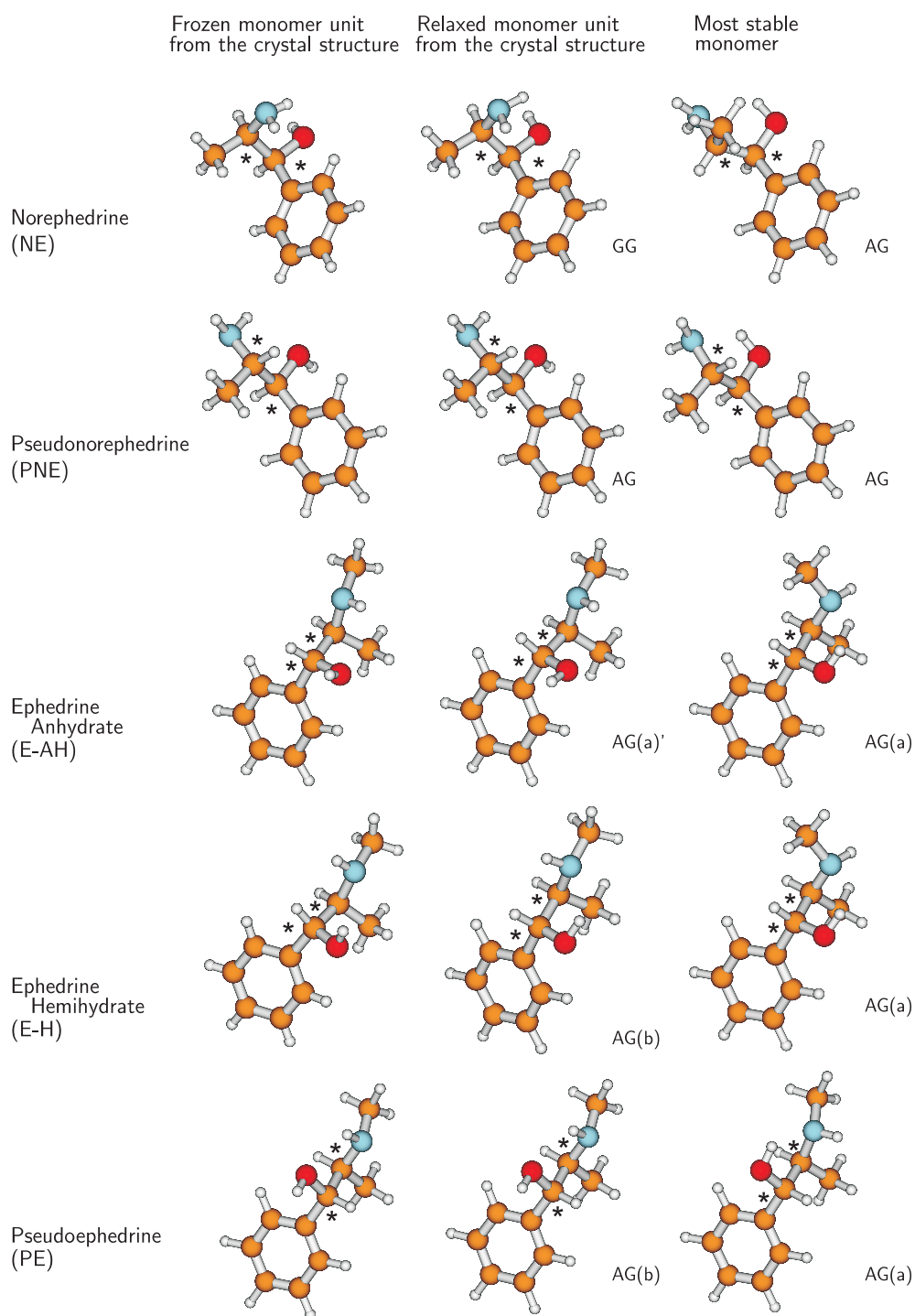
Figure 7.3.: Frozen and relaxed monomer units taken from the crystal structures [89–92] as well as the most stable monomers [82–87] (B3LYP/6-311++G(3df,2p) level) of the investigated phenylpropanolamines. Centers of chirality are marked with an asterisk (*).

The most stable structures of norephedrine, ephedrine (monomer as well as hydrated ephedrine), and pseudoephedrine were all found to have an AG or an AG(a) conformation [82–87]. In this conformations intramolecular O-H···N hydrogen bonds are established. The AG and AG(a) conformations were recalculated within the current framework using the B3LYP/6-311++G(3df,2p) level of theory (see Chapter 3). No studies have been reported for pseudonorephedrine so far. Therefore, the AG conformation was also assumed for pseudonorephedrine. The structures of the most stable monomer conformations are shown in Fig. 7.3 as well.

The energy differences without and with zero point energies between the relaxed monomer unit from the crystal structure and the most stable monomer conformation are summarized in Tab. 7.3. The conformations taken from the crystal structures are 4–12 kJ·mol^{-1} higher in energy and form intramolecular N-H···O contacts, whereas in the most stable monomers O-H···N hydrogen bonds are established. Only in the monomer unit of the ephedrine hemihydrate crystal an O-H···N bond is present as well. The types, distances, and angles of the Y-H···X contacts are also summarized in Tab. 7.3.

The energy differences between the most stable monomer conformation and the relaxed monomer unit from the crystal structure are the highest for norephedrine (12 kJ·mol^{-1} and 10 kJ·mol^{-1}). This can be explained with the energetically unfavorable GG conformation in the crystal structure and the long distance of the intramolecular Y-H···X contact in the relaxed monomer (2.8 Å compared to 2.2 Å). Also, in the case of ephedrine anhydrate the energy differences are rather high (10 kJ·mol^{-1} and 9 kJ·mol^{-1}). Both monomers establish an AG conformation, but the amino group is rotated. The AG(a)' conformation of the relaxed monomer of the crystal structure is energetically less favorable. The energy differences of the relaxed monomer from the crystal structure and the most stable monomer are lower for pseudonorephedrine (5 kJ·mol^{-1} and 4 kJ·mol^{-1}), ephedrine hemihydrate (5 kJ·mol^{-1}), and pseudoephedrine (6 kJ·mol^{-1} and 5 kJ·mol^{-1}). This can be explained with a similar conformation (AG) and similar H···X distances (2.3 Å compared to 2.1 Å for pseudonorephedrine, 2.2 Å compared to 2.2 Å for ephedrine hemihydrate, and 2.2 Å compared to 2.1 Å for pseudoephedrine). The monomer units of the ephedrine hemihydrate and the pseudoephedrine crystals adopt an AG(b) conformation which seems to be energetically favorable compared to the AG(a)' conformation found within the anhydrous ephedrine crystal. But, the energetical preference of AG(b) over AG(a)' might be subtle. The establishment of

Table 7.3.: Types, distances d in Å (d_{H-X} and d_{Y-X}), and angles α in $^\circ$ of Y-H$\cdots$X contacts as well as energy differences without and with zero point energies (ΔE and ΔE_0) of the relaxed monomer units from the crystal structure [89–92, 172] and the most stable monomers [82–87] of the investigated phenylpropanolamines in kJ·mol^{-1}. No imaginary frequencies are observed.

		d_{H-X}	d_{Y-X}	α	ΔE	ΔE_0
Norephedrine (NE)						
crystal	N-H$\cdots$O	2.8	3.0	102	11.7	10.4
stable	O-H$\cdots$N	2.2	2.8	117	0.0	0.0
Pseudonorephedrine (PNE)						
crystal	N-H$\cdots$O	2.3	2.7	102	4.9	4.3
stable	O-H$\cdots$N	2.1	2.7	120	0.0	0.0
Ephedrine Anhydrate (E-AH)						
crystal	N-H$\cdots$O	2.5	2.8	99	10.2	8.6
stable	O-H$\cdots$N	2.2	2.8	118	0.0	0.0
Ephedrine Hemihydrate (E-H)						
crystal	N-H$\cdots$O	(3.0)	(2.8)	(66)	4.9	5.1
crystal	O-H$\cdots$N	2.2	2.8	115		
stable	O-H$\cdots$N	2.2	2.8	118	0.0	0.0
Pseudoephedrine (PE)						
crystal	N-H$\cdots$O	2.2	2.7	110	5.7	4.6
stable	O-H$\cdots$N	2.1	2.7	120	0.0	0.0

an O-H$\cdots$N hydrogen bond within the ephedrine hemihydrate monomer and the shorter N-H$\cdots$O contacts of pseudoephedrine are more likely the reason for the lower energy differences.

7.3. Preliminary Spectral Considerations

The phenylpropanolamines are structurally similar to mandelic acid and methyl mandelate (Fig. 7.1). They have an alcoholic hydroxy group, an aromatic group, a methyl group, and an α-acidic CH group in common. Therefore, several vibrational modes can be expected to appear at similar wavenumbers and to have similar vibrational transition dipole vectors. Tab. 7.4 summarizes band positions of methyl mandelate and mandelic acid (see Chapters 5 and 6) which are expected to be observed. In addition, the phenylpropanolamines possess an amino or a methylamine

Table 7.4.: Wavenumbers $\tilde{\nu}$ in cm^{-1} of experimentally observed reference bands in the ATR spectra of enantiopure methyl mandelate and mandelic acid (see Chapters 5 and 6).

Assignment	Methyl Mandelate	Mandelic Acid
ν(O-H)$_{alcoholic}$	3434	3443
ν(C-H$_{aromatic,sym}$)	3103	3108
ν(C-H$_{aromatic,2}$)	3088	3091
ν(C-H$_{aromatic,3}$)	3062	3068
ν(C-H$_{aromatic,4}$)	3049	3055
ν(C-H$_{aromatic,5}$)	3035	3039
ν(C-H$_{3,asym1}$)	3033	-
ν(C-H$_{3,asym2}$)	3003	-
ν(C-H$_{3,sym}$)	2956	-
ν(C-H$_{\alpha}$)	2904	2908
ν(C-C$_{aromatic,1}$)	1600	1604
ν(C-C$_{aromatic,2}$)	1586	1589
ν(C-C$_{aromatic,3}$)	1491	1495
ν(C-C$_{aromatic,4}$)	1455	1455

group and a second CH group (β-acidic). In the following, modes involving these functional groups will be discussed in detail (for all others see Chapter 5). Predicted wavenumbers and intensities are listed in the Supplement F. Also, vibrational modes and transition dipole vectors are depicted there.

The position and the intensity of the O-H stretching band strongly depend on aggregation and the resulting interactions. The hydroxy groups of the phenyl-propanolamines are hydrogen bonded to amino groups (O-H$\cdots$N) as mentioned in Sect. 7.1. They form long strands of monomer units and are therefore expected to be further red shifted and intensified.

N-H Stretching Mode

Norephedrine and pseudonorephedrine are primary amines, ephedrine and pseu-doephedrine secondary amines. Therefore, there is a splitting resulting in an asymmetric and a symmetric N-H stretching mode for norephedrine and pseudonorephedrine but only one N-H stretching mode for ephedrine and pseudoephedrine. The asymmetric N-H stretching band can be expected at 3375 ± 25 cm^{-1} and the symmetric one at 3300 ± 30 cm^{-1} [147, 148]. The N-H

stretching band of the secondary amines usually appears around 3300 cm^{-1} as well. The position and intensity may be affected by hydrogen bonding but less so than for the O-H stretching band because the NH group is a poorer hydrogen bond donor [147]. The integrated N-H band strength of primary amines is about twice the one of secondary amines [148].

Tab. 7.5 summarizes predicted wavenumbers of the N-H and N-D stretching vibrations for the investigated phenylpropanolamines (monomers relaxed from the crystal structure and most stable monomers, see Sect. 7.2), its fragments isopropylamine, methylisopropylamine, ethylamine, and methylethylamine and the aggregated fragments of ethylamine and methylethylamine with dimethylether or methanol (see Fig. 7.4). The fragments are chosen to model the amino group and its behavior upon conformation, methylation, intramolecular coordination, and aggregation. Two conformations (I and II) of the isopropylamine as well as the methylisopropylamine fragment are present in the investigated phenylpropanolamines. Isopropylamine I is a fragment of the norephedrine crystal and of the most stable structure of pseudonorephedrine, isopropylamine II of the most stable conformer of norephedrine and of the pseudonorephedrine crystal. Methylisopropylamine I is realized in the ephedrine anhydrate crystal and in the most stable monomer of pseudoephedrine, methylisopropylamine II in the ephedrine hemihydrate crystal, the most stable monomer of ephedrine, and in the pseudoephedrine crystal. The monomers and clusters of ethylamine and methylethylamine are based on the structures of isopropylamine and methylisopropylamine. In the case of methylethylamine one trans and two gauche conformations ((a) and (b)) are considered.

The N-H stretching modes of the methylated amines are predicted to appear midway between the asymmetric and symmetric N-H stretching modes of the corresponding primary amines. Only for the monomer unit from the ephedrine hemihydrate crystal and the most stable pseudoephedrine monomer this is not true. Here, the N-H stretching of the methylated substance are approximately 30 and 40 cm^{-1} more red shifted than the average of the symmetric and asymmetric N-H stretching modes. An explanation for these deviations will be given below. The N-H stretching modes of form I and II of isopropylamine and methylisopropylamine are predicted at different wavenumbers. Form I is red shifted by approximately 10–20 cm^{-1}. Also, the position of the methyl group in methylethylamine has an influence on the wavenumber. The trans conformation shows the smallest wavenumber, followed by gauche(a) which is shifted by 9 cm^{-1} to higher wavenumber. The N-H stretching

Table 7.5.: Predicted harmonic wavenumbers ω in cm^{-1} and IR intensities I in km·mol^{-1} of the N-H and N-D stretching modes of relaxed monomers from the crystal structure (X$_{crystal}$), of the most stable monomers (X$_{stable}$, see Sect. 7.2) and of fragments of the investigated phenylpropanolamines (NE, PNE, E, and PE) on the B3LYP/6-311++G(3df,2p) level. The fragments are isopropylamine (IPA, I and II) and methylisopropylamine (MIPA, I and II) as well as (nondeuterated and ND/OD-deuterated) ethylamine (EA) and trans-, gauche(a)-, and gauche(b)-methylethylamine (MEA) with and without the aggregation partners dimethylether (DME) and methanol (MeOH) (see Fig. 7.4).

	asym		sym				
-NH$_2$	ω	I	ω	I	-NHCH$_3$	ω	I
NE$_{crystal}$	3567	3	3490	1	E-AH$_{crystal}$	3531	5
					E-H$_{crystal}$	3498	0
NE$_{stable}$	3582	3	3501	0	E$_{stable}$	3543	3
PNE$_{crystal}$	3586	6	3507	2	PE$_{crystal}$	3538	6
PNE$_{stable}$	3578	5	3491	1	PE$_{stable}$	3497	1
IPA I	3558	0	3479	2	MIPA I	3506	0
IPA II	3569	0	3492	1	MIPA II	3523	0
EA	3572	1	3494	1	trans-MEA	3513	0
					gauche(a)-MEA	3522	0
					gauche(b)-MEA	3538	1
EA+DME(d)	3559	39	3480	48	trans-MEA+DME	3497	74
EA+DME(u)	3564	24	3480	45	gauche(a)-MEA+DME	3507	74
					gauche(b)-MEA+DME	3520	99
EA+MeOH	3562	4	3486	18	trans-MEA+MeOH	3500	7
					gauche(a)-MEA+MeOH	3505	7
					gauche(b)-MEA+MeOH	3518	7
MeOH+EA+DME(u)	3540	54	3462	134			
NE$_{crystal,deut}$	2628	3	2521	1	E-AH$_{crystal,deut}$	2582	5
NE$_{stable,deut}$	2641	3	2531	1	E$_{stable,deut}$	2592	3
PNE$_{crystal,deut}$	2644	5	2534	2	PE$_{crystal,deut}$	2587	12
PNE$_{stable,deut}$	2636	4	2525	2	PE$_{stable,deut}$	2556	1
EA$_{deut}$	2632	2	2525	0	trans-MEA$_{deut}$	2569	1
					gauche(a)-MEA$_{deut}$	2575	1
					gauche(b)-MEA$_{deut}$	2588	2
EA$_{deut}$+DME(d)	2626	20	2517	25	trans-MEA$_{deut}$+DME	2558	51
EA$_{deut}$+DME(u)	2624	28	2516	27	gauche(a)-MEA$_{deut}$+DME	2566	50
					gauche-MEA(b)$_{deut}$+DME	2576	64
EA$_{deut}$+MeOD	2625	3	2520	4	trans-MEA$_{deut}$+MeOD	2559	1
					gauche(a)-MEA$_{deut}$+MeOD	2562	3
					gauche(b)-MEA$_{deut}$+MeOD	2573	2
EA-NDH$\cdots$DME(u)	3505	69	2583	1			
EA-NHD$\cdots$DME(u)	3541	1	2557	43			
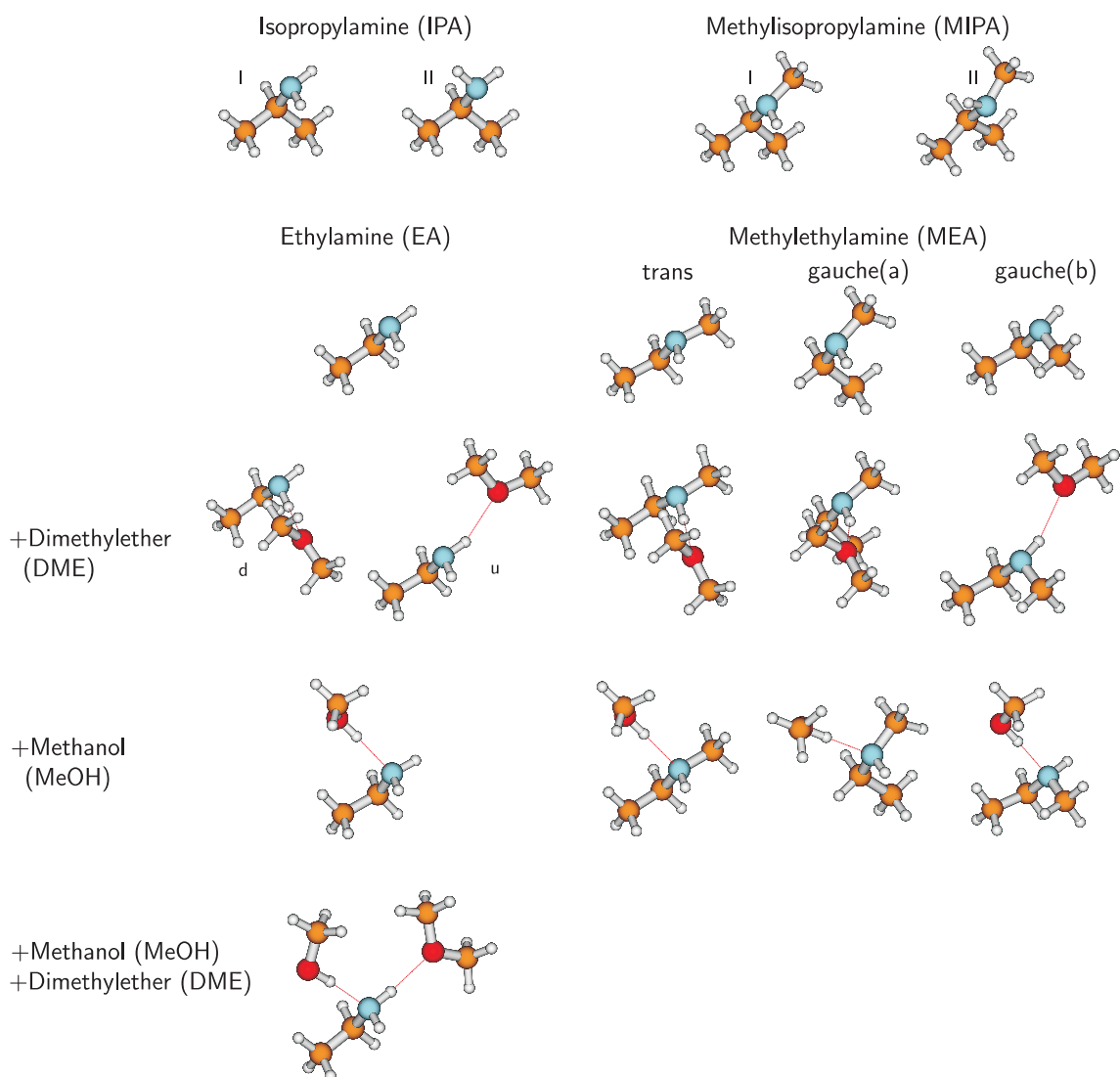
Figure 7.4.: Isopropylamine (I and II), methylisopropylamine (I and II), ethylamine, trans-, gauche(a)-, and gauche(b)-methylethylamine monomers, and complexes of ethylamine, trans-, gauche(a)-, and gauche(b)-methylethylamine with dimethylether or methanol. The two clusters of ethylamine with dimethylether are denoted d and u for down and up.

mode of gauche(b)-methylamine is predicted at $25\,\text{cm}^{-1}$ higher wavenumber than the trans-form. The predicted wavenumbers of ethylamine and methylethylamine shift upon aggregation with dimethylether or methanol. The resulting red shift is in the order of 8–$20\,\text{cm}^{-1}$. It is almost the same for aggregation leading to an N-H$\cdots$O or an O-H$\cdots$N hydrogen bond. The red shift increases to about $30\,\text{cm}^{-1}$ in the case of the cooperative O-H$\cdots$N-H$\cdots$O hydrogen bond of the methanol-ethanol-dimethylether cluster.

The deviation of the predicted N-H stretching wavenumbers of the nine phenyl-propanolamine monomers (average position of the asymmetric and symmetric N-H stretch for nonmethylated amines) compared to the predicted wavenumber of ethy-lamine ($3533\,\text{cm}^{-1}$) is between $-14\,\text{cm}^{-1}$ and $+36\,\text{cm}^{-1}$ with a mean value of $+4\,\text{cm}^{-1}$ and a root mean square (rms=$\sqrt{\frac{1}{n}\cdot\sum_{i=1}^{n}x_i^2}$) of $18\,\text{cm}^{-1}$. These wavenum-ber deviations are a result of multiple interactions taking place within the calculated monomers, such as inductive effects. In order to identify the influencing parameters and shifts, N-H stretching wavenumbers of eight methylisopropanolamines which are fragments of ephedrine and pseudoephedrine (see Fig. 7.5) were calculated in addition to the phenylpropanolamines and the fragments discussed above. The full set of 25 compounds deviates from the ethylamine N-H stretching mode average by -17 to $+36\,\text{cm}^{-1}$ with a mean value of $+7\,\text{cm}^{-1}$ and a root mean square deviation of $17\,\text{cm}^{-1}$. Tab. 7.6 summarizes the predicted wavenumbers, the deviations to the N-H stretching wavenumber of ethylamine, postulated parameters influencing these wavenumbers as well as the resulting shifts, predicted wavenumbers starting from ethylamine ($3533\,\text{cm}^{-1}$) which was chosen as the interaction free reference sys-tem and adding the influence of these parameters, and the difference between the predicted and calculated wavenumbers. Ideally, the predicted wavenumbers should have the same value as the calculated wavenumbers.

from E-AH$_{crystal}$ from E-H$_{crystal}$ from E$_{stable}$

from PE$_{crystal}$ from PE$_{stable}$
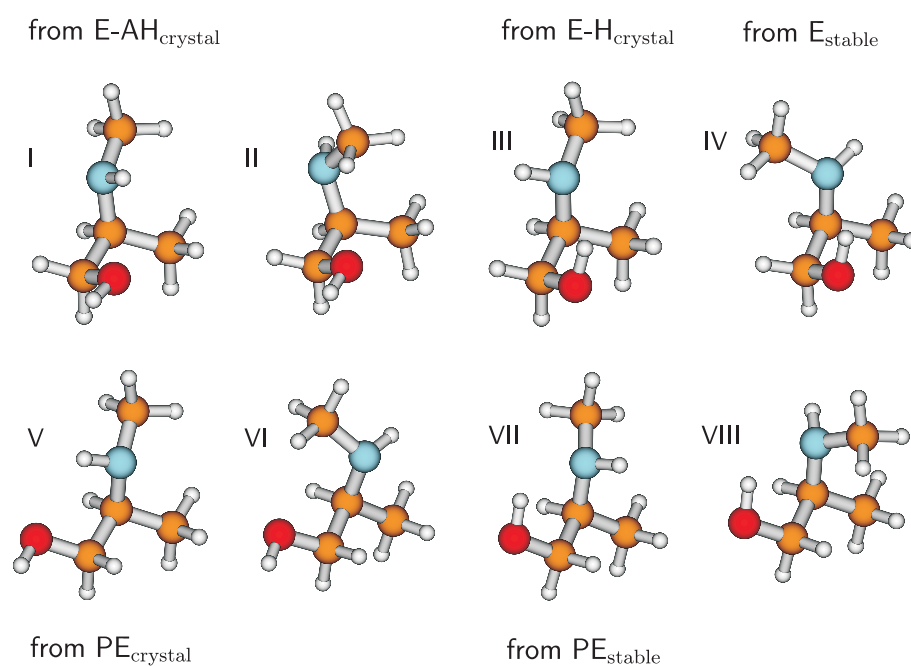
Figure 7.5.: Methylisopropanolamines I–VIII. I is a fragment of the monomer from the ephedrine anhydrate crystal, III from the ephedrine hemihydrate crystal, IV of the most stable ephedrine monomer, V of the monomer from the pseudoephedrine crystal, and VII of the most stable pseudoephedrine monomer. The methylisopropanolamines II, IV, VI, and VIII have an inverted amino group relative to I, III, V, and VI.

Table 7.6.: Predicted harmonic B3LYP/6-311++G(3df,2p) wavenumbers ω_{calc} of the N-H stretch, the distance to the N-H stretching wavenumber of ethylamine $\Delta\omega_{EA-c}$, postulated parameters influencing the predicted wavenumbers (nonterminal amine, methylated amine, no trans H-N/C-H, and Y-H···X hydrogen bonds and contacts) of ethylamine (EA), methylamine (MEA), isopropylamine (IPA), methylisopropylamine (MIPA), methylisopropanolamines (MIPOA), and the investigated phenylpropanolamines, the wavenumbers after removing the influence of the parameters ω_{pred} in cm^{-1}, and its deviation to the calculated wavenumbers $\Delta\omega_{p-c}$. An average wavenumber of the asymmetric and symmetric N-H stretching modes is used for the nonmethylated amines.

	ω_{calc}	$\Delta\omega_{EA-c}$	C-NHR-C	N-CH$_3$	no t-HNCH	O-H···N(H)	O-H···(H)N	N-H···O	C-H···O	ω_{pred}	$\Delta\omega_{p-c}$
EA	3533	0	0	0	0	0	0	0	0	3533	0
trans-MEA	3513	+20	0	−10	0	0	0	0	0	3523	+10
gauche(a)-MEA	3522	+11	0	−10	0	0	0	0	0	3523	+1
gauche(b)-MEA	3538	−5	0	−10	+15	0	0	0	0	3538	0
IPA I	3519	+14	−15	0	0	0	0	0	0	3518	−1
IPA II	3531	+2	−15	0	+15	0	0	0	0	3533	+2
MIPA I	3506	+27	−15	−10	0	0	0	0	0	3508	+2
MIPA II	3523	+10	−15	−10	+15	0	0	0	0	3523	0
MIPOA I	3532	+1	−15	−10	0	0	0	+15	+5	3528	+4
MIPOA II	3528	+5	−15	−10	+15	0	0	0	+5	3528	0
MIPOA III	3501	+32	−15	−10	+15	0	−20	0	0	3503	+2
MIPOA IV	3540	−7	−15	−10	+15	+15	0	0	0	3538	−2
MIPOA V	3528	+5	−15	−10	+15	0	0	+15	0	3538	+10
MIPOA VI	3529	+4	−15	−10	+15	0	0	0	0	3523	−6
MIPOA VII	3497	+36	−15	−10	0	0	−20	0	0	3488	−9
MIPOA VIII	3550	−17	−15	−10	+15	+15	0	0	0	3538	−12
NE$_{crystal}$	3529	+4	−15	0	+15	0	0	0	0	3518	−11
NE$_{stable}$	3542	−9	−15	0	+15	+15	0	0	0	3548	+6
PNE$_{crystal}$	3547	−14	−15	0	+15	0	0	+15	0	3548	+1
PNE$_{stable}$	3535	−2	−15	0	0	+15	0	0	0	3533	−2
E-AH$_{crystal}$	3531	+2	−15	−10	0	0	0	+15	+5	3528	−3
E-H$_{crystal}$	3498	+35	−15	−10	+15	0	−20	0	0	3503	+5
E$_{stable}$	3543	−10	−15	−10	+15	+15	0	0	0	3538	−5
PE$_{crystal}$	3538	−5	−15	−10	0	0	0	+15	0	3538	0
PE$_{stable}$	3497	+36	−15	−10	0	0	−20	0	0	3488	−9
Average	3526	+7								3525	−1

A nonterminal amine is on average red shifted by $15\,\mathrm{cm}^{-1}$ and a methylated amine by $10\,\mathrm{cm}^{-1}$. E.g., the nonterminal amine isopropylamine I is predicted by calculation at $3519\,\mathrm{cm}^{-1}$ and by the model at $3518\,\mathrm{cm}^{-1}$. Gauche(a)-methylethylamine calculated at $3522\,\mathrm{cm}^{-1}$ is the methylated analog to ethylamine and would be predicted at $3523\,\mathrm{cm}^{-1}$. The absence of a trans arrangement between the N-H and the β-acidic C-H group causes a blue shift of about $15\,\mathrm{cm}^{-1}$. E.g., gauche(b)-methylethylamine calculated at $3538\,\mathrm{cm}^{-1}$ is blue shifted by $16\,\mathrm{cm}^{-1}$ compared to gauche(a)-methylethylamine calculated at $3522\,\mathrm{cm}^{-1}$. Y-H$\cdots$X contacts within the monomer lead to a blue shift with one exception causing a red shift. The blue shift is about $15\,\mathrm{cm}^{-1}$ for the O-H$\cdots$N with an antiparallel arrangement of the N-H and O-H rotors. The blue shift is also $15\,\mathrm{cm}^{-1}$ for the N-H$\cdots$O contact and ca. $5\,\mathrm{cm}^{-1}$ for the C-H$\cdots$O contact. E.g., the O-H$\cdots$N contact in methylisopropanolamine IV calculated at $3540\,\mathrm{cm}^{-1}$ causes a blue shift of $17\,\mathrm{cm}^{-1}$ compared to methylisopropylamine II calculated at $3523\,\mathrm{cm}^{-1}$. The monomer unit from the crystal structure of pseudonorephedrine with an N-H$\cdots$O contact is predicted $16\,\mathrm{cm}^{-1}$ towards higher wavenumber (calculated at $3547\,\mathrm{cm}^{-1}$) compared to isopropylamine II calculated at $3531\,\mathrm{cm}^{-1}$. The C-H$\cdots$O contact of methylisopropanolamine II causes a blue shift of $5\,\mathrm{cm}^{-1}$ to $3528\,\mathrm{cm}^{-1}$ compared to methylisopropylamine II calculated at $3523\,\mathrm{cm}^{-1}$. Only in the case of O-H$\cdots$N hydrogen bonds with an approximately perpendicular arrangement of the NH and OH rotors, as defined by a small HNCC torsional angle, the N-H stretching wavenumbers are red shifted. Such an O-H$\cdots$(H)N hydrogen bond is e.g., present in methylisopropanolamine III at $3501\,\mathrm{cm}^{-1}$ but not in the case of methylisoproylamine II at $3523\,\mathrm{cm}^{-1}$ causing a red shift of $22\,\mathrm{cm}^{-1}$.

The differences of the predicted and calculated wavenumbers are between $-12\,\mathrm{cm}^{-1}$ and $+10\,\mathrm{cm}^{-1}$ with a mean value of $-1\,\mathrm{cm}^{-1}$ and a root mean square of $6\,\mathrm{cm}^{-1}$ for the full set of 25 compounds. This shows that the wavenumber differences of the N-H stretching mode can be formally described with the above mentioned parameters. However, it should be emphasized that these parameters only model a theoretical quantity and the description is not necessarily unique, but will be subject to revisions. Nevertheless, it provides a first instrument to predict N-H stretching wavenumbers based on the conformation and its interactions in comparison to other amines [132]. The residual deficiencies corresponding to a root mean square of $6\,\mathrm{cm}^{-1}$ are smaller than the expected model misinterpretations. Furthermore, it is reasonable to assume that the shift caused by the Y-H$\cdots$X contacts varies

within a certain range depending on the strength of the given contact.

N-H stretching intensities (summarized in Tab. 7.5) are low, but can be enhanced upon hydrogen bonding [147]. The intensity of the asymmetric stretching is generally higher than the intensity of the symmetric stretching. For the calculated isopropylamines this is not true. The intensity of the symmetric stretching remains higher on the MP2/6-311+G(d) level. Also, in the case of ethylamine and its clusters the asymmetric N-H stretching intensity is not higher than the intensity of the symmetric stretching. The predicted intensities of the investigated amines increase about 20–100 fold upon forming N-H$\cdots$O hydrogen bonds with dimethylether. The predicted intensities of the N-H stretching bands also increase when the amino group acts as the hydrogen bond acceptor (O-H$\cdots$N) in complexes with methanol but less so. The highest intensification (50–130 fold) is predicted for the methanol-ethylamine-dimethylether cluster in which a cooperative O-H$\cdots$N-H$\cdots$O hydrogen bond network is established. In jet expansions the N-H stretching bands were found to be rather weak. E.g., no N-H stretching band appears for aminoethanol monomers [182] and only the asymmetric stretching band was observed with significant band strength for the glycine ethyl ester monomer [183]. Upon aggregation a pronounced intensity increase was found e.g., for pyrrolidine clusters in jet expansions (up to three orders of magnitude) [74, 184] and dimethylamine in the gas phase [185]. Also, in the spectra of crystals an enhancement of the intensities is expected especially in the case of a cooperative hydrogen bond network.

Fig. 7.6 shows the influence of a hydrogen bond on the direction of the vibrational transition dipole vector of the N-H stretching modes for ethylamine and methylethylamine. The vectors of isopropylamine and methylisopropylamine (I and II) are shown for comparison. For the vibrational modes and vibrational transition dipole moments of the phenylpropanolamines see Supplement F. The single N-H stretching mode of the methylated amines tends to a have a vibrational transition dipole vector perpendicular to the N-H bond in direction of the lone pair. For the nonmethylated amines, the direction of both N-H stretching modes is dictated by local symmetry. The vibrational transitional dipole vector of the asymmetric stretch is perpendicular and the symmetric one parallel to a hypothetical average N-H bond. If the nonmethylated or methylated NH group engages as an N-H$\cdots$O hydrogen bond donor (aggregation with dimethylether) the vector aligns with the hydrogen bond. If the methylated amine group engages as an O-H$\cdots$N hydrogen bond acceptor (aggregation with methanol) the vibrational transition dipole vector aligns along

the hydrogen bond as well. In the case of the nonmethylated amines the local symmetry present for the monomer is conserved upon forming an O-H···N hydrogen bond (aggregation with methanol).

Overall, two N-H stretching bands can be expected for norephedrine and pseudonorephedrine, one for ephedrine hemihydrate, and one less intense N-H band for ephedrine anhydrate and pseudoephedrine. The single N-H stretching bands can be expected to appear in between the symmetric and asymmetric N-H stretching bands of the corresponding nonmethylated phenylpropanolamines. The N-H stretching modes will intensify after forming an N-H···O hydrogen bond within the crystal. The vibrational transition dipole vectors will align approximately along the hydrogen bonds.

Deuteration of the OH and NH group (ND/OD deuteration) will lead to strong red shifts. This helps identifying bands appearing in the same spectral region (e.g., C-H stretching bands). Predicted wavenumbers of the N-D stretching bands are summarized in Tab. 7.5. Wavenumbers are listed for relaxed monomers of the crystal structure, the most stable monomers, and chosen fragments (ethylamine and methylethylamine) without and with aggregation partner (dimethylether and methanol). The red shift upon deuteration is predicted to be between $930\,\mathrm{cm}^{-1}$ and $980\,\mathrm{cm}^{-1}$. The red shift is around $940\,\mathrm{cm}^{-1}$ for the asymmetric N-H/N-D stretching band, it is around $970\,\mathrm{cm}^{-1}$ for the symmetric stretching, and 940–$950\,\mathrm{cm}^{-1}$ for the methylated amines. Therefore, the splitting between the asymmetric and symmetric stretching is predicted to be larger for the N-D than for the N-H stretching mode. This rather untypical behavior is probably related to mode mixing of the N-D with a C-H stretching mode. The predicted intensities remain more or less the same upon deuteration which also results from the above mentioned mode mixing. Only for the N-D···O deuterium bonded complexes the intensity is lower than in the nondeuterated N-H···O bonded cases. A small loss of intensity can also be noticed for the O-D···N bonded clusters. Since the deuterated phenylpropanolamine crystals establish N-D···O or O-D···N deuterium bonds a decrease of intensity can be expected compared to the nondeuterated substances. In the partly deuterated ethylamine-dimethylether complexes the N-H and N-D stretching modes have a localized character. The modes of the hydrogen and deuterium bonded group appear in between the asymmetric and symmetric stretching modes with closer vicinity to the symmetric mode and are much more intense than the isolated N-H and N-D stretching mode.
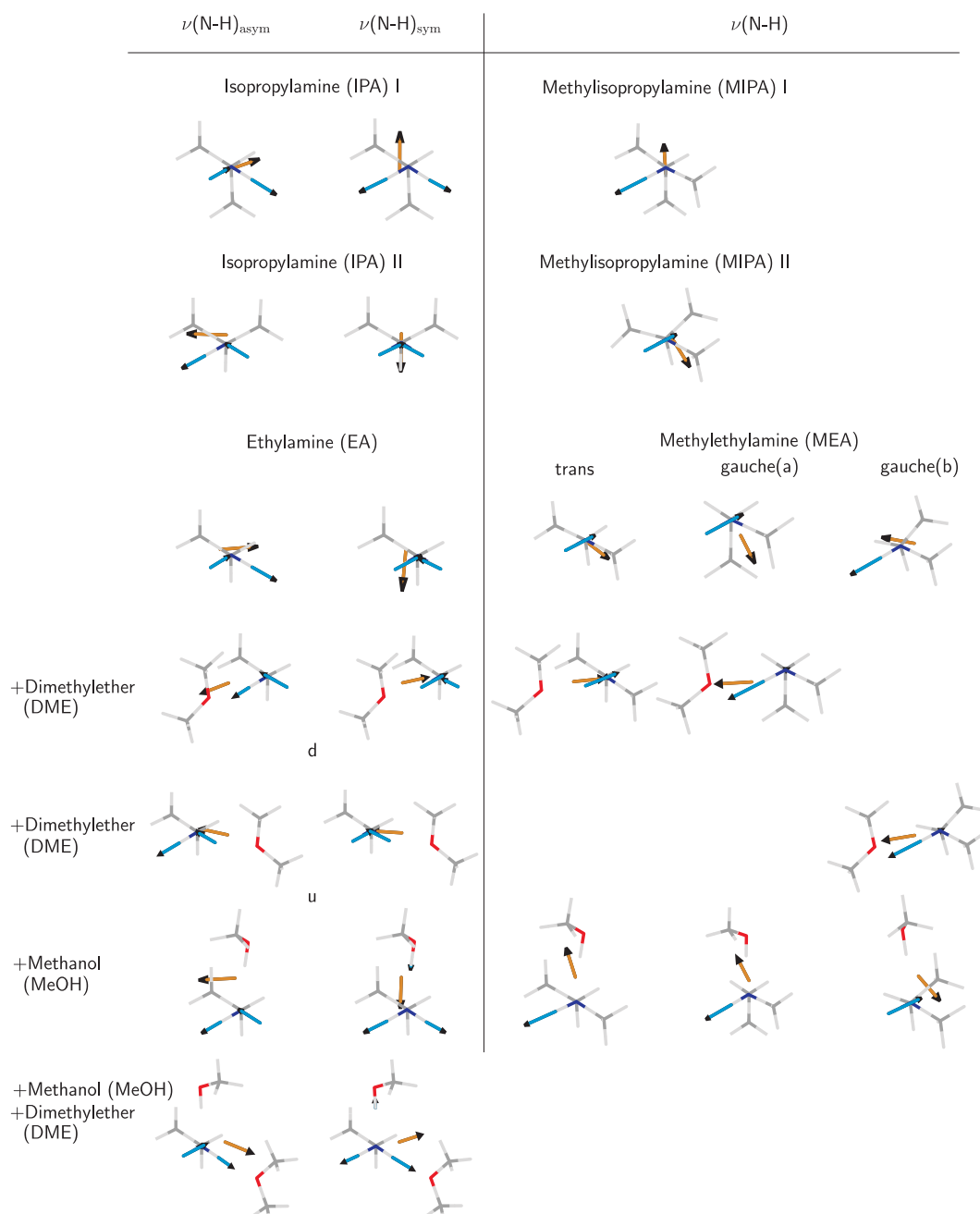
Figure 7.6.: Influence of the position of the methyl group and the influence of a hydrogen bond on the direction of the vibrational transition dipole vectors of the N-H stretching modes in ethylamine and methylethylamine. The direction of the vibrational transition dipole vectors (yellow, unit length) as well as the displacement vectors of each mode (blue) are indicated.

N-H Bending Mode

The N-H bending mode of primary amines is known to appear in the region of 1650–1590 cm^{-1} [147, 148]. The bending mode of the secondary amines is reported to appear in the region of 1650–1550 cm^{-1} by Ref. [148] and around 1500 cm^{-1} by Ref. [147]. Therefore, the bands fall into the region of the C-C$_{aromatic}$ stretching bands. They show a blue shift, intensification, and broadening upon aggregation [147, 148]. The N-H bending mode of primary amines is more intense than the one of secondary amines [148].

Tab. 7.7 summarizes the predicted wavenumbers of the N-H (and N-D) bending modes for the investigated phenylpropanolamines (monomers relaxed from the crystal structure and most stable monomers, see Sect. 7.2), its fragments isopropylamine, methylisopropylamine, ethylamine, and methylethylamine and the aggregated fragments of ethylamine and methylethylamine with dimethylether or methanol (Fig. 7.4). The N-H bending modes of the primary amines are to a great extent local modes, while the N-H bending modes of the secondary amines are mixed N-H/C-H$_3$ (or C-H$_3$/N-H) bending modes (see Supplement F and Fig. 7.7). The contribution of the N-H bend in the mixed N-H/C-H$_3$ bending modes varies for the different substances. Only the two highest frequency mixed modes are listed in Tab. 7.7. Upon ND/OD deuteration only one dominant N-D bending mode is present.

Table 7.7.: Predicted harmonic wavenumbers ω in cm^{-1} and IR intensities I in km·mol^{-1} of the N-H and N-D bending modes of relaxed monomers from the crystal structure (X$_{crystal}$), of the most stable monomers (X$_{stable}$, see Sect. 7.2) and of fragments of the investigated phenylpropanolamines (NE, PNE, E, and PE) on the B3LYP/6-311++G(3df,2p) level. The fragments are isopropylamine (IPA, I and II) and methylisopropylamine (MIPA, I and II) as well as (nondeuterated and deuterated) ethylamine (EA) and trans-, gauche(a)-, and gauche(b)-methylethylamine (MEA) with and without the aggregation partners dimethylether (DME) and methanol (MeOH) (see Fig. 7.4).

-NH$_2$	ω	I	-NHCH$_3$	ω	I	ω	I
NE$_{crystal}$	1661	21	E-AH$_{crystal}$	1523	16	1481	23
			E-H$_{crystal}$	1524	21	1489	17
NE$_{stable}$	1648	40	E$_{stable}$	1523	13	1479	12
PNE$_{crystal}$	1644	46	PE$_{crystal}$	1524	40	1488	16
PNE$_{stable}$	1649	26	PE$_{stable}$	1521	14	1482	15
IPA I	1654	29	MIPA I	1523	13	1477	13
IPA II	1653	34	MIPA II	1526	11	1479	8
EA	1654	29	trans-MEA	1518	14	1500	8
			gauche(a)-MEA	1524	12	1500	2
			gauche(b)-MEA	1520	9	1486	8
EA+DME(d)	1668	24	trans-MEA+DME	1531	16	1507	2
EA+DME(u)	1665	18	gauche(a)-MEA+DME	1534	11	1508	1
			gauche(b)-MEA+DME	1534	4	1508	2
EA+MeOH	1650	30	trans-MEA+MeOH	1528	6	1475	29
			gauche(a)-MEA+MeOH	1524	11	1478	12
			gauche(b)-MEA+MeOH	1521	13	1486	11
MeOH+EA+DME(u)	1665	19					
NE$_{crystal,deut}$	1244	20	E-AH$_{crystal,deut}$	1261	29		
NE$_{stable,deut}$	1232	27	E$_{stable,deut}$	1257	19		
PNE$_{crystal,deut}$	1231	60	PE$_{crystal,deut}$	1261	47		
PNE$_{stable,deut}$	1222	26	PE$_{stable,deut}$	1251	16		
EA$_{deut}$	1237	27	trans-MEA$_{deut}$	1265	20		
			gauche(a)-MEA$_{deut}$	1264	18		
			gauche(b)-MEA$_{deut}$	1265	20		
EA$_{deut}$+DME(d)	1244	19	trans-MEA$_{deut}$+DME	1267	17		
EA$_{deut}$+DME(u)	1246	21	gauche(a)-MEA$_{deut}$+DME	1270	14		
			gauche-MEA(b)$_{deut}$+DME	1271	18		
EA$_{deut}$+MeOD	1233	24	trans-MEA$_{deut}$+MeOD	1256	16		
			gauche(a)-MEA$_{deut}$+MeOD	1258	14		
			gauche(b)-MEA$_{deut}$+MeOD	1257	15		
EA-NDH$\cdots$DME(u)	1528	19					
EA-NDH$\cdots$DME(u)	1520	8					
EA-NHD$\cdots$DME(u)	1495	16					
EA-NHD$\cdots$DME(u)	1488	1					
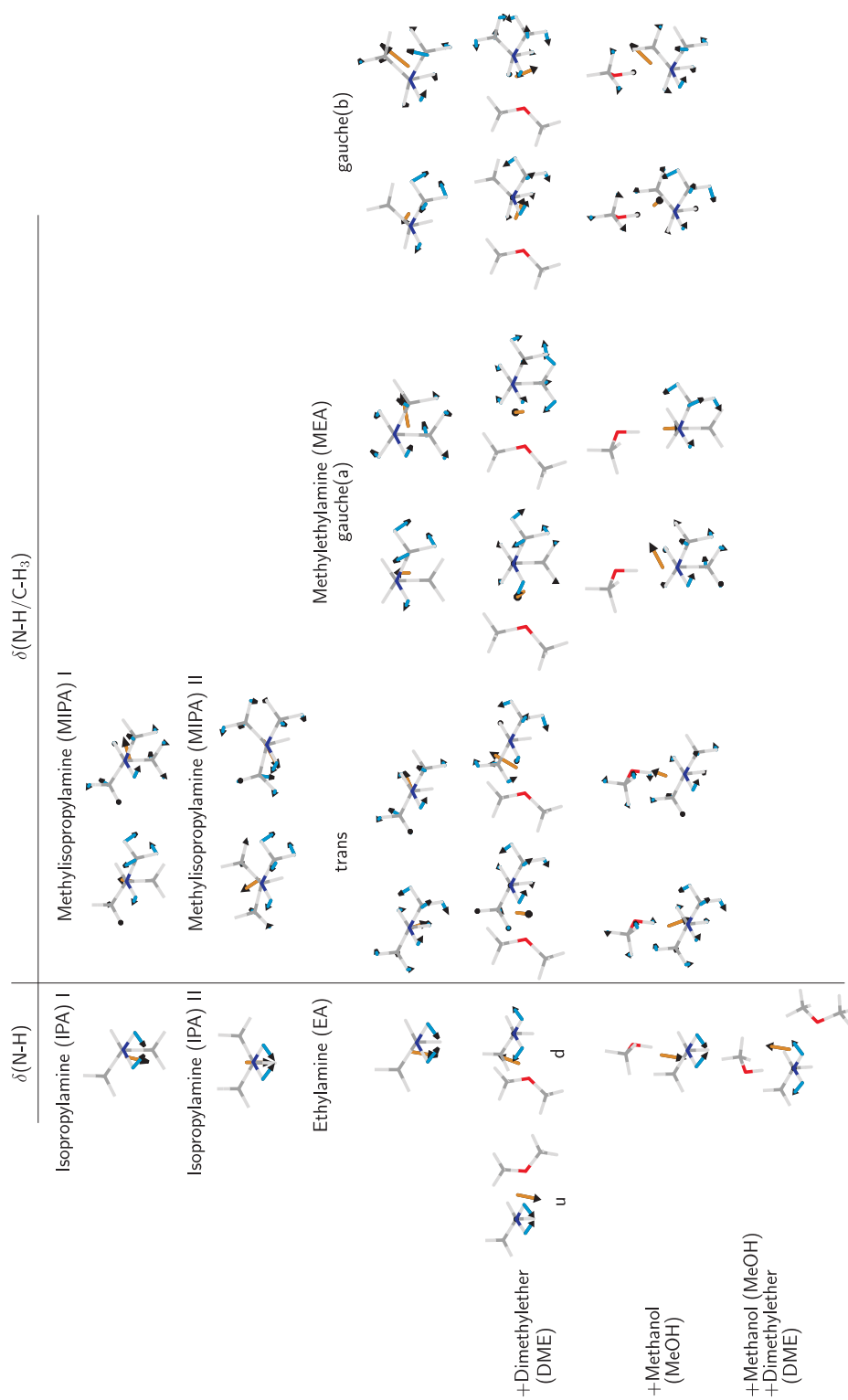
Figure 7.7.: Influence of the position of the methyl group and the influence of a hydrogen bond on the direction of the vibrational transition dipole vectors of the N-H bending modes in ethylamine and methylethylamine. The direction of the vibrational transition dipole vectors (yellow, unit length) as well as the displacement vectors of each mode (blue) are indicated.

The N-H bending modes of the primary amines are predicted at roughly $130\,\text{cm}^{-1}$ and $170\,\text{cm}^{-1}$ higher wavenumbers than the mixed N-H/C-H$_3$ bending modes of the secondary amines. In the deuterated case the N-H bend of the primary amines is predicted at about $30\,\text{cm}^{-1}$ lower wavenumber than the secondary amine bend. The shift upon deuteration is thus significantly larger for the primary amines ($420\,\text{cm}^{-1}$) than for the secondary amines ($240\,\text{cm}^{-1}$ for an averaged mixed N-H/C-H$_3$ bending mode). The aggregation with dimethylether (N-H$\cdots$O hydrogen bond) leads to an average blue shift of $10\,\text{cm}^{-1}$, whereas the aggregation with methanol (O-H$\cdots$N hydrogen bond) causes a red shift of about $10\,\text{cm}^{-1}$ on average. Only in the case of the nondeuterated methylethylamine-methanol complexes no red shift is predicted for the mixed N-H/C-H$_3$ mode at higher wavenumber. In the methanol-ethylamine-dimethylether complex ethylamine simultaneously acts as a hydrogen bond donor and acceptor. In this case, the N-H bending mode is blue shifted by $10\,\text{cm}^{-1}$. This points at a stronger influence of the N-H$\cdots$O than of the O-H$\cdots$N hydrogen bond on the spectral position of the N-H bending mode. However, in the case of ethylamine the aggregation with dimethylether (EA+DME(u)) causes a blue shift of $11\,\text{cm}^{-1}$, while the aggregation with methanol causes a red shift of $4\,\text{cm}^{-1}$. This shows that whether a red or blue shift is present for amines being hydrogen bond donor and acceptor depends on the specific case. For the partly deuterated ethylamine-dimethylether complexes two N-H(D) bending modes with a higher bending contribution of the N-H than the N-D bend (not depicted) are predicted. They fall between the positions of the nondeuterated and the deuterated amines with a tendency towards higher wavenumbers and show a mixing with C-H bends. Both modes of the hydrogen bonded complex (EA-NDH$\cdots$DME(u)) are predicted to appear at higher wavenumber than the modes of the deuterium bonded complex (EA-NHD$\cdots$DME(u)).

The N-H bending modes of the nondeuterated primary amines are predicted to be more intense than the mixed modes of the secondary amines. An exception is the predicted intensity of the monomer conformation realized in the pseudoephedrine crystal. Deuteration tends to have an intensity decreasing influence on the N-H bending mode of the primary amines. However, in most cases of the secondary amines the mixed mode is intensified. The intensities of the N-D modes of the primary and secondary amines are more or less comparable. Upon aggregation with dimethylether or methanol the intensities decrease in most cases. For a classification of the effects further evaluations are needed. In the case of the deuterated

amines aggregation leads to a decrease of the intensity for all substances. In the partly deuterated case the higher frequency mode is the more intense one for both complexes.

In Fig. 7.7 the directions of the vibrational transition dipole vectors of the N-H bending mode are shown for isolated and aggregated fragments of the phenyl-propanolamines (for the vectors of the investigated phenylpropanolamines see Supplement F). The vector bisects the two N-H bonds in the case of the primary amines. Deviations result from asymmetric substituents. The direction of the vibrational transition dipole moment of the primary amines remains more or less conserved upon aggregation. The directions of the mixed modes are quite different (also for the deuterated substances, not shown). They depend on the relative contributions of the NH and the CH groups, on the conformation, and on aggregation. For a systematic classification further evaluations would be needed.

Further Modes

O-H and N-H stretching band positions, intensities, and shapes depend much on the interactions present. However, C-H stretching bands are less influenced, especially the aromatic ones [138, 147, 186]. It can be expected that the aromatic C-H stretching bands will appear at the same position ($\pm 10\,\mathrm{cm}^{-1}$) as in the methyl mandelate and mandelic acid case (Tab. 7.4). Similar wavenumbers ($\pm 9\,\mathrm{cm}^{-1}$) are indeed predicted by quantum chemical calculations (see Supplement F). Red shifts of 15–50 cm^{-1} are calculated for the methyl C-H stretching modes of the phenyl-propanolamines compared to methyl mandelate. The methyl C-H stretching vibrations are predicted to couple with the α- and β-acidic C-H stretching and with the N-methyl C-H stretching modes in the case of ephedrine and pseudoephedrine.

Also, similar polarization behavior and thus directions of vibrational transition dipole vectors were found for several modes in the methyl mandelate and the mandelic acid case. The transition dipole vectors of the C-H$_{\mathrm{aromatic,sym}}$ and the C-C$_{\mathrm{aromatic}}$ stretching modes of the investigated phenylpropanolamines are visualized in Fig. 7.8 (see also Supplement F). The directions of the C-H$_{\mathrm{aromatic,sym}}$ (green) and the C-C$_{\mathrm{aromatic,2}}$ (brown) transition dipole vectors roughly point along the C-C$_{\mathrm{aromatic}}$ stem but deviate into the direction of the α-acidic CH group. In the case of norephedrine it is perpendicular to the C-C$_{\mathrm{aromatic}}$ stem. The vibrational transition dipole vector of the C-C$_{\mathrm{aromatic,1}}$ stretching mode (purple) is aligned along the
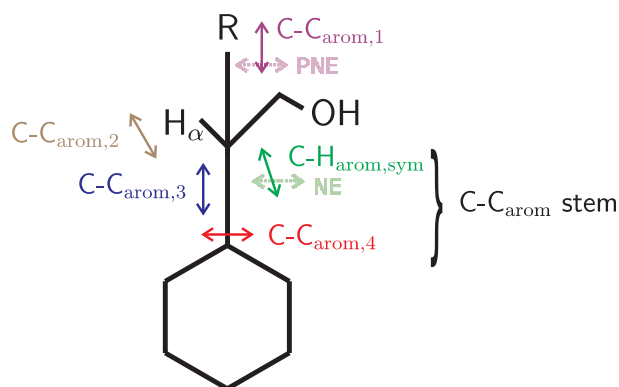
Figure 7.8.: Directions of the vibrational transition dipole vectors of several stretching modes of the investigated phenylpropanolamines. In the cases of norephedrine (NE) and pseudonorephedrine (PNE) the direction of the C-H$_{arom,sym}$ and the C-C$_{arom,1}$ stretching mode deviate as indicated, respectively.

backbone between the phenyl ring and the amine moiety (C$_{aromatic}$-C-C-N(-C)). In most cases, it is parallel to the C-C$_{aromatic}$ stem. The direction is perpendicular to the C-C$_{aromatic}$ stem in the case of pseudonorephedrine due to mixing with the N-H stretching mode. The directions of the C-C$_{aromatic,3}$ (blue) and C-C$_{aromatic,4}$ (red) transition dipole moments are parallel and perpendicular to the C-C$_{aromatic}$ stem. The directions are more or less in agreement with the observations in the methyl mandelate and mandelic acid cases.

FTIR-ATR Spectra

FTIR-ATR spectra of the investigated phenylpropanolamines are shown in Fig. 7.2. The enantiopure compounds were measured for all substances, in the case of pseudonorephedrine and pseudoephedrine also the racemic compounds were investigated. As predicted, two N-H stretching bands appear in the spectra of nor- and pseudonorephedrine and only one in the spectra of ephedrine hemihydrate and pseudoephedrine. They are located around $3330\,\text{cm}^{-1}$. Note, that the N-H stretching band of racemic pseudoephedrine is more intense than the one of the enantiopure compound. This might be an evidence for the presence of an N-H$\cdots$O bond within the racemic crystal.

   A broad O-H stretching band is present in the region of 3200–$2500\,\text{cm}^{-1}$. It overlaps with the C-H stretching modes. Four C-C$_{aromatic}$ stretching bands appear

around 1600–1450 cm^{-1} at similar positions as for methyl mandelate and mandelic acid. The bands overlap with an N-H bending band and several C-H bending modes.

In the case of ephedrine a broad band around 3500 cm^{-1} and a smaller one at 1650 cm^{-1} appear additionally. These bands can be assigned to the O-H stretching and bending modes. Ephedrine is known to be hygroscopic and can crystallize in the form of a hemihydrate [172]. The ephedrine bottle used for measurements has not been freshly opened before measurements. The ephedrine probably hydrated and the recorded FTIR-ATR spectra belong to ephedrine hemihydrate. No FTIR-ATR spectra were recorded for anhydrous ephedrine.

7.4. Norephedrine

7.4.1. Enantiopure Norephedrine

Enantiopure norephedrine (Fig. 7.9) is a white powder which melts at 51–53°C (according to the supplier, Tab. 7.1). There is no evidence that it is hygroscopic. No crystal structure is reported for enantiopure norephedrine.

Crystallization

It was not possible to sublimate crystals of enantiopure norephedrine at room temperature (22–23°C) in a time period of a few hours. The air conditioner was used to lower the room temperature and thus also the upper window of the cell to 18–20°C. The evacuation of the sublimation cell to less than 1 mbar already led to single crystals as well as a few polycrystals without the need of heating up the bottom of the cell. At temperatures above 28°C (bottom window) liquid drops of norephedrine condensed on the top window (Tab. 7.1).

The habit of the obtained norephedrine crystals was varying. Single crystals showed diverse profiles from triangular to hexagonal as well as tabular and platy habits. FTIR measurements exhibited three types of spectra (see Fig. 7.10) which might be due to different crystal faces or due to different polymorphs. Squarish tabular crystals (with variable profiles) revealed spectra denoted Face A (see Fig. 7.10). Platy crystals showed spectra named Face B, whereas Face C spectra

Frozen monomer unit   Relaxed monomer unit   Most stable
from the crystal structure   from the crystal structure   monomer
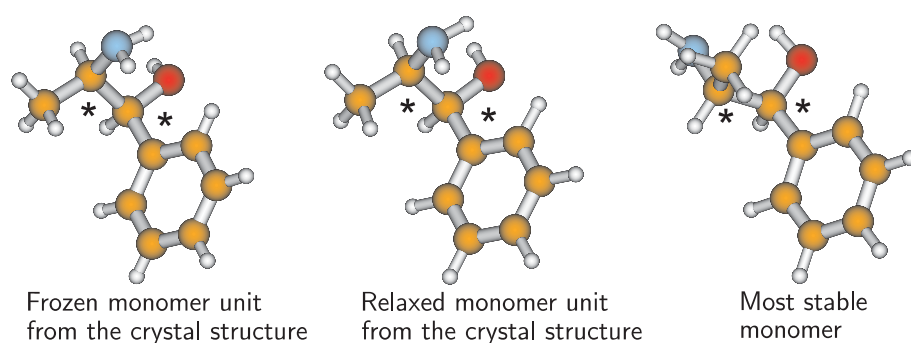
Figure 7.9.: Frozen and relaxed monomer units ((1*S*,2*R*)-enantiomer) taken from the crystal structure of racemic norephedrine [89] as well as the most stable monomer [83, 87] (B3LYP/6-311++G(3df,2p) level). Centers of chirality are marked with an asterisk (*).
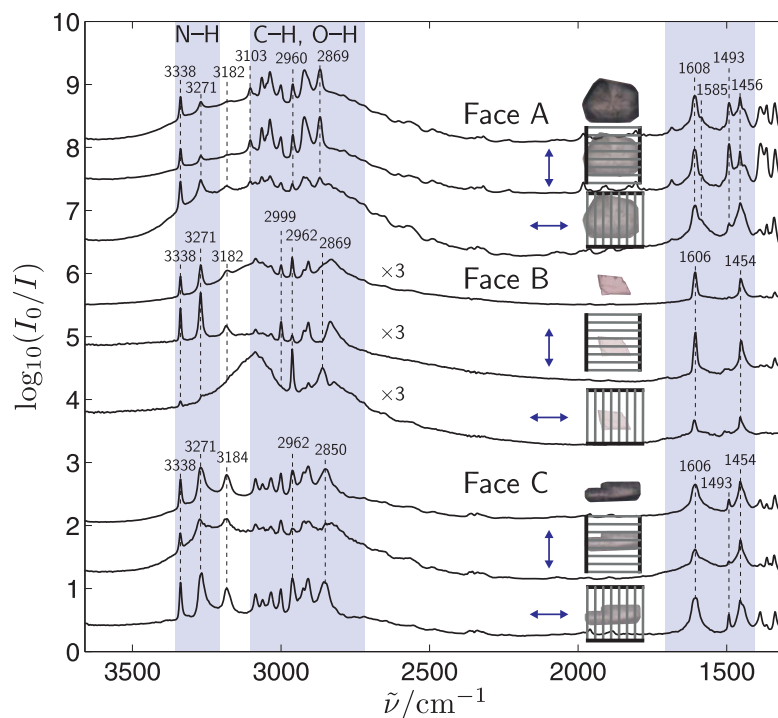
Figure 7.10.: Enantiopure norephedrine polarization FTIR spectra of face A, B, and C. The arrows show the direction of the electric field vector. Spectra of face B are multiplied by a factor of 3. The visual pictures of the measured crystals are shown above the corresponding spectra. Band positions are given in cm^{-1}.

were obtained after measuring elongated tabular crystals (see Fig. 7.10). The occurrence of the three spectral types was nearly equally distributed. It was not possible to perform rotation measurements in order to verify if the spectral differences are caused by different faces of the same polymorph. The density of sublimated crystals on the substrate was rather high, so the isolation of the designated crystals was not possible. Furthermore, the different morphologies would have made an assignment to specific faces difficult.

ND/OD-deuterated enantiopure norephedrine was obtained from a solution of (1S,2R)-norephedrine in D_2O. The solution was evacuated in the sublimation cell at a laboratory temperature of 15°C (with opened windows in winter time). Liquid drops were obtained at the bottom and the top of the cell. By lowering the room temperature to 10°C two types of polycrystals formed at the top of the cell. There
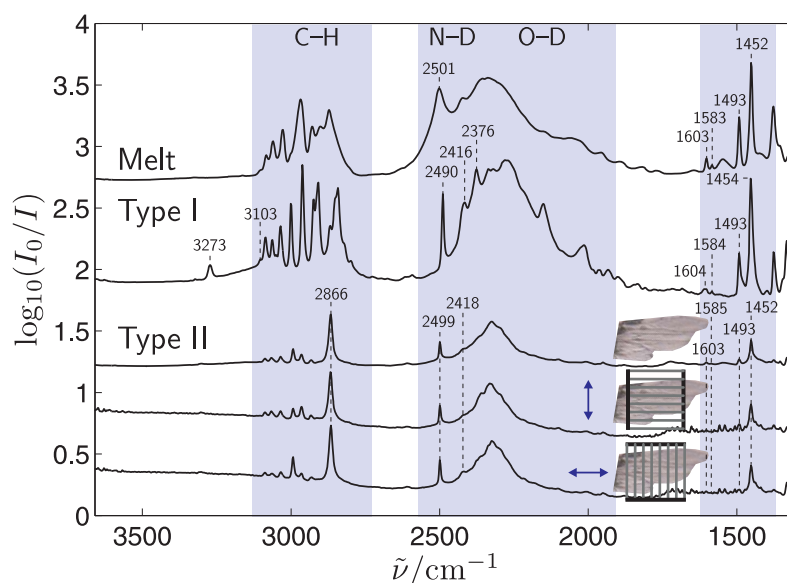
Figure 7.11.: ND/OD-deuterated enantiopure norephedrine FTIR spectra of the melt (top), of a polycrystal of type I (center), and polarized FTIR spectra of a polycrystal of type II (bottom) after sublimation. The arrows show the direction of the electric field vector. The measured section of the type II polycrystal is shown above the corresponding spectra. The type I crystal did not show much contrast and is therefore not shown. Band positions are given in cm^{-1}.

were polycrystals which contained oval single crystals of 5–10 μm (type I) as well as platy polycrystals with a defined growth direction (type II). In Fig. 7.11 FTIR spectra of a liquid drop and a polycrystal of type I as well as polarized FTIR spectra of a type II polycrystal are shown. The visual image depicted in Fig. 7.11 shows a section of the polycrystal measured. The type I spectrum shows similar C-H stretching patterns as the spectrum of the nondeuterated face C crystal. Therefore, analogous faces can be assumed. There is no nondeuterated spectrum which corresponds to the ND/OD-deuterated type II spectrum. Either the faces of the crystal correspond to different crystallographic axes or a polymorphic form is present.

FTIR Spectra

The vibrational assignments of enantiopure norephedrine are summarized in Tabs. 7.8 and 7.9. The assignments of the N-H and O-H stretching and the N-H bending modes are performed by comparison of experimental and predicted

wavenumbers (see also Sect. 7.3) as well as by comparing spectra of the nondeuterated and ND/OD deuterated substance in which the corresponding bands are shifted towards lower wavenumber. The positions and intensities of the N-H stretching modes will be discussed in Sect. 7.8. The N-H bending band is slightly blue shifted with regard to the scaled relaxed monomer prediction (see the comparison of experimental and oriented gas model spectra of racemic norephedrine in Fig. 7.18 later on) due to hydrogen bonding (Sect. 7.3).

The band at $3182/3184\,\mathrm{cm}^{-1}$ in the spectra of the nondeuterated compound (Fig. 7.10) vanishes upon deuteration (Fig. 7.11). Thus, it is also caused by the NH or OH group. It can be more specifically assigned to the N-H bending overtone with the fundamental being at $1608/1606\,\mathrm{cm}^{-1}$. The band appears about $35\,\mathrm{cm}^{-1}$ more red shifted than a harmonic overtone would be ($3216/3217\,\mathrm{cm}^{-1}$). The red shift results from a negative diagonal anharmonicity constant ($x_{1,1}$) [79] and a Fermi-resonance between the N-H bending overtone and the symmetric N-H stretching mode [187, 188].

In the spectrum of ND/OD deuterated enantiopure norephedrine three bands appear in the N-D stretching region of type I (Fig. 7.11) and only two bands in the spectra of the melt and the type II crystal. The bands at $2490\,\mathrm{cm}^{-1}$ and $2376\,\mathrm{cm}^{-1}$ in the spectrum of type I can be assigned to the asymmetric and symmetric N-D stretching modes in agreement with the assignments made for the other primary phenylpropanolamines in this Chapter. They show a larger splitting than the corresponding nondeuterated N-H stretching bands, consistent with the predictions (see Sect. 7.3). The band at $2416\,\mathrm{cm}^{-1}$ corresponds to the localized and bonded N-D stretching mode of partly deuterated norephedrine resulting from an isotopic exchange. The band at $3273\,\mathrm{cm}^{-1}$ is the analogous localized N-H stretching mode. Both bands appear in closer vicinity to the symmetric than to the asymmetric stretching mode. In the spectra of type II and the liquid an N-D stretching band at $2499/2501\,\mathrm{cm}^{-1}$ appears broadened and slightly blue shifted compared to the asymmetric N-D mode in the type I spectrum due to a weakening of the deuteration bonds. The symmetric stretch disappears in the broad O-H stretching band.

A comparison of molten phase spectra measured in the sublimation cell of ND/OD-deuterated and nondeuterated enantiopure norephedrine as well as ATR spectra of the solid state of enantiopure norephedrine is shown in Fig. 7.12. The N-H and N-D stretching bands are broadened in the liquid phase due to the lack of a periodic hydrogen bond network. Also, the positions of the N-H stretching bands

Table 7.8.: Assignments of experimental band maxima in the FTIR microscopic spectra of enantiopure norephedrine of face A, face B, face C (Fig. 7.10), FTIR-ATR spectra (without ATR correction, Fig. 7.2), FTIR spectra of the melt (not shown) as well as calculations of the relaxed monomer unit taken from the crystal structure ($Mon_{crystal}$) on the B3LYP/6-311++G(3df,2p) level. All wavenumbers are given in cm^{-1}. The stretching and bending vibrations are indicated as ν and δ and the symmetric and asymmetric vibrations with sym and asym. Tentative assignments and bands without assignment are labeled with a question mark (?).

Assignment	Face A	Face B	Face C	ATR	Melt	$Mon_{crystal}$
$\nu(N-H_{asym})$	3338	3338	3338	3339	3355	3567
$\nu(N-H_{sym})$	3271	3271	3271	3269	3290	3489
$\nu(O-H)$	3500-2500	3400–2600	3400–2500	3500–2400	3600–2500	3831
$2\delta(N-H)$	3182	3182	3184	3181	3169	
$\nu(C-H_{aromatic,sym})$	3103				3107	3199
$\nu(C-H_{aromatic,2})$	3087	3085	3085	3086	3085	3185
$\nu(C-H_{aromatic,3})$	3064	3062	3062	3065	3062	3172
$\nu(C-H_{aromatic,4})$	3048		3049			3162
$\nu(C-H_{aromatic,5})$	3037	3033	3033	3036	3030	3154
? $\nu(C-H_{3,asym1})$	3001	2999	3001	3001		3104
? $\nu(C-H_{3,asym2})$	2960	2962	2962		2970	3089
? $\nu(C-H_{3,sym})$	2922	2922	2923		2929	3028
?	2914	2908	2908	2909	2897	
? $\nu(C-H_{\alpha})$	2869	2869	2868		2873	2978
? $\nu(C-H_{\beta})$			2850			2962
$\delta(N-H)$	1608	1606	1606	1605	1585	1661
$\nu(C-C_{aromatic,1})$	1608	1606	1606	1605	1601	1644
$\nu(C-C_{aromatic,2})$	1585				1585	1622
$\nu(C-C_{aromatic,3})$	1493	1493	1493	1493	1493	1531
$\nu(C-C_{aromatic,4})$	1456	1454	1454	1452	1452	1485

Table 7.9.: Assignments of experimental band maxima in the FTIR microscopic spectra of enantiopure ND/OD-deuterated norephedrine polycrystals of type I, type II, and the melt (Fig. 7.11). All wavenumbers are given in cm^{-1}. The stretching and bending vibrations are indicated as ν and δ and the symmetric and asymmetric vibrations with sym and asym. Tentative assignments and bands without assignment are labeled with a question mark (?).

Assignment	Type I	Type II	Melt
$\nu(N-H_{localized})$	3273		
$\nu(C-H_{aromatic,sym})$	3103		
$\nu(C-H_{aromatic,2})$	3085	3087	3084
$\nu(C-H_{aromatic,3})$	3062	3066	3060
$\nu(C-H_{aromatic,4})$	3051		
$\nu(C-H_{aromatic,5})$	3035	3035	3028
? $\nu(C-H_{3,asym1})$	3001	2993	
? $\nu(C-H_{3,asym2})$	2962	2964	2968
? $\nu(C-H_{3,sym})$	2923	2932	2929
?		2908	2900
? $\nu(C-H_{\alpha})$	2868	2866	2871
? $\nu(C-H_{\beta})$	2842		
?		2798	
$\nu(N-D_{asym})$	2490	2499	2501
$\nu(N-D_{localized,bonded})$	2416	2418	2422
$\nu(N-D_{sym})$	2376		
$\nu(O-D)$	2600–1900	2450–2200	2600–1900
$\nu(C-C_{aromatic,1})$	1604	1603	1603
$\nu(C-C_{aromatic,2})$	1585	1587	1583
$\nu(C-C_{aromatic,3})$	1493	1493	1493
$\nu(C-C_{aromatic,4})$	1454	1452	1452
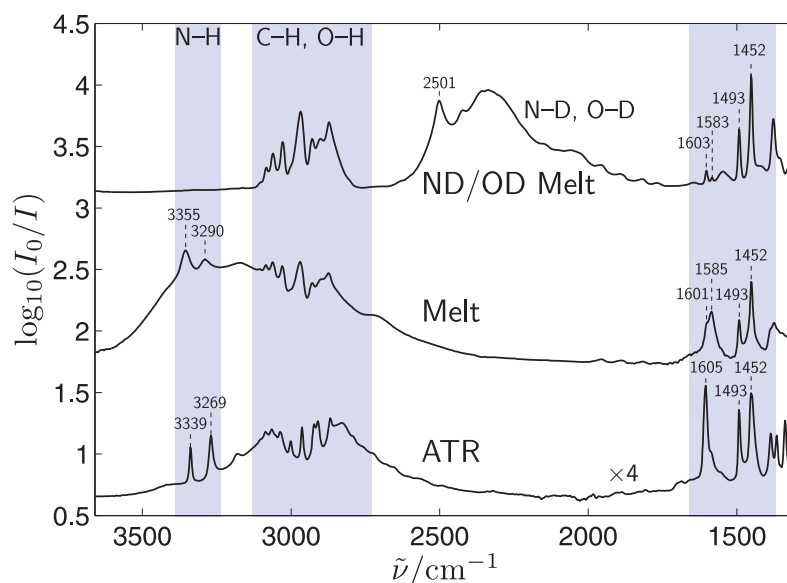
Figure 7.12.: Liquid transmission spectra of the ND/OD-deuterated and the non-deuterated melt as well as an FTIR-ATR spectrum of the nondeuterated solid sample of enantiopure norephedrine. The ATR spectrum is multiplied by a factor of 4. Band positions are given in cm^{-1}.

are less red shifted in the spectrum of the melt. In analogy, the N-H bending mode is less blue shifted. The presence of the N-H bending band in the region around $1600 \, cm^{-1}$ can nicely be recognized by a comparison with the ND/OD-deuterated norephedrine spectrum in which this mode does not appear. The positions of the C-H stretching bands are nearly the same in the ND/OD- and the nondeuterated norephedrine spectra.

The aromatic C-H and C-C$_{aromatic}$ stretching bands are assigned according to observations made in the cases of methyl mandelate, mandelic acid, and the other phenylpropanolamines in this Chapter. The tentative assignment of the aliphatic C-H stretching modes is performed on the basis of the assignments made for the other phenylpropanolamines in this Chapter.

So far, no crystal structure of enantiopure norephedrine has been published. Thus, only the spectral differences of the three faces can be used to infer the molecular orientation within the crystal. The orientation along the different faces will be discussed separately. The conclusions about the molecular orientation refer to the average over the unit cell. Single molecules within the unit cell may deviate from the proposed orientation. Note, that it is only a simplistic scheme which does not reflect

the dimensionality correctly and which does not include all functional groups.

The O-H stretching band appears for both polarizations of face A, but the intensities are approximately two times higher for a horizontal polarization. Nearly horizontally aligned O-H$\cdots$X hydrogen bonds can be assumed. The case of the NH$_2$ group is more complicated. The intensities of the asymmetric N-H stretching and the N-H bending band are nearly equal for both polarizations. For the asymmetric N-H stretching and the N-H bending mode a diagonal transition dipole vector can be assumed, while the one of the symmetric modes seems to be horizontally aligned. In Sect. 7.3 the influence of a hydrogen bond on the vibrational transition dipole vector of the NH$_2$ group was analyzed. It was shown, that in the case of an N-H$\cdots$X hydrogen bond both the asymmetric and symmetric N-H transition dipole vectors align more or less along the N-H hydrogen bond. Since the polarization behavior of the asymmetric and symmetric N-H stretching bands differ, this is only partially the case. The directions of the transition dipole vectors of the three N-H modes suggest a sidewards slightly downpointing orientation of the amine group (see Fig. 7.13). The C-C$_{aromatic,3}$ stretching band at 1493 cm^{-1} is much stronger at a vertical polarization, while the C-C$_{aromatic,4}$ stretching band at 1456 cm^{-1} shows the opposite behavior. Therefore, a vertical transition dipole vector and a vertical orientation of the C-C stem can be assumed. The symmetric C-H stretching band of the phenyl group is visible for both directions of polarization. The band seems to be more pronounced in the vertically polarized spectrum. But this is probably affected by the overlaying O-H stretching band. It can be assumed that the vibrational transition dipole vector is diagonal to the probed directions. This and the relatively strong intensity of the symmetric C-H stretching band fits to a view on the plane of the aromatic group with the C-C stem being vertically aligned (in agreement with the considerations made above).

In the spectra of face B the polarization behavior of the four N-H stretching and bending bands and the O-H stretching band differs. The N-H bands are strong for the vertical polarization, while the O-H stretching band appears in the horizontally polarized spectra. This is in agreement with a horizontal O-H and a vertical N-H hydrogen bond. The C-C$_{aromatic,3}$ stretching band does not appear in the spectra of face B. The same is true for the symmetric phenyl C-H stretching mode. A view along the C-C stem can therefore be assumed. However, the C-C$_{aromatic,4}$ stretching band at 1454 cm^{-1} is present for both polarizations, but shows a stronger intensity at a vertical polarization. This points at a rather vertical orientation of the phenyl
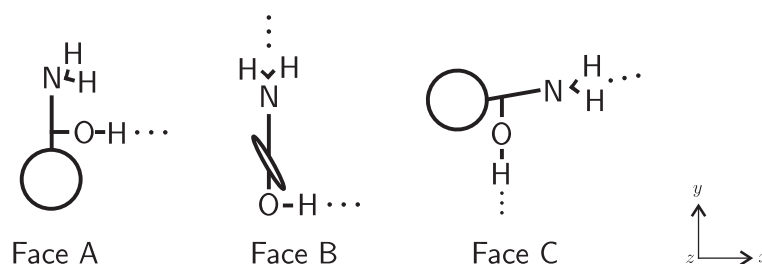
Figure 7.13.: Schematic layout of a norephedrine molecule oriented according to the measured crystal faces. Note, that this simplistic view does not reflect the dimensionality correctly and that it does not include all functional groups.

group. The proposed orientation corresponding to face B is depicted in Fig. 7.13. It shows substantial analogies to the orientation of a face A racemic crystal (see Sect. 7.4.2) rotated by $90°$ around the z-axis. This is in agreement with very similar polarization spectra and similar morphologies. It can be assumed that the crystal structures are alike.

Assuming that the tentative assignments of the C-H stretching modes in Tab. 7.8 are correct, one can also derive the orientations of the aliphatic C-H groups of face B (here the C-H stretching region does not suffer from oversaturation). The asymmetric1 methyl stretching at $2999\,\mathrm{cm}^{-1}$ is more intense for a vertical polarization, while the asymmetric2 methyl stretching at $2962\,\mathrm{cm}^{-1}$ is intense in the horizontally polarized spectrum. The symmetric stretching is stronger in the vertical polarization. Therefore, the methyl group is oriented such that one CH points upwards and the other two are diagonally aligned. The C-CH$_3$ stem points more or less into the z direction. The α-acidic C-H stretching mode is present in the horizontally polarized spectrum and the β-acidic C-H stretching in the vertically polarized one. Thus, the α-acidic CH is horizontally and the β-acidic CH vertically oriented. The proposed orientation is shown in Fig. 7.14. Note that the OH group may be rotated since the spectral information of the O-H stretching band refers to the direction of the hydrogen bond. For the NH$_2$ group this is only partially the case. The vibrational transition dipole vector of the N-H stretching mode also aligns along the hydrogen bond. However, the vector of the N-H bending mode is mainly unaffected (see Sect. 7.3).

In face C spectra the O-H stretching band is less pronounced, but shows a strong polarization dependence. It appears at a vertical polarization. Therefore, vertically

Figure 7.14.: Proposed average conformation and orientation of a norephedrine
molecule according to face B of enantiopure norephedrine.

oriented O-H hydrogen bonds with inclination towards the direction of measurement can be assumed. The asymmetric and symmetric N-H stretching bands as well as the N-H bending fundamental and overtone are present for both directions of polarization, but are more intense in the horizontally polarized spectrum. This points at rather horizontally aligned N-H hydrogen bonds. The C-C$_{aromatic,3}$ is more pronounced in the spectra of face C, while the intensity of the C-C$_{aromatic,4}$ stretching band is more or less equal for both polarizations. This leads to the inconsistent conclusion of a horizontally oriented C-C stem and a diagonally oriented phenyl ring. The truth is probably somewhere in between as depicted in Fig. 7.13.

The proposed orientations of face A and C correspond to a nearly 90° rotation around the z axis. The two orientations might correspond to similar faces of crystals which grew slightly screwed to each other. But, the fact that the two N-H stretching bands behave differently upon polarization points rather at the formation of different polymorphs. The orientations of face B and C can be obtained by a 90° rotation around the y axis. Therefore, face B and C might belong to different faces of analogous crystals. However, the morphologies are different.

The N-H stretching and bending positions which are the same for all three faces deviate only little from the positions observed for racemic norephedrine (see Fig. 7.2). A similar hydrogen bonded network and a similar conformation of the monomer units can therefore be assumed. The mismatch of the proposed orientations and the irregular habit of the sublimated crystals points at a disordered crystal structure or at the formation of polymorphs.

7.4.2. Racemic Norephedrine

Racemic norephedrine (Fig. 7.9) melts at 102°C under ambient pressure (according to the supplier, see Tab. 7.1). There is no evidence that it is hygroscopic.

Crystal Structure

Racemic norephedrine crystallizes in the monoclinic space group $P2_1/c$ by slow evaporation of a solution of chloroform (CSD REF Code: NOREPH01) [89, 172]. It contains four molecules in the unit cell (Z=4) and one molecule in the asymmetric unit (Z'=1). Norephedrine molecules of the same chirality are connected via O-H$\cdots$N hydrogen bonds (1.9 Å, green dots and circles) more or less along the crystallographic *b* axis (see Fig. 7.15 and Fig. 7.19 later on). Every molecule is connected to one opposite enantiomer by two reciprocal weak N-H$\cdots$O hydrogen bonds of 2.3 Å length along the a/c bisector (purple dots and circles). By these two interactions infinite zigzag strands of $\cdot[\cdot\cdot$O-H$\cdots$N-H$\cdot]\cdot\cdot$ hydrogen bonds along the *c* axis are formed (yellow highlight). Every molecule is part of two neighboring counterpropagating zigzag strands. In such a strand the O-H$\cdots$N hydrogen bonded molecules have the same chirality, while the N-H$\cdots$O bonds connect opposite enantiomers. The hydrogen bonded layers are connected by π-interactions between the phenyl groups.

Crystallization

In order to sublimate racemic norephedrine a freshly prepared 1:1 mixture of (1*S*,2*R*)- and (1*R*,2*S*)-norephedrine was used. In a first attempt, crystals already sublimated without tempering the bottom of the cell at a pressure below 1 mbar with the use of the air conditioner (18–20°C) as in the case of enantiopure norephedrine (see Sect. 7.4.1). FTIR spectra (not shown) are equivalent to those of the enantiopure substance. This can either be explained by the formation of enantiopure crystals or by differences between the enantiopure and racemic substance which are too small for the applied resolution.

Another 1:1 mixture of (1*S*,2*R*)- and (1*R*,2*S*)-norephedrine which was prepared in a separate flask and reevacuated every week over a period of two months behaved differently. In this case the sublimation temperature was 40°C. Crystals obtained by this procedure grew into polycrystals as well as into single platy crystals with
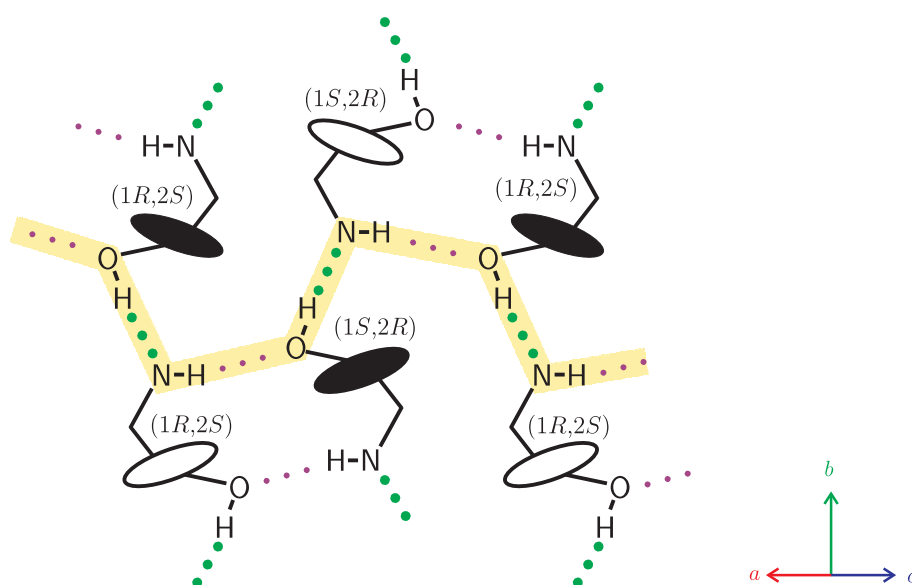
Figure 7.15.: Schematic view of the hydrogen bond network in racemic norephedrine. The O-H···N hydrogen bonds are marked with green dots and the weaker N-H···O hydrogen bonds with smaller purple dots. An infinite cooperative zigzag strand is highlighted in yellow. The phenyl rings pointing up are filled in black, whereas phenyl rings pointing down are represented by open circles. The second NH is not depicted, because it is not involved in hydrogen bonds. It also has a nonvanishing projection onto the depicted plane. The configuration of the norephedrine molecules is given.

varying profiles (as was the case for the enantiopure compound, see Sect. 7.4.1). Both crystal types led to the same spectra shown in Fig. 7.16. Differences to the spectra of the enantiopure crystals in Figs. 7.10 and 7.11 appear for a variety of bands. The formation of a hydrate can be excluded since no additional strong O-H stretching band is present. It can be assumed that racemic crystals were present. The formation of an enantiopure polymorph is also possible but less likely. The spectral differences between the enantiopure and the racemic compound will be discussed in Sect. 7.4.3. It was not possible to measure spectra of the other faces. This was due to the frequently polycrystalline nature and due to the variable profile of the single crystals, making an assignment to specific faces difficult.

ND/OD-deuterated racemic norephedrine crystals were obtained using the pretreated 1:1 mixture of (1S,2R)- and (1R,2S)-norephedrine. A spatula tip of the pestled 1:1 mixture was dissolved in 10 drops of D_2O in the open sublimation cell and heated to 30°C. After cooling the solution down to room temperature the cell was closed and evacuated. A solid substance with undefined habit crystallized from the solution. Crystalline strings with a defined direction of growth were used for FTIR polarization measurements (see Fig. 7.17). A visual picture of the measured section of the crystal is shown above the spectra.

Sublimation of the ND/OD-deuterated racemic norephedrine at 45°C led to platy crystals with variable profiles (triangular–hexagonal) as well. Polarization spectra are equivalent to the ones measured using the crystals obtained directly from the solution (see Fig. 7.17). It can be noticed that a partial exchange of deuterium by hydrogen from ND to NH and from OD to OH took place during the sublimation process. The N-H and O-H stretching bands as well as the band at $2422 \, \text{cm}^{-1}$ and the region around $1450 \, \text{cm}^{-1}$ increase, while the N-D and O-D stretching bands decrease compared to the spectra recorded using crystals from the solution.

A comparison of nondeuterated and ND/OD-deuterated polarization spectra (Figs. 7.16 and 7.17) of racemic norephedrine exhibits similarities in the C-H stretching region and in the behavior of the N-H and N-D as well as the O-H and O-D stretching bands. Thus, it is likely that analogous faces had been measured. All spectra are therefore denoted Face A.
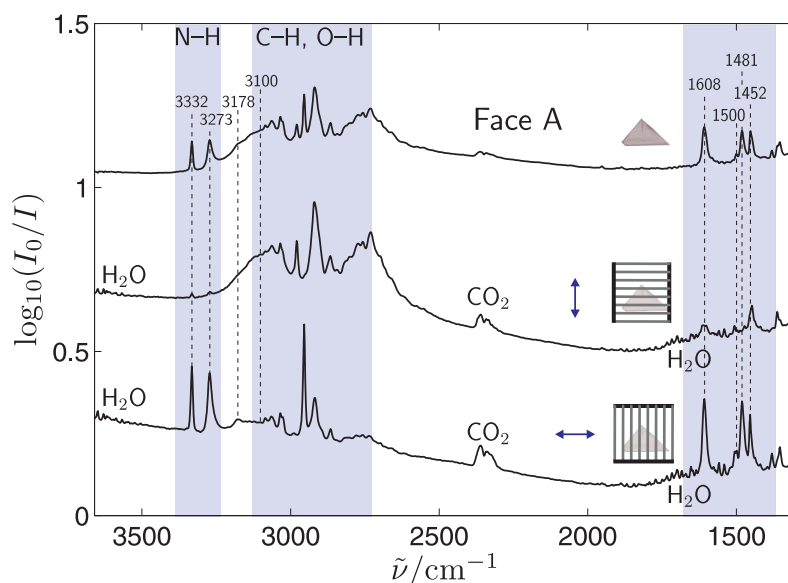
Figure 7.16.: Racemic norephedrine polarization FTIR spectra of face A. The arrows show the direction of the electric field vector. The visual pictures of the measured crystal are shown above the corresponding spectra. Band positions are given in cm^{-1}.

FTIR Spectra

The assignments of the experimental bands of racemic norephedrine are summarized in Tab. 7.10. The N-H and O-H modes are assigned according to the quantum chemical predictions and the preliminary spectral considerations in Sect. 7.3. The experimental bands are also assigned by the comparison of nondeuterated and ND/OD-deuterated pseudonorephedrine spectra as well as by comparison with the spectral positions of the other investigated phenylpropanolamines.

A comparison of the spectra of the ND/OD-deuterated crystals obtained from a solution and by sublimation (Fig. 7.17) reveals an N-H/D bending mode of partly deuterated norephedrine at $1452\,cm^{-1}$. The band intensifies after the ND/OD-deuterated substance is exposed to humidity during the sublimation process analogous to the localized N-H and N-D stretching bands. The experimental position is also in agreement with the predicted wavenumbers of an N-DH$\cdots$O and an N-HD$\cdots$O bonded amine group (see Sect. 7.3). The N-D bending mode of fully ND/OD-deuterated norephedrine appears at $1211\,cm^{-1}$ (not shown).

The aromatic C-H and the C-C$_{aromatic}$ wavenumbers are in agreement with
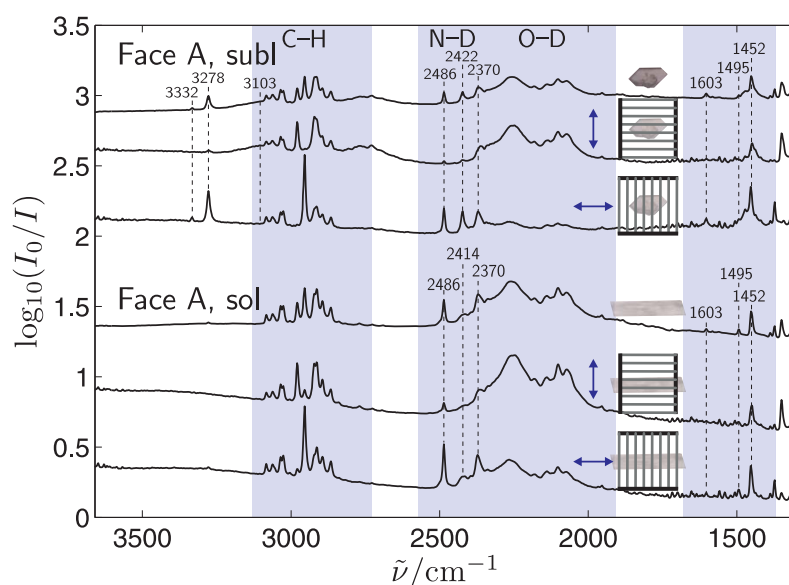
Figure 7.17.: ND/OD-deuterated racemic norephedrine polarization FTIR spectra of face A. Crystals were obtained from a solution of D_2O (bottom, sol) and by sublimation (top, subl). The arrows show the direction of the electric field vector. The visual pictures of the measured crystals are shown above the corresponding spectra. The crystal obtained from the solution extended beyond the measured section which is displayed. Band positions are given in cm^{-1}.

Table 7.10.: Assignments of experimental band maxima in the FTIR microscopic spectra of nondeuterated (Fig. 7.16) and ND/OD-deuterated racemic norephedrine of face A (Fig. 7.17), FTIR-ATR spectra (without ATR correction, Fig. 7.2) as well as calculations of the relaxed monomer unit taken from the crystal structure ($Mon_{crystal}$) on the B3LYP/6-311++G(3df,2p) level. All wavenumbers are given in cm^{-1}. The stretching and bending vibrations are indicated as ν and δ and the symmetric and asymmetric vibrations with sym and asym. Tentative assignments and bands without assignment are labeled with a question mark (?).

Assignment	Face A	Face A (ND/OD)	ATR	$Mon_{crystal}$
ν(N-H$_{asym}$)	3332	3332	3331	3567
ν(N-H$_{localized}$)		3278		
ν(N-H$_{sym}$)	3273		3270	3489
ν(O-H)	3300–2500	3200–2600	3300–2500	3831
2δ(N-H)	3178		3179	
?	3116			
ν(C-H$_{aromatic,sym}$)	3100	3103	3101	3199
ν(C-H$_{aromatic,2}$)	3085	3084	3083	3185
ν(C-H$_{aromatic,3}$)	3064	3062	3065	3172
ν(C-H$_{aromatic,4}$)				3162
ν(C-H$_{aromatic,5}$)	3035	3035	3034	3154
?	3028	3026		
? ν(C-H$_{3,asym1}$)	3004	3004		3104
? ν(C-H$_{3,asym2}$)	2979	2979	2980	3089
?	2954	2954	2953	
? ν(C-H$_{3,sym}$)	2920	2922	2918	3028
?				
?		2914		
?		2895		
? ν(C-H$_{\alpha}$)	2866	2866	2866	2978
? ν(C-H$_{\beta}$)	2844	2840	2845	2962
?	2800		2799	
?	2773	2770	2772	
?	2758		2756	
?	2731	2727	2728	
?	2698	2692	2696	
ν(N-D$_{asym}$)		2486		
ν(N-D$_{localized,bonded}$)		2422 (sol: 2413)		
ν(N-D$_{sym}$)		2370		
ν(O-D)		2500–1900		
δ(N-H)	1608		1607	1661
ν(C-C$_{aromatic,1}$)	1603	1603	1607	1644
ν(C-C$_{aromatic,2}$)	1583	1582	1584	1622
ν(C-C$_{aromatic,3}$)	1500	1495	1499	1531
δ(O-H/C-H$_{\alpha}$/C-H$_{\beta}$)	1481		1481	1439
ν(C-C$_{aromatic,4}$)	1452	1452	1452	1485
δ(N-H/D)		1452	1452	

the spectral positions of methyl mandelate, mandelic acid, and the other phenyl-propanolamines in this Chapter. A tentative assignment of the aliphatic C-H stretching modes is performed after the determination of the molecular orientation in agreement with the assignments of the other phenylpropanolamines in this Chapter.

Fig 7.16 shows a strong dependence of the N-H and O-H stretching bands on the direction of polarization. The O-H and both N-H stretching band intensities are complementary and thus the transition dipole moments of these modes are approximately perpendicular to each other within face A (see Supplement F) and more or less aligned with the polarizer grid position. A similar but less pronounced contrast is found for the N-D and the O-D stretching bands (see Fig. 7.17). Quantum chemical calculations of the isolated relaxed crystal monomer ((1R,2S)-norephedrine) predict nearly parallel transition dipole vectors of the asymmetric N-H stretching mode and the O-H stretching vibration, while the one of the symmetric N-H stretching mode is perpendicular (see Supplement F). The transition dipole vectors of the N-H stretching modes cannot be predicted well using monomer calculations. The vectors of both N-H stretching modes tend to align along the N-H$\cdots$O hydrogen bond as shown for ethylamine in Sect. 7.3. The remaining polarization contrast between the N-H and O-H stretching bands can partly be explained by a rotation of the O-H group during structure optimization (see Fig. 7.9). The angle between the OH group and the bisector of the NH$_2$ group decreases by 18° (from 122° to 104°). Furthermore, the O-H$\cdots$N and N-H$\cdots$O hydrogen bonds are nearly orthogonal to each other in the crystal structure (Figs. 7.15 and 7.19) [89]. It can therefore be assumed that also the vibrational transition dipole vectors are nearly orthogonal to each other which would match the above mentioned experimental observations. The same is true for the N-D (2486 cm^{-1} and 2370 cm^{-1}) and O-D stretching bands. The bands at 3278 cm^{-1} and at 2422 cm^{-1} can be assigned to localized deuterium bonded modes of partly deuterated norephedrine as in the case of enantiopure norephedrine (see Sect. 7.4.1). They show the same polarization behavior as the asymmetric and symmetric modes.

A strong dependence on the direction of polarization is also found for the bands at 1608 cm^{-1}, 1500 cm^{-1}, and 1481 cm^{-1}. All of these bands are intense for a horizontal polarization in analogy to the N-H stretching bands. The band at 1608 cm^{-1} is due to an overlap of the C-C$_{aromatic,1}$ stretching and the N-H bending mode. The N-H bending band vanishes almost completely after deuteration revealing a less

intense band at $1603\,\mathrm{cm}^{-1}$. This band is only caused by the C-C$_{\mathrm{aromatic,1}}$ stretching since the N-D bending is shifted towards lower wavenumbers upon deuteration. The C-C$_{\mathrm{aromatic,1}}$ stretching band seems to intensify for a horizontal polarization. But since the sublimated crystals are not fully deuterated (the N-H bending mode might lead to an increase of intensity in the region of $1603\,\mathrm{cm}^{-1}$) and because there are contributions of atmospheric water vapor, the intensity differences are not reliable. The bands at $1500\,\mathrm{cm}^{-1}$ and $1481\,\mathrm{cm}^{-1}$ might be due to a combination of the C-C$_{\mathrm{aromatic,3}}$ stretching and a mixed bending mode of the O-H, the α- and β-acidic C-H groups (denoted OH in the right part of Fig 7.18). The mixed O-H, α- and β-acidic C-H mode is predicted at $92\,\mathrm{cm}^{-1}$ lower wavenumbers than the C-C$_{\mathrm{aromatic,3}}$ mode, but it might appear at higher wavenumbers due to a blue shift caused by the hydrogen bonds within the crystal. After deuteration both bands vanish exhibiting the former presence of an O-H or N-H mode. A band appearing at $1495\,\mathrm{cm}^{-1}$ can clearly be assigned to the C-C$_{\mathrm{aromatic,3}}$ stretching mode. The two absorptions at $1500\,\mathrm{cm}^{-1}$ and $1481\,\mathrm{cm}^{-1}$ are only observed for racemic norephedrine and not for enantiopure norephedrine or the other phenylpropanolamines investigated in the present work. A coupling of the C-C$_{\mathrm{aromatic,3}}$ stretching and the mixed O-H/C-H$_{\alpha}$/C-H$_{\beta}$ bending mode probably causes a splitting towards higher and lower wavenumbers.

The band at $1452\,\mathrm{cm}^{-1}$ is rather independent of the direction of polarization for both the nondeuterated and the ND/OD-deuterated racemic norephedrine. Only a slight increase in intensity can be observed for a horizontal polarization. This band is probably caused by a combination of the C-H$_3$ bending and the C-C$_{\mathrm{aromatic,4}}$ stretching modes.

An assignment of the molecular orientation of racemic norephedrine within the crystal is difficult since it was not possible to measure more than one face and because of the effect of hydrogen bonding on the relative direction of vibrational transition dipole vectors of the N-H and O-H and the N-D and O-D stretching bands (see above). The measured face of racemic norephedrine (face A) most likely corresponds to a view between the crystallographic a and c axes (a/c). In this a/c view the hydrogen bonded network of O-H$\cdots$N and N-H$\cdots$O connected strands is most pronounced. It can be assumed that these two rather strong interactions determine the direction of the crystallization growth. A comparison of experimental (nondeuterated and deuterated) polarization FTIR-spectra of face A and oriented gas model polarization spectra of the a/c view is shown in Fig. 7.18. There is a good

agreement between the intensity ratios of the O-H stretching band as well as the N-H bending and the mixed O-H/C-H$_\alpha$/C-H$_\beta$ bending mode. This supports the assignment of face A to the a/c view. A mismatch with regard to the intensity ratios of the N-H stretching band can be noticed. As discussed above, this discrepancy results from the influence of the N-H$\cdots$O hydrogen bond within the crystal which itself is nearly orthogonal to the O-H$\cdots$N hydrogen bond. A mismatch of the experimental and simulated N-H stretching band is therefore expected. The C-C$_{\mathrm{aromatic,3}}$ mode does not appear in the spectra, while the intensity of the C-C$_{\mathrm{aromatic,4}}$ band is equal for both polarizations. It can be inferred that the C-C stem points into the direction of the radiation with the phenyl ring being intermediate a horizontal and vertical position which is the case in the a/c view. Overall, there is some evidence that face A corresponds to the a/c view. In order to verify this assumption measurements of the two other faces would be needed.

The C-H stretching region is more complicated. The aromatic C-H stretching modes appear at similar wavenumbers as in the spectra of methyl mandelate and mandelic acid (see Tabs. 7.4 and 7.10) but the aliphatic C-H stretches are more red shifted as predicted by the monomer calculations (see Supplement F). An assignment by comparing the predicted and experimental sequence is not possible due to the presence of additional bands, probably caused by overtones of the C-H bending modes. Nonetheless, the polarization behavior provides some hints for a tentative assignment. The methyl group is horizontally aligned in the proposed orientation (see Fig. 7.19). Therefore, the symmetric stretching band should be more intense in the horizontally polarized spectra such as the band at 2954 cm^{-1}. However, the band at 2954 cm^{-1} does not appear in the spectra of enantiopure norephedrine. The symmetric methyl stretching mode is therefore tentatively assigned to the band at 2920 cm^{-1}. Note, that the experimental and predicted polarization behavior do not match. The C-H$_{3,\mathrm{asym2}}$ mode has a vertically aligned transition dipole vector and matches the behavior of the band at 2979 cm^{-1}. The other asymmetric methyl mode points into the direction of measurement with a contribution in the vertical direction. Its polarization behavior fits the band at 3028 cm^{-1}. Nonetheless, this mode is assigned to the band at 3004 cm^{-1} since it matches the assignments in the spectra of the other phenylpropanolamines. Also, the scaled position is in better agreement with the band at 3004 cm^{-1}. The vibrational transition dipole vectors of the acidic C-H modes are predicted to align more or less along the C-H bond (see Supplement F). Therefore, the α-acidic C-H stretching mode should appear for both
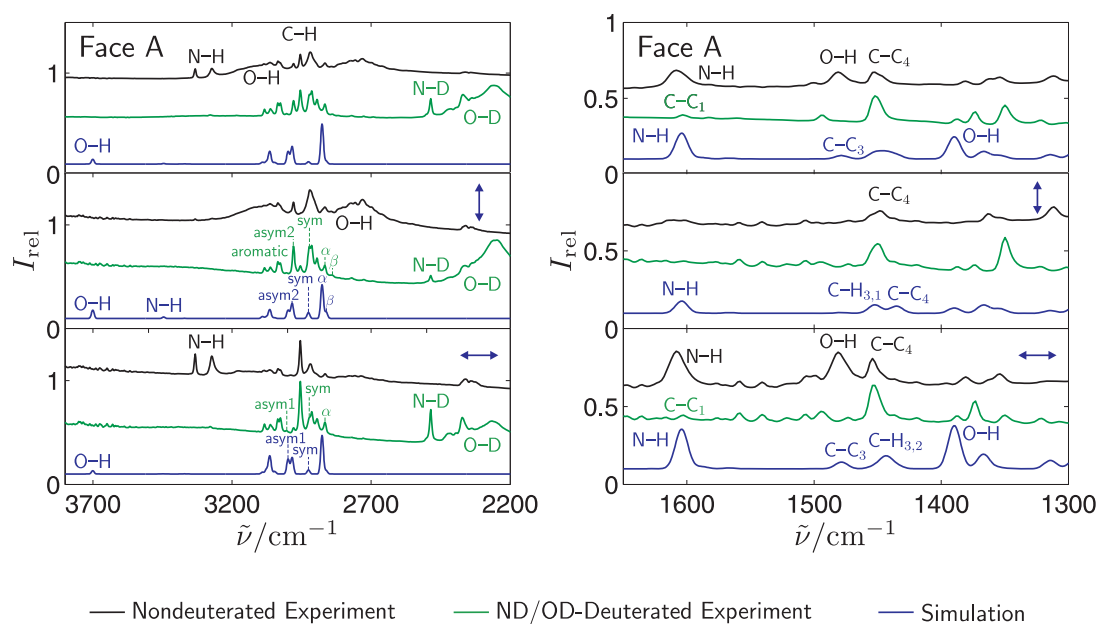
Figure 7.18.: Comparison of experimental and oriented gas model polarization spectra without deuteration (B3LYP/6-311++G(3df,2p) level) of face A of racemic norephedrine. The nondeuterated spectra (top, black), the ND/OD-deuterated spectra (center, green), and oriented gas model spectra (bottom, blue) are shown. Harmonic wavenumbers are scaled by a factor of 0.966 to account for anharmonicity. Assigned bands in the left part are stretching modes. The aromatic, asymmetric (asym1 and asym2), symmetric, and acidic C-H stretching modes (α and β) are indicated. The N-H bending, several C-C$_{aromatic}$ stretching (abbreviated C-C$_x$), and the mixed O-H/C-H$_\alpha$/C-H$_\beta$ bending modes (abbreviated O-H) are shown in the right part.
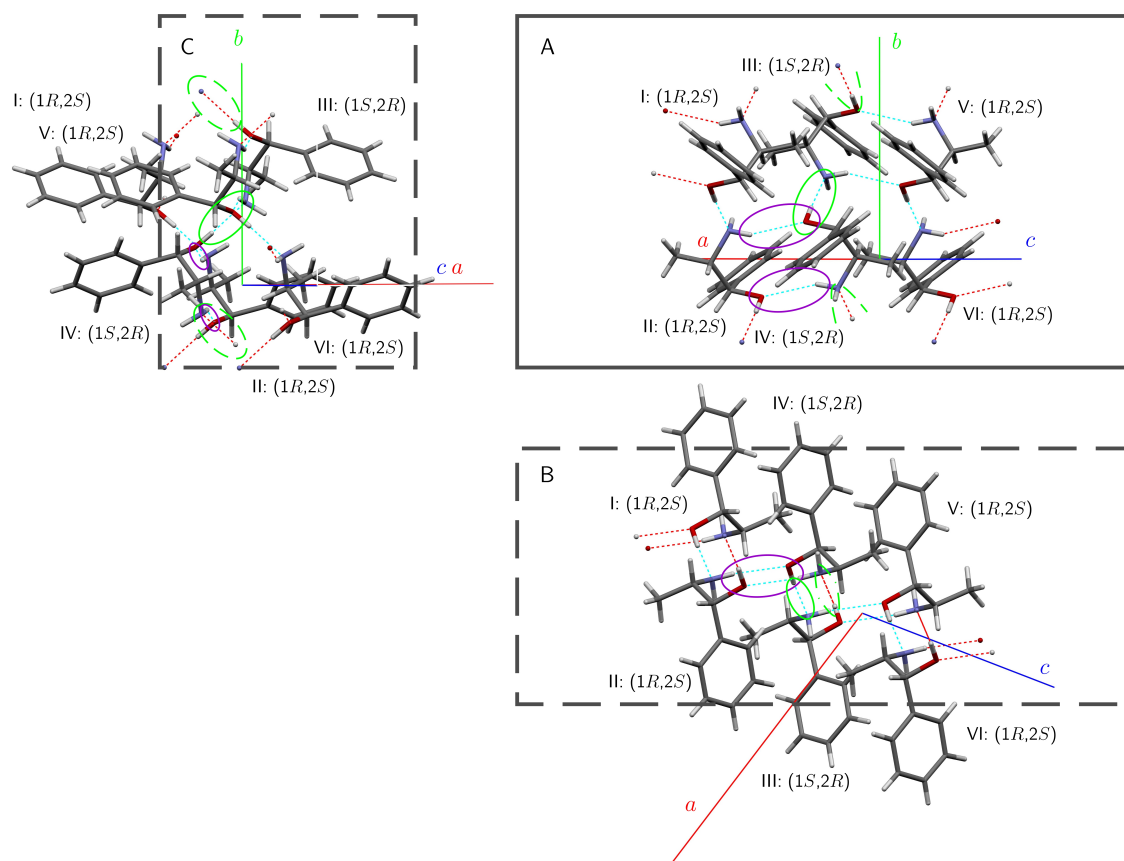
Figure 7.19.: Molecular orientation of racemic norephedrine along the three crystal faces. The crystal structure was taken from Ref. [89]. The configurations of the individual molecules are labeled. The shape of the frames does not imply a crystal habit. Green circles mark selected O-H···N and purple circles N-H···O hydrogen bonds.

polarizations. It is assigned to the band at $2866\,\text{cm}^{-1}$. The β-acidic mode has a vertically aligned transition dipole, but shows predominantly into the direction of measurement. It is assigned to the band at $2844\,\text{cm}^{-1}$. The unassigned bands in Tab. 7.10 probably belong to overtone or combination modes of the C-H group.

7.4.3. Comparison of Enantiopure and Racemic Norephedrine

There are spectral differences for enantiopure and racemic norephedrine microcrystals and powder (see Figs. 7.20 and 7.2) as a result of different crystal structures, itself a manifestation of chirality recognition. Toda et al. investigated the racemic crystal formation of a powdered (1*S*,2*R*)- and (1*R*,2*S*)-norephedrine mixture via IR spectroscopy in Nujoll mull and by X-ray structure analysis [165]. They found a shift of $5 \, \text{cm}^{-1}$ from $3335 \, \text{cm}^{-1}$ (enantiopure norephedrine) to $3330 \, \text{cm}^{-1}$ (racemic compound) and no shift for the band at $3270 \, \text{cm}^{-1}$. They incorrectly assigned these bands to the O-H and not to the N-H stretching vibration. Within this project the asymmetric N-H stretching band shifted from $3338 \, \text{cm}^{-1}$ to $3332 \, \text{cm}^{-1}$ (see Fig. 7.20 as well as Tabs. 7.8 and 7.10) in the FTIR spectra of the microcrystals. Thus, a comparable red shift of $6 \, \text{cm}^{-1}$ was found. The symmetric N-H stretching band slightly blue shifts from $3271 \, \text{cm}^{-1}$ in the enantiopure case to $3273 \, \text{cm}^{-1}$ in the spectra of racemic norephedrine. In Ref. [165] no shift is reported. The symmetric N-H stretching mode is slightly more intense in the ATR spectra of the racemic compound (Fig. 7.2).

Further spectral differences between enantiopure and racemic norephedrine can be noticed in the O-H, C-H, and C-C stretching as well as O-H, N-H, and C-H$_3$ bending region (see Figs. 7.2 and 7.20). These differences will not be discussed in detail. However, it should be emphasized, that in the case of the racemic compound the O-H stretching band has more intense contributions at lower wavenumber which points at stronger O-H hydrogen bonds. Also, the higher intensity of the N-H bending band of the enantiopure compound as well as the appearance of the mixed O-H bending band at $1481 \, \text{cm}^{-1}$ in the spectra of the racemic compound are noteworthy.

An indication of the chirality recognition is also the difference in temperature used for the sublimation. In order to crystallize the enantiopure compound a temperature range of 18–20°C was used. On the other hand, the racemic compound crystallized at 40°C which is significantly higher. Also, the melting temperature of racemic norephedrine (~ 100°C) is significantly higher than the melting temperature of enantiopure norephedrine (~ 50°C). It can be assumed that the racemic crystals are more stable than the enantiopure compound. This assumption could be verified by measuring the relative vapor pressures via mass spectrometry as performed in the case of methyl mandelate (Chapter 5).

A study of lattice energies using Dreiding II force field of seven homochiral and
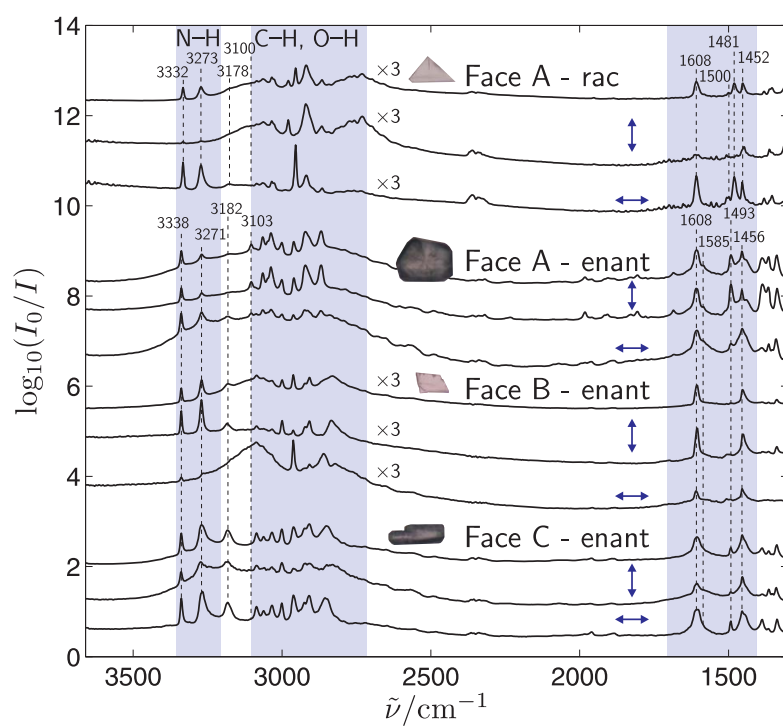
Figure 7.20.: Comparison of racemic (rac) and enantiopure (enant) norephedrine polarization FTIR spectra. The arrows show the direction of the electric field vector.

racemic neuroactive substances (e.g., ephedrine derivatives) suggests van der Waals interactions to be the major force for chiral discrimination [189]. Electrostatic and hydrogen bonding energies are assumed to have a minor influence although they are difficult to estimate.

7.5. Pseudonorephedrine

Enantiopure pseudonorephedrine (Fig. 7.21) is a white powder which melts at 76°C (according to the supplier, Tab. 7.1). There is no evidence that it is hygroscopic.

Crystal Structure

(1*S*,2*S*)-Pseudonorephedrine was crystallized as block-like crystals by vapor diffusion from ethyl acetate and hexanes (CSD REF Code: GEVNEB) [90]. The determined space group is $P2_1$ (see also Ref. [172]). Pseudonorephedrine contains two molecules in the unit cell (*Z*=2) and one molecule in the asymmetric unit (*Z*'=1). Infinite strands of ·[··O-H···N-H·]·· hydrogen bonded zigzag chains (O-H···N: 2.0 Å, N-H···O: 2.5 Å) are formed along the crystallographic *a* axis (see Fig. 7.26 later on). Every molecule is part of two hydrogen bonded strands which are aligned parallel along the *b* axis. In a third dimension van der Waals interactions of the phenyl and the methyl groups take place.

Crystallization

Pseudonorephedrine sublimates at substrate temperatures around 35°C within minutes. The habit of the crystals is tabular. The rotation spectra in Fig. 7.22 of two microcrystals show that there are clear differences concerning the C-H and C-C$_{\text{aromatic}}$ stretching bands of face A and of face B and C. These differences can be used to

Frozen monomer unit from the crystal structure

Relaxed monomer unit from the crystal structure

Most stable monomer
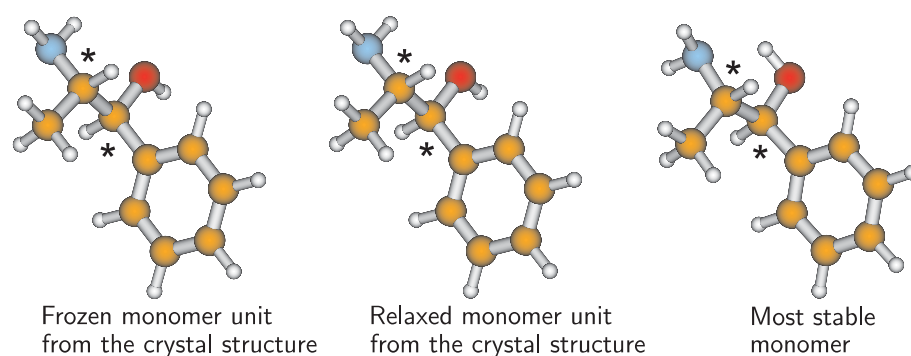
Figure 7.21.: Frozen and relaxed monomer units taken from the crystal structure of pseudonorephedrine [90] as well as the most stable monomer (assumed, B3LYP/6-311++G(3df,2p) level). Centers of chirality are marked with an asterisk (*).
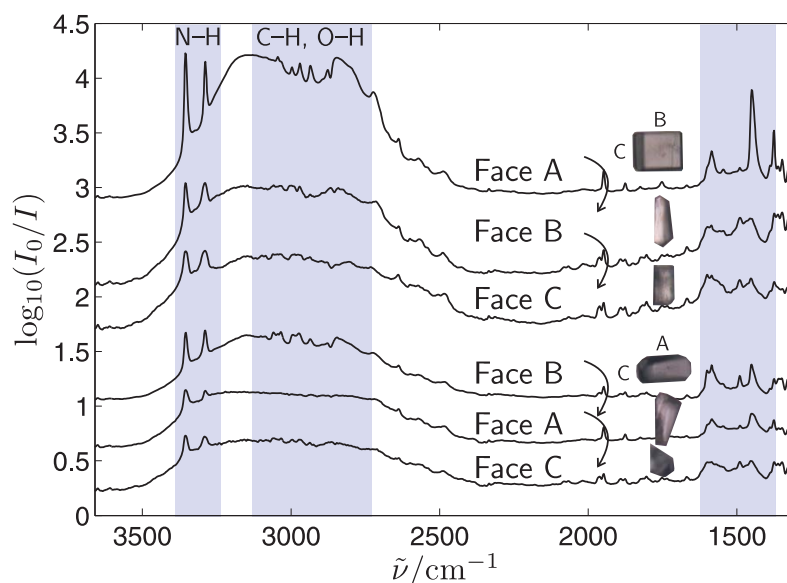
Figure 7.22.: Enantiopure pseudonorephedrine FTIR spectra obtained after rotation of crystals showing type A and type B spectra. Rotating the crystal interconverts the spectral types A and B and exhibits a spectrum of type C. The visual pictures of the measured crystals are shown above the corresponding spectra. The saturation of the spectra is substantial.

assign spectra to face A. On the other hand, the spectra of face B and C are quite similar. Subtle differences in the intensity of the O-H stretching and the contour of the region below $2000\,\mathrm{cm}^{-1}$ can be used to tentatively distinguish spectra of face B and C. The distribution of crystals growing on face A, B, and C was found to be largely equal. In Fig 7.23 FTIR polarization spectra of face A and B are shown.

In order to obtain ND/OD-deuterated pseudonorephedrine the pestled compound (tip of spatula) was dissolved in 8 drops of D_2O in the unclosed sublimation cell. The cell was heated up to $35°C$ to accelerate the solvation process. After cooling back to room temperature the cell was closed and evacuated. ND/OD-deuterated pseudonorephedrine started to crystallize due to the evaporation of D_2O to a crystal size of 0.05–1 mm within minutes. Crystals obtained by this procedure had a platy habit. Polarized FTIR spectra of the crystals are shown in Fig. 7.24. In the case of the crystals obtained from solution no correlation between the face (habit) and the type of spectra was possible. The denominations Face A and Face B were made after comparison with spectral types of sublimated crystals.

Sublimated ND/OD-deuterated pseudonorephedrine crystals were grown by us-
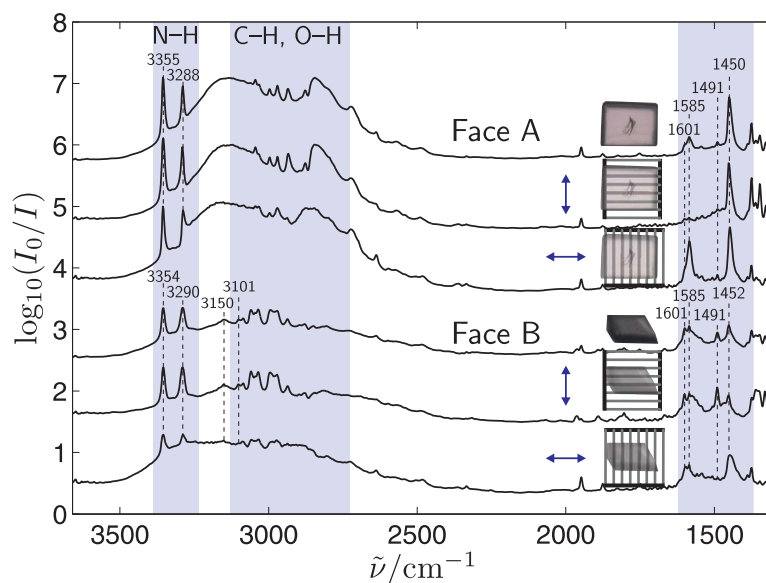
Figure 7.23.: Enantiopure pseudonorephedrine polarization FTIR spectra of face A and B. The arrows show the direction of the electric field vector. The visual pictures of the two measured crystals are shown above the corresponding spectra. Band positions are given in cm^{-1}.

ing the crystals obtained after evaporation of D_2O. Spectra of sublimated ND/OD-deuterated pseudonorephedrine crystals are shown in Fig. 7.25. The assignment of spectral types to faces was performed by comparing the habit of the ND/OD-deuterated and nondeuterated crystals. Spectra shown in Figs. 7.24 and 7.25 were recorded in the closed sublimation cell (not on the removed CaF_2 substrate).

FTIR Spectra

The assignments of the experimental bands are summarized in Tab. 7.11 for non-deuterated and in Tab. 7.12 for ND/OD-deuterated pseudonorephedrine. The N-H and O-H stretching and the (mixed) bending modes are assigned according to the quantum chemical predictions and the preliminary spectral considerations in Sect. 7.3. The experimental bands are also assigned by comparison of non-deuterated and ND/OD-deuterated pseudonorephedrine spectra. In analogy to norephedrine, also the N-H bending overtone is assigned.

The aromatic C-H and the $C-C_{aromatic}$ wavenumbers are in agreement with the spectral positions of methyl mandelate, mandelic acid, and the other phenyl-
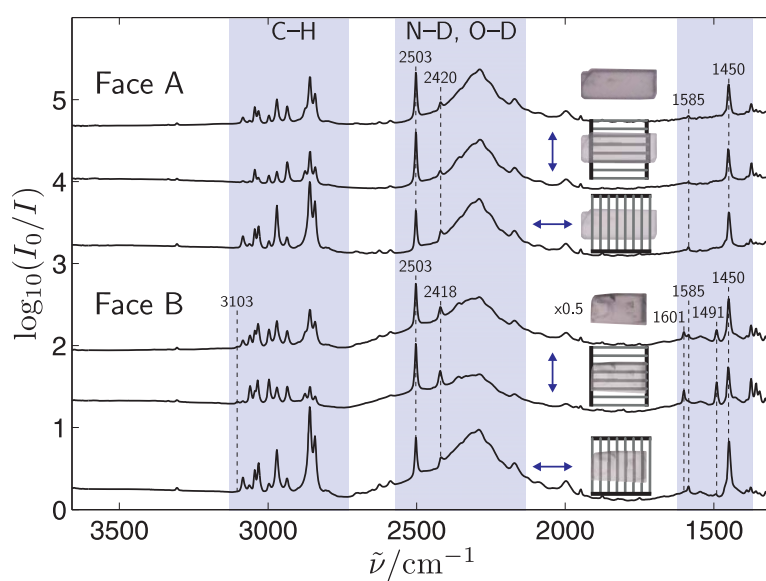
Figure 7.24.: ND/OD-deuterated enantiopure pseudonorephedrine polarization FTIR spectra crystallized from D_2O solution of type A and B. The arrows show the direction of the electric field vector. The visual pictures of the measured crystals are shown above the corresponding spectra. The visual picture of the crystal exhibiting a type B spectrum was multiplied by a factor of 0.5. Band positions are given in cm^{-1}.
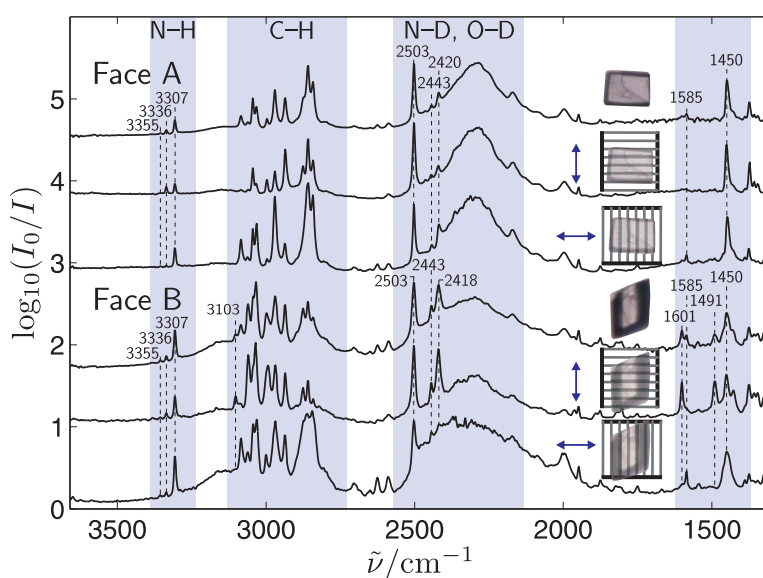
Figure 7.25.: ND/OD-deuterated enantiopure pseudonorephedrine polarization FTIR spectra of sublimated crystals of face A and B are shown. The arrows show the direction of the electric field vector. The visual pictures of the measured crystals are shown above the corresponding spectra. Band positions are given in cm^{-1}.

propanolamines in this Chapter. The assignment of the aliphatic C-H stretching modes will be performed after determination of the molecular orientation on the basis of their polarization behavior. Also, the assignments of the mixed modes will be confirmed by their polarization behavior.

The bands at $3355/3354\,\mathrm{cm}^{-1}$ and $3288/3290\,\mathrm{cm}^{-1}$ in Fig. 7.23 can be assigned to the asymmetric and the symmetric N-H stretching modes. Two bands at $2503\,\mathrm{cm}^{-1}$ and $2420/2418\,\mathrm{cm}^{-1}$ appear in the N-D stretching region of ND/OD-deuterated pseudonorephedrine obtained out of the solution (Fig. 7.24). These bands are caused by the asymmetric and the symmetric N-D stretching modes. After sublimation of the ND/OD deuterated compound two further bands at $3336\,\mathrm{cm}^{-1}$ and $3307\,\mathrm{cm}^{-1}$ arise in the N-H stretching region and one further band at $2443\,\mathrm{cm}^{-1}$ in the N-D stretching region (Fig. 7.25). These bands can be assigned to localized N-H and N-D stretching modes of partly deuterated pseudonorephedrine (see Sect. 7.3). The more intense and more red shifted band at $3307\,\mathrm{cm}^{-1}$ is caused by the hydrogen bonded N-H, while the band at $3336\,\mathrm{cm}^{-1}$ probably corresponds to the free N-H stretching mode. In the N-D stretching region only the bonded N-D band at $2443\,\mathrm{cm}^{-1}$ is present. An explanation will be given in Sect. 7.8.

The N-H and O-H stretching bands are present in the spectra of both face A and B for both polarizations (see Fig. 7.23). Thus, the O-H and N-H hydrogen bonds are visible in both orientations. The symmetric aromatic C-H stretching band at $3101\,\mathrm{cm}^{-1}$ appears only in the vertically polarized spectrum of face B. The C-C stem is thus not visible in the orientation of face A, while it is vertically oriented in the case of face B (see Supplement F). The $\text{C-C}_{\mathrm{aromatic,1}}$ and $\text{C-C}_{\mathrm{aromatic,2}}$ stretching bands at $1601\,\mathrm{cm}^{-1}$ and $1585\,\mathrm{cm}^{-1}$ are overlayed by the N-H bending mode. The resulting broad band is present in the spectra of face A and B. It almost vanishes after deuteration (see Figs. 7.24 and 7.25) revealing the contribution of the $\text{C-C}_{\mathrm{aromatic,1}}$ and $\text{C-C}_{\mathrm{aromatic,2}}$ stretching modes. Their polarization dependence is in agreement with the orientation of the C-C stem stated above. Furthermore, it can be inferred that the α-acidic CH group is horizontally aligned in Face A and B. The broad band around $1600\,\mathrm{cm}^{-1}$ in the nondeuterated pseudonorephedrine spectra decreases almost completely in the vertically polarized spectra of face A (Fig. 7.23). A decrease in intensity can also be observed in the horizontally polarized spectra of face B. Since most contributions belong to the N-H bending mode, it can be inferred that the amine group is rather horizontally aligned in the case of face A and more or less vertically aligned in the case of face B. The $\text{C-C}_{\mathrm{aromatic,3}}$ stretching band

Table 7.11.: Assignments of experimental band maxima in the FTIR microscopic spectra of enantiopure pseudonorephedrine of face A, face B, face C (Fig. 7.23), FTIR-ATR spectra (without ATR correction, Fig. 7.2) as well as calculations of the relaxed monomer unit taken from the crystal structure ($Mon_{crystal}$) on the B3LYP/6-311++G(3df,2p) level. All wavenumbers are given in cm^{-1}. The stretching and bending vibrations are indicated as ν and δ and the symmetric and asymmetric vibrations with sym and asym. Unassigned bands are labeled with a question mark (?).

Assignment	Face A	Face B	Face C	ATR	$Mon_{crystal}$
$\nu(N\text{-}H_{asym})$	3355	3354	3355	3354	3586
$\nu(N\text{-}H_{sym})$	3288	3290	3288	3289	3507
$\nu(O\text{-}H)$	3500–2500	3500–2500	3500–2500		3839
$2\delta(N\text{-}H)$		3150			
$\nu(C\text{-}H_{aromatic,sym})$		3101		3104	3188
$\nu(C\text{-}H_{aromatic,2})$		3085		3084	3181
$\nu(C\text{-}H_{aromatic,3})$		3059	3060	3061	3171
$\nu(C\text{-}H_{aromatic,4})$	3045	3045		3046	3161
$\nu(C\text{-}H_{aromatic,5})$	3033	3035		3034	3153
$\nu(C\text{-}H_{3,asym1})$	2997	2994	2997	2997	3109
$\nu(C\text{-}H_{3,asym2})$	2970	2972	2970	2970	3084
$\nu(C\text{-}H_{3,sym})$	2935	2937	2935	2936	3027
$2\delta(C\text{-}H)$	2877	2879	2878		
$\nu(C\text{-}H_{\alpha})$	2860			2864	2996
$\nu(C\text{-}H_{\beta})$	2844			2843	2933
?		1963			
?	1948	1948	1948	1948	
?	1876	1892	1876		
?		1803			
?	1751	1751	1751		
$\delta(N\text{-}H)$	1615–1550	1630–1530			1644
$\nu(C\text{-}C_{aromatic,1})/\delta(NH)$	1601	1601	1603	1601	1642
$\nu(C\text{-}C_{aromatic,2})$	1585	1585	1585	1582	1622
$\nu(C\text{-}C_{aromatic,3})$	1491	1491	1491	1491	1528
$\delta(C\text{-}H_{3,1})$	1450	1452	1450	1447	1502
$\delta(C\text{-}H_{3,2})$	1450	1452	1450	1447	1498
$\nu(C\text{-}C_{aromatic,4})$	1450	1452	1450	1447	1486
$\delta(C\text{-}H_3/C\text{-}H_{\beta})$	1450	1452	1450	1447	1415
$\delta(O\text{-}H/C\text{-}H_{\alpha}/C\text{-}H_{\beta})$	1450	1452	1450	1447	1408

Table 7.12.: Assignments of experimental band maxima in the FTIR microscopic spectra of enantiopure ND/OD-deuterated pseudonorephedrine of face A and face B (Figs. 7.24 and 7.25). All wavenumbers are given in cm^{-1}. The stretching and bending vibrations are indicated as ν and δ and the symmetric and asymmetric vibrations with sym and asym. Unassigned bands are labeled with a question mark (?).

Assignment	Face A	Face B
$\nu(\text{N-H}_{asym})$	3355	3355
$\nu(\text{N-H}_{localized,free})$	3336	3336
$\nu(\text{N-H}_{localized,bonded})$	3307	3307
$\nu(\text{O-H}_{sym})$		3200–2700
$\nu(\text{C-H}_{aromatic,sym})$		3103
$\nu(\text{C-H}_{aromatic,2})$	3085	3085
$\nu(\text{C-H}_{aromatic,3})$	3060	3060
$\nu(\text{C-H}_{aromatic,4})$	3045	3045
$\nu(\text{C-H}_{aromatic,5})$	3033	3031
$\nu(\text{C-H}_{3,asym1})$	2997	2997
$\nu(\text{C-H}_{3,asym2})$	2970	2970
$\nu(\text{C-H}_{3,sym})$	2935	2935
$2\delta(\text{C-H})$	2875	2875
$\nu(\text{C-H}_{\alpha})$	2860	2860
$\nu(\text{C-H}_{\beta})$	2842	2842
$2\delta(\text{C-H})$	2806	2806
$2\delta(\text{C-H})$	2798	2798
$\nu(\text{N-D}_{asym})$	2503	2503
$\nu(\text{N-D}_{localized,bonded})$	2443	2443
$\nu(\text{N-D}_{sym})$	2420	2418
$\nu(\text{O-D})$	2500–1800	2500–1800
$\nu(\text{C-C}_{aromatic,1})$	1601	1601
$\nu(\text{C-C}_{aromatic,2})$	1585	1585
?	1547	1545
$\nu(\text{C-C}_{aromatic,3})$		1491
$\nu(\text{C-C}_{aromatic,4})$	1450	1450

appears in the horizontally polarized spectra of face A. It is highest in intensity in the case of a vertical polarization of face B which is in agreement with a vertical orientation of the C-C stem. The C-C$_{aromatic,4}$ band at $1450\,\text{cm}^{-1}$ and $1452\,\text{cm}^{-1}$ is present in all spectra of face A and B. It has an unusually high intensity in the spectra of face A. This increase can be explained by two C-H$_3$, a mixed C-H$_3$/C-H$_\beta$, and a mixed O-H/C-H$_\alpha$/C-H$_\beta$ bending mode at the same spectral position. The slight intensity decrease upon deuteration (see Fig. 7.24) supports the additional assignment of the O-H/C-H$_\alpha$/C-H$_\beta$ bending mode to the band at $1450/1452\,\text{cm}^{-1}$.

The spectral differences appearing upon polarization can be used to fix the molecular orientation of face A to a view along the crystallographic c axis and face B to a view along the crystallographic b axis (see Fig. 7.26). Since there is no noticeable change in conformation due to structure optimization (see Fig. 7.21), monomer calculations should predict the experimental behavior to a reasonable extent.

A comparison of experimental face A and face B spectra with oriented gas model spectra is shown in Fig. 7.27. As expected the red shift of the O-H and N-H stretching modes is underestimated. Good agreement can be noticed for the experimental and predicted intensity ratios of the O-H stretching mode. There is a lack of agreement between the experimental and oriented gas model intensity of the N-H stretching band of face B. In the spectra measured using a vertical polarization the N-H stretching bands are clearly visible, while the simulation predicts them to have no intensity. The weakness of the N-H stretching transition moments can lead to unexpected aggregation-induced reorientations of the dipole moment derivatives [183]. The molecular orientation of face B is shown in Fig. 7.26. It can be seen that the N-H···O hydrogen bonds are almost perfect horizontally aligned. Therefore, also by comparison of the molecular orientation and crystal face no N-H stretching bands would be predicted for a vertical polarization. The mismatch might result from a turned orientation than the proposed one or from polymorphism. Reasonable agreement can be noticed in the lower part of Fig. 7.26 showing that the assignment of face A to a view along the crystallographic c axis and of face B to a view along the crystallographic b axis is trustworthy.

The knowledge of the molecular orientation and the polarized spectra can be used to assign the bands in the aliphatic C-H stretching region. A comparison of experimental and oriented gas model polarization spectra of the C-H stretching region is shown in the upper part of Fig. 7.27. There is good agreement of the position and polarization behavior of the methyl stretching bands in the ND/OD-deuterated and
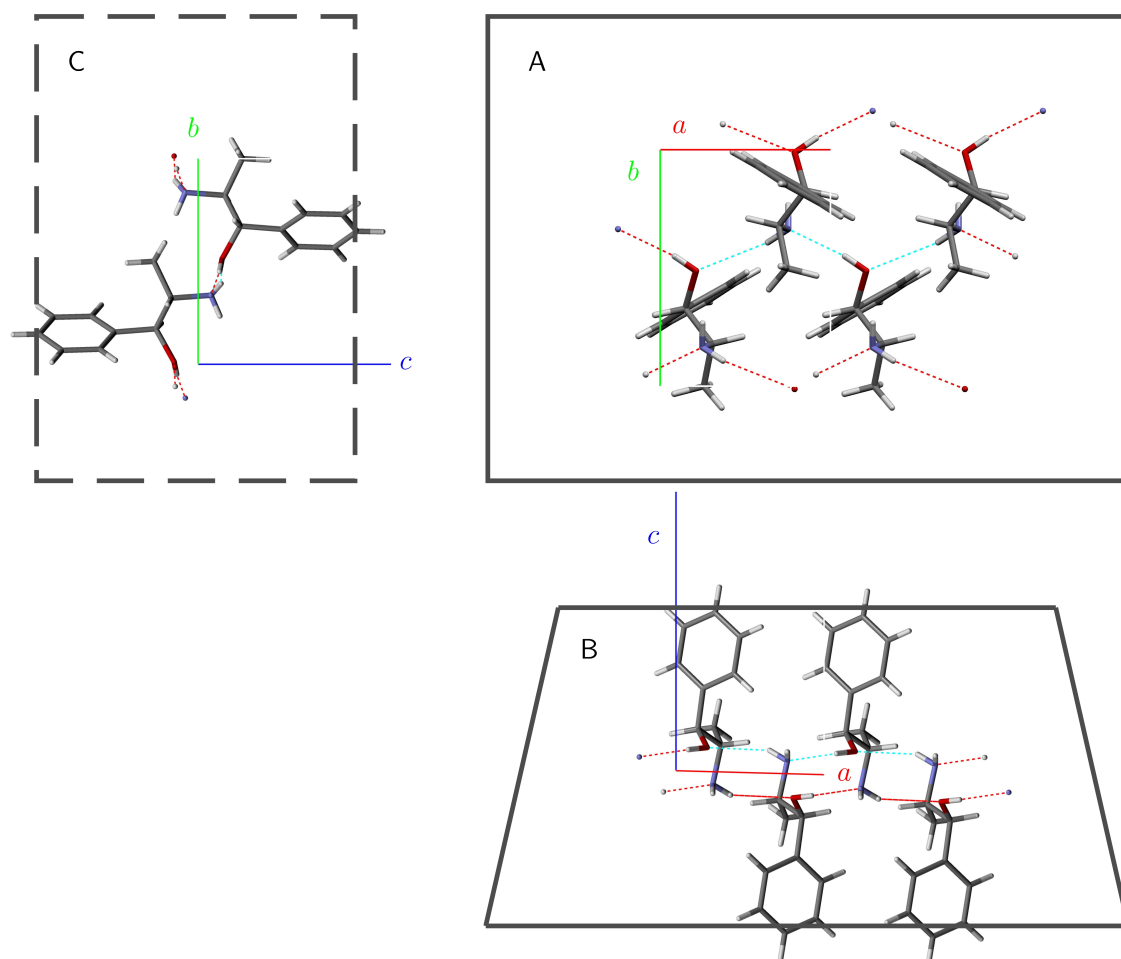
Figure 7.26.: Molecular orientation of pseudonorephedrine along the three crystal faces. The crystal structure was taken from Ref. [90]. The continuous frames mark the observed faces, whereas the unobserved face is dash-framed.
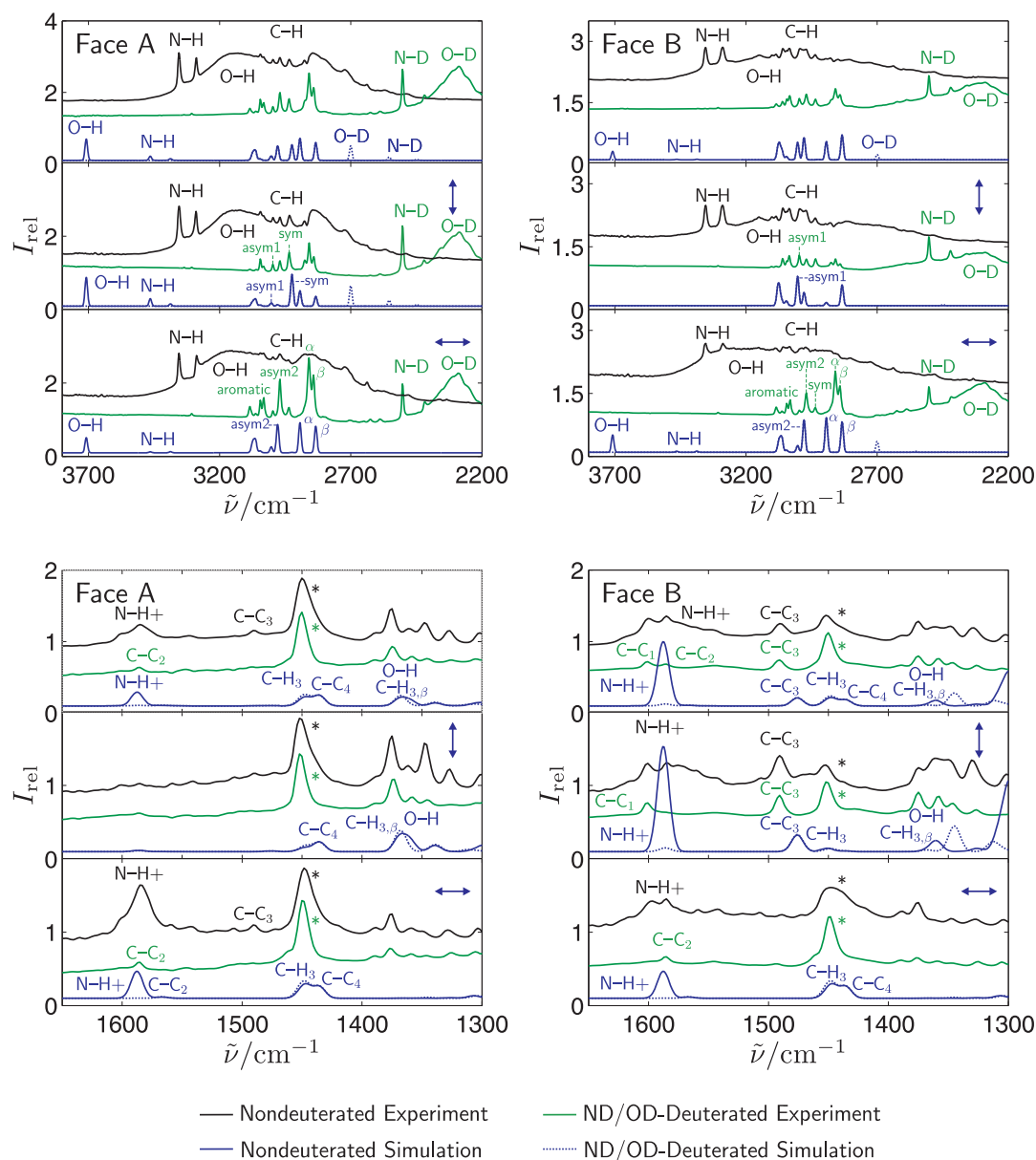
Figure 7.27.: Comparison of experimental and oriented gas model polarization spectra without deuteration (B3LYP/6-311++G(3df,2p) level) of face A (left) and face B (right) of pseudonorephedrine. The nondeuterated spectra (top, black), the ND/OD-deuterated spectra (center, green), and oriented gas model spectra (bottom, blue) of nondeuterated (solid line) and ND/OD-deuterated (dashed line) are shown. Harmonic wavenumbers are scaled by a factor of 0.966 to account for anharmonicity. Assigned bands in the two upper parts are stretching modes. C-H stretching modes are indicated. The N-H bending, $C-C_{aromatic,1}$, and $C-C_{aromatic,2}$ (abbreviated N-H+), other $C-C_{aromatic}$ stretching modes (abbreviated $C-C_x$), $C-H_3$ bending modes, a mixed $C-H_3/C-H_\beta$ bending mode (abbreviated $C-H_{3,\beta}$), and a mixed $O-H/C-H_\alpha/C-H_\beta$ bending mode (abbreviated O-H) are shown in the lower part. The asterisk (*) marks the experimental position of the $C-C_4$ bending mode, both $C-H_3$ bending modes, the mixed $C-H_3/C-H_\beta$ bending mode, and the mixed $O-H/C-H_\alpha/C-H_\beta$ bending mode.

163

the oriented gas model spectra (scaled by a factor of 0.966, see Chapter 3). Thus, the bands at 2997/2994 cm^{-1}, 2970/2972 cm^{-1}, and 2933/2935 cm^{-1} can unambiguously be assigned to two asymmetric and the symmetric methyl stretching bands. Also, the polarization behavior of the bands at 2860 cm^{-1} and 2844 cm^{-1} is in good agreement with the predicted direction of the vibrational transition dipole vector of the α- and β-acidic C-H stretching modes. Only, in the case of the vertically polarized spectrum of face B the experimental and predicted behavior of the β-acidic mode deviates. Since, the β-acidic C-H bond is more or less horizontally aligned in the molecular orientation of face B (matches the experimental behavior), the strong intensity in the oriented gas model spectrum is probably an artifact of the rotation method. The scaled red shift of the α-acidic mode is slightly under- and the one of the β-acidic slightly overestimated.

The band at 2877/2879 cm^{-1} cannot be assigned to a C-H stretching mode. It is probably caused by C-H bending overtone. The same is true for the more red shifted bands at 2806 cm^{-1} and 2798 cm^{-1} in the ND/OD-deuterated spectra.

7.6. Ephedrine

Enantiopure anhydrous ephedrine (Fig. 7.28) is a white powder which melts at 37–39°C (according to the supplier, Tab. 7.1). It is a hygroscopic substance. The enantiopure hemihydrate melts at 39–43°C. It is a white to clear substance.

FTIR-ATR spectra have only been recorded for the hemihydrate of ephedrine (see Fig. 7.2). It has not been possible to measure FTIR-ATR spectra of the anhydrous compound. The ephedrine sample used for the measurements was stored in a bottle which had been opened a few months before. Probably, the sample was hydrated in the bottle. Remeassurements with a fresh substance should be carried out.

Crystal Structures

In the case of ephedrine, the crystal structures of anhydrous (1*R*,2*S*)-ephedrine (E-AH) and (1*R*,2*S*)-ephedrine hemihydrate (E-H) are available [91, 172]. The crystal structure of anhydrous ephedrine crystallized from an alcoholic solution was solved by Collier et al. (CSD REF Code: EPHE) [91]. They report a needle-like habit with the *a* axis representing the fastest growth direction. Anhydrous ephedrine crystallizes in the space group $P2_12_12_1$ (see also Ref. [172]). There are four molecules in the unit cell (*Z*=4) and one molecule in the asymmetric unit (*Z*'=1). O-H···N hydrogen bonds

Frozen monomer unit
from the crystal structure

Relaxed monomer unit
from the crystal structure

Most stable
monomer
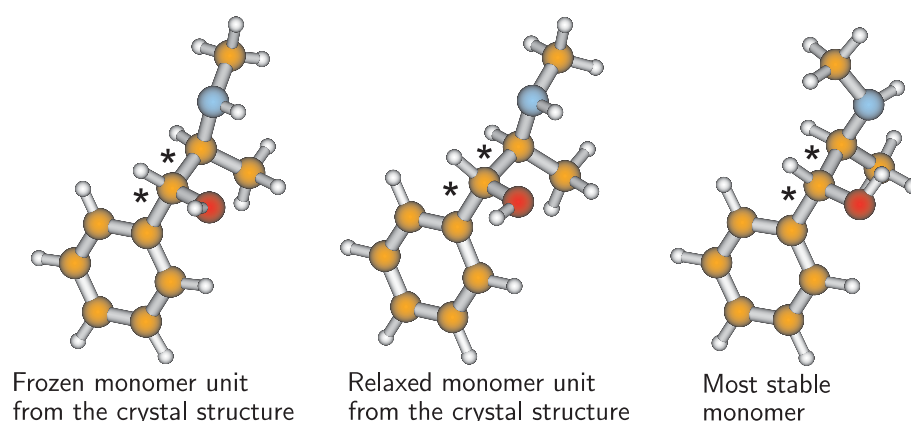
Figure 7.28.: Frozen and relaxed monomer units taken from the crystal structure of anhydrous ephedrine [91] as well as the most stable monomer [82, 85, 87] (B3LYP/6-311++G(3df,2p) level). Centers of chirality are marked with an asterisk (*).
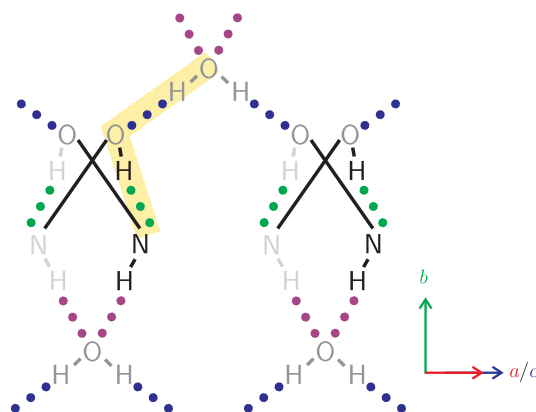
Figure 7.29.: Schematic view of the hydrogen bond network in ephedrine hemi-hydrate. The O-H···N hydrogen bonds are marked with green dots, N-H···O hydrogen bonds with purple dots, and O-H···O hydrogen bonds with blue dots. A finite cooperative hydrogen bonded strand is highlighted in yellow. Black atoms are above, gray atoms in, and light gray atoms beyond the plane of the water molecules. The ephedrine molecules are reduced to the OH and NH group connected by a straight line.

(2.0 Å) which run along the crystallographic c axis connect the molecules along the a axis (see Fig. 7.32 later on). The strands are connected by π-interactions of the phenyl and the methyl group.

Malone and Parvez reported the space group $B22_12$ for ephedrine hemihydrate in 1978 [172]. A reassignment of platy ephedrine hemihydrate crystals obtained from an aqueous solution led a correction of the space group to $C222_1$ by Collier et al. in 1978 (CSD REF Code: EPHEDH04) [91]. Ephedrine hemihydrate has 8 ephedrine and 6 water molecules in the unit cell. In the asymmetric unit there are one ephedrine and one water molecule as unraveled by X-ray and neutron studies [91, 172, 190]. Two ephedrine molecules form dimeric units which are connected by two O-H···N hydrogen bonds (1.9 Å) along the crystallographic c axis (see Fig. 7.29 and Fig. 7.34 later on). These dimers are linked together by O-H···O hydrogen bonds along the a axis with water being a double proton donor (2.0 Å). It connects the ephedrine dimers to chains. As visualized in Fig. 7.29, there are cooperative (blue and green) and anti-cooperative hydrogen bonds (purple). The chains are held together by π-stacking of two phenyl rings and van der Waals interactions of a phenyl and a methyl group.

Crystallization

In the case of the sublimation experiments only one sublimated polycrystal of an-hydrous ephedrine was obtained. It consisted of tabular single crystals. All other sublimation attempts led to a condensation of droplets at the upper window (above 18°C). At temperatures below 18°C nothing happened. It is conceivable that the obtained polycrystal grew on powder of ephedrine sticking on the upper CaF_2 sub-strate. But this is rather unlikely since the CaF_2 windows had been cleaned be-fore every measurement. Also, as stated above, the powder probably consisted of ephedrine hemihydrate and not the anhydrous compound. The recorded polarized FTIR spectra of the anhydrous ephedrine crystal are shown in Fig. 7.30.

A single crystal of ephedrine hemihydrate was obtained from an aqueous so-lution. The crystal has a platy habit. Fig. 7.31 shows the visual picture and the polarization FTIR spectra of this crystal. Ivanova et al. recorded linear polarized and nonpolarized IR spectra of ephedrine hemihydrate (grown by slow evaporation from an aqueous solution at room temperature) [191]. The differences to ATR and crystal spectra measured in this work might be due to the KBr pellet technique they used.

For both, the anhydrous and the ephedrine hemihydrate, only one face of one crystal has been measured. The observed faces are arbitrarily denoted Face A. No ND/OD deuteration experiments were carried out for ephedrine (neither anhydrous nor hemihydrate).

FTIR Spectra

The vibrational assignments of ephedrine anhydrate and ephedrine hemihydrate are summarized in Tab. 7.13. The assignments of the N-H and O-H stretching and the mixed C-H_3/N-H bending modes are performed by comparison of experimental and predicted wavenumbers (see also Sect. 7.3).

In the ephedrine hydrate spectra an O-H stretching band pattern appears less red shifted than in the spectra of the other investigated phenylpropanolamines. It is caused by the crystal water which acts as a double proton donor for weaker O-H···O hydrogen bonds and as a double proton acceptor for N-H···O hydrogen bonds (see Sect. 7.3). Cooperative and anti-cooperative effects more or less cancel each other out and additionally cause a less red shifted O-H stretching band [130, 192]. The water O-H stretching band shows contributions to lower wavenumbers (3421 cm^{-1})
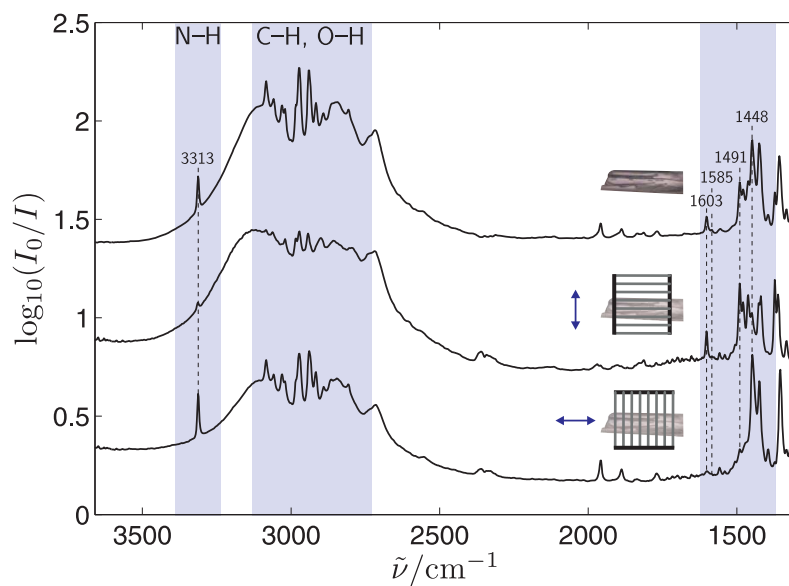
Figure 7.30.: Enantiopure anhydrous ephedrine polarization FTIR spectra. The arrows show the direction of the electric field vector. The visual pictures of the measured crystal are shown above the corresponding spectra. Band positions are given in cm^{-1}.
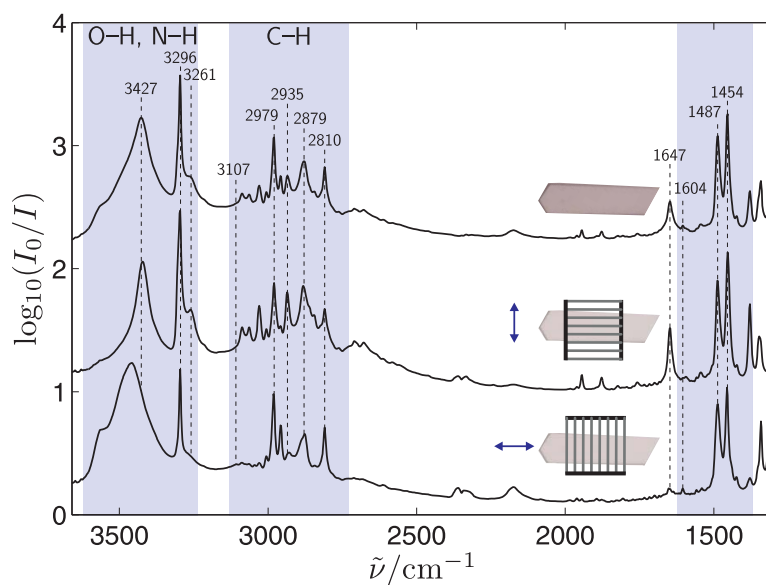
Figure 7.31.: Enantiopure ephedrine hemihydrate polarization FTIR spectra. The arrows show the direction of the electric field vector. The visual pictures of the measured crystal are shown above the corresponding spectra. Band positions are given in cm^{-1}.

at a vertical polarization which can be assigned to the symmetric stretch. The asymmetric contribution appears at higher wavenumber (3460 cm^{-1}) for the horizontal polarization. In the ATR spectrum of ephedrine hemihydrate (Fig. 7.2) a broad band at 3200–2200 cm^{-1} is present which can be assigned to the O-H stretching mode of ephedrine. The O-H bending mode of water appears at 1647 cm^{-1}. The shoulder of the N-H stretching band probably results from an asymmetric coupling of the two NH groups bonded to the same water molecule.

The aromatic C-H and C-C$_{aromatic}$ stretching bands of ephedrine anhydrate and hydrate are assigned according to observations made in the case of methyl mandelate, mandelic acid, and the other phenylpropanolamines in this Chapter. The tentative assignment of the aliphatic C-H stretching modes is performed on the basis of the pseudonorephedrine and pseudoephedrine assignments and the predictions. Note, that the predicted C-H stretching positions of ephedrine hemihydrate deviate from the predictions of the other phenylpropanolamines. Nonetheless, the experimental positions are tentatively assigned in analogy.

Face A of anhydrous ephedrine probably corresponds to a view along the crystallographic *b* axis as depicted in Fig. 7.32. But since spectra of the other two faces are missing the assignment cannot be verified. Fig. 7.33 shows a comparison between the experimental spectra of face A and the oriented gas model spectra of a view along the crystallographic *b* axis. There is reasonable agreement regarding the intensity changes of the experimental and simulated N-H and C-C$_{aromatic}$ stretching bands. One might notice that the experimental intensity change of the O-H stretching band does not agree with the simulated one. In Fig. 7.32 the hydrogen bonds in the view of face A are depicted. The O-H$\cdots$N hydrogen bonds run more or less along the *c* axis. Thus, one would predict the O-H stretching mode to be excited at a vertical polarization as it is the case in the experimental spectra. The discrepancy of experimental and simulated behavior results from a slight rotation of the O-H group during the monomer relaxation. In Fig. 7.28 a comparison of a frozen and a relaxed monomer is displayed showing the structural modification upon relaxation. The C$_{aromatic}$-C-O-H dihedral angle changes by ca. 30° (from 99° to 67°). This rotation of the O-H group has an effect on the direction of the calculated transition dipole vector. The divergence of experimental and simulated intensity changes of the O-H stretching band in Fig. 7.33 can therefore be explained.

In the lower wavenumber region good agreement between experimental and oriented gas model polarization spectra can be found for the C-C$_{aromatic,1}$, C-C$_{aromatic,3}$,

Table 7.13.: Assignments of experimental band maxima in the FTIR microscopic spectra of enantiopure anhydrous ephedrine (AH, Fig. 7.30) and ephedrine hemihydrate (H, Fig. 7.31), FTIR and IR-DFG Vapor Phase (Vap FT and Vap DFG, Ref. [193]) and calculations of the monomer unit taken from the crystal structure of ephedrine anhydrate (Mon$_{crystal,AH}$) and ephedrine hemihydrate Mon$_{crystal,H}$ on the B3LYP/6-311++G(3df,2p) level. All wavenumbers are given in cm^{-1}. The stretching and bending vibrations are indicated as ν and δ and the symmetric and asymmetric vibrations with sym and asym. Tentative assignments and bands without assignment are labeled with a question mark (?).

Assignment	AH	H	Vap FT	Vap DFG	Mon$_{crystal,AH}$	Mon$_{crystal,H}$
ν(O-H)$_{water}$		3427				
ν(N-H)$_{sym}$	3313	3296			3531	3498
ν(N-H)$_{asym}$		3261				
ν(O-H)	3440–2400	(3200–2200)			3842	3733
ν(C-H$_{aromatic,sym}$)		3107			3189	3203
ν(C-H$_{aromatic,2}$)	3084	3087			3182	3184
ν(C-H$_{aromatic,3}$)	3062	3064	3070	3074	3170	3170
ν(C-H$_{aromatic,4}$)	3058				3160	3159
ν(C-H$_{aromatic,4}$)		3045			3160	3159
ν(C-H$_{aromatic,5}$)	3030	3030	3034	3037	3148	3146
? ν(C-H$_{3,asym1}$)	3020				3102	3114
? ν(C-H$_{3,asym2}$)					3096	3108
?		3006				
?	2983	2981				
? ν(NC-H$_{3,asym1}$)	2974	2979	2974	2971	3082	3101
? ν(NC-H$_{3,asym2}$)		2958			3038	3068
? ν(C-H$_{3,sym}$)	2940	2935		2943	3034	3042
?		2929				
?	2916			2915		
?	2891	2881	2886			
?		2879				
? ν(C-H$_{\alpha/\beta,sym}$)	2866			2856	3013	2931
? ν(C-H$_{\alpha/\beta,asym}$)	2846	2844			3002	2914
? ν(NC-H$_{3,sym}$)	2806	2810			2952	2947
?		2796				
?		2717				
?		2555				
?		1971				
?		1959				
?		1901				
?		1836				
?		1813				
?		1770				
δ(O-H)$_{water}$		1647				
ν(C-C$_{aromatic,1}$)	1603	1604			1642	1645
ν(C-C$_{aromatic,2}$)	1585				1621	1623
ν(C-C$_{aromatic,3}$)	1491	1487			1527	1530
? δ(C-H$_{3,1}$/N-H)	1479				1523	1524
? δ(C-H$_{3,2}$/N-H)	1462				1509	1508
ν(C-C$_{aromatic,4}$)	1448	1454			1484	1483
δ(C-H$_{3,4}$/N-H)					1492	1498
? δ(N-H/C-H$_3$)	1425				1481	1489
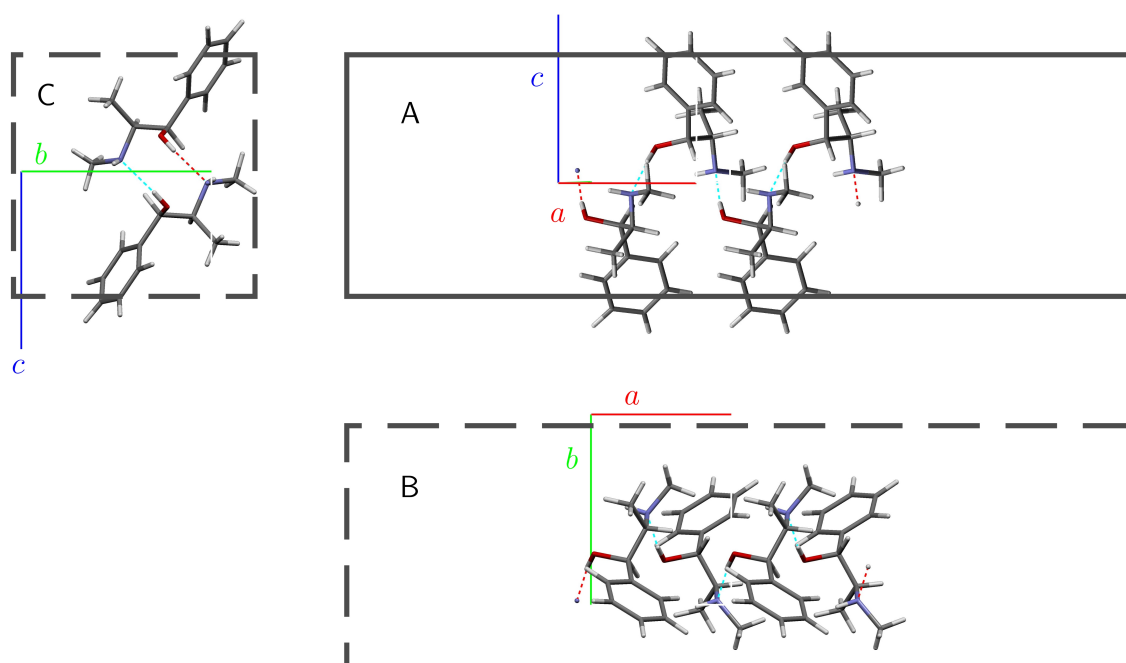
Figure 7.32.: Molecular orientation of anhydrous ephedrine along the three crystal
faces. The crystal structure was taken from Ref. [91]. The continu-
ous frame marks the observed face, whereas the unobserved faces are
dash-framed.
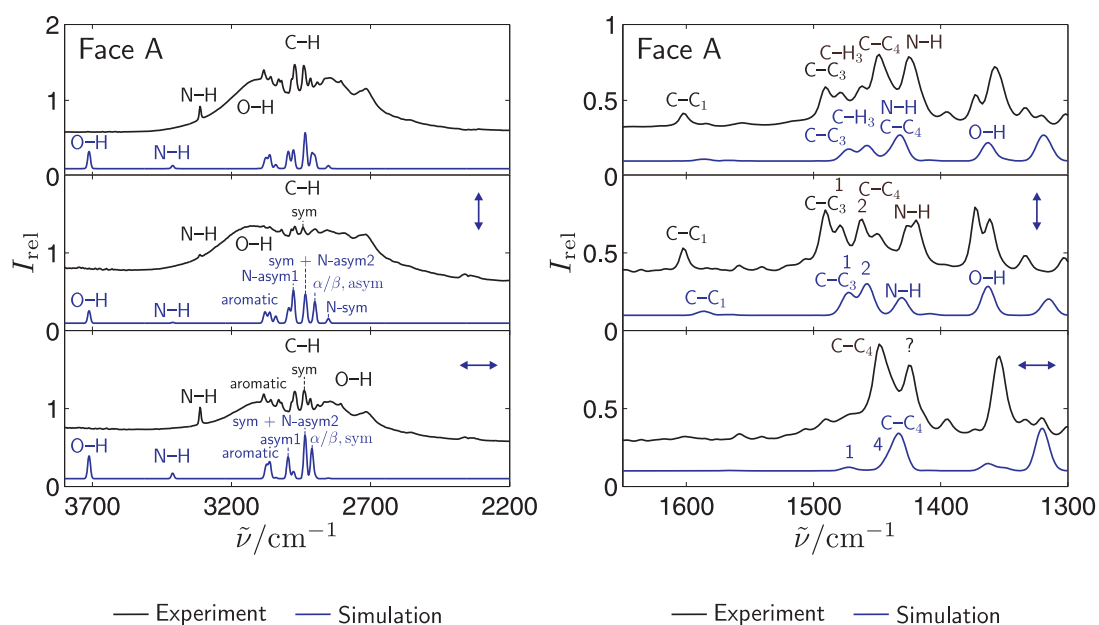
Figure 7.33.: Comparison of experimental (top, black) and oriented gas model (bottom, blue) polarization spectra (B3LYP/6-311++G(3df,2p) level) of face A of anhydrous ephedrine. Assigned bands in the left part are stretching modes. The C-C$_{aromatic}$ stretching modes (abbreviated C-C$_x$), mixed C-H$_3$/N-H bending modes (abbreviated C-H$_3$ and 1, 2, 4 for the individual modes), a mixed N-H/C-H$_3$ bending mode (abbreviated N-H), and a mixed O-H/C-H$_3$ bending mode (abbreviated O-H) are shown in the lower part. The question mark (?) labels an unassigned band.

and C-C$_{aromatic,4}$ stretching modes. These bands appear at $1603\,cm^{-1}$, $1491\,cm^{-1}$, and $1448\,cm^{-1}$. The mixed C-H$_3$/N-H bending modes and the mixed C-H$_3$/N-H bending mode cannot unambiguously be assigned. For the assignment performed in Fig. 7.33 and in Tab. 7.13 the calculated order was used. The above mentioned modes are predicted to be more intense at a vertical polarization. This is in good agreement with the experimental vertically polarized spectrum. Here, several bands appear in the region from $1500–1400\,cm^{-1}$. All in all, Fig. 7.33 shows that it is justified to assume the molecular orientation depicted in Fig. 7.32.

A further indication for the proposed molecular orientation is the consistency of interactions within the crystal and the habit of the grown crystal. As described above a polycrystal consisting of tabular single crystals was obtained. The strongest interaction is the O-H$\cdots$N hydrogen bond followed by N-H$\cdots$O hydrogen contacts. These are located in the *ac* plane. Therefore, it can be concluded that face A corresponds to a view along the *b* axis. Nevertheless, spectra of the other faces would be valuable.

An assignment of the molecular orientation of ephedrine hemihydrate is more difficult. According to the comparison of habit and interactions one would expect that face A corresponds to a view along the crystallographic *b* axis. In this view the hydrogen bond network is most pronounced (see Fig. 7.34). However, the crystal was not obtained by sublimation but from an aqueous solution. Therefore, external interactions might have an influence on the crystallization growth and on the crystals habit. The conclusion of the analysis of the polarization spectra is different. Face A does not correspond to a view along the crystallographic *b* axis. As can be seen in Fig. 7.31 there is a striking change in intensity in the case of the O-H bending mode of the water molecule appearing at $1647\,cm^{-1}$. The direction of the vibrational transition dipole vector of this mode runs along the crystallographic *b* axis. Therefore, it cannot be excited in the view along the *b* axis. The symmetric aromatic C-H stretching mode exhibits some intensity in the horizontally polarized spectrum. A rather diagonal orientation of the C-C stem with the phenyl plane less visible can be inferred since the vibrational transition dipole vector deviates by about $30°$ from the C-C$_{aromatic}$ axis (see Supplement F). This would match a view along the crystallographic *b* axis. However, this orientation is already excluded.

Interestingly, both the C-C$_{aromatic,3}$ and the C-C$_{aromatic,4}$ stretching band at $1487\,cm^{-1}$ and $1454\,cm^{-1}$ are quite high in intensity for both directions of polarization. It can be assumed that the reason is an underlying mixed band with con-
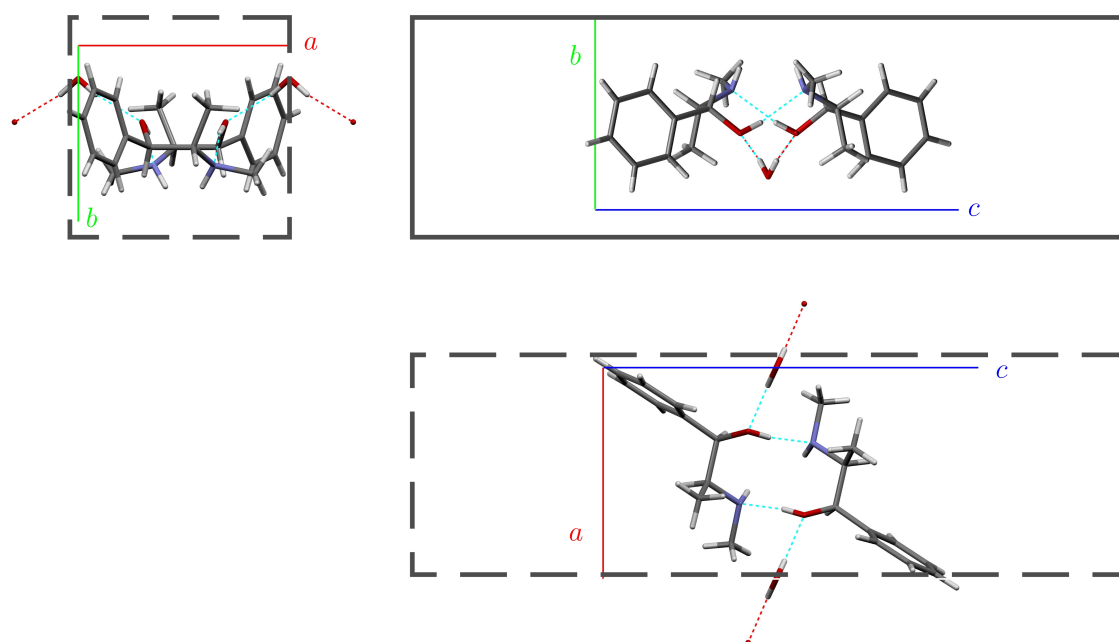
Figure 7.34.: Molecular orientation of ephedrine hemihydrate along the three crystal faces. The crystal structure was taken from Ref. [91]. The continuous frame marks the observed face, whereas the unobserved faces are dash-framed.

tributions of the OH (or NH) group which also causes a shift to lower and higher wavenumbers respectively compared to the positions in the spectra of the other phenylpropanolamines. An ND/OD-deuteration of ephedrine hemihydrate might help to solve this question and to unravel the assignment of the C-H stretching modes. With this information the molecular orientation might more confidently be assigned.

7.7. Pseudoephedrine

7.7.1. Enantiopure Pseudoephedrine

Enantiopure pseudoephedrine (see Fig. 7.35) is a white powder which melts at 116–120°C (according to the supplier, Tab. 7.1). There is no evidence that it is hygroscopic.

Crystal Structure

(1*S*,2*S*)-pseudoephedrine crystallizes in the space group *P*2$_1$2$_1$2$_1$ (CSD REF Code: PSEPD) [92,172]. It contains four molecules in the unit cell (*Z*=4) and one molecule in the asymmetric unit (*Z*'=1). The molecules are held together by isolated O-H···N hydrogen bonds (1.9 Å) which are aligned in a zigzag manner along the crystallographic *b* axis (see Fig. 7.40 later on). The hydrogen bonded chains are connected by weak aromatic C-H···O interactions (2.2 Å) along the *a* axis and by van der Waals interactions of the phenyl and the methyl group in another dimension. The formation of needle-like racemic pseudoephedrine crystals was reported by Duddu et al. and characterized by its X-ray diffraction pattern [173].

Frozen monomer unit from the crystal structure   Relaxed monomer unit from the crystal structure   Most stable monomer
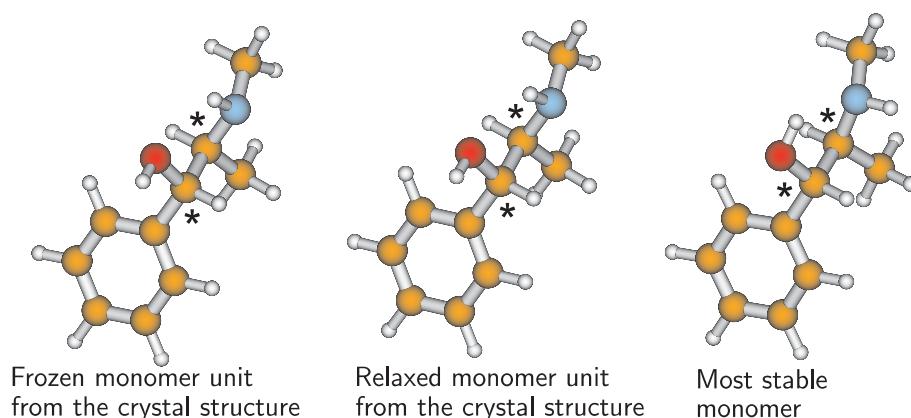
Figure 7.35.: Frozen and relaxed (1*S*,2*S*)-monomer units taken from the crystal structure of enantiopure pseudoephedrine [92] as well as the most stable monomer [82, 86, 87] (B3LYP/6-311++G(3df,2p) level). Centers of chirality are marked with an asterisk (*).

Crystallization

Enantiopure pseudoephedrine crystals were obtained in a temperature range of 30°C to 45°C. The tabular crystals exhibit two types of spectra (see Fig. 7.36) with similar abundance. It is possible to assign the two spectral types to two different faces of the crystals by rotating the crystal. As can be seen in Fig. 7.37 rotating a crystal showing spectra of face A leads to the spectral type of face B and vice versa. The rotation experiments also exhibit spectra corresponding to face C of the crystal.

ND/OD-deuterated crystals were obtained from a solution of a tip of spatula of enantiopure pseudoephedrine in 15 drops of D_2O. The solution was heated up to 55°C and cooled down to room temperature in the open sublimation cell. The cell was subsequently evacuated. During the evacuation process platy crystals grew into a polycrystal in the solution. Polarization FTIR measurements were carried out on monocrystalline fragments of the polycrystal which are shown in Fig. 7.38. Spectra of two different faces A and B were obtained.

Sublimated ND/OD-deuterated crystals grew on top of the cell after heating it up to 35°C. Monocrystals with a tabular habit were obtained. Polarization FTIR spectra measured of the two faces A and B correspond to those measured using the polycrystals from the solution (see Figs. 7.38 and 7.39).

A comparison of the spectra and visual pictures of the nondeuterated and the ND/OD-deuterated enantiopure pseudoephedrine crystals (Figs 7.36 and 7.39) shows similarities in the C-H and C-C$_{aromatic}$ stretching region as well as in the habit of the crystals. Face A and face B belong to analogous faces of the nondeuterated and the ND/OD-deuterated crystals. FTIR spectra of face A and B of enantiopure pseudoephedrine (see Figs. 7.36, 7.38, and 7.39) can easily be distinguished by the intensity of the O-H and O-D stretching bands which are much higher in the case of face B.

FTIR Spectra

The vibrational assignments are summarized in Tabs. 7.14 and 7.15. The assignments of the N-H and O-H stretching and the mixed N-H/C-H$_3$ bending modes are performed by comparison of experimental and predicted wavenumbers (see also Sect. 7.3) and by the behavior upon the ND/OD-deuteration. The N-D stretching position will be addressed below. The tentative assignments of the N-H/C-H$_3$ and C-H$_3$/N-H bending modes are supported by further considerations after determin-
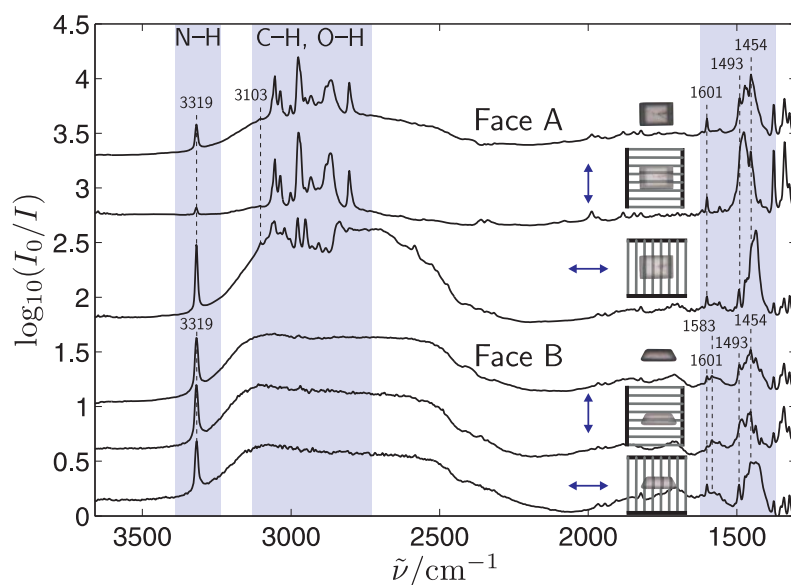
Figure 7.36.: Enantiopure pseudoephedrine polarization FTIR spectra of face A. The arrows show the direction of the electric field vector. The visual pictures of the measured crystals are shown above the corresponding spectra. Band positions are given in cm^{-1}.
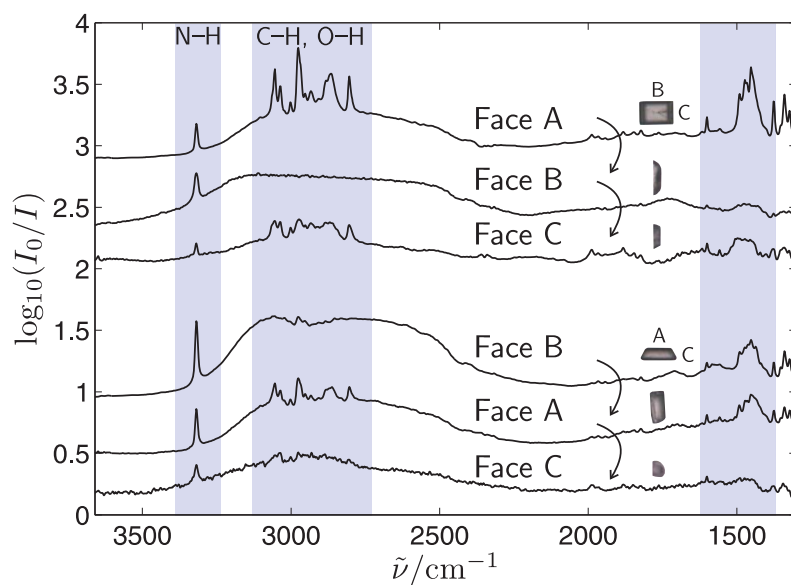
Figure 7.37.: Enantiopure pseudoephedrine FTIR spectra obtained after rotation of crystals showing type A and type B spectra. Rotating the crystal interconverts the spectral types A and B and exhibits oversaturated spectra of type C. The visual pictures of the measured crystals are shown above the corresponding spectra.
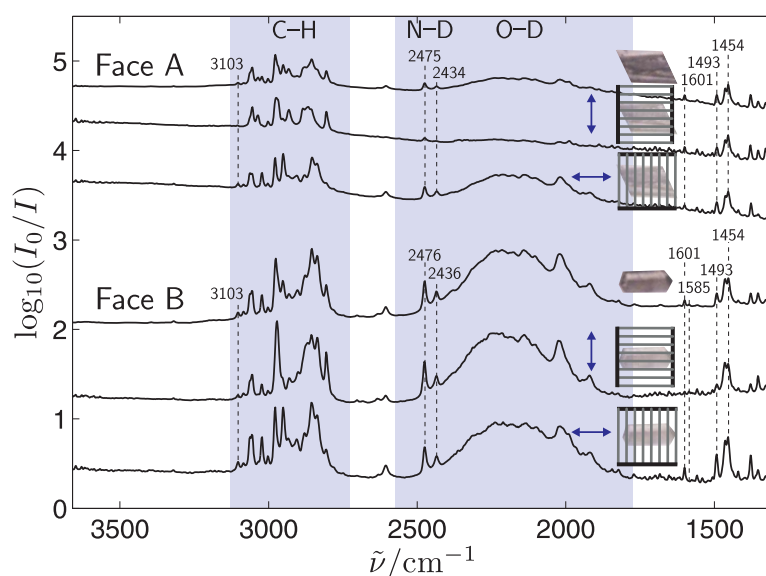
Figure 7.38.: ND/OD-deuterated enantiopure pseudoephedrine polarization FTIR spectra of face A and B. Crystals were obtained from a solution of D_2O. The arrows show the direction of the electric field vector. The visual pictures of the measured crystals are shown above the corresponding spectra. The visual picture of the crystal showing face A was cut at the long axis of the crystal. Band positions are given in cm^{-1}.
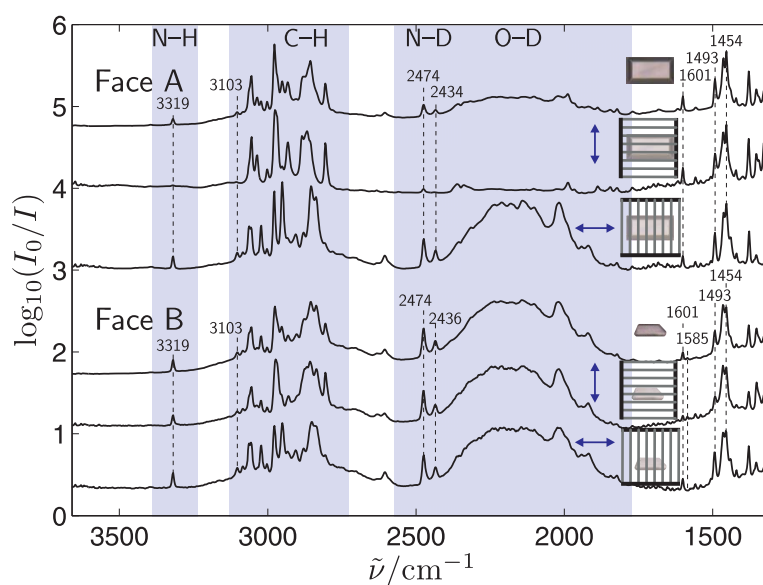
Figure 7.39.: ND/OD-deuterated enantiopure pseudoephedrine polarization FTIR spectra of of face A and B. Crystals were obtained by sublimation. The arrows show the direction of the electric field vector. The visual pictures of the measured crystals are shown above the corresponding spectra. Band positions are given in cm^{-1}.

ing the molecular orientation later on. The aromatic C-H and C-C$_{aromatic}$ stretching bands are assigned according to observations made in the case of methyl mandelate, mandelic acid, and the other phenylpropanolamines in this Chapter. The aliphatic C-H stretching modes will be assigned after the determination of the molecular orientation of the two faces.

In the nondeuterated spectra only one N-H stretching band appears (as expected), whereas there seem to be two N-D stretching bands at $2475\,cm^{-1}$ and $2434/2436\,cm^{-1}$ in the ND/OD-deuterated spectra. They result from a Fermi-resonance of the N-D stretching fundamental and the N-D bending overtone at $1226\,cm^{-1}$ (not shown) [194]. The assignment is supported by their polarization behavior and by their behavior upon deuteration.

Polarization FTIR spectra of face A clearly show a dependence of the N-H and O-H stretching bands on the direction of polarization. Both bands gain intensity with a polarization parallel to the long crystal axis. Thus, a horizontal alignment of the isolated O-H$\cdots$N hydrogen bonds and of the N-H axis can be assumed. In the case of face B the N-H and O-H stretching bands are high in intensity for both directions of polarization. This behavior matches a diagonal alignment of the O-H$\cdots$N hydrogen bonds and the N-H group. Since the intensities of the N-H and O-H stretching bands are higher in intensity in the spectra of face B, the O-H$\cdots$N hydrogen bonds and the N-H axis are more visible in the orientation of face B. The C-C$_{aromatic}$ stretching bands only show subtle differences between face A and B spectra. The C-C$_{aromatic,1}$, C-C$_{aromatic,3}$, and C-C$_{aromatic,4}$ stretching bands are present in both face A and B spectra with nearly equal intensities for both polarizations. The C-C$_{aromatic,1}$ and C-C$_{aromatic,3}$ are more intense in the face A spectra. Therefore, a diagonal orientation of the C-C stem and the C-N-C-C-C$_{aromatic}$ backbone can be assumed for both faces with a better visibility in the case of face A (see Supplement F). The appearance of the symmetric aromatic C-H stretching in all spectra and for all polarizations supports this conclusion. The C-C$_{aromatic,2}$ stretching band at $1583\,cm^{-1}$ appears only in face B spectra. This points at a better visibility of the α- and β-acidic C-H axes in the orientation of face B since the vibrational transition dipole vector of the C-C$_{aromatic,2}$ stretching mode is parallel to these axes (see Supplement F).

The polarization behavior of the N-H and O-H stretching bands as well as the subtle differences in the C-C$_{aromatic}$ stretching region can be used to infer the molecular orientation within the crystals. Face A corresponds to a view along the crystallo-

Table 7.14.: Assignments of experimental band maxima in the FTIR microscopic spectra of enantiopure pseudoephedrine of face A, face B, face C (Fig. 7.36), FTIR-ATR spectra (without ATR correction, Fig. 7.2), IR-DFG Vapor Phase (Gas, Ref. [193]) as well as calculations of the relaxed monomer unit taken from the crystal structure (Mon$_{crystal}$) on the B3LYP/6-311++G(3df,2p) level. All wavenumbers are given in cm^{-1}. The stretching and bending vibrations are indicated as ν and δ and the symmetric and asymmetric vibrations with sym and asym. Tentative assignments and bands without assignment are labeled with a question mark (?).

Assignment	Face A	Face B	Face C	ATR	Gas	Mon$_{crystal}$
ν(N-H)	3319	3318	3319	3317		3539
ν(O-H)	3300–2300	3300–2300				3839
ν(C-H$_{aromatic,sym}$)	3103					3188
ν(C-H$_{aromatic,2}$)	3075				3074	3181
ν(C-H$_{aromatic,3}$)	3061					3171
ν(C-H$_{aromatic,4}$)	3055		3055	3055		3161
ν(C-H$_{aromatic,5}$)	3036		3037	3037	3038	3153
?	3022			3024		
?	3002		3001	3005		
ν(C-H$_{3,asym1}$)	2976		2977	2974	2980	3109
? ν(C-H$_{3,asym2}$)	2968?	2968?	2970			3100
? ν(NC-H$_{3,asym1}$)	2968?	2968?	2970			3091
ν(NC-H$_{3,asym2}$)	2952	2952	2952	2953		3053
ν(C-H$_{3,sym}$)	2933		2933	2931	2939	3033
?	2907		2906	2905	2914	
?	2881			2881	2886	
ν(C-H$_\alpha$)	2868		2864	2864	2856	2993
ν(C-H$_\beta$)	2837		2837	2837		2897
ν(NC-H$_{3,sym}$)	2804		2804	2802		2926
?		2779	2775			
?		2706				
?		2752				
?		2613				
?	2585					
?					2559	
ν(C-C$_{aromatic,1}$)	1601	1601	1601	1601		1642
ν(C-C$_{aromatic,2}$)		1583		1583		1622
?			1558	1558		
?			1541			
?			1506			
ν(C-C$_{aromatic,3}$)	1493	1493	1496			1528
?			1489			
δ(N-H/C-H$_3$)$_1$	1473	1473	1473	1477		1524
δ(C-H$_3$/N-H)$_3$	1464	1462	1466	1464		1491
ν(C-C$_{aromatic,4}$)	1454	1454	1456	1452		1486
δ(N-H/C-H$_3$)$_2$	1437	1437	1437			1487
?	1421	1417	1420			
?	1406					

Table 7.15.: Assignments of experimental band maxima in the FTIR microscopic spectra of enantiopure ND/OD-deuterated pseudoephedrine of face A and face B (Figs. 7.38 and 7.39). All wavenumbers are given in cm^{-1}. The stretching and bending vibrations are indicated as ν and δ and the symmetric and asymmetric vibrations with sym and asym. Tentative assignments and bands without assignment are labeled with a question mark (?).

Assignment	Face A	Face B
ν(N-H)	3319	3319
ν(O-H)	3100–2800	3200–2600
ν(C-H$_{aromatic,sym}$)	3103	3103
ν(C-H$_{aromatic,2}$)	3084	3084
ν(C-H$_{aromatic,3}$)	3062	3062
ν(C-H$_{aromatic,4}$)	3055	3057
ν(C-H$_{aromatic,5}$)	3036	
?	3022	3022
?	3003	3003
ν(C-H$_{3,asym1}$)	2976	2976
? ν(C-H$_{3,asym2}$)	2968 ?	2970
? ν(NC-H$_{3,asym1}$)	2968 ?	2970
ν(NC-H$_{3,asym2}$)	2950	2952
ν(C-H$_{3,sym}$)	2932	2931
?	2906	2906
?	2885	
?	2879	2877
ν(C-H$_\alpha$)	2868	2868
?	2854	2854
ν(C-H$_\beta$)		2842
?	2837	2837
ν(NC-H$_{3,sym}$)	2806	2806
?	2631	2631
?	2605	2605
ν(N-D)	2475	2476
2δ(N-D)	2434	2436
ν(O-D)	2500–1800	2500–1800
ν(C-C$_{aromatic,1}$)	1601	1601
ν(C-C$_{aromatic,2}$)		1585
ν(C-C$_{aromatic,3}$)	1493	1493
?	1464	1466
ν(C-C$_{aromatic,4}$)	1454	1454

graphic c axis, whereas face B can be assigned to the a axis as depicted in Fig. 7.40. Comparisons of the experimental nondeuterated and ND/OD-deuterated as well as the oriented gas model spectra are shown in Fig. 7.41. It can be seen that there is a good agreement regarding the intensity ratios of a variety of bands. There is a good match between the intensity ratios of the O-H as well as N-H stretching bands of face A and B. Also, the increase and decrease of the $C-C_{aromatic}$ stretching bands are in agreement between experiment and simulation. The region between $1500\,cm^{-1}$ and $1400\,cm^{-1}$ appears to be more complicated. There are contributions of the $C-C_{aromatic,3}$ and $C-C_{aromatic,4}$ stretching modes as well as several mixed $N-H/C-H_3$ and mixed $C-H_3/NH$ bending modes.

Further evidence for the assignment of face A to view c and face B to view a is the consistency of interactions and habit of the crystals. As can be seen in Fig. 7.40 and as described above the $O-H\cdots N$ hydrogen bonded chain runs along the crystallographic b axis and determines the growth direction. It therefore corresponds to the long crystal axis of the tabular crystals. The other growth directions are determined by $C-H\cdots O$ contacts along the a axis and by van der Waals interactions. Therefore, the crystal habit is in agreement with the assignment of the molecular orientation.

The experimental and predicted polarized spectra of the two faces can now be used to assign vibrational modes in the aliphatic C-H stretching region (see Tabs. 7.14 and 7.15). In Fig. 7.41 a tentative assignment is performed on the basis of the experimental and predicted polarization behavior. Also, the predicted wavenumbers of the methyl and N-methyl C-H stretching modes (scaled by a factor of 0.966, see Chapter 3) match the observed band positions. In the case of the α-acidic mode the relative shift is under- and in the case of the β-acidic C-H stretching mode it is overestimated as observed for pseudonorephedrine (see Sect. 7.5). This leads to a change of the sequence of the symmetric N-methyl and the β-acidic mode. In order to unravel the positions of the asymmetric1 N-methyl and the asymmetric2 methyl C-H stretching modes, further evaluations are needed. They are both preliminarily assigned to the shoulder at $2968\,cm^{-1}$. However, it is rather unlikely that both modes actually correspond to this band. The positions of the methyl and the acidic C-H stretching bands match the assignments made in the case of pseudonorephedrine.
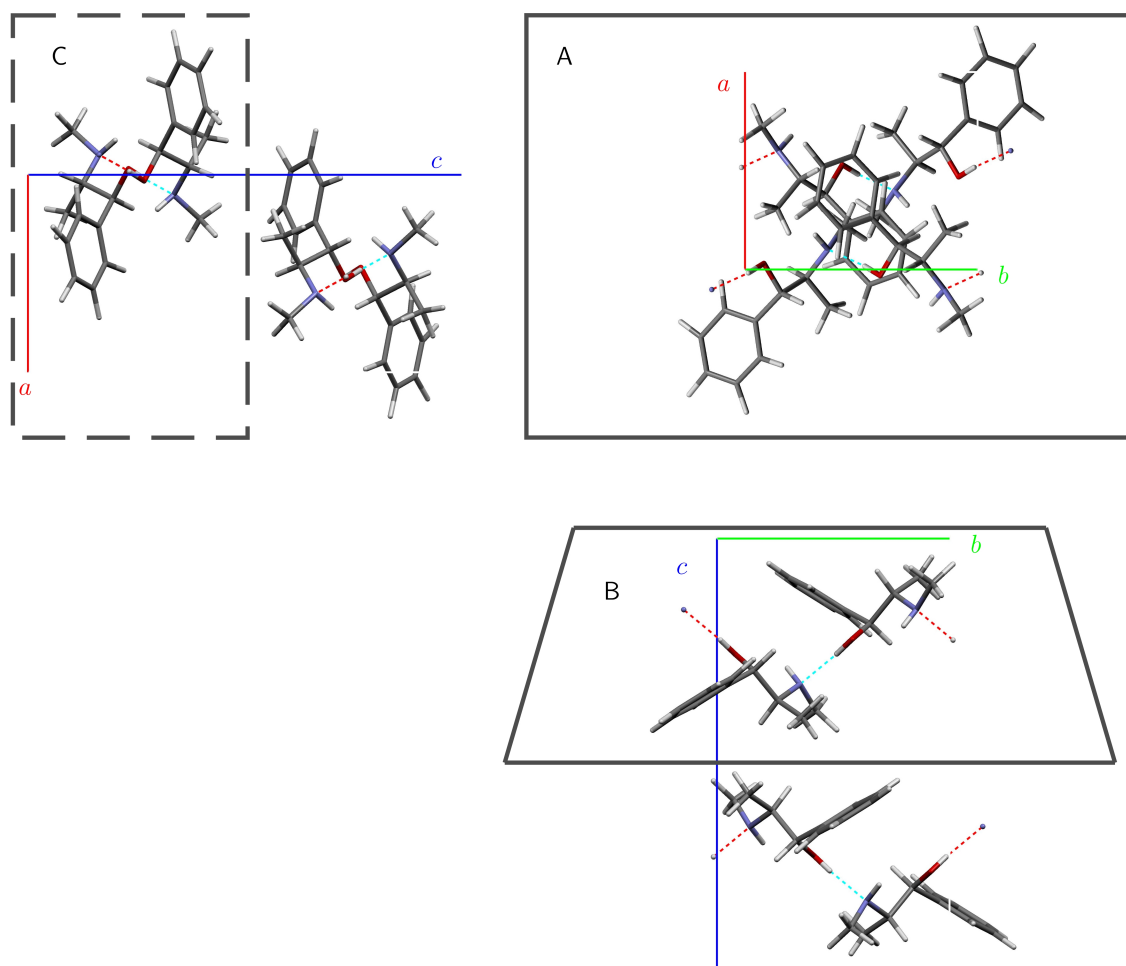
Figure 7.40.: Molecular orientation of enantiopure pseudoephedrine along the three crystal faces. The crystal structure was taken from Ref. [92]. The continuous frames mark the observed faces, whereas the unobserved face is dash-framed.
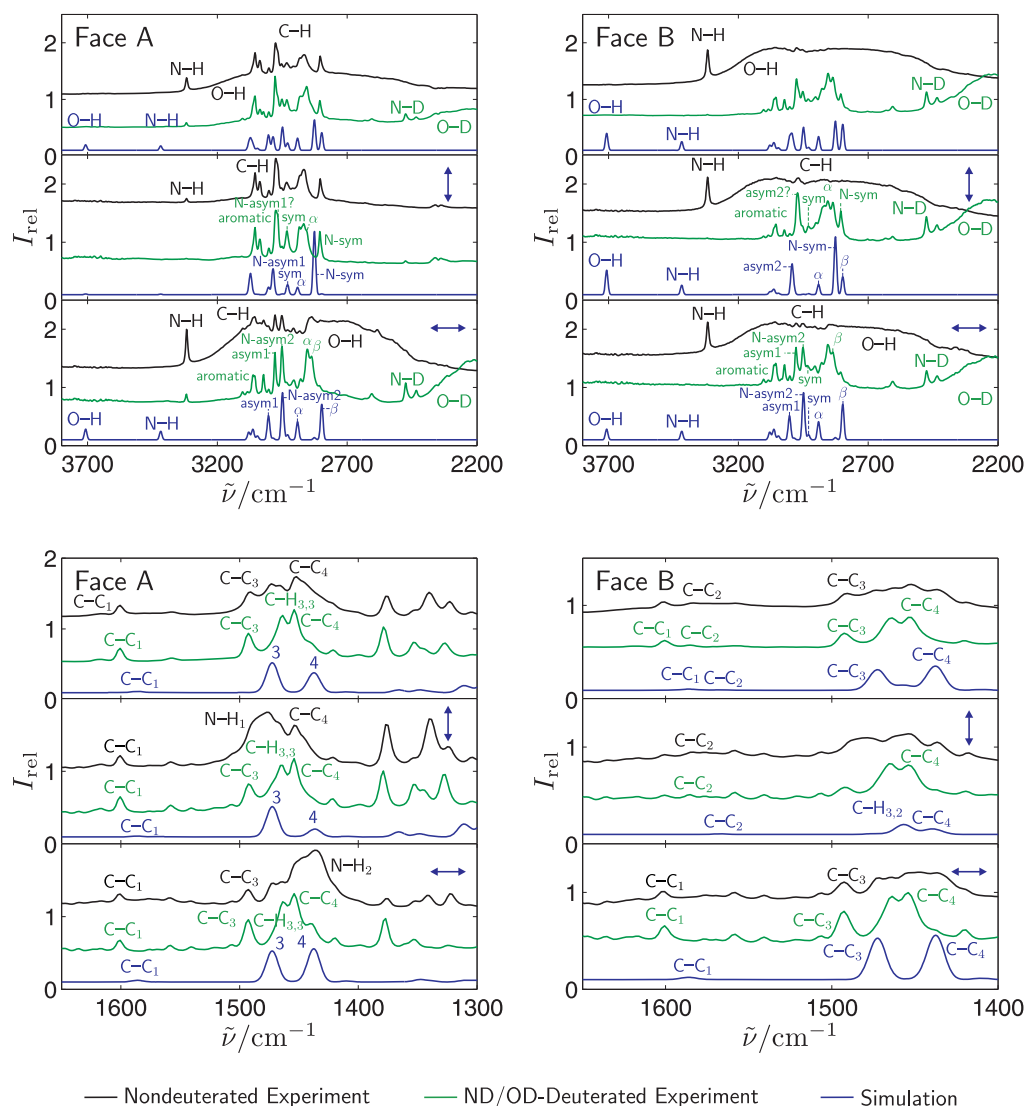
Figure 7.41.: Comparison of experimental and oriented gas model polarization spectra without deuteration (B3LYP/6-311++G(3df,2p) level) of face A (left) and face B (right) of enantiopure pseudoephedrine. The nondeuterated spectra (top, black), the ND/OD-deuterated spectra (center, green), and oriented gas model spectra (bottom, blue) are shown. Harmonic wavenumbers are scaled by a factor of 0.966 to account for anharmonicity. Assigned bands in the upper part are stretching modes. C-H stretching modes are indicated. The C-C$_{aromatic}$ stretching (abbreviated C-C$_x$), mixed N-H/C-H$_3$ bending (abbreviated N-H$_x$), mixed C-H$_3$/N-H bending (abbreviated C-H$_{3,x}$), mixed (N-H/C-H$_3$)$_1$ bending (abbreviated 3), a mixed (N-H/C-H$_3$)$_2$, and the mixed (C-H$_3$/NH)$_2$ bending modes (abbreviated 4) are shown in the lower part.

7.7.2. Racemic Pseudoephedrine

Racemic pseudoephedrine (see Fig. 7.35) is a white powder. Its melting temperature is 119°C [173]. So far, the crystal structure of racemic pseudoephedrine has not been determined.

Crystallization

In order to crystallize racemic pseudoephedrine a 1:1 mixture of (1*S*,2*S*)- and (1*R*,2*R*)-pseudoephedrine was pestled and filled into the sublimation cell. The crystallization was performed using a temperature range of 35°C to 50°C (Tab. 7.1). Platy monocrystals as well as polycrystals consisting of needles were obtained. Polarization spectra of two different faces are shown in Fig. 7.42. The spectra can be assigned to the racemic compound since the N-H stretching position of $3301/3300\,\mathrm{cm^{-1}}$ differs compared to the one of the enantiopure compound at $3319/3318\,\mathrm{cm^{-1}}$ (Fig. 7.36) showing that chirality recognition is taking place.
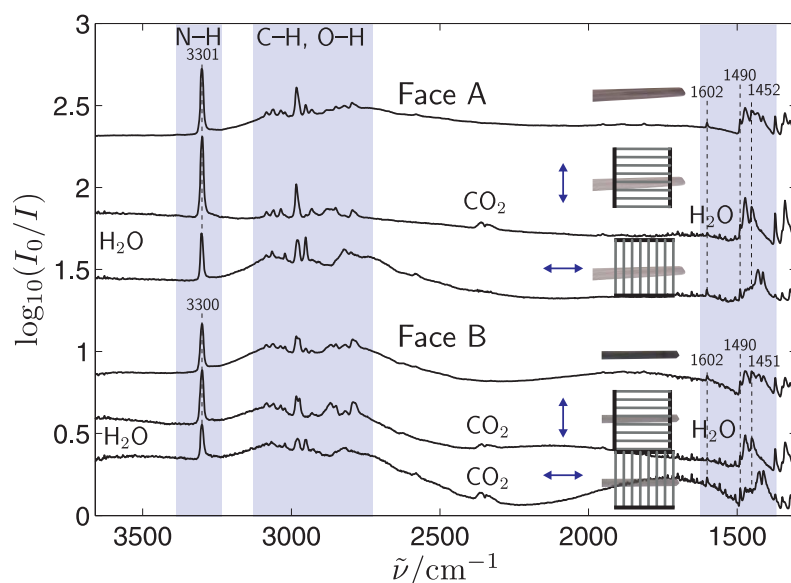
Figure 7.42.: Racemic pseudoephedrine polarization FTIR spectra of face A and face B. Spectral artifacts are caused by the needle-like habit and the small aperture. The arrows show the direction of the electric field vector. The visual pictures of the measured crystals are shown above the corresponding spectra. Band positions are given in $\mathrm{cm^{-1}}$.

Figure 7.43.: Racemic pseudoephedrine FTIR spectra of needle-like crystals. The spectrum of face A was obtained after rotation of a crystal growing on face B. The visual pictures of the measured crystals are shown above the corresponding spectra. Artifacts are caused by the needle-like habit and the small aperture.

Further comparisons of enantiopure and racemic pseudoephedrine will be made in Sect. 7.7.3.

The racemic pseudoephedrine crystals mainly grew on face A but in approximately 5% also face B was observed. In Fig. 7.43 the FTIR spectra of a crystal initially showing face A and after rotation showing face B are depicted. Fig. 7.42 shows polarized FTIR spectra of face A and B.

ND/OD-deuterated racemic pseudoephedrine was obtained from a solution of a 1:1 mixture of (1S,2S)- and (1R,2R)-pseudoephedrine in D_2O. In order to dissolve the powdered mixture the open sublimation cell was heated up to 60°C and the solution manually stirred. Afterwards, the solution was cooled down to room temperature (22-24°C). Then the sublimation cell was evacuated. During the evacuation process the racemic compound started to crystallize. Polycrystals formed from single crystals of a needle-like to platy habit were obtained. Polarization FTIR spectra are shown in Fig. 7.44. Sublimation at 40°C led to polycrystals constituted of needle-like single crystals. FTIR spectra of these sublimated ND/OD-deuterated racemic pseudoephedrine crystals show spectral similarities to the one of face A
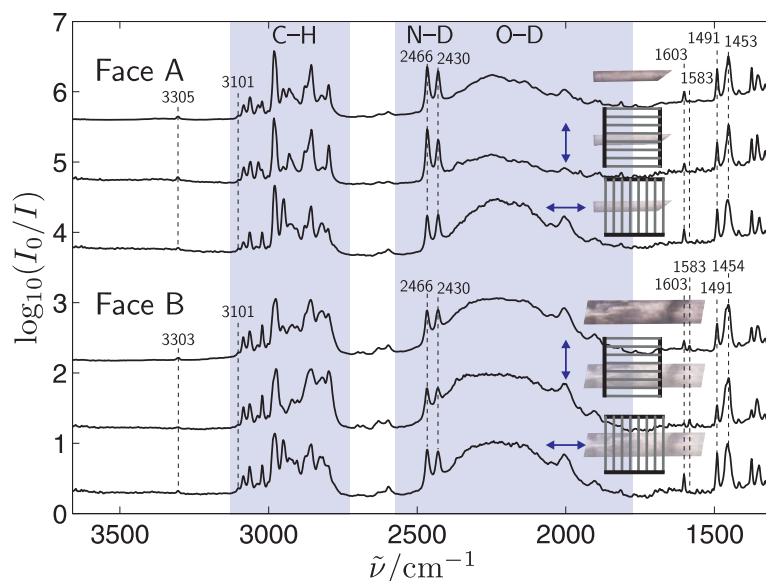
Figure 7.44.: ND/OD-deuterated racemic pseudoephedrine polarization FTIR spectra of face A and face B crystallized from a solution of D_2O. The arrows show the direction of the electric field vector. The visual pictures of the measured crystals are shown above the corresponding spectra. Band positions are given in cm^{-1}.

obtained from the solution (not depicted). Again, two N-D stretching bands and only one N-H stretching band seem to be present as it is the case in the spectra of enantiopure pseudoephedrine.

FTIR Spectra

The assignments of the experimental bands are summarized in Tabs. 7.16 and 7.17. The N-H and O-H stretching bands are assigned by comparison of the experimental and predicted wavenumbers (see also Sect. 7.3) and by their behavior upon ND/OD-deuteration. There is a Fermi-resonance of the N-D stretching fundamental with the N-D bending overtone with positions at 2466 and 2430 cm^{-1} (fundamental at 1226 cm^{-1}, not shown). The aromatic C-H and C-$C_{aromatic}$ stretching bands are assigned according to the observations made in the case of methyl mandelate, mandelic acid, and the other phenylpropanolamines in this Chapter.

The crystal structure of racemic pseudoephedrine has not been published so far. Information regarding the average molecular orientation can only be obtained by analysis of the present FTIR polarization spectra. The proposed orientations are

Table 7.16.: Assignments of experimental band maxima in the FTIR microscopic spectra of racemic pseudoephedrine of face A, face B (Fig. 7.42), and FTIR-ATR spectra (without ATR correction, Fig. 7.2). All wavenumbers are given in cm^{-1}. The stretching and bending vibrations are indicated as ν and δ and the symmetric and asymmetric vibrations with sym and asym. Tentative assignments and bands without assignment are labeled with a question mark (?).

Assignment	Face A	Face B	ATR
ν(N-H)	3301	3300	3298
ν(O-H)	3210–2620		
ν(C-H$_{aromatic,2}$)	3085	3084	3084
ν(C-H$_{aromatic,3}$)	3065	3067	3063
ν(C-H$_{aromatic,5}$)	3035	3036	3038
?	3022	3022	3022
?	3004	3006	
? ν(C-H$_{3,asym1}$)	2982	2983	
? ν(C-H$_{3,asym2}$)		2974	2972
? ν(NC-H$_{3,asym1}$)		2974	2972
? ν(NC-H$_{3,asym2}$)	2951	2951	2951
? ν(C-H$_{3,sym}$)	2931	2930	2932
?	2910		
?	2904		
?	2882		
?	2877		
? ν(C-H$_{\alpha}$)	2864	2869	2864
? ν(C-H$_{\beta}$)	2851	2850	2849
?	2822	2819	2818
? ν(NC-H$_{3,sym}$)	2795	2792	2782
?	2584		
?	2579	2580	
aromatic	1967		
aromatic	1953		
ν(C-C$_{aromatic,1}$)	1602	1602	1603
ν(C-C$_{aromatic,2}$)		1584	1584
ν(C-C$_{aromatic,3}$)	1490	1490	1491
δ(N-H/C-H$_3$)$_1$	1473	1472	1476
δ(C-H$_3$/N-H)$_3$	1465	1465	1465
ν(C-C$_{aromatic,4}$)	1452	1450	1450
δ(N-H/C-H$_3$)$_2$	1438		1433
?		1425	
?	1414	1412	1414

Table 7.17.: Assignments of experimental band maxima in the FTIR microscopic spectra of ND/OD-deuterated racemic pseudoephedrine of face A and face B (Fig. 7.44). All wavenumbers are given in cm^{-1}. The stretching and bending vibrations are indicated as ν and δ and the symmetric and asymmetric vibrations with sym and asym. Tentative assignments and bands without assignment are labeled with a question mark (?).

Assignment	Face A	Face B
ν(N-H)	3305	3303
ν(C-H$_{aromatic,sym}$)	3101	3101
ν(C-H$_{aromatic,2}$)	3084	3085
ν(C-H$_{aromatic,3}$)	3062	3064
ν(C-H$_{aromatic,5}$)	3035	3037
?	3022	3022
?	3003	3003
? ν(C-H$_{3,asym1}$)	2981	2976
? ν(C-H$_{3,asym2}$)		2976
? ν(NC-H$_{3,asym1}$)		2976
? ν(NC-H$_{3,asym2}$)	2950	2952
? ν(C-H$_{3,sym}$)	2931	2931
?		2921
?		2904
?	2877	
? ν(C-H$_\alpha$)	2856	2858
? ν(C-H$_\beta$)	2856	2858
?	2822	2820
? ν(NC-H$_{3,sym}$)	2798	2798
?		2700
?		2682
?	2628	2630
?	2605	2605
?	2598	2598
ν(N-D)	2466	2466
2δ(N-D)	2430	2430
ν(O-D)	2500–1800	2500–1800
ν(C-C$_{aromatic,1}$)	1603	1603
ν(C-C$_{aromatic,2}$)	1583	1583
ν(C-C$_{aromatic,3}$)	1491	1491
ν(C-C$_{aromatic,4}$)	1453	1454
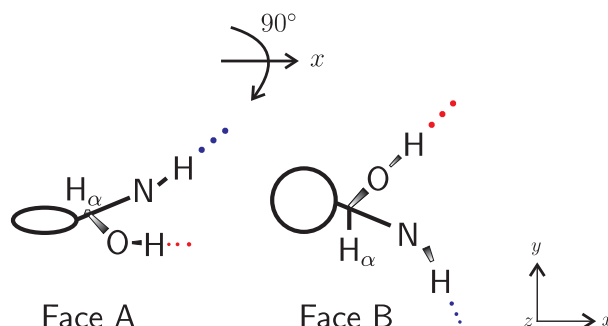
Figure 7.45.: Schematic layout of a pseudoephedrine molecule oriented according to face A and B. Note, that this simplistic view does not reflect the dimensionality correctly and that it does not include all functional groups.

depicted in Fig. 7.45. Note, that it is only a simplistic scheme which does not reflect the dimensionality correctly and which does not include all functional groups.

The N-H stretching band at $3301/3300\,\mathrm{cm}^{-1}$ is more red shifted than the ones of ephedrine anhydrate at $3313\,\mathrm{cm}^{-1}$ and of enantiopure pseudoephedrine at $3319/3318\,\mathrm{cm}^{-1}$ which do not form intermolecular N-H hydrogen bonds within the crystal structure (see Sect. 7.7.1). The position of the N-H stretching band of racemic pseudoephedrine is closer to the N-H stretching band of ephedrine hemihydrate at $3296\,\mathrm{cm}^{-1}$ which does form N-H$\cdots$O hydrogen bonds. The N-H stretching band of racemic pseudoephedrine is also more intense than the one of enantiopure pseudoephedrine (see Fig. 7.2). Therefore, it can be assumed that N-H hydrogen bonds, which are stronger than in the enantiopure case, are formed in the crystal structure of racemic pseudoephedrine.

The O-H and N-H stretching bands appear for both faces which is in contrast to the needle-like habit but in agreement with the platy habit. The O-H stretching band is slightly more intense and broader for face B. In the case of a vertical polarization of face A it almost vanishes. In contrast, the N-H stretching band is slightly more intense in the case of face A spectra. It decreases in intensity in the case of a horizontal polarization of face A. Therefore, a nearly horizontal alignment of the O-H hydrogen bonds and a rather vertical alignment with good visibility can be assumed for the N-H hydrogen bonds of face A. There is a good visibility of the horizontally oriented O-H hydrogen bond and a more diagonal alignment of the N-H hydrogen bond in the orientation of face B.

The quality of the nondeuterated spectra in the lower wavenumber region is poor

due to the needle-like habit and a small aperture. Nonetheless, the comparison to the ND/OD-deuterated spectra shows the influence of mixed N-H/C-H$_3$ bending modes between $1500\,\text{cm}^{-1}$ and $1350\,\text{cm}^{-1}$. The mixed modes appear at higher wavenumber for a vertical polarization and at lower wavenumber in the case of a horizontal polarization of both face A and B. The behavior of the C-C$_{\text{aromatic}}$ stretching bands is most pronounced in the ND/OD-deuterated spectra. The C-C$_{\text{aromatic},1}$ stretching band at $1602\,\text{cm}^{-1}$ appears in all spectra but the vertically polarized one of face B (see Fig. 7.44). In this case the C-C$_{\text{aromatic},2}$ stretching band at $1584\,\text{cm}^{-1}$ is present. The C-C$_{\text{aromatic},3}$ and C-C$_{\text{aromatic},4}$ bands appear in all spectra. Thus, the C-C stem is diagonally aligned with the phenyl ring being turned within the orientation of face A. In the case of face B the plane of the phenyl ring is visible and the C-C stem horizontally aligned. These conclusions are supported by the presence of the symmetric aromatic C-H stretching modes in all spectra except the vertically polarized spectrum of face B.

The proposed orientations in Fig. 7.45 may be converted into each other by a $90°$ rotation around the *y*-axis. There are some deviations which are only minor. All in all, the conclusions are in agreement with each other. A diagonally bisected crystal might exhibit a more pronounced polarization behavior of the C-C$_{\text{aromatic}}$ stretching bands. Therefore, it might reveal further information regarding the molecular orientation within the racemic pseudoephedrine crystal.

7.7.3. Comparison of Enantiopure and Racemic Pseudoephedrine

Sublimated crystals of pseudoephedrine show effects of chirality recognition. They are most pronounced in the position and intensity of the N-H stretching band (see Tabs. 7.14 and 7.16 as well as Figs. 7.2 and 7.46). It is red shifted by $18\,\mathrm{cm^{-1}}$ from $3319\,\mathrm{cm^{-1}}$ to $3301\,\mathrm{cm^{-1}}$ for the racemic compound. For comparison, the position of the N-H stretching band of anhydrous ephedrine is $3313\,\mathrm{cm^{-1}}$ and $3296\,\mathrm{cm^{-1}}$ for ephedrine hemihydrate. This rather large shift points at different hydrogen contacts of the NH group. Probably, the red shift results from shorter and stronger N-H$\cdots$O hydrogen contacts in the crystal structure of racemic pseudoephedrine as assumed in Sect. 7.7.2. Further differences are apparent in the case of the O-H stretching band and in the region of the mixed N-H/C-H and C-H/N-H bending modes. The bands of the enantiopure compound are more red shifted. It can be assumed that the O-H hydrogen bonds are stronger within the enantiopure crystals. In the racemic crystals a weakening of the O-H hydrogen bonds seems to occur in order to establish stronger N-H contacts.

Different ratios of (1*S*,2*S*)- and (1*R*,2*R*)-pseudoephedrine (1:1, 2:1, 3:1, and 9:1) were sublimated and investigated by FTIR imaging in order to observe the influence of the enantiomeric ratio on chirality recognition. The mixtures were pestled and filled into the sublimation cell. The crystallization was performed using a temperature range of $35°$C to $50°$C (Tab. 7.1). FTIR images were recorded to differentiate between the enantiopure and the racemic compound. The N-H stretching regions of 3335–$3310\,\mathrm{cm^{-1}}$ (Enant) and 3310–$3290\,\mathrm{cm^{-1}}$ (Rac) were integrated. Afterwards the integrated area of Enant was subtracted from Rac (Rac−Enant). Fig. 7.47 shows visual pictures as well as FTIR images of the obtained crystals.

In the case of a 1:1 ratio block-like/platy as well as needle-like racemic crystals were obtained. Using a 2:1 ratio led to a polycrystal consisting of racemic needles. In the case of a 3:1 ratio both the enantiopure as well as the racemic compound were sublimated. The polycrystal consists of both compounds and has an undefined habit. Nonetheless, the enantiopure and the racemic compound can be visually distinguished. The enantiopure compound consists of thick, blocky crystals whereas racemic pseudoephedrine crystallizes in the form of needles. In the case of a 9:1 ratio the undefined polycrystal solely consists of the enantiopure compound.

In summary, mixtures of (1*S*,2*S*)- and (1*R*,2*R*)-pseudoephedrine show significant
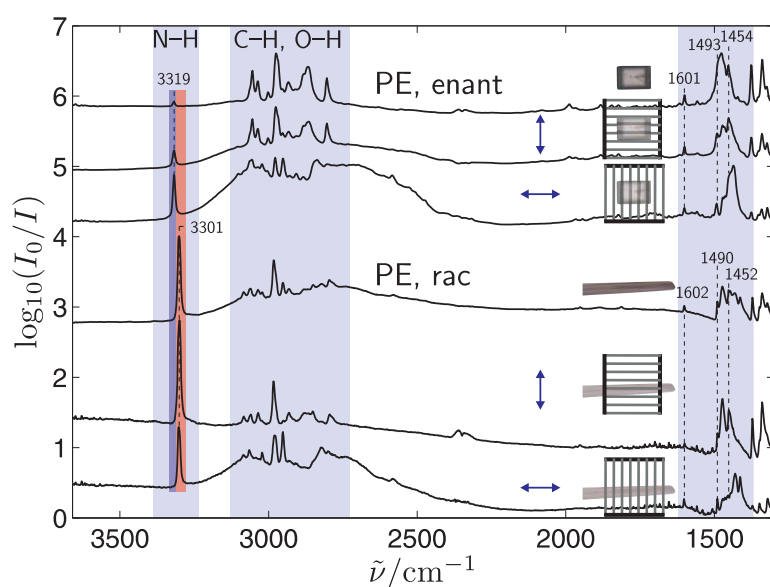
Figure 7.46.: Enantiopure and racemic pseudoephedrine polarization FTIR spectra. The arrows show the direction of the electric field vector. The visual pictures of the measured crystals are shown abov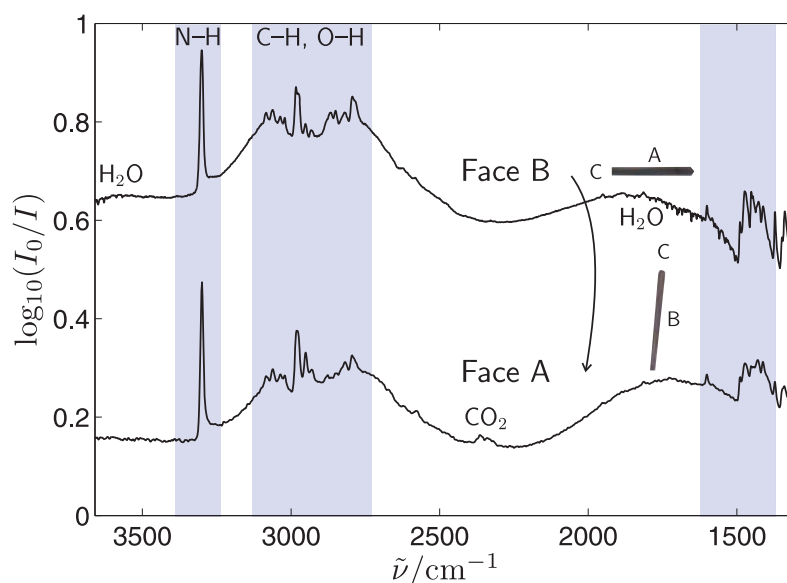e the corresponding spectra. Band positions are given in cm^{-1}. Regions Enant and Rac used for integration are marked in blue and red, respectively.
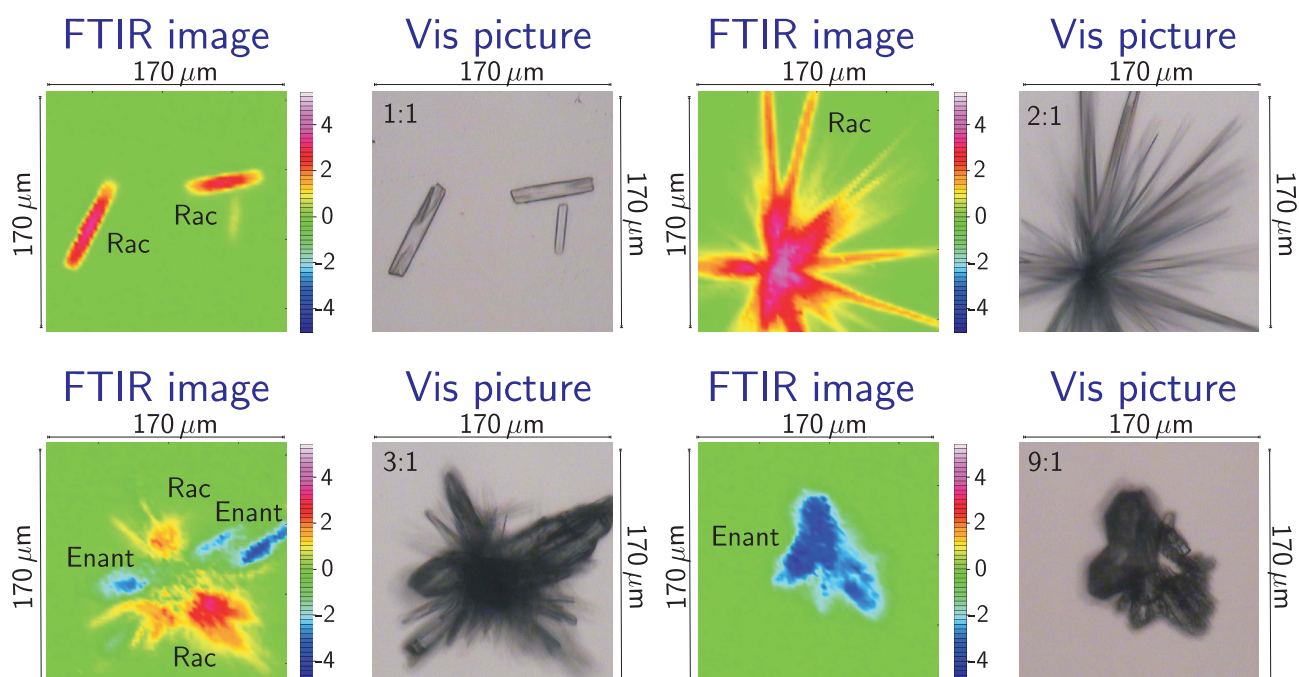
Figure 7.47.: Chemical images of pseudoephedrine crystals. Different ratios (see upper left corners) of the two enantiopure substances were used. Red colors show the racemic compound. Blue colors show the enantiopure compound.

indication of chirality recognition phenomena. 1:1 and 2:1 mixtures lead to racemic crystals, while at more dissimilar ratios predominantly the enantiopure compound was obtained. A tendency of racemic crystals to grow at slightly higher temperatures was observed. This would lead to the conclusion that the enantiopure crystals are more stable than racemic pseudoephedrine. However, a negative Gibbs free energy ($\Delta G = -0.55\,\text{kcal·mol}^{-1}$) was determined for the formation of the racemate from opposite enantiomers in the solid state by X-ray powder diffraction [173]. This rather points at a higher stability of the racemate. The slightly higher sublimation temperatures may be influenced by other parameters e.g., pressure and ambient temperature or by kinetic factors. The measurement of the relative vapor pressure via mass spectrometry as performed in the methyl mandelate case can shed further light into this question.

7.8. Spectral Comparisons

A variety of vibrational modes are assigned in the spectra of the sublimated phenyl-propanolamines in this Chapter. In this Section, the spectral positions of analogous modes will be compared and analyzed on the basis of the interactions within the crystal structures, the different monomer conformations (Sect. 7.2), and the preliminary spectral considerations made in Sect. 7.3.

O-H/O-D Stretch

Broad and red shifted O-H stretching bands resulting from O-H$\cdots$N hydrogen bonds are found for all of the investigated phenylpropanolamines in the region of 3300–$2300\,\mathrm{cm}^{-1}$. The O-D stretching bands appear in the region of 2600–$1800\,\mathrm{cm}^{-1}$ and exhibit a structure which may result from symmetric and asymmetric couplings or from two quantum excitations. Since the O-H stretching bands are red shifted into the region of the C-H stretching bands, unambiguous information about the band structuring is difficult to obtain.

The largest red shift and broadening is found for enantiopure pseudoephedrine and the smallest red shift and broadening in the case of pseudonorephedrine (Fig. 7.2). As summarized in Tab. 7.18, the O-H$\cdots$N hydrogen bonds in enantiopure pseudoephedrine are mostly isolated whereas in pseudonorephedrine cooperatively strengthened infinite chains of hydrogen bonds are found. Thus, one would expect stronger O-H$\cdots$N hydrogen bonds in the case of pseudonorephedrine [130, 192], which is in conflict with the observed red shifts.

Table 7.18.: Hydrogen bonds of the OH and NH group formed as a donor (D) and acceptor (A) as well as cooperative patterns involving infinite chains (coop$_\infty$), the cooperativity between two hydrogen bonds (coop$_2$), and anti-cooperativity (a-coop) in some phenylpropanolamines.

	OH			NH		
NE, rac	N-H$\cdots$O-H$\cdots$N	DA	coop$_\infty$	O-H$\cdots$N-H$\cdots$O	DA	coop$_\infty$
PNE	N-H$\cdots$O-H$\cdots$N	DA	coop$_\infty$	O-H$\cdots$N-H$\cdots$O	DA	coop$_\infty$
E-AH	C-H$\cdots$O-H$\cdots$N	D(A)		O-H$\cdots$N-H	A	
E-H	O-H$_{\mathrm{water}}\cdots$O-H$\cdots$N	DA	coop$_2$	O-H$\cdots$N-H$\cdots$O$_{\mathrm{water}}\cdots$H-N	DA	a-coop
PE, enant	C-H$\cdots$O-H$\cdots$N	D(A)		O-H$\cdots$N-H	A	

Table 7.19.: Experimental crystal $\tilde{\nu}_{\text{cryst}}$ and predicted monomer positions ω_{mon} (B3LYP/6-311++G(3df,2p)) in cm^{-1} of conformations corresponding to the conformations found in the crystals (Fig. 7.3) ordered in the sequence of the O-H stretching bands (smallest to largest) as observed in the experimental crystal spectra. The experimental crystal wavenumbers have an error of $\pm 50\,cm^{-1}$.

	Conformation	$\tilde{\nu}_{\text{cryst}}$	ω_{mon}
PNE	AG	≈ 2980	3839
E-AH	AG(a)'	≈ 2950	3842
NE, rac	GG	≈ 2900	3831
PE, enant	AG(b)	≈ 2840	3838
E-H	AG(b)	≈ 2720	3733

The experimental O-H stretching band sequence in the crystal spectra deviates from the sequence of the predicted monomers of conformations corresponding to the structures in the crystal (Tab. 7.19). Therefore, the sequence of the O-H stretching bands cannot solely be explained by conformational differences but by other interactions formed upon crystal aggregation which compete with cooperativity on the hydrogen bond strengths. This is in agreement with the sublimation temperatures of enantiopure pseudoephedrine and pseudonorephedrine being in the same order (Tab. 7.1) and with the H-N and O-N distances of the hydrogen bond being smaller in the isolated case of pseudoephedrine (Tab. 7.2). There may be local reasons, such as the geometrical availability of the free electrons of nitrogen, or more global effects, such as dipole interactions leading to cohesion or packing forces in the crystal structure. Further investigations are needed in order to specify the forces. Probably, a variety of different interactions competing with each other are present.

The O-H stretching band pattern of water in the ephedrine hemihydrate spectra at 3630–3330 cm^{-1} is less red shifted and less broadened than the alcoholic O-H stretching bands of the investigated phenylpropanolamines (Fig. 7.2). This is in agreement with the formation of less stable O-H$\cdots$O instead of O-H$\cdots$N hydrogen bonds. The O-H stretching band shows polarization dependent high and low frequency contributions of asymmetric and symmetric modes.

N-H Stretch

Asymmetric and symmetric N-H stretching modes of the primary amines as well as localized N-H stretching modes of partly deuterated primary and nondeuterated secondary amines are assigned in the region of 3360–3270 cm^{-1}. In the case of the primary amines norephedrine (enantiopure and racemic) and pseudonorephedrine a Fermi-resonance of the symmetric N-H stretching fundamental with the N-H bending overtone is found. Ephedrine hemihydrate shows a coupling of the NH groups of two ephedrine molecules leading to an asymmetric and a symmetric N-H stretching band. The N-D stretching bands appear in the spectral region of 2503–2370 cm^{-1}. A Fermi-resonance takes place between the N-D stretching fundamental and the N-D bending overtone in the case of enantiopure and racemic pseudoephedrine.

The N-H stretching bands in the crystal spectra are intensified and red shifted compared to the predicted monomer modes of corresponding conformations but less so than the O-H stretching bands (Supplement F). The intensification of the N-H stretching bands is larger for the more red shifted N-H stretching bands (Fig. 7.2) and thus in agreement with the presence of stronger hydrogen bonds. In the case of the primary amines especially the intensity of the symmetric, or more properly bonded N-H stretch increases with increasing red shift. This is also true for the symmetric N-D stretching bands (Figs. 7.11, 7.17, and 7.24) and in agreement with the predictions (Tab. 7.5).

There is a red shift and intensification of the experimental crystal N-H stretching bands compared to the predicted monomer N-H stretching modes of corresponding conformations which cannot solely be explained by the formation of hydrogen bonds. In the following, the shifts caused by other effects than hydrogen bonds will be estimated. Tab. 7.20 lists the difference between experimental and predicted N-H stretching wavenumbers (average of the asymmetric and symmetric stretch for nonmethylated amines) of ethylamine and ephedrine monomers in the gas phase [82, 195]. The difference between the experimental and the predicted values of -154 cm^{-1} and -165 cm^{-1} reflects the error of the method e.g., anharmonicity. Therefore, a correction shift of -160 cm^{-1} (mean value) is applied on the predicted wavenumbers of the investigated phenylpropanolamines. Their experimental and predicted wavenumbers (uncorrected and corrected) as well as the differences and ratios between the experimental and the corrected predicted wavenumbers are also given in Tab. 7.20. In the case of the primary amines also the average

wavenumber of the asymmetric and the symmetric N-H stretching modes are listed. Deperturbed positions $\tilde{\nu}_0(A)$ (without Fermi-resonance) are estimated from the observed bands $\tilde{\nu}(A)$ and $\tilde{\nu}(B)$ by the following equation [196]:

$$\tilde{\nu}_0(A) = \frac{\tilde{\nu}(A) + \tilde{\nu}(B)}{2} + \frac{\Delta\tilde{\nu}_0}{2} = \frac{\tilde{\nu}(A) + \tilde{\nu}(B)}{2} + \frac{\Delta\tilde{\nu}}{2} \cdot \frac{R - 1}{R + 1} \qquad (7.1)$$

with B being the less intense band at lower wavenumber. $\Delta\tilde{\nu}_0$ and $\Delta\tilde{\nu}$ are the deperturbed and the observed (perturbed) wavenumber differences of $A - B$ and R is the ratio of the integrated intensities $\frac{I(A)}{I(B)}$ of the two modes.

The deviations of -43 to $-78\,\text{cm}^{-1}$ reflected in ratios of 0.987–0.977 between experimental crystal and corrected predicted monomer wavenumbers illustrate the divergence between experiment and prediction after accounting for anharmonicity. They result from intermolecular interactions upon aggregation which are not considered in monomer calculations. The divergence is the largest for racemic norephedrine and pseudonorephedrine (-56 to $-78\,\text{cm}^{-1}$) in which the amine group simultaneously acts as a hydrogen bond donor and acceptor and cooperative hydrogen bonds are established (Tab. 7.18). The deperturbed symmetric (bonded) and the asymmetric (free) N-H stretching modes show a similar red shift (70–75 cm^{-1}). A red shift of $32\,\text{cm}^{-1}$ is predicted for both N-H stretching modes of the methanol-ethylamine-dimethylether complex (Sect. 7.3) which serves as a model case for the influence of O-H$\cdots$N-H$\cdots$O hydrogen bonds. Accounting for the predicted red shift of an amine group acting as a hydrogen bond donor and acceptor still leaves a divergence between experiment and prediction of -38 to $-43\,\text{cm}^{-1}$ for the deperturbed symmetric and the asymmetric mode for norephedrine and pseudonorephedrine.

In the case of ephedrine anhydrate and enantiopure pseudoephedrine the divergence is -58 to $-60\,\text{cm}^{-1}$. Here, the NH group only acts as a hydrogen bond acceptor. For the methylethylamine-methanol complexes, in which the amine group is the hydrogen bond acceptor, a red shift of 13–20 cm^{-1} is predicted. The divergence between experiment and predictions can thus be corrected to a value of -38 to $-47\,\text{cm}^{-1}$.

The smallest divergence is found for the symmetric N-H stretch of ephedrine hemihydrate. Here, the N-H$\cdots$O hydrogen bonds are anti-cooperative and therefore, the N-H stretching band is less red shifted (43 cm^{-1}) compared to the predictions. As discussed in Sect. 7.3, the low lying predicted wavenumber of ephedrine

Table 7.20.: Experimental gas phase $\tilde{\nu}$ and predicted N-H stretching wavenumbers ω of the ethylamine (EA) and the most stable ephedrine monomer (E AG(a)) [82, 195] on the B3LYP/6-311++G(3df,2p) level as well as the difference $\Delta(\tilde{\nu} - \omega)$ in cm^{-1}. Experimental crystal $\tilde{\nu}$, predicted ω (B3LYP/6-311++G(3df,2p)), and predicted N-H stretching wavenumbers corrected by -160 cm^{-1} ω_{corr} as well as the difference between the experimental and predicted wavenumbers $\Delta(\tilde{\nu} - \omega_{\text{corr}})$, the corrected difference between the experimental and predicted wavenumbers $\Delta(\tilde{\nu} - \omega_{\text{corr}})_{\text{corr}}$ in cm^{-1} and the ratio $\frac{\tilde{\nu}}{\omega_{\text{corr}}}$ are listed. An average of the asymmetric and the symmetric N-H stretching wavenumbers (av) of the primary phenylpropanolamines and in some cases deperturbed N-H stretching positions (0) are given.

	$\tilde{\nu}$	ω	$\Delta(\tilde{\nu} - \omega)$		
EA	3379	3533	-154		
E AG(a)	3378	3543	-165		

	$\tilde{\nu}$	ω	ω_{corr}	$\Delta(\tilde{\nu} - \omega_{\text{corr}})$	$\frac{\tilde{\nu}}{\omega_{\text{corr}}}$	$\Delta(\tilde{\nu} - \omega_{\text{corr}})_{\text{corr}}$
NE, rac - asym	3332	3567	3407	-75	0.978	-43
NE, rac - sym	3273	3489	3329	-56	0.983	-24
NE, rac - sym, 0	3259	3489	3329	-70	0.979	-38
NE, rac - av	3303	3528	3368	-65	0.981	-33
NE, rac - av, 0	3296	3528	3368	-72	0.979	-40
PNE - asym	3354	3586	3426	-72	0.979	-40
PNE - sym	3289	3507	3347	-58	0.983	-26
PNE - sym, 0	3269	3507	3347	-78	0.977	-46
PNE, av	3322	3547	3387	-65	0.981	-33
PNE, av, 0	3312	3547	3387	-75	0.978	-43
E-AH	3313	3531	3371	-58	0.983	$-(38\text{--}45)$
E-H, sym	3296	3498	3338	-43	0.987	-43
E-H, asym	3261	3498	3338	-77	0.977	-77
E-H, av	3279	3498	3338	-59	0.982	-59
PE, enant	3319	3539	3379	-60	0.982	$-(40\text{--}47)$

hemihydrate is a result of O-H$\cdots$(H)N dipole interactions. The resulting red shift of $20\,\text{cm}^{-1}$ (Tab. 7.6) might be overestimated by the quantum chemical calculations and therefore, the monomer prediction of the wavenumber too low in comparison to the other parameters and the other N-H stretching predictions in general. However, the deviation increases to $-59\,\text{cm}^{-1}$ for the average of the asymmetric and the symmetric N-H stretching mode. It is then in the same order as the deviations of the other phenylpropanolamines.

Summing up, the corrected red shifts of deperturbed experimental N-H stretching modes compared to the corrected predictions of corresponding modes are in the range of $-(38\text{--}59)\,\text{cm}^{-1}$ (Tab. 7.20). The corrected differences may be caused by local effects, such as aromatic interactions which do not take place in the monomer (experiment and prediction) or by global effects, such as packing forces (see above). Packing constraints are known to cause a red shift as found for the *n*-propanol O-H stretching band in a crystalline argon matrix compared to the gas phase [197].

N-D Stretch

The N-D stretching bands are further red shifted than the N-H stretching positions, as expected. Tab. 7.21 summarizes the experimental and predicted positions of the N-H and N-D stretching modes and the ratios of the N-H and N-D stretching wavenumbers. The observed ratio of 1.339–1.381 shows deviations to both sides of the harmonically approximated ratio of 1.369 ($\sqrt{\frac{\mu_\text{D}}{\mu_\text{H}}}$). Larger ratios are observed for the symmetric N-H stretching modes (perturbed and deperturbed) of enantiopure and racemic norephedrine. The deviations to the harmonic approximation can be explained by anharmonicity which was found to increase for larger aggregates in the case of the methanol O-H stretching mode [129]. The ratios deviate less for the bonded than the free vibrations. This is surprising since anharmonicity can be expected to increase upon hydrogen bonding [198–200].

The experimental ratios of the N-H and N-D stretching wavenumbers are smaller than the predicted ones (Tab. 7.21). They only deviate by 1–2% with exception of the perturbed symmetric stretch of racemic norephedrine (0.3%). Assuming that the deviations should be in the same order, it is probably due to the Fermi-resonance.

In the spectra of partly deuterated norephedrine (enantiopure and racemic) and pseudonorephedrine also localized N-H and N-D stretching bands are assigned (Tab. 7.21). In all cases the bonded localized N-H and N-D modes are observed.

Table 7.21.: Experimental $\tilde{\nu}$ and predicted N-H and N-D stretching wavenumbers ω (B3LYP/6-311++G(3df,2p)) of the nondeuterated and deuterated phenylpropanolamines in cm^{-1} as well as the ratio of the N-H and N-D positions of corresponding modes. Deperturbed symmetric N-H and N-D stretching positions (0) are given as well.

	$\tilde{\nu}_{N-H}$	$\tilde{\nu}_{N-D}$	$\frac{\tilde{\nu}_{N-H}}{\tilde{\nu}_{N-D}}$	ω_{N-H}	ω_{N-D}	$\frac{\omega_{N-H}}{\omega_{N-D}}$
NE, enant - asym	3338	2490	1.341			
NE, enant - sym	3271	2376	1.377			
NE, enant - sym, 0	3256	2376	1.370			
NE, enant - localized, bonded	3273	2416	1.355			
NE, rac - asym	3332	2486	1.340	3567	2628	1.357
NE, rac - sym	3273	2370	1.381	3490	2521	1.384
NE, rac - sym, 0	3259	2370	1.375	3490	2521	1.384
NE, rac - localized, bonded	3278	2422	1.353			
PNE, enant - asym	3355	2503	1.340	3586	2644	1.356
PNE, enant - sym	3289	2419	1.360	3507	2534	1.384
PNE, enant - sym, 0	3269	2419	1.351	3507	2534	1.384
PNE, enant - localized, bonded	3307	2443	1.354			
PNE, enant - localized, free	3336					
E-AH, enant	3313			3531	2582	1.368
E-H, enant, sym	3296			3498		
E-H, enant, asym	3261			3498		
PE, enant	3319	2475	1.341	3538	2587	1.368
PE, enant, 0	3319	2464	1.347	3538	2587	1.368
PE, rac	3301	2466	1.339			
PE, rac, 0	3301	2451	1.347			
Harmonic prediction			1.369			1.369

This is in agreement with the predicted intensity enhancement of the bonded in contrast to the free mode of the partly deuterated ethylamine-dimethylether complex as visualized for the ethylamine-dimethylether predictions in Fig. 7.48 (see also Tab. 7.5).

In the spectra of partly deuterated pseudonorephedrine also the free N-H stretching mode is assigned. The analogous free N-D stretching mode which is predicted to have a similar intensity as the free N-H stretching mode does not appear. The appearance of the free N-H stretching band in the partly deuterated spectra of pseudonorephedrine can be explained by two arguments. First, the free (dangling) deuterium is preferentially exchanged by humidity. Thus, the free N-D stretching mode is depleted first and the free N-H stretching mode emerges preferentially (kinetic exchange argument). Accordingly, if the nondeuterated substance is sublimated in a D_2O atmosphere the free N-D stretching mode should arise from a kinetic point of view (not performed). Secondly, deuterium is the better hydrogen bond donor and N-D$\cdots$O hydrogen bonds are preferentially established because of the reduced zero point energy destabilization of the librational modes [201, 202]. Therefore, the free N-H stretching band is more likely to appear in the spectra of partly deuterated primary amines than the free N-D stretching mode (no matter if a deuterium-hydrogen or a hydrogen-deuterium exchange takes place). The intensity increase of the free N-H and the intensity decrease of the free N-D stretching mode are indicated by gray arrows in Fig. 7.48.

Next to O-H and N-H stretching also N-H bending bands are assigned by comparison of nondeuterated and ND/OD-deuterated spectra as well as by comparison of experiment and prediction. The N-H bend of the primary amines appears at higher wavenumbers than the mixed modes of the secondary amines, in agreement with the predictions (Tab. 7.7). The assignments of the localized bending modes are confirmed by their polarization behavior in the experimental and oriented gas model spectra. In the case of the secondary amines the comparison of experimental and oriented gas model spectra is not reliable since the vibrational dipole vector changes unpredictably upon hydrogen bonding (Sect. 7.3). The N-H bending overtones are found to couple with the symmetric N-H stretching fundamentals in the case of the primary amines (see above).

The aromatic C-H and the C-C$_{aromatic}$ stretching modes appear at similar positions for all investigated phenylpropanolamines as well as methyl mandelate and mandelic acid. It can be assumed that this is also true for other structurally simi-
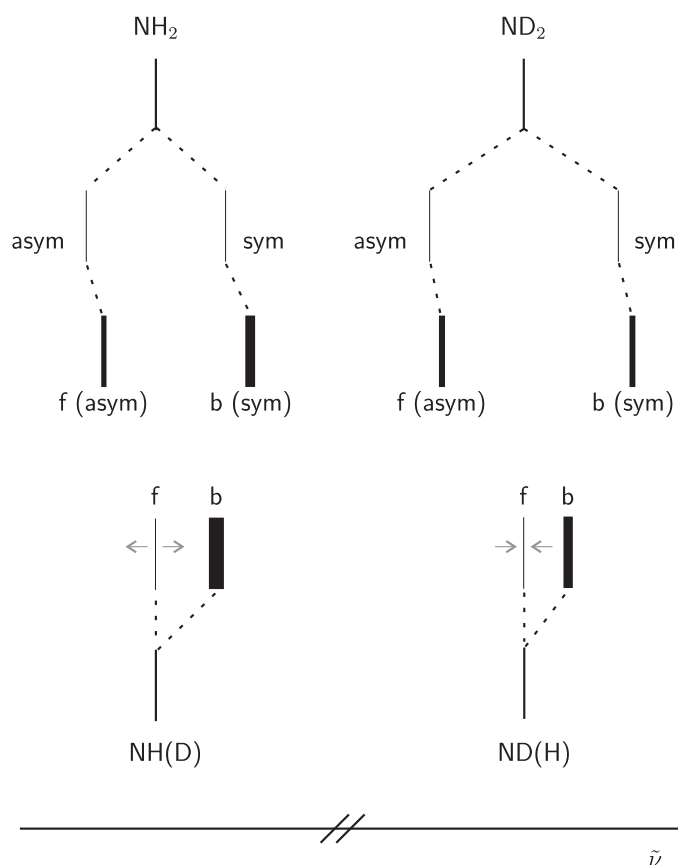
Figure 7.48.: Splitting of the N-H and N-D stretching modes of the nondeuter-ated, fully ND-deuterated, and partly ND-deuterated ethylamine-dimethylether complex. Asym and sym label the asymmetric and symmetric modes and f and b the free and bonded modes. The split-tings and the intensities (thickness of bars) reflect the predictions of the methylamine-dimethylether complex (Sect. 7.3). The arrows (widening and narrowing of the bars) indicate the intensity increase and decrease of the free modes upon an asymmetric isotope exchange.

lar substances. Furthermore, the polarization behavior of the symmetric aromatic C-H and the C-C$_{aromatic}$ stretching mode are reliable indicators of the phenyl and the α-acidic CH group and can be used to infer the molecular orientation.

7.9. Conclusions

The polarized FTIR microspectroscopic method was applied to the phenyl-propanolamines norephedrine, pseudonorephedrine, ephedrine, and pseudoephedrine. Chirality recognition was observed for norephedrine and pseudoephedrine crystals. An anhydrate and a hydrate were obtained in the case of ephedrine. It was shown that for sublimated crystals the main direction of growth is determined by the direction of hydrogen bonds. As expected, the strongest interaction determines the direction of growth unlike for crystals obtained from a solution.

It was shown that the O-H stretching red shifts cannot be explained by cooperativity and that therefore competing interactions influence the hydrogen bond strengths. Localized and coupled as well as free and bonded N-H and N-D stretching bands were assigned based on isotope studies and predictions. Also, several localized and mixed N-H stretching and bending modes were assigned. In some cases, the bending overtone was found to couple with the stretching fundamental. Red shifts were explained by different N-H hydrogen contacts as well as by conformational differences. The assignment of the aliphatic C-H stretching bands was difficult and is only preliminary. ND/OD deuteration studies of ephedrine anhydrate and hemihydrate would be helpful for a more confident assignment.

The molecular orientations were inferred on the basis of the experimental and predicted polarization behavior and compared to the crystal structures where available. The polarization behavior of the hydrogen bonded stretching, the symmetric aromatic C-H stretching, and the C-C$_{arom}$ stretching bands were found to be helpful indicators in some cases. A tentative average conformation of the molecules in the unit cell was deduced for enantiopure norephedrine and for racemic pseudoephedrine since the crystal structures are not solved yet.

8. Summary & Outlook

Adaptive aggregation and chirality recognition of sublimated microcrystals were the subjects of this dissertation. The phenomenon of adaptive aggregation was exemplified on the simple model case of the ethanol-water dimer investigated by a combined Raman- and FTIR-jet study. Ethanol was found to exhibit a gauche conformation upon complexation by water because that allows the water to establish a secondary weak hydrogen bond [11, 14, 81]. It would be interesting to see how an increased aliphatic chain influences the hydrogen bonds by introducing competing dispersion interactions [132]. The study of highly polar fluorinated alcohols [133] in combination with water [134] would also be of interest.

For the first time, polarized transmission FTIR microspectroscopy was applied to study conformational and chiral effects of hydrogen bonded sublimated crystals. The method was tested on methyl mandelate [37]. It was found that not the most stable conformation [38] but an energetically less favorable monomer conformation is present in the crystal. Here, adaptive aggregation takes place due to beneficial intermolecular interactions. Chirality recognition studies revealed the formation of a rather rare mixed 3:1 crystal next to the prevalent 1:1 racemate [38]. Both contain the less stable monomer conformation as well. Enantiopure methyl mandelate was used to show the suitability of polarized transmission FTIR microspectroscopy for the inference of the molecular orientation within a crystal and for the assignment of vibrational bands. The polarization behavior and vibrational transition dipole vectors, respectively, of hydrogen bonded O-H stretching, C-H stretching, and C-$C_{aromatic}$ stretching bands were revealed and associated with specific orientations of the hydrogen bonds and certain axes within the molecules.

The method was extended to mandelic acid [37]. Results gained for methyl mandelate were confirmed and the aromatic C-H stretching modes were assigned. Mandelic acid crystallizes in one enantiomeric and two racemic forms [88, 161, 166–168]. The racemate was not studied within the present framework. Its investigations might support the interpretation of further bands at lower wavenum-

bers [20, 164, 165]. Also, the appearance of polymorphism in the case of the racemate is worth to be studied. Further chirality recognition effects might occur for co-crystals of mandelic acid and methyl mandelate [58]. The sublimation of mixed methyl mandelate-mandelic acid crystals was performed without success due to different vapor pressures (see also Ref. [181]). A prior co-crystallization from solution and a subsequent sublimation might be more successful.

The polarized transmission FTIR microspectroscopic method was also applied to some neuroactive phenylpropanolamines which are structurally similar to methyl mandelate and mandelic acid. The molecular orientation was inferred for most of the investigated substances. In the cases of enantiopure norephedrine and racemic pseudoephedrine no crystal structures were available. A tentative average orientation of the molecules within the unit cell was obtained based on their polarization behavior. Further evaluation of the C-H stretching bands would help to assign the molecular conformation and orientation more accurately. Measurements on block-like racemic pseudoephedrine crystals might provide a better spectral quality. Determining the crystal structure with other techniques would be worthwhile in order to reassess the postulated orientation proposed within this work.

Chirality recognition was observed in the cases of norephedrine and pseudoephedrine. FTIR images were recorded for pseudoephedrine in order to observe the influence of the enantiomeric ratio on chirality recognition. Analogous measurements could be carried out for norephedrine. Mass spectroscopy as it was performed in the case of methyl mandelate would be suitable to determine the relative vapor pressures and phase diagrams of the enantiopure and racemic compounds.

In the case of ephedrine, an anhydrate and a hydrate were obtained. The sublimation of prepared ephedrine hemihydrate might allow the study of other faces. Also, the ND/OD deuteration might shed new light into the interpretation. A spectral comparison might provide valuable information regarding the influence of conformational differences and the integration of water into the crystal structure on the position and intensity of various bands.

Several N-H stretching bands in the spectra of the investigated phenylpropanolamines were assigned. Their red shifts were analyzed in terms of hydrogen bond and conformational influence. Both were found to affect the N-H stretching position. Raman-jet spectroscopy using a heatable nozzle [203, 204] might reveal the isolated monomer spectra of the phenylpropanolamine conformations present in the crystals. With this information, the influence of the conformation on the N-H

stretching position can be further evaluated.

Within the scope of F. Ziegler's Bachelor thesis, the methylxanthines caffeine, theophylline, and theobromine were investigated by the polarization FTIR (not presented in this work). Caffeine was found to crystallize in a needle-like habit. Thus, a small aperture needed to be applied which decreased the spectral quality. Nonetheless, the molecular orientation of one face was determined and C-H stretching bands assigned. The measurements of theophylline and theobromine were repeated by J. Wallbaum and T. Nack in the framework of an internship [152], in which the investigations were extended through recrystallization and deuteration studies. The interpretation of these results is still in progress. Measurements on other methylxanthines e.g., isocaffeine may clarify the interpretation [205, 206].

The experimental results of this work were compared with harmonic monomer calculations. Vibrational crystal phase calculations would be desirable to account for intermolecular interactions [36]. A cooperation was started with R. Tonner on enantiopure methyl mandelate. Preliminary results are encouraging. Anharmonic monomer calculations could be applied as well and compared to experiment and the harmonic calculations.

Deuteration studies were used to support the vibrational assignment in the cases of methyl mandelate and the phenylpropanolamines. Time-dependent isotope exchange studies of deuterated crystals might provide information about the exchange rates [207]. In case of the primary amines it might be possible to observe the kinetics of the bonded versus the free N-D group.

The polarized transmission FTIR microspectroscopic method can be extended to the investigation of polymorphism. As mentioned above, there are two known polymorphs of racemic mandelic acid which are worth to be studied. The methylxanthines caffeine and theophylline also show polymorphism [208–213] and exist as anhydrates and hydrates [214–216]. Also, the investigation of unknown polymorphs which do not crystallize by standard crystallization methods is of interest [170].

The sublimation cell constructed and tested within this work can be further improved. The CaF_2 crystals within the windows of the sublimation cell were randomly oriented. The influence of the preferential growth direction should be investigated with an oriented CaF_2 substrate [149]. Interactions between the windows and the substrate might change the preferred face exhibited by the microcrystals. The application of the ATR technique can be extended to crystals. An ATR ob-

jective could improve the spatial resolution of the microscopic measurements by a factor of five. A higher resolution would open the possibility to analyze and characterize even smaller crystals in the range of a few micrometers. Remeasurements of the methylxanthines with this technique would be worthwhile. Since the ATR device needs to be in contact with the sample, a new sublimation cell with a sealed opening for the ATR crystal would need to be constructed. In order to investigate less volatile substances higher sublimation temperatures need to be applied. A heating plate which can achieve higher temperatures would be needed.

During the course of the studies conducted for this dissertation, a macro jet setup for the imaging of jet expansions was newly constructed and tested. The jet-images will provide information of the spatial distribution of different monomer conformations and clusters within the jet expansion. This provides information of conformational preferences and conditions for adaptive aggregation which might be valuable for the further improvement of the sublimation experiments. The project is continued by J. Zischang [217].

A. Matlab Script: Oriented Gas Model Spectra

```matlab
% Loading data
load view_c.mat % Atom coordinates of the frozen monomer unit along the c axis
load out.mat % Atom coordinates of the relaxed monomer unit
load out_der.mat % x, y, and z components of the dipole derivative, wabenumber,
and intensity

% Rotation of view c along the x-axis by 180°
Rx180=[1,0,0;0,cos(pi),-1*sin(pi);0,sin(pi),cos(pi)];
view_c1=Rx180*view_c1';
view_c1=view_c1';
view_c2=Rx180*view_c2';
view_c2=view_c2';
view_c3=Rx180*view_c3';
view_c3=view_c3';
view_c4=Rx180*view_c4';
view_c4=view_c4';

%Mean values of coordinates
mean_end1(1,1:3)=mean(view_c1(:,1:3));
mean_end2(1,1:3)=mean(view_c2(:,1:3));
mean_end3(1,1:3)=mean(view_c3(:,1:3));
mean_end4(1,1:3)=mean(view_c4(:,1:3));
mean_anfang(1,1:3)=mean(out(:,1:3));

%Translation of mean values into the origin
for i=1:length(view_c1(:,1));
mean_end_voll1(i,1:3)=mean_end1(1,1:3);
mean_end_voll2(i,1:3)=mean_end2(1,1:3);
mean_end_voll3(i,1:3)=mean_end3(1,1:3);
mean_end_voll4(i,1:3)=mean_end4(1,1:3);
mean_anfang_voll(i,1:3)=mean_anfang(1,1:3);
end
```

```
out_trans=out-mean_anfang_voll;
view_c1_trans=view_c1-mean_end_voll1;
view_c2_trans=view_c2-mean_end_voll2;
view_c3_trans=view_c3-mean_end_voll3;
view_c4_trans=view_c4-mean_end_voll4;

mean_end_neu1(1,1:3)=mean(view_c1_trans(:,1:3));
mean_end_neu2(1,1:3)=mean(view_c2_trans(:,1:3));
mean_end_neu3(1,1:3)=mean(view_c3_trans(:,1:3));
mean_end_neu4(1,1:3)=mean(view_c4_trans(:,1:3));
mean_anfang_neu(1,1:3)=mean(out_trans(:,1:3));

%Angle corresponding z-axis, molecule 1
The oriented monomer units need to be compared with the ones of the crystal
structure since the angles for the rotation are not correctly calculated in every case.
If the orientation of the relaxed monomer deviates from the one within the crystal
structure, the rotation can be manually performed.
for i=1:length(view_c1(:,1));
for j=1:length(view_c1(1,:));
amalb1(i,1)=view_c1_trans(i,1)*out_trans(i,1)+view_c1_trans(i,2)*out_trans(i,2);
betraga1(i,1)=(view_c1_trans(i,1)^2+view_c1_trans(i,2)^2)^(1/2);
betragb1(i,1)=(out_trans(i,1)^2+out_trans(i,2)^2)^(1/2);
cosalpha1(i,1)=amalb1(i,1)/(betraga1(i,1)*betragb1(i,1));
alpha_z_voll1(i,1)=acos(cosalpha1(i,1));
end
end
alpha_z1=mean(alpha_z_voll1);

clear mean_anfang mean_anfang_neu mean_anfang_voll
clear mean_end1 mean_end_neu1 mean_end_voll1

%In analogy, angle corresponding z-axis, molecules 2–4
...

%Rotation around z-axis, molecule 1
Rz1=[cos(alpha_z1),-1*sin(alpha_z1),0;sin(alpha_z1),cos(alpha_z1),0;0,0,1];
z_strich1=Rz1*out_trans';
z1=z_strich1';

der1=out_der(1:3,:);
der_z_strich1=Rz1*der1;
der_z1=der_z_strich1';
```

```matlab
clear dif_mean1 dif_mean_voll1

%In analogy, rotation around z-axis, molecule 2–4
...

%Angle corresponding y-axis, molecule 1
for i=1:length(view_c1(:,1));
for j=1:length(view_c1(1,:));
amalb1(i,1)=view_c1_trans(i,1)*z1(i,1)+view_c1_trans(i,3)*z1(i,3);
betraga1(i,1)=(view_c1_trans(i,1)^2+view_c1_trans(i,3)^2)^(1/2);
betragb1(i,1)=(z1(i,1)^2+z1(i,3)^2)^(1/2);
cosalpha1(i,1)=amalb1(i,1)/(betraga1(i,1)*betragb1(i,1));
alpha_y_voll1(i,1)=acos(cosalpha1(i,1));
end
end
alpha_y1=mean(alpha_y_voll1);

%In analogy, angle corresponding y-axis, molecules 2–4
...

%Rotation around y-axis, molecule 1
Ry1=[cos(alpha_y1),0,sin(alpha_y1);0,1,0;-1*sin(alpha_y1),0,cos(alpha_y1)];
y_strich1=Ry1*z1';
y1=y_strich1';
der_y_strich1=Ry1*der_z1';
der_y1=der_y_strich1';

%In analogy, rotation around y-axis, molecule 2–4
...

%Angle corresponding x-axis, molecule 1
for i=1:length(view_c1(:,1));
for j=1:length(view_c1(1,:));
amalb1(i,1)=view_c1_trans(i,2)*y1(i,2)+view_c1_trans(i,3)*y1(i,3);
betraga1(i,1)=(view_c1_trans(i,2)^2+view_c1_trans(i,3)^2)^(1/2);
betragb1(i,1)=(y1(i,2)^2+y1(i,3)^2)^(1/2);
cosalpha1(i,1)=amalb1(i,1)/(betraga1(i,1)*betragb1(i,1));
alpha_x_voll1(i,1)=acos(cosalpha1(i,1));
end
end
alpha_x1=mean(alpha_x_voll1)+0.1;
```

A. Matlab Script: Oriented Gas Model Spectra

```
%In analogy, angle corresponding x-axis, molecules 2–4
...

%Rotation around x-axis, molecule 1
Rx1=[1,0,0;0,cos(alpha_x1),-1*sin(alpha_x1);0,sin(alpha_x1),cos(alpha_x1)];
x_strich1=Rx1*y1';
x1=x_strich1';
der_x_strich1=Rx1*der_y1';
der_x1=der_x_strich1';

clear amalb1 betraga1 betragb1 cosalpha1
clear alpha_y_voll1 alpha_z_voll1

%In analogy, rotation around x-axis, molecule 2–4
...

%New orientation, molecule 1
out_rot_c1=x1;
out_der_rot_c1=der_x1;

clear x_strich1 y_strich1 z_strich1 der_x1 der_y1 der_z1 der_x_strich1
der_y_strich1 der_z_strich1
clear alpha_y1 alpha_z1

%In analogy, new orientation, molecule 2–4
...

%Rotation matrix for the rotation from view c to view a resp. view b
Rx90=[1,0,0;0,cos(pi/2),-1*sin(pi/2);0,sin(pi/2),cos(pi/2)];
Ry90=[cos(pi/2),0,sin(pi/2);0,1,0;-1*sin(pi/2),0,cos(pi/2)];
Rz90=[cos(pi/2),-1*sin(pi/2),0;sin(pi/2),cos(pi/2),0;0,0,1];
Rz135=[cos(3*pi/4),-1*sin(3*pi/4),0;sin(3*pi/4),cos(3*pi/4),0;0,0,1];
Rx270=[1,0,0;0,cos(pi*1.5),-1*sin(pi*1.5);0,sin(pi*1.5),cos(pi*1.5)];
Ry270=[cos(pi*1.5),0,sin(pi*1.5);0,1,0;-1*sin(pi*1.5),0,cos(pi*1.5)];
Rz270=[cos(pi*1.5),-1*sin(pi*1.5),0;sin(pi*1.5),cos(pi*1.5),0;0,0,1];

%Rotation to view a, molecule 1
a1=Rz90*out_rot_c1';
a11=Rx270*a1;
out_rot_a1=a11';

der_a1=Rz90*out_der_rot_c1';
der_a11=Rx270*der_a1;
```

IV

```matlab
out_der_rot_a1=der_a11';
```

%In analogy, rotation to view a, molecule 2–4
...

%Rotation to view b, molecule 1
```matlab
b1=Rz270*out_rot_c1';
b11=Ry270*b1;
out_rot_b1=b11';

der_b1=Rz270*out_der_rot_c1';
der_b11=Ry270*der_b1;
out_der_rot_b1=der_b11';
```

%In analogy, rotation to view b, molecule 2–4
...

%Intensity of view a
```matlab
for k=1:length(out_der(1,:));
out_der_rot_a_strich1=out_der_rot_a1';
out_der_rot_a_strich2=out_der_rot_a2';
out_der_rot_a_strich3=out_der_rot_a3';
out_der_rot_a_strich4=out_der_rot_a4';

der_a1(1,k)=(out_der_rot_a_strich1(1,k))^2+(out_der_rot_a_strich1(2,k))^2;
der_a2(1,k)=(out_der_rot_a_strich2(1,k))^2+(out_der_rot_a_strich2(2,k))^2;
der_a3(1,k)=(out_der_rot_a_strich3(1,k))^2+(out_der_rot_a_strich3(2,k))^2;
der_a4(1,k)=(out_der_rot_a_strich4(1,k))^2+(out_der_rot_a_strich4(2,k))^2;
der_alt(1,k)=(out_der(1,k))^2+(out_der(2,k))^2+(out_der(3,k))^2;

der_a=(der_a1+der_a2+der_a3+der_a4)/4;
der_a_rel(1,k)=(der_a(1,k)/der_alt(1,k));

I_a(2,k)=out_der(5,k)*der_a_rel(1,k);
I_a(1,k)=out_der(4,k);
end
```

%In analogy, intensity of view b and c
...

%Polarized intensity along y-axis of view a
```matlab
for k=1:length(out_der(1,:));
out_der_rot_a_strich1=out_der_rot_a1';
```

```
out_der_rot_a_strich2=out_der_rot_a2';
out_der_rot_a_strich3=out_der_rot_a3';
out_der_rot_a_strich4=out_der_rot_a4';

der_a_pol01(1,k)=out_der_rot_a_strich1(2,k)^2;
der_a_pol02(1,k)=out_der_rot_a_strich2(2,k)^2;
der_a_pol03(1,k)=out_der_rot_a_strich3(2,k)^2;
der_a_pol04(1,k)=out_der_rot_a_strich4(2,k)^2;
der_alt(1,k)=(out_der(1,k))^2+(out_der(2,k))^2+(out_der(3,k))^2;

der_a_pol0(1,k)=(der_a_pol01(1,k)+der_a_pol02(1,k)+der_a_pol03(1,k)+der_a_pol04(1,k))/4;
der_a_pol0_rel(1,k)=(der_a_pol0(1,k)/der_alt(1,k));

I_a_pol0(2,k)=out_der(5,k)*der_a_pol0_rel(1,k);
I_a_pol0(1,k)=out_der(4,k);

end
%In analogy, polarized intensities along x-axis of view a as well as along y- and
x-axis of view b and c
...

%Saving results in *.dat format
dlmwrite('a.dat',a,'\t')
dlmwrite('a_pol0.dat',a_pol0,'\t')
dlmwrite('a_pol90.dat',a_pol90,'\t')
dlmwrite('b.dat',b,'\t')
dlmwrite('b_pol0.dat',b_pol0,'\t')
dlmwrite('b_pol90.dat',b_pol90,'\t')
dlmwrite('c.dat',c,'\t')
dlmwrite('c_pol0.dat',c_pol0,'\t')
dlmwrite('c_pol90.dat',c_pol90,'\t')
```

B. Substances

Table B.1.: Used substances, chemical formulas, CAS-numbers, suppliers, and purity.

Substance	Formula	CAS-No.	Supplier	Purity
(R)-(−)-Methyl mandelate	$C_9H_{10}O_3$	20698-91-3	Alfa Aesar	99%
(S)-(+)-Methyl mandelate	$C_9H_{10}O_3$	21210-43-5	Alfa Aesar	99%
(S)-(+)-Methyl mandelate	$C_9H_{10}O_3$	21210-43-5	ABCR	99%
(RS)-(±)-Methyl mandelate	$C_9H_{10}O_3$	4358-87-6	Fluka	≥98.0%
(R)-(−)-Mandelic acid	$C_8H_8O_3$	611-71-2	Alfa Aesar	98%
(S)-(+)-Mandelic acid	$C_8H_8O_3$	17199-29-0	ABCR	99%
(S)-(−)-Methyl lactate	$C_4H_8O_3$	27871-49-4	Aldrich	98%
Methanol-d3	CD_3OH	1849-29-2	Euriso-top	HDO+D2O <0.1%
Sulfuric acid	H_2SO_4	7664-93-9	Fisher Scientific	48%
Diethyl ether	$C_4H_{10}O$	60-29-7	Sigma-Aldrich	≥99.0%
Potassium carbonate	K_2CO_3	584-08-7	Grüssing	99.5%
Sodium chloride	$NaCl$	7647-14-5	AnalaR Normapur	99.99%
Sodium sulfate	Na_2SO_4	7757-82-6	ABCR	99%
Water	H_2O	7732-18-5	Carl Roth	p.a.
Deuterium oxide	D_2O	7789-20-0	Euriso-top	99.9%
(R)-(−)-Methyl mandelate	$C_9H_{10}O_3$	20698-91-3	Alfa Aesar	99%
(RS)-(±)-Methyl mandelate	$C_9H_{10}O_3$	4358-87-6	Fluka	≥98.0%
(R)-Alanine ethyl ester hydrochloride	$C_5H_{11}NO_2 \cdot HCl$	1115-59-9	Aldrich	99%
(RS)-(±)-Menthol	$C_{10}H_{20}O$	89-78-1	Aldrich	≥99.0%
Ethyl acetamidoacetate	$C_6H_{11}NO_3$	1906-82-7	Aldrich	98%
(RS)-(±)-1-Indanol	$C_9H_{10}O$	6351-10-6	Fluka	≥98.0%
(RS)-(±)-Alanine ethyl ester hydrochloride	$C_5H_{11}NO_2 \cdot HCl$	617-27-6	Acros Organics	99%
(1S,2R)-(+)-Norephedrine	$C_9H_{13}NO$	37577-28-9	Aldrich	98%
(1R,2S)-(−)-Norephedrine	$C_9H_{13}NO$	492-41-1	Aldrich	99%
(1R,2R)-(−)-Pseudo-norephedrine	$C_9H_{13}NO$	37577-07-4	Aldrich	≥98.0%
(1R,2S)-(−)-Ephedrine	$C_{10}H_{15}NO$	299-42-3	Aldrich	≥98.0%
(1S,2S)-(+)-Pseudoephedrine	$C_{10}H_{15}NO$	90-82-4	Aldrich	≥96.0%
(1R,2R)-(−)-Pseudoephedrine	$C_{10}H_{15}NO$	321-97-1	Aldrich	≥96.0%

Table B.1.: Continuation

Substance	Formula	CAS-No.	Supplier	Purity
Deuterium oxide	D_2O	7789-20-0	Aldrich	99.9%
Water	H_2O	7732-18-5	Fluka Chemika	puriss. p.a.
Water	H_2O	7732-18-5	Carl Roth	p.a.
Deuterium oxide	D_2O	7789-20-0	Cambridge Isotope Lab.	99.9%
Deuterium oxide	D_2O	7789-20-0	Euriso-top	99.9%
Methanol	CH_4O	67-56-1	Acros Organics	>99.5%
Methanol-d1	CH_3OD	1455-13-6	Cambridge Isotope Lab.	99%
Ethanol	C_2H_6O	64-17-5	Merck-Suchardt	$\geq$99.5%
Ethanol	C_2H_6O	64-17-5	Carl Roth	$\geq$99.8% p.a.
Ethanol-d1	C_2H_5OD	1624-36-8	Aldrich	99%
Helium	He	7400-59-7	Air Liquid	99.996%
Argon	Ar	7440-37-1	Air Liquid	99.998%

C. Matlab Script: Mass Spectrometry

```matlab
dateien=dir('*.txt')
anz_dateien=length(dateien)
% Number of columns: time + two times number of fragments of interest
resultate=zeros(anz_dateien,9)
% Column 1:
for i=1:anz_dateien
% Time in minutes (here: 5)
time_dat=(i-1)*5
daten=dlmread(dateien(i).name,',',20,0);
data=zeros(length(daten),2);
data(:,1)=daten(:,1);
data(:,2)=daten(:,2);

% Search of maximum intensity in a specified range
window_size=10;
% Interval to be searched (here: 10)
peak_pos1s=499; % here: m/z=51
peak_pos1e=peak_pos1s+window_size;
peak_pos2s=779; % here: m/z=79
peak_pos2e=peak_pos2s+window_size;
peak_pos3s=1060; % here: m/z=107
peak_pos3e=peak_pos3s+window_size;

% Writing data in matrix
% 1. Column: time
resultate(i,1)=time_dat;
% Fragment 1
% 2. Column: intensity of fragment 1
[resultate(i,2),index_data]=max(data(peak_pos1s:peak_pos1e,2));
% 3. Column: m/z of fragment 1
resultate(i,3)=data(peak_pos1s+index_data-1,1);
% Fragment 2
% 4. Column: intensity of fragment 2
[resultate(i,4),index_data]=max(data(peak_pos2s:peak_pos2e,2));
% 5. Column: m/z of fragment 2
```

```
resultate(i,5)=data(peak_pos2s+index_data-1,1);
% Fragment 3
% 6. Column: intensity of fragment 3
[resultate(i,6),index_data]=max(data(peak_pos3s:peak_pos3e,2));
% 7. Column: m/z of fragment 3
resultate(i,7)=data(peak_pos3s+index_data-1,1);

% Saving of matrix
save 'resultate.erg' resultate -ASCII -DOUBLE
save 'resultate.mat' resultate -MAT
end
```

X

D. Jet Parameters and Experimental Conditions

D.1. Filet-Jet Parameters

Table D.1.: Parameters of the FTIR-jet for the mixed alcohol-water systems.

Optic-Parameters	
Source Setting	Tungsten
Beamsplitter	CaF_2
Detector	InSb 2 mm
Channel	X1
Aperture	3.5 mm
Opt. filter setting	$4000\text{--}2860\,cm^{-1}$
Scanner velocity	80 kHz
Stabilization delay	2 s
Delay before measurement	0 s
Gain	on
Signal enhancement	auto
Reference enhancement	auto
Resolution	$2.0\,cm^{-1}$
Acquisition-Parameters	
Wanted high frequency limit	$15800\,cm^{-1}$
Wanted low frequency limit	$0\,cm^{-1}$
Acquisition mode	Single-Sided Fast-Return
Correlation mode	–
Low pass filter	–
High pass filter	–
FT-Parameters	
Frequency limits	$15800\text{--}0\,cm^{-1}$
Phase correction mode	Mertz
Phase resolution	$16\,cm^{-1}$
Zero filling factor	4
Apodization function	Norton-Beer-Medium

Table D.2.: Experimental FTIR-jet conditions for the mixed methanol-water and for the mixed ethanol-water system. ϑ denotes the saturator temperature. Also given are the opening times of the mixing valves.

	methanol-water	ethanol-water
ϑ(alcohol)/°C	−15	−10
time$_{open}$(alcohol)/s	0.1	0.4
time$_{closed}$(alcohol)/s	4.08	2.4
ϑ(water)/°C	+5	+5
time$_{open}$(water)/s	0.92	1.04
time$_{closed}$(water)/s	1.88	1.8
time$_{open}$(helium)/s	3.32	2.72
time$_{closed}$(helium)/s	0.1	0.1

D.2. Raman-Jet Parameters

Table D.3.: Experimental Raman-jet conditions for the mixed methanol-water system.

	overview	dimer region	trimer region			
Roots pumps	$500\,\mathrm{m^3 \cdot h^{-1}}$	$500\,\mathrm{m^3 \cdot h^{-1}}$	$500\,\mathrm{m^3 \cdot h^{-1}}$			
Roots pumps	$250\,\mathrm{m^3 \cdot h^{-1}}$	$250\,\mathrm{m^3 \cdot h^{-1}}$	$250\,\mathrm{m^3 \cdot h^{-1}}$			
Rotary vane pumps	$100\,\mathrm{m^3 \cdot h^{-1}}$	$100\,\mathrm{m^3 \cdot h^{-1}}$	$100\,\mathrm{m^3 \cdot h^{-1}}$			
Dimension of vacuum chamber/cm³	60 x 60 x 40 (square footprint)	60 x 60 x 40 (square footprint)	60 x 60 x 40 (square footprint)			
Nozzle distance/mm	1	3	3			
Objective	Nikon Nikkor ($\varnothing$=50 mm, f/1.2)	Nikon Nikkor ($\varnothing$=50 mm, f/1.2)	Nikon Nikkor ($\varnothing$=50 mm, f/1.2)			
Monochromator slit width/μm	75	75	75			
Focussing lens	Linos ARB2 ($\varnothing$=22.4 mm, f/7)	Linos ARB2 ($\varnothing$=22.4 mm, f/7)	Linos ARB2 ($\varnothing$=22.4 mm, f/7)			
Monochromator	McPherson 2051 (f=1000 mm, f/8.7, 1200 gr/mm grating)	McPherson 2051 (f=1000 mm, f/8.7, 1200 gr/mm grating)	McPherson 2051 (f=1000 mm, f/8.7, 1200 gr/mm grating)			
			1:0	3:1	1:1	0:1
ϑ(methanol)/°C	–25	–28	–28	–25	–28	–
time$_{\mathrm{open}}$(methanol)/s		0.48			2	
time$_{\mathrm{closed}}$(methanol)/s		1.76			3	
ϑ(water)/°C	+1	+9.5	–	+1	+7.5	+3
time$_{\mathrm{open}}$(water)/s		2.28			5	
time$_{\mathrm{closed}}$(water)/s		0.1			0.1	
Number of scans	6	6	6	6	6	6
Scan duration/s	200	300	300	300	300	300

Table D.4.: Experimental Raman-jet conditions for the mixed deuterated methanol-deuterium oxide system.

Roots pumps	$500 \, m^3 \cdot h^{-1}$			
Roots pumps	$250 \, m^3 \cdot h^{-1}$			
Rotary vane pumps	$100 \, m^3 \cdot h^{-1}$			
Dimension of vacuum chamber/cm^3	60 x 60 x 40 (square footprint)			
Nozzle distance/mm	3			
Objective	Nikon Nikkor ($\varnothing$=50 mm, f/1.2)			
Monochromator slit width/μm	75			
Focussing lens	Linos ARB2 ($\varnothing$=22.4 mm, f/7)			
Monochromator	McPherson 2051 (f=1000 mm, f/8.7, 1200 gr/mm grating)			
	1:0	3:1	1:1	0:1
ϑ(deuterated methanol)/°C	−28	−28	−25	−
time$_{open}$(deuterated methanol)/s		1.0		
time$_{closed}$(deuterated methanol)/s		1.5		
ϑ(deuterium oxide)/°C	−	+7.5	+1	+1
time$_{open}$(deuterium oxide)/s		2.5		
time$_{closed}$(deuterium oxide)/s		0.1		
Number of scans	6			
Scan duration/s	300			

Table D.5.: Experimental Raman-jet conditions for the mixed ethanol-water system.

	overview	dimer region	trimer region					
Roots pumps	$250\,\mathrm{m^3 \cdot h^{-1}}$	$250\,\mathrm{m^3 \cdot h^{-1}}$	$250\,\mathrm{m^3 \cdot h^{-1}}$					
Rotary vane pumps	$100\,\mathrm{m^3 \cdot h^{-1}}$	$100\,\mathrm{m^3 \cdot h^{-1}}$	$100\,\mathrm{m^3 \cdot h^{-1}}$					
Dimension of vacuum chamber/cm^3	22 x 14 x 14 (cylindrical)	60 x 60 x 40 (square footprint)	60 x 60 x 40 (square footprint)					
Nozzle distance/mm	1	3	2					
Objective	Edmund Optics E32-886 ($\varnothing$=50 mm, f/3)	Nikon Nikkor ($\varnothing$=50 mm, f/1.2)	Nikon Nikkor ($\varnothing$=50 mm, f/1.2)					
Monochromator slit width/μm	75	75	100					
Focussing lens	Edmund Optics L45-354 ($\varnothing$=50 mm, f/7)	Edmund Optics L45-354 ($\varnothing$=50 mm, f/7)	Newport PAC087AR.14 ($\varnothing$=51 mm, f/4)					
Monochromator	McPherson 2051 (f=1000 mm, f/8.7, 1200 gr/mm grating)	McPherson 2051 (f=1000 mm, f/8.7, 1200 gr/mm grating)	McPherson 205f (f=500 mm, f/3.2, 1800 gr/mm grating)					
			1:0	5:1	2:1	1:1	1:3	0:1
ϑ(ethanol)/$^\circ$C	−8	−8	−10	−8	−10	−21	−24	−
ϑ(water)/$^\circ$C	+9	+9	−	−4	+2	+6	+7	+3
Number of scans	5	6	6	6	6	12	12	6
Scan duration/s	600	600	600	600	600	300	300	600

Table D.6.: Experimental Raman-jet conditions for the mixed deuterated ethanol-deuterium oxide system.

Roots pumps	$500\,\text{m}^3\cdot\text{h}^{-1}$
Roots pumps	$250\,\text{m}^3\cdot\text{h}^{-1}$
Rotary vane pumps	$100\,\text{m}^3\cdot\text{h}^{-1}$
Dimension of vacuum chamber/cm^3	60 x 60 x 40 (square footprint)
Nozzle distance/mm	2
Objective	Nikon Nikkor ($\varnothing$=50 mm, f/1.2)
Monochromator slit width/μm	75
Focussing lens	Linos ARB2 ($\varnothing$=22.4 mm, f/7)
Monochromator	McPherson 2051 (f=1000 mm, f/8.7, 1200 gr/mm grating)
ϑ(deuterated ethanol)/°C	–8
ϑ(deuterium oxide)/°C	+9
Number of scans	4
Scan duration/s	300

E. Quantum Chemical Predictions of the Mixed Alcohol-Water Clusters

Table E.1.: Differences between the experimental $\tilde{\nu}_{\mathrm{ww}}(\mathrm{exp})$ and the calculated harmonic wavenumber $\omega_{\mathrm{ww}}(\mathrm{th})$ in cm^{-1} for the water and the deuterated water dimer on different levels. For the larger basis sets, the difference approaches twice the expected O-H oscillator anharmonic constant, as it should.

$\tilde{\nu}_{\mathrm{ww}}(\mathrm{exp})$-$\omega_{\mathrm{ww}}(\mathrm{th})$	B3-S	MP2-S	MP2-M	MP2-L
$(H_2O)_2$	–48	–152	–138	–161
$(D_2O)_2$	–5	–76	–71	–88

Table E.2.: Shifted MP2-S/MP2-M average of predicted Raman and IR wavenumbers $\tilde{v}$ in cm^{-1} as well as relative Raman and IR intensities (σ'_{rel} in $10^{-36} \cdot \text{m}^2 \cdot \text{sr}^{-1}$ and I_{rel} in km·mol^{-1}, respectively) for pure and mixed dimers and trimers in the methanol-water system. A methanol mole fraction of x_{m}=0.75 for the Raman and of x_{m}=0.50 for the IR case is assumed. For the scaling procedure, see Chapter 4.

	Raman		IR	
Cluster	$\tilde{v}$	σ'_{rel}	$\tilde{v}$	I_{rel}
ww	3602	9	3602	66
wm	3563	28	3563	82
mw	3615	25	3615	94
mm	3577	79	3577	110
www	3478	2		
			3529	15
			3540	13
mww	3445	16	3445	18
			3519	39
			3543	42
mmw	3436	49	3436	17
			3505	49
			3539	50
mmm	3438	56		
			3492	22
			3513	20

Table E.3.: Shifted MP2-S/MP2-M average of predicted Raman wavenumbers $\tilde{v}$ in cm^{-1} as well as relative intensities σ'_{rel} in $10^{-36} \cdot \text{m}^2 \cdot \text{sr}^{-1}$ for pure and mixed dimers and trimers in the deuterated methanol-deuterium oxide system. A deuterated methanol mole fraction of x_{m}=0.75 is assumed. For the scaling procedure, see Chapter 4.

Cluster	$\tilde{v}$	σ'_{rel}
ww	2632	6
wm	2607	24
mw	2663	27
mm	2637	72
www	2549	2
mww	2529	15
mmw	2524	41
mmm	2539	50

Table E.4.: Shifted MP2-S/MP2-M average of predicted Raman and IR wavenumbers $\tilde{v}$ in cm^{-1} as well as relative Raman and IR intensities (σ'_{rel} in $10^{-36} \cdot \mathrm{m}^2 \cdot \mathrm{sr}^{-1}$ and I_{rel} in km·mol^{-1}, respectively) for pure and mixed dimers and trimers in the ethanol-water system. An ethanol mole fraction of x_{e}=0.50 for the Raman and of x_{e}=0.67 for the IR case is assumed. For the scaling procedure, see Chapter 4.

Cluster	Raman		IR	
	$\tilde{v}$	σ'_{rel}	$\tilde{v}$	I_{rel}
ww	3602	36	3602	29
we$_{g+}$	3544	36	3544	70
we$_t$	3551	34	3551	72
we$_{g-}$	3557	42	3557	82
e$_t$w	3601	45	3601	89
e$_g$w	3599	33	3599	73
e$_{g+}$e$_{g+}$	3542	32	3542	169
www	3478	8		
			3529	4
			3540	4
eww	3428	22	3428	15
			3516	21
			3530	24
eew	3417	27	3417	10
			3473	75
			3524	54
eee	3413	11		
			3469	56
			3478	57

Table E.5.: Electronic energies without (E_e) and with zero point energy correction (E_0) in E_h for water, deuterium oxide, methanol, deuterated methanol, and ethanol monomers. Also, calculated wavenumbers (ω(th)) in cm^{-1}, scattering activities (A_{Raman}) in $Å^4 \cdot u^{-1}$, scattering cross sections (σ') in $10^{-36} \cdot m^2 \cdot sr^{-1}$, and IR intensities ($I_{IR}$) in $km \cdot mol^{-1}$ of the symmetric (*sym*) and asymmetric (*asym*) O-H stretching vibration on different levels are listed.

Conformer	E_e	E_0	ω(th)	A_{Raman}	σ'	I_{IR}
B3-S						
w$_{sym}$	-76.443809	-76.422595	3763	87	86	0
w$_{asym}$			3881	43	43	32
w$_{deut,sym}$		-76.428368	2709	45	76	1
w$_{deut,asym}$			2847	23	36	21
m	-115.753876	-115.702703	3789	80	79	13
m$_{deut}$		-115.705938	2759	46	75	11
e$_t$	-155.081600	-155.001820	3787	117	114	11
e$_g$	-155.081326	-155.001474	3772	76	75	9
MP2-S						
w$_{sym}$	-76.244710	-76.223080	3827	83	79	3
w$_{asym}$			3971	37	33	50
w$_{deut,sym}$		-76.228965	2755	43	70	3
w$_{deut,asym}$			2913	20	30	31
m	-115.407363	-115.355145	3850	70	66	22
m$_{deut}$		-115.358426	2803	39	62	17
e$_t$	-154.592998	-154.511924	3833	99	95	20
e$_g$	-154.592769	-154.511308	3824	66	63	16
MP2-M						
w$_{sym}$	-76.2900916	-76.268685	3833	82	79	12
w$_{asym}$			3960	33	30	72
w$_{deut,sym}$		-76.274512	2763	43	70	8
w$_{deut,asym}$			2901	17	26	43
m	-115.469427	-115.417405	3864	66	62	40
m$_{deut}$		-115.420687	2813	38	60	28
e$_t$	-154.676546	-154.595686	3851	95	91	38
e$_g$	-154.676137	-154.595188	3839	64	62	30
MP2-L						
w$_{sym}$	-76.3184531	-76.296870	3861	84	79	10
w$_{asym}$			3989	26	23	76
w$_{deut,sym}$		-76.302746	2783	44	71	7
w$_{deut,asym}$			2923	14	21	45
m	-115.5139438	-115.461857	3899	65	60	41
m$_{deut}$		-115.465151	2839	37	59	28
e$_t$	-154.7373550	-154.656377	3884	64	88	39
e$_g$	-154.7370287	-154.656022	3874	65	60	32

Table E.6.: Dissociation energies without (D_e) and with zero point energy correction (D_0) in kJ·mol^{-1} for pure and mixed methanol-water dimers. Also, calculated wavenumbers (ω(th)) in cm^{-1}, scattering activities (A_{Raman}) in Å^4·u^{-1}, scattering cross sections (σ') in 10^{-36}·m^2·sr^{-1}, and IR intensities (I_{IR}) in km·mol^{-1} of the donor (D) and acceptor (A) symmetric (*sym*) and asymmetric (*asym*) O-H stretching vibration on different levels are listed. The S basis set does not predict the correct order.

Conformer	D_e	D_0	Vibration	ω(th)	A_{Raman}	σ'	I_{IR}
B3-S							
ww	30.97	19.93	D$_{sym}$	3650	163	170	301
			A$_{sym}$	3779	82	81	6
			D$_{asym}$	3849	57	54	64
			A$_{asym}$	3889	36	34	60
wm	29.64	20.43	D$_{sym}$	3624	183	194	376
			A	3801	70	68	26
			D$_{asym}$	3846	58	55	65
mw	29.70	21.39	D	3669	167	173	374
			A$_{sym}$	3780	88	86	4
			A$_{asym}$	3890	38	36	61
mm	28.00	21.71	D	3643	190	199	451
			A	3803	71	69	26
MP2-S							
ww	32.71	21.69	D$_{sym}$	3754	141	141	238
			A$_{sym}$	3835	78	74	6
			D$_{asym}$	3939	47	43	105
			A$_{asym}$	3969	32	29	80
wm	32.73	23.38	D$_{sym}$	3722	151	153	304
			A	3855	64	61	35
			D$_{asym}$	3932	48	44	103
mw	33.00	24.41	D	3765	130	129	345
			A$_{sym}$	3835	84	80	3
			A$_{asym}$	3970	33	30	81
mm	32.97	26.35	D	3732	139	140	404
			A	3856	68	65	34

Table E.6.: continuation

Conformer	D_e	D_0	Vibration	$\omega(\text{th})$	A_{Raman}	σ'	I_{IR}
MP2-M							
ww	24.39	15.06	D_{sym}	3740	149	149	287
			A_{sym}	3824	66	63	17
			D_{asym}	3927	44	41	113
			A_{asym}	3944	28	26	98
wm	26.48	18.14	D_{sym}	3695	146	149	351
			A	3852	58	55	53
			D_{asym}	3920	46	43	110
mw	24.56	17.33	D	3754	142	142	404
			A_{sym}	3823	69	67	9
			A_{asym}	3944	29	27	99
mm	26.80	21.20	D	3711	140	142	477
			A	3854	63	60	50
MP2-L							
ww	22.24	13.09	D_{sym}	3763	148	147	297
			A_{sym}	3849	65	62	15
			D_{asym}	3957	39	36	120
			A_{asym}	3973	23	21	99
wm	25.37	17.26	D_{sym}	3721	145	147	374
			A	3887	57	53	54
			D_{asym}	3952	43	39	116
mw	22.44	15.54	D	3778	144	142	424
			A_{sym}	3848	68	65	9
			A_{asym}	3973	24	22	99
mm	25.82	20.32	D	3735	141	142	503
			A	3888	61	57	52

Table E.7.: Dissociation energies with zero point energy correction (D_0) in kJ·mol^{-1} for pure and mixed deuterated methanol-deuterium oxide dimers. Also, calculated wavenumbers (ω(th)) in cm^{-1}, scattering activities (A_{Raman}) in Å^4·u^{-1}, scattering cross sections (σ') in 10^{-36}·m^2·sr^{-1}, and IR intensities (I_{IR}) in km·mol^{-1} of the donor (D) and acceptor (A) symmetric (*sym*) and asymmetric (*asym*) O-D stretching vibration on different levels are listed. The S basis set does not predict the correct order.

Conformer	D_0	Vibration	ω(th)	A_{Raman}	σ'	I_{IR}
B3-S						
ww	22.69	D$_{sym}$	2637	86	150	143
		A$_{sym}$	2721	43	72	5
		D$_{asym}$	2814	28	45	59
		A$_{asym}$	2853	19	29	36
wm	22.41	D$_{sym}$	2621	92	164	183
		A	2768	39	64	19
		D$_{asym}$	2810	29	46	63
mw	23.23	D	2671	97	167	216
		A$_{sym}$	2721	44	74	3
		A$_{asym}$	2854	20	31	36
mm	22.75	D	2653	103	179	262
		A	2769	40	66	19
MP2-S						
ww	24.42	D$_{sym}$	2708	73	123	112
		A$_{sym}$	2761	41	68	6
		D$_{asym}$	2884	24	37	80
		A$_{asym}$	2912	17	25	48
wm	25.45	D$_{sym}$	2687	76	130	144
		A	2807	36	58	24
		D$_{asym}$	2877	37	24	84
mw	26.34	D	2741	81	134	201
		A$_{sym}$	2761	37	60	1
		A$_{asym}$	2913	17	26	48
mm	27.52	D	2718	76	127	233
		A	2808	38	61	23

Table E.7.: continuation

Conformer	D_0	Vibration	$\omega(\text{th})$	A_{Raman}	σ'	I_{IR}
MP2-M						
ww	17.37	D_{sym}	2703	79	134	136
		A_{sym}	2756	34	56	12
		D_{asym}	2871	22	34	85
		A_{asym}	2890	15	22	57
wm	19.97	D_{sym}	2673	75	128	167
		A	2804	33	53	34
		D_{asym}	2864	22	34	87
mw	18.94	D	2733	92	153	231
		A_{sym}	2757	25	42	5
		A_{asym}	2890	15	23	57
mm	22.14	D	2703	76	129	270
		A	2806	36	57	33
MP2-L						
ww	15.36	D_{sym}	2720	79	133	140
		A_{sym}	2774	33	54	11
		D_{asym}	2893	19	29	89
		A_{asym}	2911	12	18	57
wm	19.06	D_{sym}	2692	74	127	178
		A	2830	33	52	35
		D_{asym}	2887	20	31	91
mw	17.08	D	2750	241	396	241
		A_{sym}	2775	24	40	6
		A_{asym}	2911	13	19	56
mm	21.26	D	2721	77	130	286
		A	2831	35	55	33

Table E.8.: Dissociation energies without (D_e) and with zero point energy correction (D_0) in kJ·mol^{-1} for pure and mixed methanol-water trimers. Also, calculated wavenumbers (ω(th)) in cm^{-1}, scattering activities (A_{Raman}) in Å^4·u^{-1}, scattering cross sections (σ') in 10^{-36}·m^2·sr^{-1}, and IR intensities (I_{IR}) in km·mol^{-1} of the O-H stretching vibration on different levels are listed. The S basis set does not predict the correct order.

Conformer	D_e	D_0	ω(th)	A_{Raman}	σ'	I_{IR}
B3-S						
$w_d w_d w_u$	90.41	63.54	3503	257	288	29
			3554	38	42	556
			3571	42	45	488
			3859	70	66	54
			3864	65	61	61
			3866	73	69	53
$m_u w_d w_d$	87.69	64.43	3494	256	288	171
			3557	78	85	513
			3579	42	46	525
			3864	75	71	61
			3866	81	76	53
$m_d w_d w_u$	87.96	64.57	3493	265	298	131
			3547	52	56	568
			3583	59	64	516
			3857	74	70	59
			3864	72	68	55
$m_d m_d w_u$	84.86	64.84	3501	265	297	144
			3561	96	104	530
			3575	59	64	666
			3858	81	76	58
$m_d m_u w_d$	84.56	65.02	3510	311	347	26
			3552	58	64	747
			3576	57	61	572
			3863	77	73	58
$m_d m_d m_u$	81.56	65.37	3515	312	347	43
			3560	83	90	733
			3570	73	79	704

Table E.8.: continuation

Conformer	D_e	D_0	$\omega(\text{th})$	A_{Raman}	σ'	I_{IR}
MP2-S						
$w_d w_d w_u$	93.90	67.82	3636	249	262	20
			3680	27	28	433
			3692	30	30	377
			3935	65	59	67
			3939	50	45	96
			3943	56	51	101
$m_u w_d w_d$	93.33	70.09	3613	226	240	157
			3672	73	75	412
			3692	28	28	409
			3933	63	58	84
			3939	66	60	93
$m_d w_d w_u$	93.43	70.42	3608	225	240	171
			3669	65	67	385
			3694	34	35	424
			3929	61	56	87
			3941	60	55	93
$m_d m_d w_u$	92.68	72.75	3604	206	220	208
			3677	99	102	344
			3690	38	38	545
			3927	65	59	86
$m_d m_u w_d$	91.96	72.66	3612	257	273	89
			3652	55	57	594
			3686	41	42	461
			3935	68	62	89
$m_d m_d m_u$	91.09	75.08	3606	229	244	150
			3650	72	75	626
			3683	68	70	500

Table E.8.: continuation

Conformer	D_e	D_0	ω(th)	A_{Raman}	σ'	I_{IR}
MP2-M						
$w_d w_d w_u$	73.78	50.18	3609	258	275	15
			3667	29	30	499
			3678	29	30	450
			3911	46	43	117
			3915	44	41	131
			3916	67	62	70
$m_u w_d w_d$	75.04	54.57	3568	219	238	235
			3655	84	87	429
			3683	28	29	484
			3911	57	53	110
			3915	64	59	101
$m_d w_d w_u$	75.04	54.33	3569	228	247	205
			3648	65	68	462
			3683	38	39	492
			3907	54	50	113
			3915	57	53	99
$m_d m_d w_u$	76.18	58.76	3558	239	261	147
			3624	68	72	702
			3677	47	49	516
			3909	61	57	104
$m_d m_u w_d$	75.73	58.59	3567	264	287	90
			3622	49	52	757
			3673	45	47	519
			3912	64	59	101
$m_d m_d m_u$	77.06	63.03	3559	266	290	24
			3623	59	62	773
			3632	52	55	779

Table E.8.: continuation

Conformer	D_e	D_0	ω(th)	A_{Raman}	σ'	I_{IR}
MP2-L						
$w_d w_d w_u$	69.08	46.16	3621	254	269	11
			3685	28	29	518
			3694	28	28	475
			3939	44	40	120
			3943	36	33	140
			3944	70	64	71
$m_u w_d w_d$	71.74	51.64	3584	220	237	213
			3671	76	79	470
			3701	30	30	521
			3941	50	45	121
			3943	66	60	98
$m_d w_d w_u$	71.70	51.39	3585	229	246	183
			3665	59	61	504
			3702	38	39	526
			3937	50	46	119
			3943	56	51	101
$m_d m_d w_u$	74.36	56.96	3574	242	262	122
			3640	60	63	771
			3697	47	48	541
			3940	59	53	108
$m_d m_u w_d$	74.08	56.83	3582	260	281	78
			3641	47	49	796
			3691	45	46	557
			3941	60	55	104
$m_d m_d m_u$	76.77	62.37	3573	265	287	16
			3641	56	58	853
			3650	51	54	787

Table E.9.: Dissociation energies with zero point energy correction (D_0) in kJ·mol^{-1} for pure and mixed deuterated methanol-deuterium oxide trimers. Also, calculated wavenumbers (ω(th)) in cm^{-1}, scattering activities (A_{Raman}) in Å^4·u^{-1}, scattering cross sections (σ') in 10^{-36}·m^2·sr^{-1}, and IR intensities (I_{IR}) in km·mol^{-1} of the O-D stretching vibration on different levels are listed. The B3-S level does not predict the correct order.

Conformer	D_0	ω(th)	A_{Raman}	σ'	I_{IR}
B3-S					
w$_d$w$_d$w$_u$	70.00	2541	146	271	13
		2576	20	36	275
		2586	21	38	243
		2816	31	49	51
		2822	31	50	55
		2822	33	53	48
m$_u$w$_d$w$_d$	69.50	2535	132	246	101
		2579	45	81	243
		2602	28	51	292
		2819	36	57	57
		2821	37	58	50
m$_d$w$_d$w$_u$	69.71	2534	139	258	78
		2570	29	52	286
		2609	38	67	274
		2814	34	54	57
		2821	34	54	50
m$_d$m$_d$w$_u$	68.76	2541	127	236	114
		2593	69	125	244
		2604	30	54	381
		2815	38	60	56
m$_d$m$_u$w$_d$	68.82	2552	157	290	24
		2581	41	74	401
		2604	31	56	321
		2819	37	59	55
m$_d$m$_d$m$_u$	67.92	2564	164	300	43
		2594	49	89	396
		2601	37	66	415

Table E.9.: continuation

Conformer	D_0	ω(th)	A_{Raman}	σ'	I_{IR}
MP2-S					
$w_d w_d w_u$	74.02	2631	142	250	8
		2661	13	22	208
		2668	14	25	182
		2876	29	45	52
		2879	22	34	68
		2881	26	40	96
$m_u w_d w_d$	75.49	2618	116	206	91
		2661	44	76	176
		2683	19	32	236
		2874	29	44	73
		2880	31	47	77
$m_d w_d w_u$	75.28	2613	117	208	95
		2655	35	61	187
		2688	25	43	221
		2869	28	44	75
		2881	27	42	76
$m_d m_d w_u$	76.70	2611	100	178	127
		2677	65	111	161
		2688	19	33	311
		2868	30	47	75
$m_d m_u w_d$	76.50	2627	140	248	21
		2652	25	44	354
		2684	24	42	253
		2876	32	50	76
$m_d m_d m_u$	77.74	2630	122	215	95
		2660	38	67	352
		2683	37	64	287

Table E.9.: continuation

Conformer	D_0	ω(th)	A_{Raman}	σ'	I_{IR}
MP2-M					
$w_d w_d w_u$	55.87	2614	145	259	7
		2654	14	25	245
		2661	14	25	217
		2856	22	34	89
		2860	24	37	99
		2861	27	42	57
$m_u w_d w_d$	59.06	2588	115	207	124
		2650	47	82	205
		2678	19	33	260
		2853	28	43	88
		2859	29	45	80
$m_d w_d w_u$	58.92	2589	120	216	107
		2643	35	62	229
		2681	25	43	256
		2851	26	40	91
		2859	26	40	77
$m_d m_d w_u$	62.18	2584	118	213	97
		2637	47	82	355
		2678	27	46	284
		2852	29	45	84
$m_d m_u w_d$	61.96	2596	142	256	32
		2631	25	44	426
		2675	26	45	280
		2855	31	48	81
$m_d m_d m_u$	65.31	2597	145	261	17
		2639	31	54	428
		2646	27	48	440

Table E.9.: continuation

Conformer	D_0	$\omega(\text{th})$	A_{Raman}	σ'	I_{IR}
MP2-L					
$w_d w_d w_u$	51.68	2624	143	253	6
		2668	14	25	250
		2674	14	24	227
		2876	20	31	92
		2880	22	34	94
		2881	26	39	67
$m_u w_d w_d$	55.98	2598	113	203	122
		2660	44	76	216
		2693	22	37	275
		2872	26	40	91
		2877	28	43	81
$m_d w_d w_u$	55.94	2601	118	211	106
		2656	34	60	240
		2696	26	44	273
		2873	24	37	93
		2880	25	38	79
$m_d m_d w_u$	60.40	2597	119	213	88
		2650	44	76	387
		2693	28	47	299
		2875	28	42	86
$m_d m_u w_d$	60.22	2606	139	249	31
		2644	26	45	444
		2688	26	45	301
		2876	29	45	83
$m_d m_d m_u$	64.77	2607	146	260	13
		2652	30	52	474
		2659	27	47	445

Table E.10.: Dissociation energies without (D_e) and with zero point energy correction (D_0) in kJ·mol^{-1} for **m$_3$w** and **m$_4$**. Also, calculated wavenumbers (ω(th)) in cm^{-1}, scattering activities (A_{Raman}) in Å^4·u^{-1}, scattering cross sections (σ') in 10^{-36}·m^2·sr^{-1}, and IR intensities (I_{IR}) in km·mol^{-1} of the O-H stretching vibration on different levels are listed.

Conformer	D_e	D_0	ω(th)	A_{Raman}	σ'	I_{IR}
B3-S						
m$_3$w	147.40	119.34	3325	398	487	100
			3399	38	45	1555
			3425	59	68	1329
			3457	131	150	372
			3858	78	74	52
m$_4$	143.10	119.33	3337	429	521	0
			3416	23	27	1681
			3416	23	27	1681
			3448	194	223	159
MP2-S						
m$_3$w	161.39	132.88	3451	372	427	62
			3515	16	17	1455
			3535	72	80	1021
			3579	89	96	421
			3926	70	64	81
m$_4$	160.59	136.12	3443	381	440	0
			3517	20	22	1519
			3517	20	22	1519
			3549	157	172	161
MP2-M						
m$_3$w	134.68	109.54	3330	362	441	107
			3420	19	22	1775
			3452	74	85	1203
			3519	85	94	564
			3899	67	62	89
m$_4$	136.84	115.57	3314	367	451	0
			3421	21	25	1905
			3421	21	25	1905
			3467	147	168	196

Table E.11.: Dissociation energies without (D_e) and with zero point energy correction (D_0) in kJ·mol^{-1} of pure and mixed ethanol-water dimers for dissociation into e$_t$ and w (values for dissociation into e$_g$ and w are given in parentheses). Also, calculated wavenumbers (ω(th)) in cm^{-1}, scattering activities (A_{Raman}) in Å^4·u^{-1}, scattering cross sections (σ') in 10^{-36}·m^2·sr^{-1}, and IR intensities (I_{IR}) in km·mol^{-1} of the donor (D) and acceptor (A) symmetric (*sym*) and asymmetric (*asym*) O-H stretching vibration on different levels are listed. The S basis set does not predict the correct order.

Conformer	D_e	D_0	Vibration	ω(th)	A_{Raman}	σ'	I_{IR}
B3-S							
ww	30.98	19.93	D$_{sym}$	3650	163	170	301
			A$_{sym}$	3779	82	81	6
			D$_{asym}$	3849	57	54	64
			A$_{asym}$	3889	36	34	60
we$_{g+}$	29.47	20.22	D$_{sym}$	3610	168	178	387
		(21.13)	A	3784	68	67	18
			D$_{asym}$	3845	65	62	60
we$_t$	29.69	20.51	D$_{sym}$	3616	171	182	376
			A	3798	98	96	24
			D$_{asym}$	3845	56	54	63
we$_{g-}$	28.59	19.98	D$_{sym}$	3618	207	220	433
		(20.89)	A	3783	66	65	19
			D$_{asym}$	3845	59	56	68
e$_t$w	28.99	21.06	D	3667	228	236	400
			A$_{sym}$	3780	91	89	4
			A$_{asym}$	3891	39	37	60
e$_g$w	27.93	19.45	D	3661	171	178	341
		(20.36)	A$_{sym}$	3780	91	90	4
			A$_{asym}$	3890	39	37	60
e$_{g+}$e$_{g+}$	25.58	19.58	D	3624	188	198	430
		(21.40)	A	3784	71	70	18
e$_t$e$_t$	27.03	21.05	D	3636	243	256	485
			A	3799	97	95	23
e$_{g-}$e$_t$	26.02	19.67	D	3628	183	193	421
		(20.58)	A	3798	92	90	22
e$_{g-}$e$_{g-}$	25.21	19.09	D	3630	221	233	470
		(20.91)	A	3784	64	63	18

Table E.11.: continuation

Conformer	D_e	D_0	Vibration	ω(th)	A_{Raman}	σ'	I_{IR}
MP2-S							
ww	32.71	21.69	D_{sym}	3754	141	141	238
			A_{sym}	3835	78	74	6
			D_{asym}	3939	47	43	105
			A_{asym}	3969	32	29	80
we_{g+}	34.11	23.87	D_{sym}	3699	135	138	290
		(25.49)	A	3831	61	59	25
			D_{asym}	3926	55	51	91
we_t	34.37	24.05	D_{sym}	3711	144	146	300
			A	3836	87	83	31
			D_{asym}	3929	47	43	100
we_{g-}	31.89	22.22	D_{sym}	3716	168	170	347
		(23.84)	A	3831	60	58	27
			D_{asym}	3930	49	45	108
$e_t w$	32.93	24.32	D	3750	171	171	369
			A_{sym}	3834	89	86	4
			A_{asym}	3970	35	31	81
$e_g w$	32.63	23.35	D	3748	126	126	306
		(24.97)	A_{sym}	3831	90	86	3
			A_{asym}	3967	35	31	80
$e_{g+}e_{g+}$	34.57	26.54	D	3695	124	127	358
		(29.78)	A	3829	72	69	25
$e_t e_t$	35.32	27.69	D	3704	172	175	429
			A	3837	90	87	32
$e_{g-}e_t$	35.32	27.36	D	3702	127	129	362
		(28.98)	A	3834	85	82	31
$e_{g-}e_{g-}$	32.00	24.71	D	3708	149	152	401
		(27.95)	A	3831	62	60	26

Table E.11.: continuation

Conformer	D_e	D_0	Vibration	ω(th)	A_{Raman}	σ'	I_{IR}
MP2-M							
ww	24.39	15.06	D_{sym}	3740	149	149	287
			A_{sym}	3824	66	63	17
			D_{asym}	3927	44	41	113
			A_{asym}	3944	28	26	98
we_{g+}	28.22	19.67	D_{sym}	3680	133	137	341
		(20.98)	A	3831	57	55	39
			D_{asym}	3917	56	52	104
we_t	28.12	19.67	D_{sym}	3681	139	143	349
			A	3837	81	78	48
			D_{asym}	3917	49	46	108
we_{g-}	26.04	17.86	D_{sym}	3688	160	164	393
		(19.16)	A	3829	55	53	40
			D_{asym}	3919	49	45	115
$e_t w$	24.31	17.43	D	3742	188	188	432
			A_{sym}	3823	72	69	10
			A_{asym}	3944	30	27	98
$e_g w$	23.74	16.63	D	3740	138	138	351
			A_{sym}	3820	76	73	10
			A_{asym}	3942	30	28	98
$e_{g+}e_{g+}$	29.12	23.10	D	3678	122	126	403
			A	3828	67	65	37
$e_t e_t$	29.44	23.67	D	3685	172	176	500
			A	3838	90	87	48
$e_{g-}e_t$	29.23	23.32	D	3687	124	127	408
			A	3837	83	79	48
$e_{g-}e_{g-}$	26.02	20.96	D	3703	134	136	407
			A	3832	63	61	39

Table E.11.: continuation

Conformer	D_e	D_0	Vibration	ω(th)	A_{Raman}	σ'	I_{IR}
MP2-L							
ww	22.24	13.09	D_{sym}	3763	148	147	297
			A_{sym}	3849	65	62	15
			D_{asym}	3957	39	36	120
			A_{asym}	3973	23	21	99
we_{g+}	27.38	19.02	D_{sym}	3705	130	133	349
		(19.95)	A	3863	57	54	39
			D_{asym}	3948	53	48	109
we_t	27.12	18.88	D_{sym}	3707	137	139	364
			A	3869	80	75	49
			D_{asym}	3949	45	41	114
we_{g-}	25.22	17.31	D_{sym}	3714	168	171	420
		(18.24)	A	3861	60	57	42
			D_{asym}	3951	49	44	122
$e_t w$	22.15	15.68	D	3765	190	188	454
			A_{sym}	3848	71	68	10
			A_{asym}	3973	25	22	98
$e_g w$	22.72	15.17	D	3762	139	138	373
		(16.10)	A_{sym}	3846	74	71	10
			A_{asym}	3971	25	23	97
$e_{g+}e_{g+}$	30.72	23.22	D	3704	118	120	406
		(25.09)	A	3860	67	63	38
$e_t e_t$	28.69	23.25	D	3711	167	170	506
			A	3872	67	81	49
$e_{g-}e_t$	28.83	23.15	D	3712	120	122	416
		(25.02)	A	3871	82	78	49
$e_{g-}e_{g-}$	26.86	19.62	D	3678	133	137	412
		(21.48)	A	3804	63	62	39

Table E.12.: Dissociation energies with zero point energy correction (D_0) in kJ·mol^{-1} for pure and mixed deuterated ethanol-deuterium oxide dimers for dissociation into e_t and w (values for dissociation into e_g and w are given in parentheses). Also, calculated wavenumbers (ω(th)) in cm^{-1}, scattering activities (A_{Raman}) in Å^4·u^{-1}, scattering cross sections (σ') in 10^{-36}·m^2·sr^{-1}, and IR intensities (I_{IR}) in km·mol^{-1} of the donor (D) and acceptor (A) symmetric (*sym*) and asymmetric (*asym*) O-D stretching vibration on different levels are listed. Only the L basis set does predict the correct order.

Conformer	D_0	Vibration	ω(th)	A_{Raman}	σ'	I_{IR}
B3-S						
ww	22.69	D$_{sym}$	2637	86	150	143
		A$_{sym}$	2721	43	72	5
		D$_{asym}$	2814	28	45	59
		A$_{asym}$	2853	19	29	36
we$_{g+}$	22.19	D$_{sym}$	2611	87	154	188
	(23.10)	A	2754	41	67	13
		D$_{asym}$	2809	30	48	59
we$_t$	22.49	D$_{sym}$	2616	87	155	183
		A	2764	50	82	17
		D$_{asym}$	2809	28	44	61
e$_{g+}$e$_{g+}$	20.54	D	2640	103	180	247
	(22.36)	A	2755	43	71	13
MP2-S						
ww	24.42	D$_{sym}$	2708	73	123	112
		A$_{sym}$	2761	41	68	6
		D$_{asym}$	2884	24	37	80
		A$_{asym}$	2912	17	25	48
we$_{g+}$	26.06	D$_{sym}$	2672	71	122	137
	(27.50)	A	2789	36	59	18
		D$_{asym}$	2872	26	40	77
we$_t$	26.28	D$_{sym}$	2681	73	126	143
		A	2793	45	72	22
		D$_{asym}$	2874	23	36	82
e$_{g+}$e$_{g+}$	27.90	D	2691	69	118	206
	(30.76)	A	2788	42	68	18

Table E.12.: continuation

Conformer	D_0	Vibration	$\omega(\text{th})$	A_{Raman}	σ'	I_{IR}
MP2-M						
ww	17.37	D_{sym}	2703	79	134	136
		A_{sym}	2756	34	56	12
		D_{asym}	2871	22	34	85
		A_{asym}	2890	15	22	57
we$_{g+}$	21.48	D_{sym}	2663	71	123	163
	(22.74)	A	2788	35	56	26
		D_{asym}	2861	26	40	84
we$_t$	21.50	D_{sym}	2664	73	126	167
		A	2794	42	68	31
		D_{asym}	2861	23	36	86
e$_{g+}$e$_{g+}$	23.99	D	2679	69	119	229
	(26.52)	A	2786	41	66	24
MP2-L						
ww	15.36	D_{sym}	2720	79	133	140
		A_{sym}	2774	33	54	11
		D_{asym}	2893	19	29	89
		A_{asym}	2911	12	18	57
we$_{g+}$	20.78	D_{sym}	2682	70	119	167
	(21.72)	A	2812	35	56	26
		D_{asym}	2883	24	37	87
we$_t$	20.67	D_{sym}	2683	72	123	175
		A	2817	42	66	32
		D_{asym}	2884	21	32	89
e$_{g+}$e$_{g+}$	24.03	D	2698	68	115	231
	(25.92)	A	2810	41	66	25

Table E.13.: Dissociation energies without (D_e) and with zero point energy correction (D_0) in kJ·mol^{-1} for pure and mixed ethanol-water trimers (trans conformation and equal molecules pointing in the same direction). Also, calculated wavenumbers (ω(th)) in cm^{-1}, scattering activities (A_{Raman}) in Å^4·u^{-1}, scattering cross sections (σ') in 10^{-36}·m^2·sr^{-1}, and IR intensities (I_{IR}) in km·mol^{-1} of the O-H stretching vibration on different levels are listed.

Conformer	D_e	D_0	ω(th)	A_{Raman}	σ'	I_{IR}
B3-S						
www	90.41	63.54	3503	257	288	29
			3554	38	42	556
			3571	42	45	488
			3859	70	66	54
			3864	65	61	61
			3866	73	69	53
eww	86.61	63.96	3489	266	300	228
			3557	105	114	481
			3581	56	60	553
			3862	73	69	60
			3866	89	84	53
eew	82.57	63.60	3498	287	323	184
			3562	165	180	519
			3576	79	85	737
			3857	83	79	59
eee	77.79	63.24	3516	424	472	54
			3559	124	135	818
			3571	110	120	769

Table E.13.: continuation

Conformer	D_e	D_0	ω(th)	A_{Raman}	σ'	I_{IR}
MP2-S						
www	93.90	67.82	3636	249	262	20
			3680	27	28	433
			3692	30	30	377
			3935	65	59	67
			3939	50	45	96
			3943	56	51	101
eww	93.66	70.61	3599	225	241	218
			3667	105	108	391
			3689	27	28	396
			3929	62	57	86
			3939	75	68	89
eew	92.93	73.13	3593	278	298	57
			3635	61	64	611
			3668	56	58	484
			3924	75	69	89
eee	91.79	75.91	3582	334	360	18
			3627	80	85	686
			3635	77	81	723
MP2-M						
www	73.78	50.18	3609	258	275	15
			3667	29	30	499
			3678	29	30	450
			3911	46	43	117
			3915	44	41	131
			3916	67	62	70
eww	75.59	55.49	3547	209	229	324
			3654	119	123	362
			3682	30	31	481
			3908	58	53	107
			3915	71	66	102
eew	77.95	61.19	3542	255	281	125
			3600	62	66	731
			3669	64	67	481
			3905	74	68	105
eee	79.75	67.08	3535	328	361	20
			3600	72	77	824
			3610	79	84	823

Table E.13.: continuation

Conformer	D_e	D_0	ω(th)	A_{Raman}	σ'	I_{IR}
MP2-L						
www	69.08	46.16	3621	269	254	11
			3685	29	28	518
			3694	28	28	475
			3939	40	44	120
			3943	33	36	140
			3944	64	70	71
eww	72.25	52.80	3566	227	209	304
			3671	114	110	402
			3700	33	32	518
			3939	48	53	113
			3944	64	70	104
eew	76.05	59.75	3936			109
			3689			497
			3617			771
			3557			118

F. Quantum Chemical Predictions of the Investigated Microcrystals

F.1. Methyl Mandelate

Table F.1.: Predicted harmonic wavenumbers ω in cm^{-1} and intensities I in km·mol^{-1} of a methyl mandelate monomer unit relaxed from the crystal structure (Mon$_{crystal}$) and the most stable methyl mandelate monomer (Mon$_{stable}$) on the B3LYP/6-311++G(3df,2p) and MP2/6-311++G(2d,p) level. The stretching and bending vibrations are indicated as ν and δ and the symmetric and asymmetric vibrations with sym and asym.

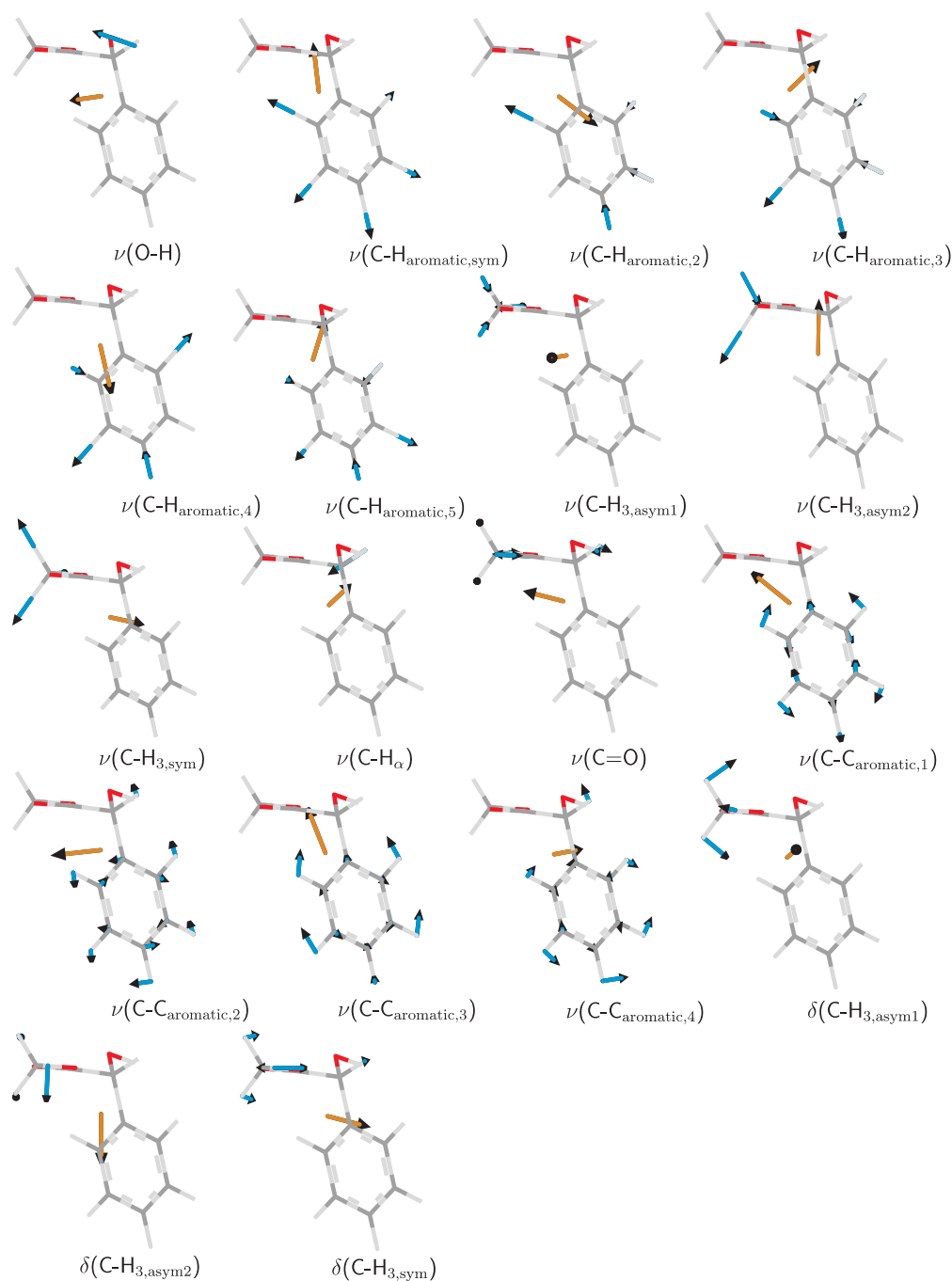| | B3LYP/6-311++G(3df,2p) | | | | MP2/6-311++G(2d,p) | | | |
| | Mon$_{crystal}$ | | Mon$_{stable}$ | | Mon$_{crystal}$ | | Mon$_{stable}$ | |
Assignment	ω	I	ω	I	ω	I	ω	I
ν(O-H)	3835	36	3723	105	3818	42	3714	109
ν(C-H$_{aromatic,sym}$)	3190	9	3193	6	3214	10	3194	5
ν(C-H$_{aromatic,2}$)	3184	12	3184	17	3205	9	3185	18
ν(C-H$_{aromatic,3}$)	3174	16	3173	19	3197	4	3174	19
ν(C-H$_{aromatic,4}$)	3164	1	3163	1	3189	1	3164	1
ν(C-H$_{aromatic,5}$)	3156	3	3155	3	3181	3	3157	3
ν(C-H$_{3,asym1}$)	3152	12	3159	9	3215	8	3162	9
ν(C-H$_{3,asym2}$)	3121	17	3127	14	3183	12	3131	13
ν(C-H$_{3,sym}$)	3050	31	3054	28	3093	28	3057	28
ν(C-H$_{\alpha}$)	3019	24	3012	18	3066	18	3017	18
ν(C=O)	1817	214	1777	243	1790	176	1767	246
ν(C-C$_{aromatic,1}$)	1640	1	1641	4	1634	1	1641	4
ν(C-C$_{aromatic,2}$)	1624	1	1626	0	1618	1	1626	0
ν(C-C$_{aromatic,3}$)	1527	7	1528	9	1518	6	1530	10
ν(C-C$_{aromatic,4}$)	1488	9	1488	8	1480	10	1489	8
δ(C-H$_{3,asym1}$)	1501	10	1499	9	1530	10	1495	10
δ(C-H$_{3,asym2}$)	1488	9	1488	10	1521	8	1484	9
δ(C-H$_{3,sym}$)	1476	12	1478	15	1499	7	1473	14

Figure F.1.: Fundamental stretching (ν) and bending modes (δ) of a methyl mandelate monomer along the crystallographic b axis (B3LYP/6-311++G(3df,2p) level). The relaxed monomer was taken from the crystal structure of enantiopure methyl mandelate (see Chapter 5) [38]. The direction of the vibrational transition dipole vectors (yellow, unit length) as well as the displacement vectors of each mode (blue) are indicated.
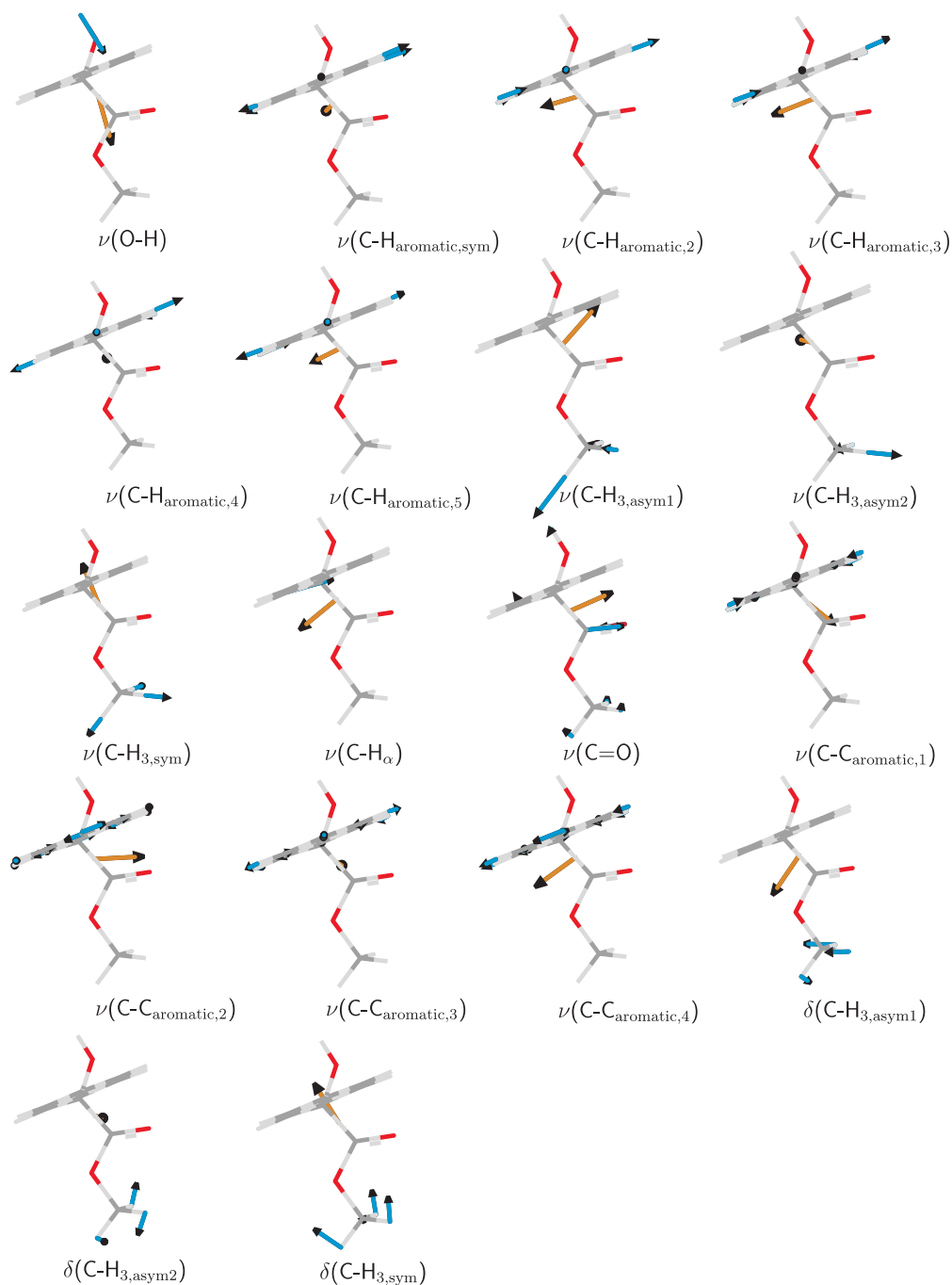
Figure F.2.: Fundamental stretching (ν) and bending modes (δ) of a methyl mandelate monomer along the crystallographic *a* axis (B3LYP/6-311++G(3df,2p) level). The relaxed monomer was taken from the crystal structure of enantiopure methyl mandelate (see Chapter 5) [38]. The direction of the vibrational transition dipole vectors (yellow, unit length) as well as the displacement vectors of each mode (blue) are indicated.

F.2. Mandelic Acid

Table F.2.: Predicted harmonic wavenumbers ω in cm^{-1} and intensities I in km·mol^{-1} of a mandelic acid monomer unit relaxed from the crystal structure (Mon$_{crystal}$) on the B3LYP/6-311++G(3df,2p) (B3LYP) and MP2/6-311++G(2d,p) (MP2) level (see Figs. F.3 and F.4). The stretching vibrations are indicated as ν and the symmetric vibration with sym.

|	B3LYP		MP2	
Assignment	ω	I	ω	I
ν(O-H)$_{alcoholic}$	3733	107	3730	111
ν(O-H)$_{acidic}$	3757	82	3748	99
ν(C-H$_{aromatic,sym}$)	3193	6	3217	6
ν(C-H$_{aromatic,2}$)	3185	16	3210	9
ν(C-H$_{aromatic,3}$)	3175	17	3200	10
ν(C-H$_{aromatic,4}$)	3165	2	3191	1
ν(C-H$_{aromatic,5}$)	3157	2	3182	3
ν(C-H$_{\alpha}$)	3007	17	3038	12
ν(C=O)	1800	316	1780	263
ν(C-C$_{aromatic,1}$)	1641	4	1635	3
ν(C-C$_{aromatic,2}$)	1626	0	1621	0
ν(C-C$_{aromatic,3}$)	1528	10	1520	8
ν(C-C$_{aromatic,4}$)	1487	8	1478	9
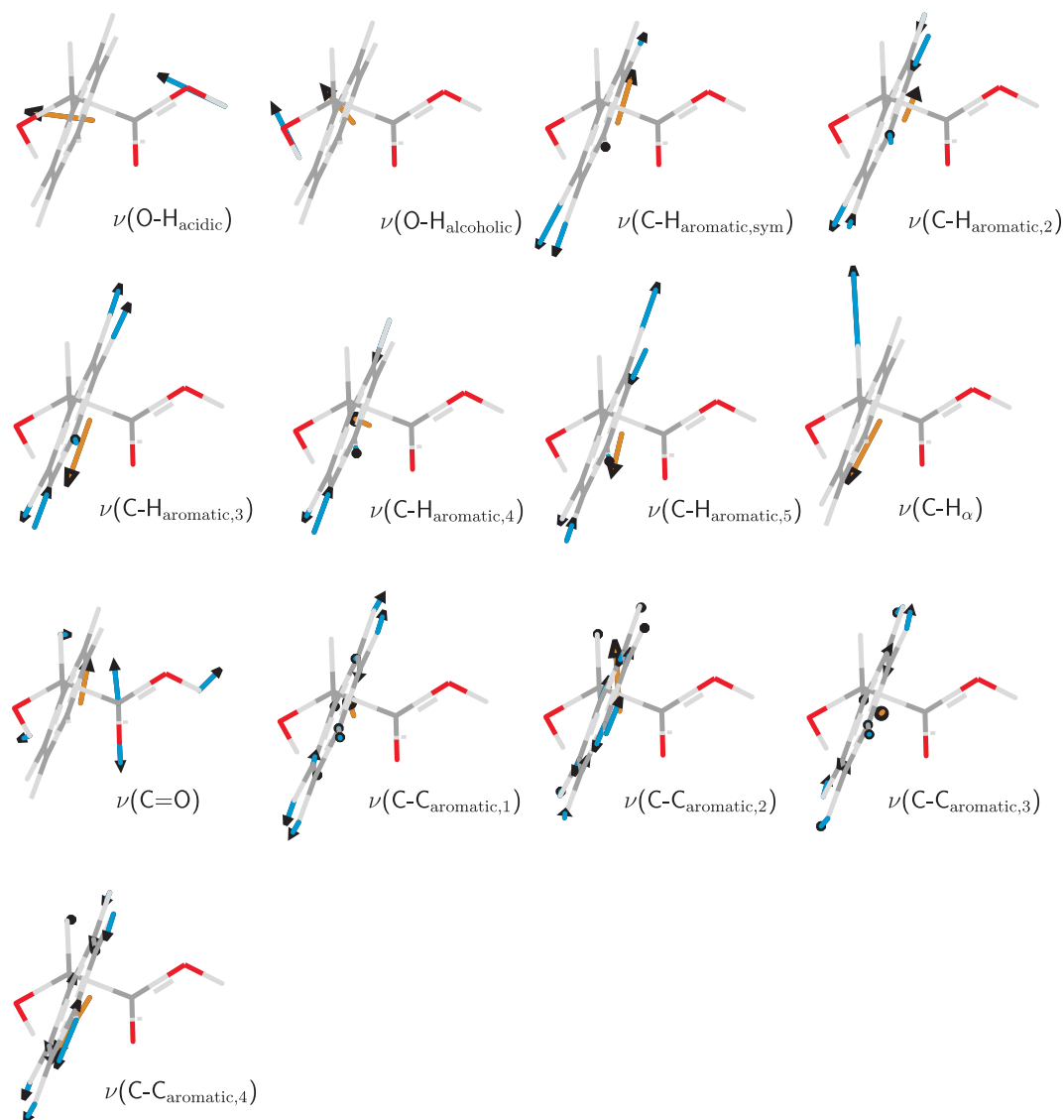
Figure F.3.: Fundamental stretching (ν) and bending modes (δ) of mandelic acid along the crystallographic c axis (B3LYP/6-311++G(3df,2p) level). The relaxed monomer was taken from the crystal structure of enantiopure mandelic acid [88]. The direction of the vibrational transition dipole vectors (yellow, unit length) as well as the displacement vectors of each mode (blue) are indicated.
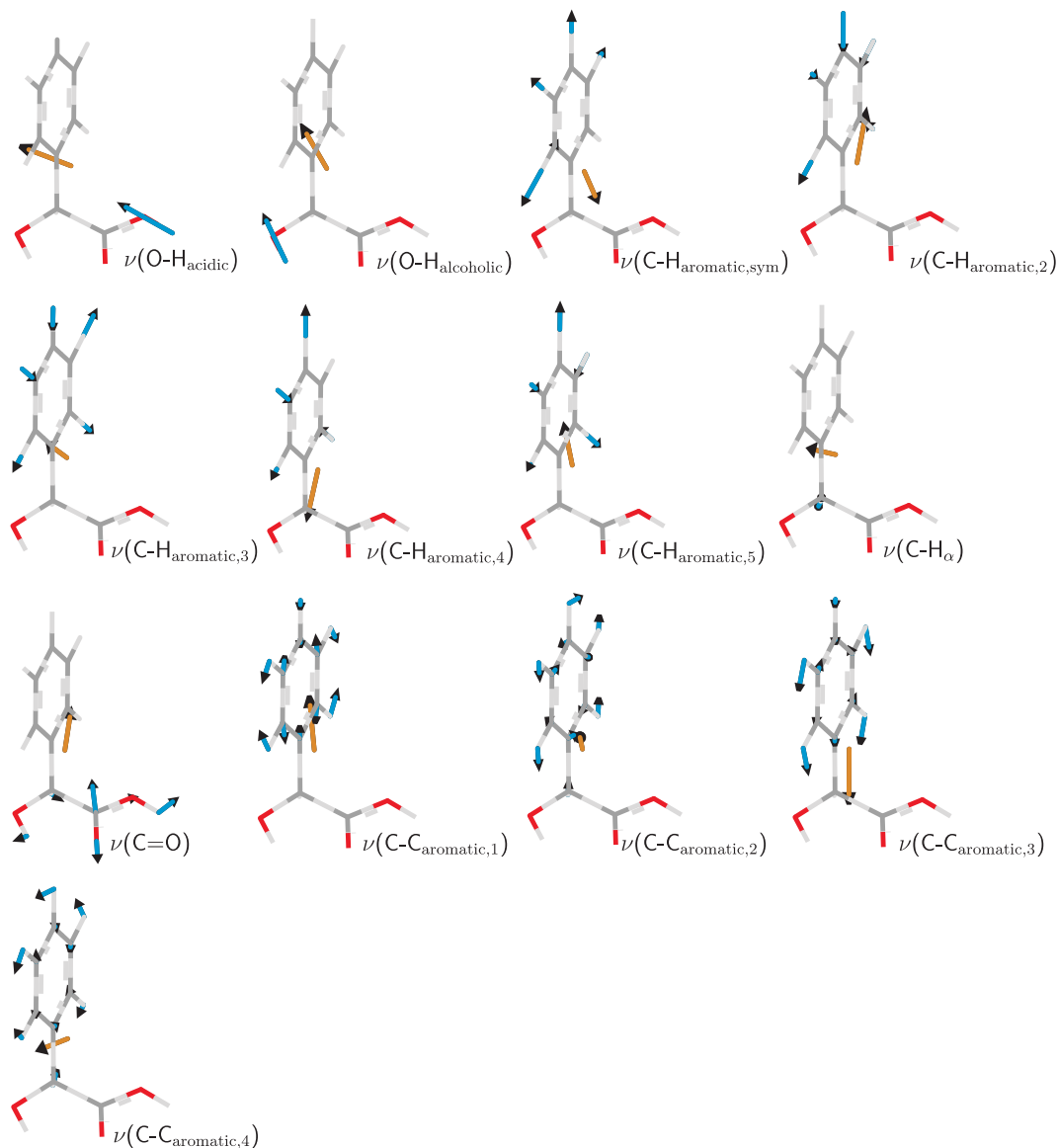
Figure F.4.: Fundamental stretching (ν) and bending modes (δ) of mandelic acid along the crystallographic *a* axis (B3LYP/6-311++G(3df,2p) level). The relaxed monomer was taken from the crystal structure of enantiopure mandelic acid [88]. The direction of the vibrational transition dipole vectors (yellow, unit length) as well as the displacement vectors of each mode (blue) are indicated.

F.3. Norephedrine

Table F.3.: Predicted harmonic wavenumbers ω in cm^{-1} and intensities I in km·mol^{-1} of a relaxed norephedrine monomer unit taken from the crystal structure [89] (Mon$_{crystal}$) and the most stable norephedrine monomer (Mon$_{stable}$) on the B3LYP/6-311++G(3df,2p) level. The stretching and bending vibrations are indicated as ν and δ and the symmetric and asymmetric vibrations with sym and asym.

	Mon$_{crystal}$		Mon$_{stable}$	
Assignment	ω	I	ω	I
ν(O-H)	3831	26	3718	99
ν(N-H)$_{asym}$	3567	3	3582	3
ν(N-H)$_{sym}$	3489	1	3501	0
ν(C-H$_{aromatic,sym}$)	3199	4	3202	3
ν(C-H$_{aromatic,2}$)	3185	18	3183	19
ν(C-H$_{aromatic,3}$)	3172	23	3171	23
ν(C-H$_{aromatic,4}$)	3162	2	3159	1
ν(C-H$_{aromatic,5}$)	3154	4	3146	9
ν(C-H$_{3,asym1}$)	3104	23	3116	16
ν(C-H$_{3,asym2}$)	3089	29	3090	20
ν(C-H$_{3,sym}$)	3028	16	3030	26
ν(C-H$_{\alpha}$)	2978	58	2923	51
ν(C-H$_{\beta}$)	2962	37	2972	45
δ(N-H)	1661	21	1648	40
ν(C-C$_{aromatic,1}$)	1644	2	1644	2
ν(C-C$_{aromatic,2}$)	1622	1	1623	0
ν(C-C$_{aromatic,3}$)	1531	7	1530	10
δ(C-H$_{3,asym1}$)	1504	4	1504	3
δ(C-H$_{3,asym2}$)	1494	6	1496	5
ν(C-C$_{aromatic,4}$)	1485	8	1484	10
δ(O-H/C-H$_{\alpha}$/C-H$_{\beta}$)	1439	20	1427	31
δ(C-H$_{3,sym}$)	1415	11	1423	12

L

ν(O-H) ν(N-H)$_{asym}$ ν(N-H)$_{sym}$ ν(C-H$_{aromatic,sym}$)

ν(C-H$_{aromatic,2}$) ν(C-H$_{aromatic,3}$) ν(C-H$_{aromatic,4}$) ν(C-H$_{aromatic,5}$)

ν(C-H$_{3,asym1}$) ν(C-H$_{3l,asym2}$) ν(C-H$_{3,sym}$) ν(C-H$_{\alpha}$)

ν(C-H$_{\beta}$) δ(N-H) ν(C-C$_{aromatic,1}$) ν(C-C$_{aromatic,2}$)

ν(C-C$_{aromatic,3}$) δ(C-H$_{3,asym1}$) δ(C-H$_{3,asym2}$) ν(C-C$_{aromatic,4}$)

δ(O-H/C-H$_{\alpha}$/C-H$_{\beta}$) δ(C-H$_{3,sym}$)
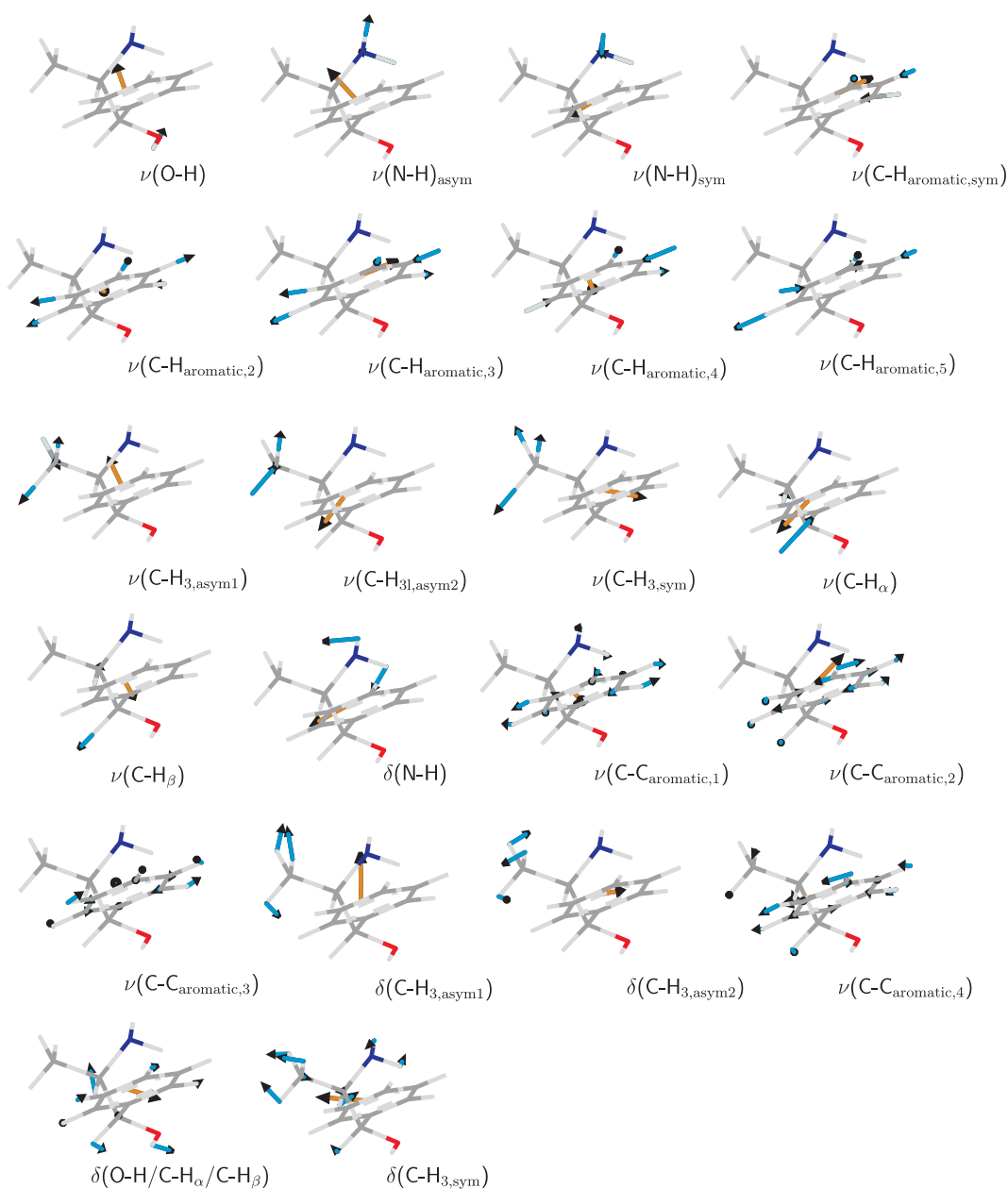
Figure F.5.: Fundamental stretching (ν) and bending modes (δ) of norephedrine along the crystallographic a/c plane (B3LYP/6-311++G(3df,2p) level). The relaxed monomer was taken from the crystal structure of racemic norephedrine [89]. The direction of the vibrational transition dipole vectors (yellow, unit length) as well as the displacement vectors of each mode (blue) are indicated.

F.4. Pseudonorephedrine

Table F.4.: Predicted harmonic wavenumbers ω in cm^{-1} and intensities I in km·mol^{-1} of a relaxed pseudonorephedrine monomer unit taken from the crystal structure [90] (Mon$_{crystal}$) and the most stable norephedrine monomer (Mon$_{stable}$) on the B3LYP/6-311++G(3df,2p) level. The stretching and bending vibrations are indicated as ν and δ and the symmetric and asymmetric vibrations with sym and asym.

|	Mon$_{crystal}$		Mon$_{stable}$	
Assignment	ω	I	ω	I
ν(O-H)	3839	30	3683	136
ν(N-H)$_{asym}$	3586	6	3578	5
ν(N-H)$_{sym}$	3507	2	3491	1
ν(C-H$_{aromatic,sym}$)	3188	10	3189	8
ν(C-H$_{aromatic,2}$)	3181	19	3182	20
ν(C-H$_{aromatic,3}$)	3171	16	3170	21
ν(C-H$_{aromatic,4}$)	3161	0	3160	1
ν(C-H$_{aromatic,5}$)	3153	5	3151	6
ν(C-H$_{3,asym1}$)	3109	24	3100	25
ν(C-H$_{3,asym2}$)	3084	29	3077	32
ν(C-H$_{3,sym}$)	3027	22	3015	16
ν(C-H$_\alpha$)	2996	33	2931	45
ν(C-H$_\beta$)	2933	38	3032	18
δ(N-H)	1644	46	1649	26
ν(C-C$_{aromatic,1}$)	1642	1	1644	1
ν(C-C$_{aromatic,2}$)	1622	0	1624	0
ν(C-C$_{aromatic,3}$)	1528	6	1530	6
δ(C-H$_{3,1}$)	1502	3	1501	7
δ(C-H$_{3,2}$)	1498	5	1493	2
ν(C-C$_{aromatic,4}$)	1486	8	1486	8
δ(C-H$_3$/C-H$_\beta$)	1415	6	1410	5
δ(O-H/C-H$_\alpha$/C-H$_\beta$)	1408	8	1432	66
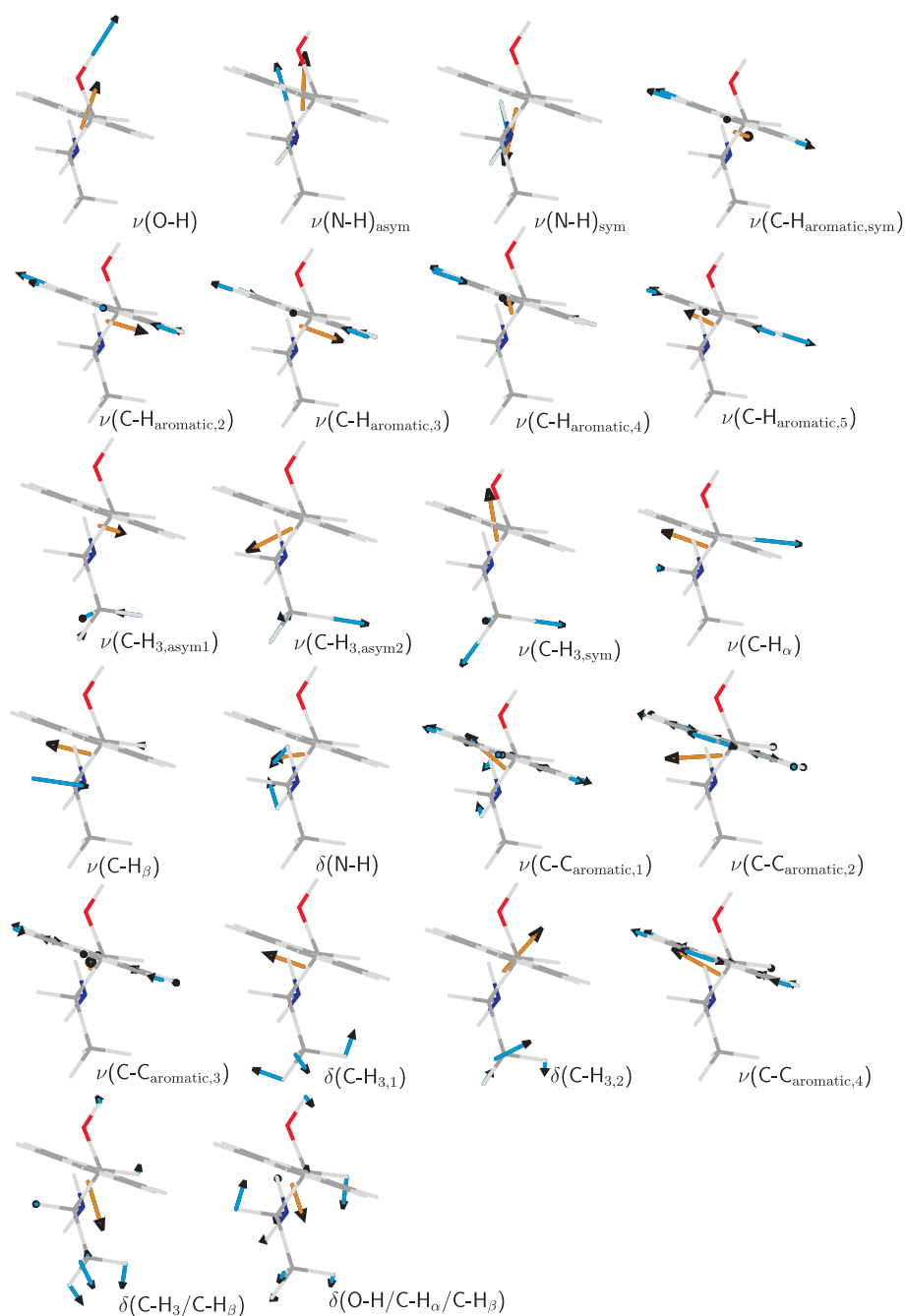
Figure F.6.: Fundamental stretching (ν) and bending modes (δ) of pseudonorephedrine along the crystallographic c axis (B3LYP/6-311++G(3df,2p) level). The relaxed monomer was taken from the crystal structure of enantiopure pseudonorephedrine [90]. The direction of the vibrational transition dipole vectors (yellow) as well as the displacement vectors of each mode (blue) are indicated.
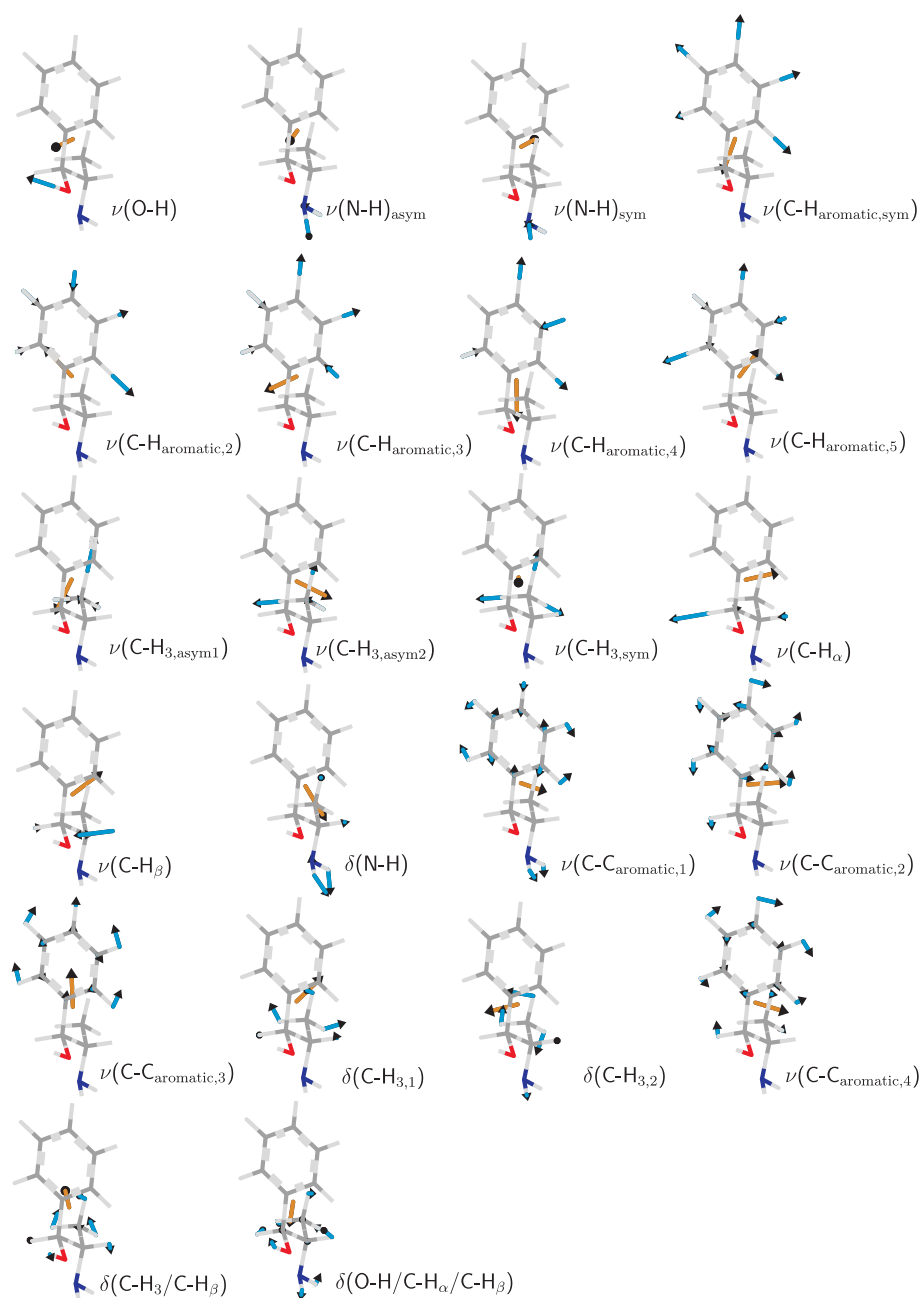
Figure F.7.: Fundamental stretching (ν) and bending modes (δ) of pseudonorephedrine along the crystallographic *b* axis (B3LYP/6-311++G(3df,2p) level). The relaxed monomer was taken from the crystal structure of enantiopure pseudonorephedrine [90]. The direction of the vibrational transition dipole vectors (yellow) as well as the displacement vectors of each mode (blue) are indicated.

F.5. Ephedrine

Table F.5.: Predicted harmonic wavenumbers ω in cm^{-1} and intensities I in km·mol^{-1} of relaxed ephedrine monomer units taken from the crystal structures of ephedrine anhydrate and ephedrine hemihydrate [91] (Mon$_{crystal,AH}$ and Mon$_{crystal,H}$, respectively) and the most stable ephedrine monomer (Mon$_{stable}$) on the B3LYP/6-311++G(3df,2p) level. The stretching and bending vibrations are indicated as ν and δ and the symmetric and asymmetric vibrations with sym and asym.

|	Mon$_{crystal,AH}$		Mon$_{crystal,H}$		Mon$_{stable}$	
Assignment	ω	I	ω	I	ω	I
ν(O-H)	3842	35	3733	99	3701	106
ν(N-H)	3531	5	3498	0	3543	2
ν(C-H$_{aromatic,sym}$)	3189	9	3203	3	3201	3
ν(C-H$_{aromatic,2}$)	3182	18	3184	19	3183	20
ν(C-H$_{aromatic,3}$)	3170	18	3170	23	3170	23
ν(C-H$_{aromatic,4}$)	3160	0	3159	1	3159	1
ν(C-H$_{aromatic,5}$)	3148	6	3146	9	3146	9
ν(C-H$_{3,asym1}$)	3102	20	3114	17	3119	16
ν(C-H$_{3,asym2}$)	3096	32	3108	20	3089	20
ν(NC-H$_{3,asym1}$)	3082	33	3101	24	3098	26
ν(NC-H$_{3,asym2}$)	3038	44	3068	34	3061	28
ν(C-H$_{3,sym}$)	3034	16	3042	13	3029	26
ν(C-H$_{\alpha/\beta,sym}$)	3013	24	2931	68	2957	101
ν(C-H$_{\alpha/\beta,asym}$)	3002	18	2914	43	2939	28
ν(NC-H$_{3,sym}$)	2952	92	2947	88	2952	38
ν(C-C$_{aromatic,1}$)	1642	4	1645	5	1644	7
ν(C-C$_{aromatic,2}$)	1621	0	1623	0	1622	0
ν(C-C$_{aromatic,3}$)	1527	6	1530	9	1530	11
δ(C-H$_{3,1}$/N-H)	1523	16	1524	21	1523	13
δ(C-H$_{3,2}$/N-H)	1509	11	1508	5	1507	5
δ(C-H$_{3,3}$/N-H)	1503	1	1504	1	1502	6
δ(C-H$_{3,4}$/N-H)	1492	4	1498	7	1496	1
ν(C-C$_{aromatic,4}$)	1484	8	1483	9	1484	9
δ(N-H/C-H$_3$)	1481	23	1489	17	1479	12
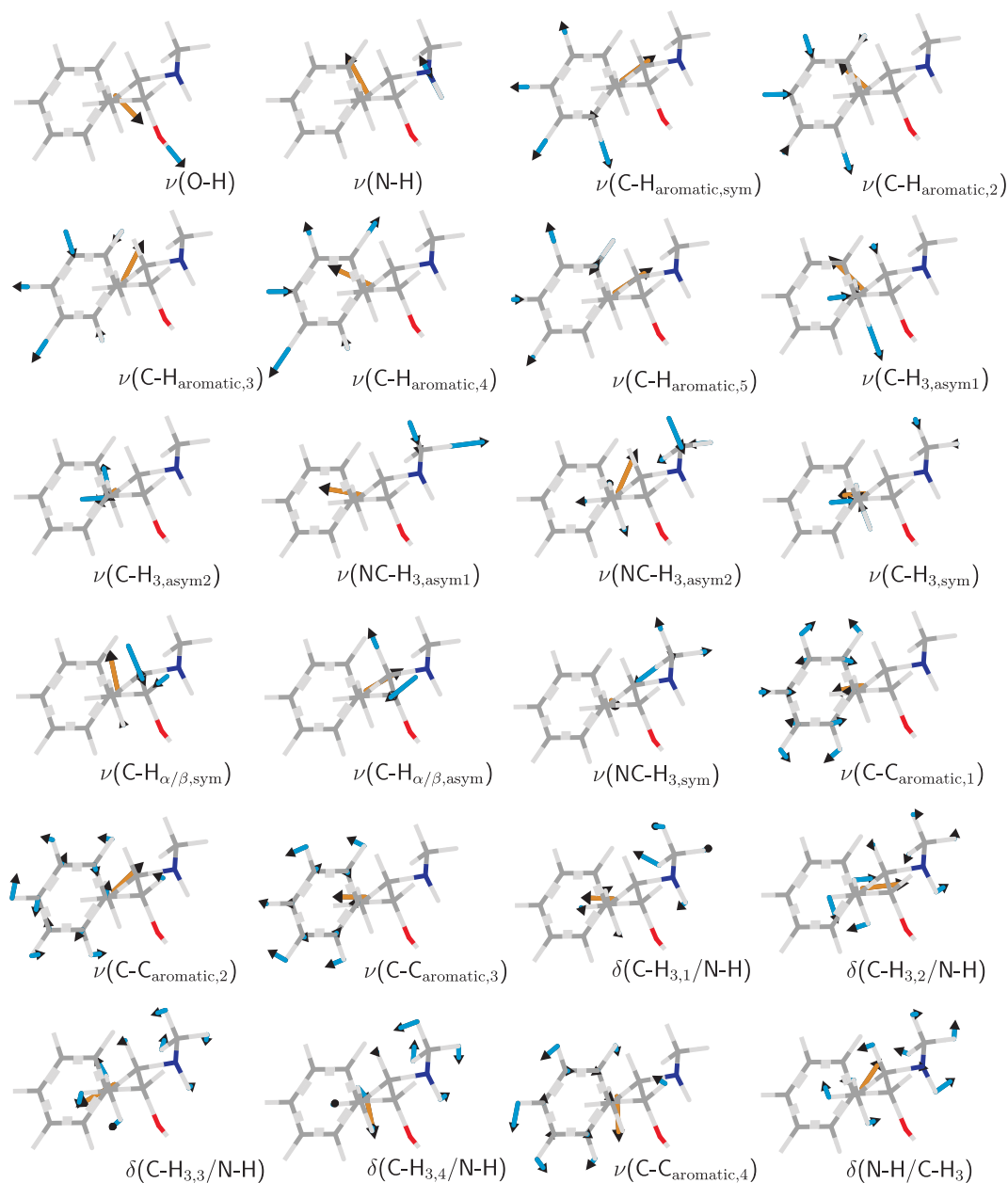
Figure F.8.: Fundamental stretching (ν) and bending modes (δ) of ephedrine along the crystallographic b axis (B3LYP/6-311++G(3df,2p) level). The relaxed monomer was taken from the crystal structure of ephedrine anhydrate [91]. The direction of the vibrational transition dipole vectors (yellow) as well as the displacement vectors of each mode (blue) are indicated.
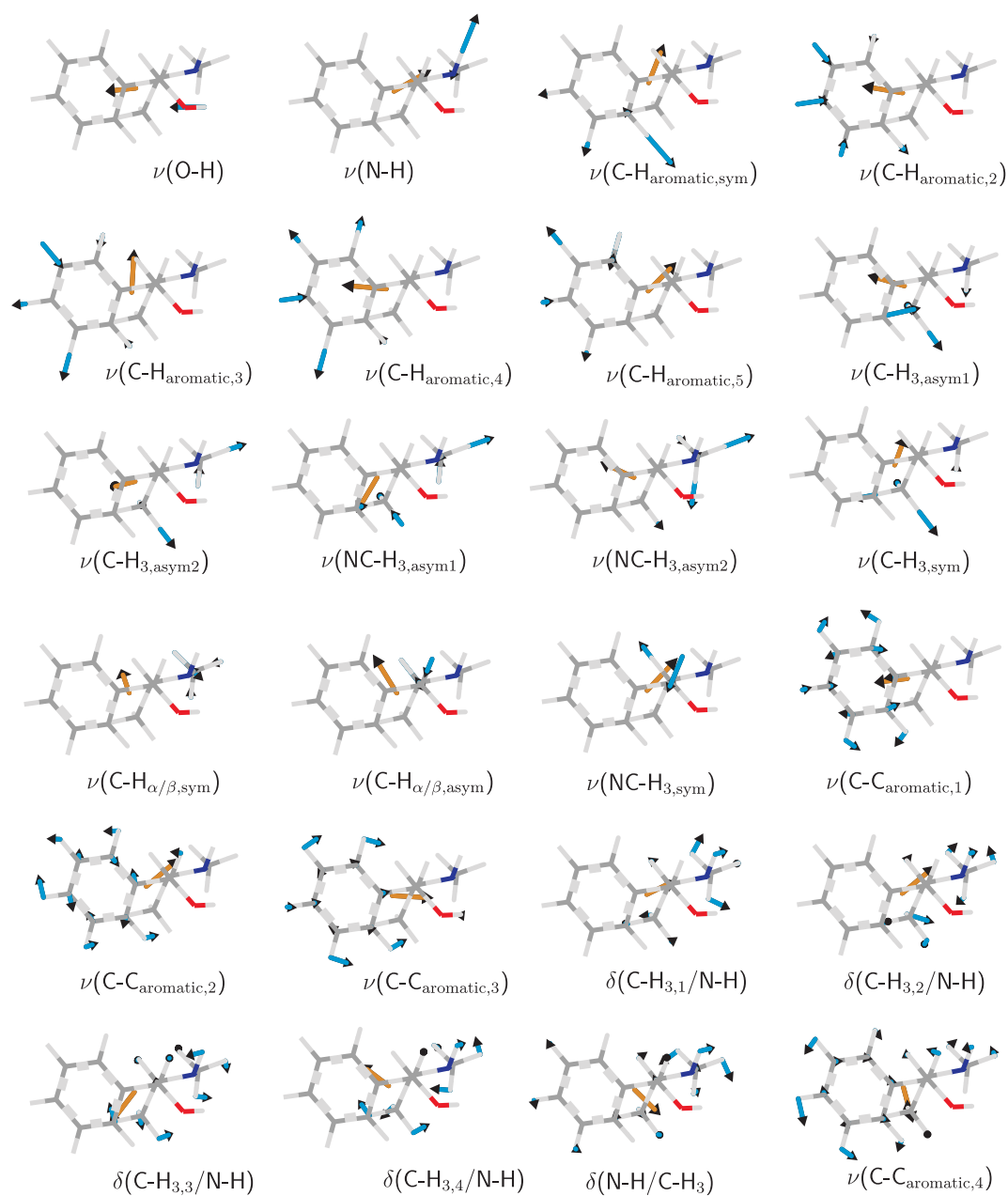
Figure F.9.: Fundamental stretching (ν) and bending modes (δ) of ephedrine along the crystallographic *b* axis (B3LYP/6-311++G(3df,2p) level). The relaxed monomer was taken from the crystal structure of ephedrine hemihydrate [91]. The direction of the vibrational transition dipole vectors (yellow) as well as the displacement vectors of each mode (blue) are indicated.

F.6. Pseudoephedrine

Table F.6.: Predicted harmonic wavenumbers ω in cm^{-1} and intensities I in km·mol^{-1} of a relaxed pseudoephedrine monomer unit taken from the crystal structure [92] (Mon$_{crystal}$) and the most stable pseudoephedrine monomer (Mon$_{stable}$) on the B3LYP/6-311++G(3df,2p) level. The stretching and bending vibrations are indicated as ν and δ and the symmetric and asymmetric vibrations with sym and asym.

| Assignment	Mon$_{crystal}$		Mon$_{stable}$	
	ω	I	ω	I
ν(O-H)	3839	31	3661	162
ν(N-H)	3539	6	3497	1
ν(C-H$_{aromatic,sym}$)	3188	11	3189	7
ν(C-H$_{aromatic,2}$)	3181	19	3182	21
ν(C-H$_{aromatic,3}$)	3171	14	3170	20
ν(C-H$_{aromatic,4}$)	3161	0	3159	1
ν(C-H$_{aromatic,5}$)	3153	5	3150	7
ν(C-H$_{methyl,asym1}$)	3109	28	3102	25
ν(C-H$_{methyl,asym2}$)	3100	26	3081	29
ν(NC-H$_{3,asym1}$)	3091	27	3094	25
ν(NC-H$_{3,asym2}$)	3053	42	3056	32
ν(C-H$_{3,sym}$)	3033	14	3017	11
ν(C-H$_\alpha$)	2993	31	2929	45
ν(NC-H$_{3,sym}$)	2926	108	2969	81
ν(C-H$_\beta$)	2897	48	2927	22
ν(C-C$_{aromatic,1}$)	1642	2	1644	3
ν(C-C$_{aromatic,2}$)	1622	1	1624	0
ν(C-C$_{aromatic,3}$)	1528	5	1530	6
δ(N-H/C-H$_3$)$_1$	1524	40	1520	14
δ(C-H$_3$/N-H)$_1$	1510	2	1509	9
δ(C-H$_3$/N-H)$_2$	1507	4	1497	3
δ(C-H$_3$/N-H)$_3$	1491	8	1495	4
δ(N-H/C-H$_3$)$_2$	1487	16	1487	10
ν(C-C$_{aromatic,4}$)	1486	10	1482	15
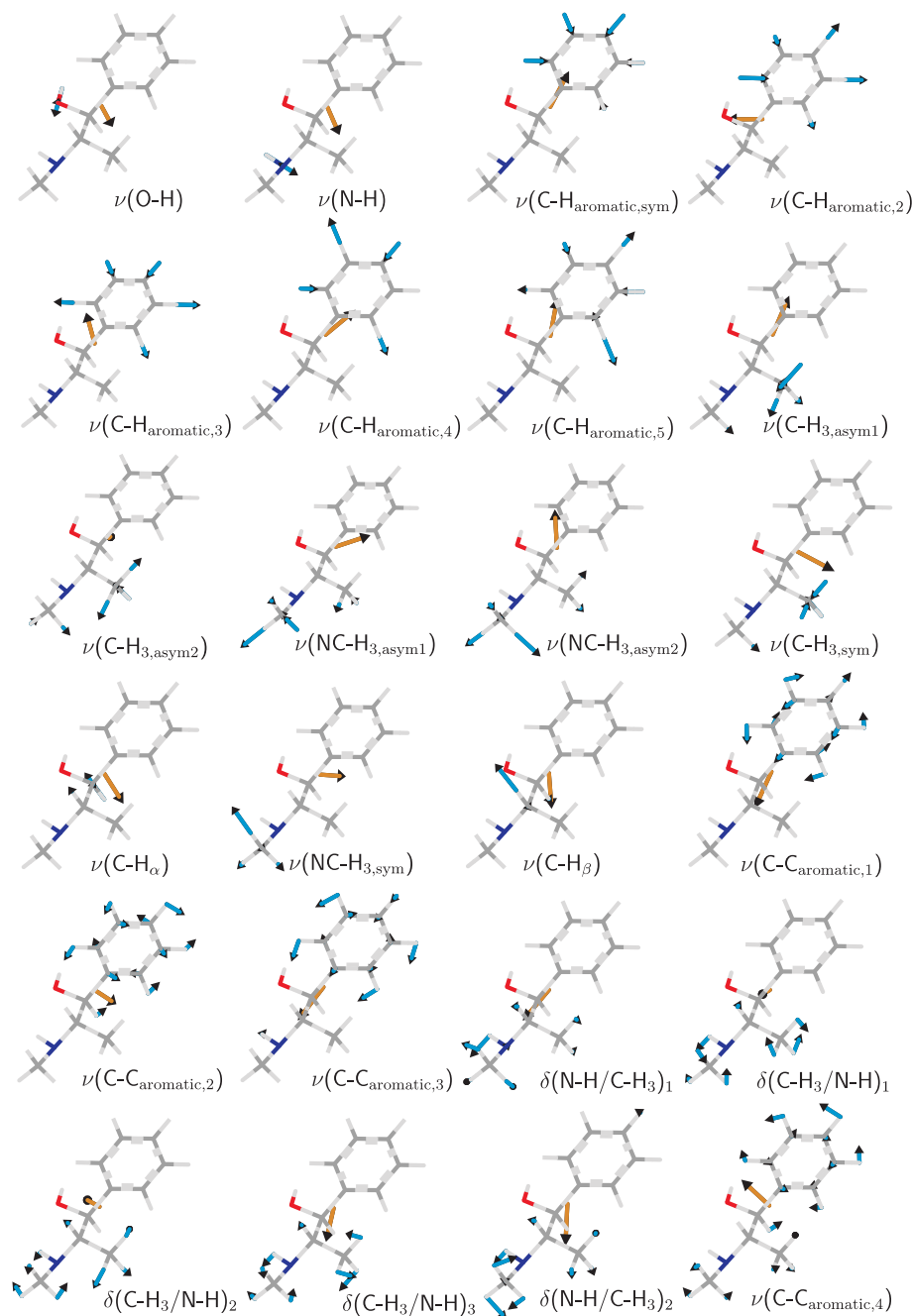
Figure F.10.: Fundamental stretching (ν) and bending modes (δ) of pseudoephedrine along the crystallographic *c* axis (B3LYP/6-311++G(3df,2p) level). The relaxed monomer was taken from the crystal structure of enantiopure pseudoephedrine [92]. The direction of the vibrational transition dipole vectors (yellow) as well as the displacement vectors of each mode (blue) are indicated.
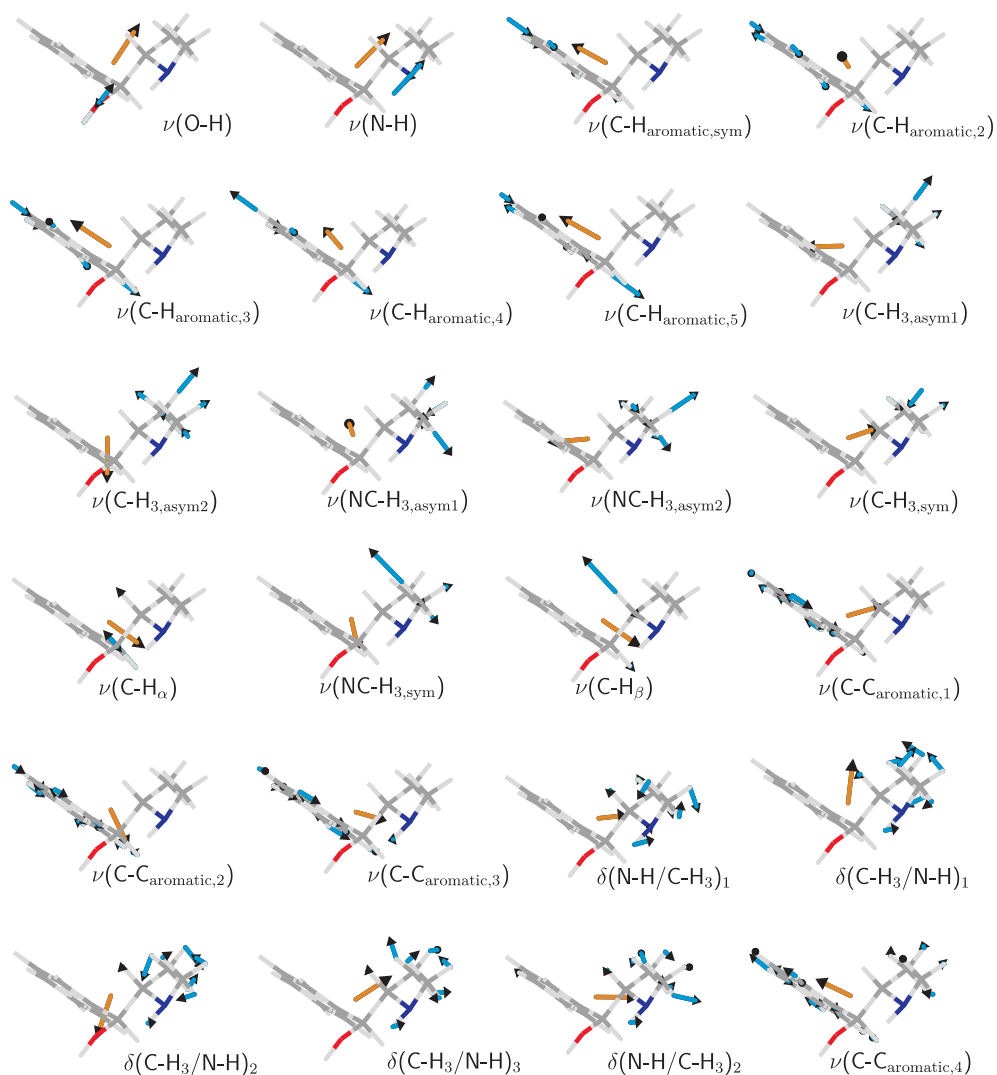
Figure F.11.: Fundamental stretching (ν) and bending modes (δ) of pseu-doephedrine along the crystallographic *a* axis (B3LYP/6-311++G(3df,2p) level). The relaxed monomer was taken from the crystal structure of enantiopure pseudoephedrine [92]. The direction of the vibrational transition dipole vectors (yellow) as well as the displacement vectors of each mode (blue) are indicated.

Bibliography

[1] R. Bentley. The Nose as a Stereochemist. Enantiomers and Odor. *Chem. Rev.*, 106:4099–4112, 2006.

[2] E. Fischer. Einfluss der Configuration auf die Wirkung der Enzyme. *Ber. Dtsch. Chem. Ges.*, 27:2985–2993, 1894.

[3] A. Zehnacker and M. A. Suhm. Chirality Recognition between Neutral Molecules in the Gas Phase. *Angew. Chem. Int. Ed.*, 47:6970–6992, 2008.

[4] A. Zehnacker, editor. *Chiral recognition in the gas phase*. CRC Press, Boca Raton, 2010.

[5] D. Scuderi, K. Le Barbu-Debus, and A. Zehnacker. The role of weak hydrogen bonds in chiral recognition. *Phys. Chem. Chem. Phys.*, 13:17916–17929, 2011.

[6] M. Albrecht, J. Will, and M. A. Suhm. Chirality Recognition in Menthol and Neomenthol: Preference for Homoconfigurational Aggregation. *Angew. Chem. Int. Ed.*, 49:6203–6206, 2010.

[7] E. Arunan, G. R. Desiraju, R. A. Klein, J. Sadlej, S. Scheiner, I. Alkorta, D. C. Clary, R. H. Crabtree, J. J. Dannenberg, P. Hobza, H. G. Kjaergaard, A. C. Legon, B. Mennucci, and D. J. Nesbitt. Defining the hydrogen bond: An account (IUPAC Technical Report). *Pure Appl. Chem.*, 83:1619–1636, 2011.

[8] E. Arunan, G. R. Desiraju, R. A. Klein, J. Sadlej, S. Scheiner, I. Alkorta, D. C. Clary, R. H. Crabtree, J. J. Dannenberg, P. Hobza, H. G. Kjaergaard, A. C. Legon, B. Mennucci, and D. J. Nesbitt. Definition of the hydrogen bond: An account (IUPAC Recommendations 2011). *Pure Appl. Chem.*, 83:1637–1641, 2011.

[9] G. C. Pimentel and A. L. McClellan. *The Hydrogen Bond*. W. H. Freeman and Company, San Francisco, 1960.

[10] C. Emmeluth, V. Dyczmons, T. Kinzel, P. Botschwina, M. A. Suhm, and M. Yáñez. Combined jet relaxation and quantum chemical study of the pairing preferences of ethanol. *Phys. Chem. Chem. Phys.*, 7:991–997, 2005.

[11] M. Nedić, T. N. Wassermann, Z. Xue, P. Zielke, and M. A. Suhm. Raman spectroscopic evidence for the most stable water/ethanol dimer and for the negative mixing energy in cold water/ethanol trimers. *Phys. Chem. Chem. Phys.*, 10:5953–5956, 2008.

[12] J. J. Lee, S. Hesse, and M. A. Suhm. Conformational instability upon dimerization: Prolinol. *J. Mol. Spectrosc.*, 976:397–404, 2010.

[13] J. Pickworth Glusker and K. N. Trueblood. *Crystal Structure Analysis. A Primer*. IUCr Texts on Crystallography. Oxford University Press, Oxford, 2010.

[14] M. Nedić, T. N. Wassermann, R. W. Larsen, and M. A. Suhm. A combined Raman- and infrared jet study of mixed methanol-water and ethanol-water clusters. *Phys. Chem. Chem. Phys.*, 13:14050–14063, 2011.

[15] D. E. Bugay. Characterization of the solid-state: spectroscopic techniques. *Adv. Drug Deliv. Rev.*, 48:43–65, 2001.

[16] K. Nakamoto, editor. *Infrared and Raman Spectra of Inorganic and Coordination Compounds, Part A*. Wiley, Hoboken, 2009.

[17] R. Salzer and H. W. Siesler, editors. *Infrared and Raman Spectroscopic Imaging*. Wiley-VCH, Weinheim, 2009.

[18] J. Bernstein. Polymorphism – A Perspective. *Cryst. Growth Des.*, 11:632–650, 2011.

[19] A. Gavezzotti, editor. *Molecular Aggregation*. Oxford University Press, Oxford, 2007.

[20] R. J. Davey, G. Dent, R. K. Mughal, and S. Parveen. Concerning the Relationship between Structural and Growth Synthons in Crystal Nucleation:

Solution and Crystal Chemistry of Carboxylic Acids as Revealed through IR Spectroscopy. *Cryst. Growth Des.*, 6:1788–1796, 2006.

[21] G. R. Desiraju. On the presence of multiple molecules in the crystal asymmetric unit (Z'>1). *Cryst. Eng. Commun.*, 9:91–92, 2007.

[22] B. Sarma, S. Roy, and A. Nangia. Polymorphs of 1,1-bis(4-hydroxyphenyl)cyclohexane and multiple Z' crystal structures by melt and sublimation crystallization. *Chem. Comm.*, 47:4918–4920, 2006.

[23] K. M. Anderson, A. E. Goeta, and J. W. Steed. Supramolecular Synthon Frustration Leads to Crystal Structures with $Z' > 1$. *Cryst. Growth Des.*, 8:2517–2524, 2008.

[24] R. A. Fletton, R. W. Lancaster, R. K. Harris, A. M. Kenwright, K. J. Packer, D. N. Waters, and A. Yeadon. A Comparative Spectroscopic Investigation of Two Polymorphs of 4'-Methyl-2'-nitroacetanilide using Solid-state Infrared and High-resolution Solid-state Nuclear Magnetic Resonance Spectroscopy. *J. Chem. Soc., Perkin Trans. 2*, 11:1705–1709, 1986.

[25] M. Drozd and J. Baran. Polarized IR-microscope spectra of guanidinium hydrogenselenate single crystal. *Spectrochim. Acta Part A*, 61:2953–2965, 2005.

[26] N. G. Teixeira, R. L. Moreira, M. R. B. Andreeta, A. C. Hernandes, and A. Dias. Micro Far-Infrared Reflectivity of $CaNb_2O_6$ Single Crystal Fibers Grown by the Laser-Heated Pedestal Growth Technique. *Cryst. Growth Des.*, 11:3472–3478, 2011.

[27] H. T. Flakus and B. Hachuła. Polarized IR Spectra of the Hydrogen Bond in Two Different Oxindole Polymorphs with Cyclic Dimers in Their Lattices. *J. Phys. Chem. A*, 115:12150–12160, 2011.

[28] H. Hoshina, Y. Morisawa, H. Sato, H. Minamide, I. Noda, Y. Ozaki, and C. Otani. Polarization and temperature dependent spectra of poly(3-hydroxyalkanoate)s measured at terahertz frequencies. *Phys. Chem. Chem. Phys.*, 13:9173–9179, 2011.

[29] R. Rungsawang, Y. Ueno, I. Tomita, and K. Ajito. Angle-Dependent Terahertz Time-Domain Spectroscopy of Amino Acid Single Crystals. *J. Phys. Chem. B*, 110:21259–21263, 2006.

[30] V. H. Whitley, D. E. Hooks, K. J. Ramos, J. F. O'Hara, A. K. Azad, A. J. Taylor, J. Barber, and R. D. Averitt. Polarization orientation dependence of the far infrared spectra of oriented single crystals of 1,3,5-trinitro-*S*-triazine (RDX) using terahertz time-domain spectroscopy. *Anal. Bioanal. Chem.*, 395:315–322, 2009.

[31] V. H. Whitley, D. E. Hooks, K. J. Ramos, T. H. Pierce, J. F. O'Hara, A. K. Azad, A. J. Taylor, J. Barber, and R. D. Averitt. Orientation Dependent Far-Infrared Terahertz Absorptions in Single Crystal Pentaerythritol Tetranitrate (PETN) Using Terahertz Time-Domain Spectroscopy. *J. Phys. Chem. A*, 115:439–442, 2011.

[32] B. A. Zakharov, B. A. Kolesov, and E. V. Boldyreva. Monitoring selected hydrogen bonds in crystal hydrates of amino acid salts: combining variable-temperature single-crystal X-ray diffraction and polarized Raman spectroscopy. *Phys. Chem. Chem. Phys.*, 13:13106–13116, 2011.

[33] R. L. Moreira, N. G. Teixeira, M. R. B. Andreeta, A. C. Hernandes, and A. Dias. Polarized Micro-Raman Scattering of $CaNb_2O_6$ Single Crystal Fibers Obtained by Laser Heated Pedestal Growth. *Cryst. Growth Des.*, 10:1569–1573, 2010.

[34] G. C. Pimentel and A. L. McClellan. The Infrared Spectra of Napthalene Crystals, Vapor, and Solutions. *J. Chem. Phys.*, 20:270–277, 1952.

[35] J. Baran and H. Ratajczak. Polarised IR and Raman spectra of the γ-glycine single crystal. *Spectrochim. Acta Part A*, 61:1611–1626, 2005.

[36] R. Tonner. Adsorption of Proline and Glycine on the $TiO_2(110)$ Surface: A Density Functional Theory Study. *Chem. Phys. Chem.*, 11:1053–1061, 2010.

[37] M. Nedić and M. A. Suhm. Detailed Assignment of the CH Chromophores in Methyl Mandelate and Mandelic Acid: A Multi-Experimental Approach Using Polarized FTIR Microspectroscopy of Sublimated Crystals. *Cryst. Growth Des.*, 12:1933–1942, 2012.

[38] M. Albrecht, A. Borba, K. Le Barbu-Debus, B. Dittrich, R. Fausto, S. Grimme, A. Mahjoub, M. Nedić, U. Schmitt, L. Schrader, M. A. Suhm, A. Zehnacker-Rentien, and J. Zischang. Chirality influence on the aggregation of methyl mandelate. *New J. Chem.*, 34:1266–1285, 2010.

[39] J. M. Hollas. *Modern Spectroscopy*. John Wiley & Sons, Inc., Chichester, New York, Brisbane, Toronto, Singapore, 1997.

[40] P. R. Griffiths and J. A. de Haseth. *Fourier Transform Infrared Spectrometry*. John Wiley & Sons, Inc., Hoboken, 2007.

[41] G. Turrell. *Infrared and Raman Spectra of Crystals*. Academic Press, London, New York, 1972.

[42] R. A. Alberty and R. J. Silbey. *Physical Chemistry*. John Wiley & Sons, Inc., New York, Chichester, Brisbane, Toronto, Singapore, 1992.

[43] J. M. Chalmers and P. R. Griffiths, editors. *Handbook of Vibrational Spectroscopy*. John Wiley & Sons, Ltd., Chichester, 2002.

[44] E. B. Wilson, J. C. Decius, and P. C. Cross. *Molecular Vibrations*. Dover Publications, New York, 1980.

[45] A. V. Iogansen. Direct proportionality of the hydrogen bonding energy and the intensification of the stretching $\nu(XH)$ vibration in infrared spectra. *Spectrochim. Acta. A*, 55:1585–1612, 1999.

[46] C. M. Huggins and G. C. Pimentel. Systematics of the infrared spectral properties of hydrogen bonding systems: frequency shift, half width and intensity. *J. Phys. Chem.*, 60:1615–1619, 1956.

[47] B. Schrader, editor. *Infrared and Raman Spectroscopy*. VCH, Weinheim, New York, 1995.

[48] MATLAB, Version 7.9.0 (R2009b). The MathWorks Inc., Natick, Massachusetts, 2009.

[49] M. Atoji and W. N. Lipscomb. The Crystal Structure of Hydrogen Fluoride. *Acta Cryst.*, 7:173–175, 1954.

[50] S. P. Habuda and Y. V. Gagarinsky. Nuclear magnetic resonance data on proton positions in solid HF. *Acta Cryst., Sect. B*, 27:1677–1678, 1971.

[51] B. J. Howard, T. R. Dyke, and W. Klemperer. The molecular beam spectrum and the structure of the hydrogen fluoride dimer. *J. Chem. Phys.*, 81:5417–5425, 1984.

[52] D. W. Michael and J. M. Lisy. Vibrational predissociation spectroscopy of $(HF)_3$. *J. Chem. Phys.*, 85:2528–2537, 1986.

[53] M. A. Suhm, J. T. Farrell, S. H. Ashworth, and D. J. Nesbitt. High-resolution infrared spectroscopy of DF trimer: A cyclic ground state structure and DF stretch induced intramolecular vibrational coupling. *J. Chem. Phys.*, 98:5985–5989, 1993.

[54] T. A. Blake, S. W. Sharpe, and S. S. Xantheas. Rotationally resolved spectroscopy of a librational fundamental band of hydrogen fluoride tetramer. *J. Chem. Phys.*, 113:707–718, 2000.

[55] A. Karpfen and O. Yanovitskii. Structure and vibrational spectra of neutral, protonated and deprotonated hydrogen bonded polymers: an ab initio SCF study on chain-like hydrogen fluoride clusters. *J. Mol. Struct. (Theochem)*, 307:81–97, 1994.

[56] A. Karpfen and O. Yanovitskii. Cooperativity in hydrogen bonded clusters: an improved ab initio SCF study on the structure and energetics of neutral, protonated and deprotonated chains and of neutral, cyclic hydrogen fluoride oligomers. *J. Mol. Struct. (Theochem)*, 314:211–227, 1994.

[57] D. Basavaiah and P. R. Krishna. Synthesis of Chiral α-Aryl-α-Hydroxyacetic Acids: Substituent Effects in Pig Liver Acetone Powder (PLAP) Induced Enantioselective Hydrolysis. *Tetrahedron*, 51(8):2403–2416, 1995.

[58] S. K. Tulashie, J. von Langermann, H. Lorenz, and A. Seidel-Morgenstern. Chiral Task-Specific Solvents for Mandelic Acid and Their Impact on Solution Thermodynamics and Crystallization Kinetics. *Cryst. Growth Des.*, 11:240–246, 2011.

[59] H. T. Flakus, N. Rekik, and A. Jarczyk. Polarized IR Spectra of the Hydrogen Bond in 2-Thiopheneacetic Acid and 2-Thiopheneacrylic Acid Crystals: H/D Isotopic and Temperature Effects. *J. Phys. Chem. A*, 116:2117–2130, 2012.

[60] B. Mellish. *Wire-grid polarizer*. Available online at http://en.wikipedia.org/wiki/File:Wire-grid-polarizer.svg; visited on April 10th 2012.

[61] OPUS, Version 6.5. Bruker Optik GmbH, Ettlingen, 2008.

[62] E. N. Lewis, P. J. Treado, R. C. Reeder, G. M. Story, A. E. Dowrey, C. Marcott, and I. W. Levin. Fourier Transform Spectroscopic Imaging Using an Infrared Focal-Plane Array Detector. *Anal. Chem.*, 67:3377–3381, 1995.

[63] C. Corsi. History highlights and future trends of infrared sensors. *J. Mod. Optics*, 57:1663–1686, 2010.

[64] M. Born and E. Wolf, editors. *Principles of Optics. Electromagnetic Theory of Propagation, Interference and Diffraction of Light*. Pergamon Press, Oxford, New York, Toronto, Sydney, Braunschweig, 1975.

[65] K. Nasirzadeh, R. Neueder, and W. Kunz. Vapor Pressure Determination of the Aliphatic C_5 to C_8 1-Alcohols. *J. Chem. Eng. Data*, 51:7–10, 2006.

[66] M. Albrecht, V. A. Soloshonok, L. Schrader, M. Yasumoto, and M. A. Suhm. Chirality-dependent sublimation of α-(trifluoromethyl)-lactic acid: Relative vapor pressures of racemic, eutectic, and enantiomerically pure forms, and vibrational spectroscopy of isolated (S,S) and (S,R) dimers. *J. Fluorine Chem.*, 131:495–504, 2010.

[67] RGA, Version 3.05. Stanford Research Systems, Inc., Sunnyvale, California, 2005.

[68] G. Scoles, D. Bassi, U. Buck, and D. Lainé. *Atomic and Molecular Beam Methods. Volume I.* Oxford University Press, Oxford, 1988.

[69] M. Herman, R. Georges, M. Hepp, and D. Hurtmans. High resolution Fourier transform spectroscopy of jet-cooled molecules. *Int. Rev. Phys. Chem.*, 19:277–325, 2000.

[70] T. Häber, U. Schmitt, and M. A. Suhm. FTIR-spectroscopy of molecular clusters in pulsed supersonic slit-jet expansions. *Phys. Chem. Chem. Phys.*, 1:5573–5582, 1999.

[71] N. Borho. *Chirale Erkennung in Molekülclustern: Maßgeschneiderte Aggregation von α-Hydroxyestern*. PhD Thesis, Universität Göttingen, 2005.

[72] C. A. Rice, N. Borho, and M. A. Suhm. Dimerization of Pyrazole in Slit Jet Expansions. *Z. Phys. Chem.*, 219:379–388, 2005.

[73] N. Borho and M. A. Suhm and K. Le Barbu-Debus and A. Zehnacker. Intra-*vs*. intermolecular hydrogen bonding: dimers of alpha-hydroxyesters with methanol. *Phys. Chem. Chem. Phys.*, 8:4449–4460, 2006.

[74] S. Hesse. *Schwache Wechselwirkungen zwischen organischen Molekülen: Strukturelle Vielfalt und ihre schwingunsspektroskopischen Auswirkungen.* PhD Thesis, Universität Göttingen, 2010.

[75] T. N. Wassermann. *Umgebungseinflüsse auf die C–C- und C–O-Torsionsdynamik in Molekülen und Molekülaggregaten: Schwingungsspektroskopie bei tiefen Temperaturen*. PhD Thesis, Universität Göttingen, 2010.

[76] P. Zielke. *Ramanstreuung am Überschallstrahl: Wasserstoffbrückendynamik aus neuer Perspektive*. PhD Thesis, Universität Göttingen, 2007.

[77] Z. Xue. *Raman spectroscopy of carboxylic acid and water aggregates*. PhD Thesis, Universität Göttingen, 2011.

[78] P. Zielke and M. A. Suhm. Concerted proton motion in hydrogen-bonded trimers: A spontaneous Raman scattering perspective. *Phys. Chem. Chem. Phys.*, 8:2826–2830, 2006.

[79] Z. Xue and M. A. Suhm. Probing the stiffness of the simplest double hydrogen bond: The symmetric hydrogen bond modes of jet-cooled formic acid dimer. *J. Chem. Phys.*, 131:054301, 2009.

[80] T. N. Wassermann and M. A. Suhm. Ethanol Monomers and Dimers Revisited: A Raman Study of Conformational Preferences and Argon Nanocoating Effects. *J. Phys. Chem. A*, 114:8223–8233, 2010.

[81] M. Nedić. *„Der kleinste Schnaps der Welt"– Experimentelle und theoretische Untersuchungen zu kleinen Alkohol-Wasser-Clustern*. Hausarbeit im Rahmen der Ersten Staatsprüfung für das Lehramt an Gymnasien, Universität Göttingen, 2008.

[82] P. Butz, R. T. Kroemer, N. A. Macleod, and J. P. Simons. Conformational Preferences of Neurotransmitters: Ephedrine and Its Diastereoisomer, Pseudoephedrine. *J. Phys. Chem. A*, 105:544–551, 2001.

[83] P. Butz, R. T. Kroemer, N. A. Macleod, E. G. Robertson, and J. P. Simons. Conformational Preferences of Neurotransmitters: Norephedrine and the Adrenaline Analogue, 2-Methylamino-1-phenylethanol. *J. Phys. Chem. A*, 105:1050–1056, 2001.

[84] P. Butz, R. T. Kroemer, N. A. Macleod, and J. P. Simons. Hydration of neurotransmitters: a spectroscopic and computational study of ephedrine and its diasterisomer pseudoephedrine. *Phys. Chem. Chem. Phys.*, 4:3566–3574, 2002.

[85] R. Karaminkov, S. Chervenkov, P. Härter, and H. J. Neusser. Resonance-enhanced two-photon ionization mass spectroscopy of ephedrine: Indication for a state-selective fragmentation in a flexible molecule. *Chem. Phys. Lett.*, 442:238–244, 2007.

[86] R. Karaminkov, S. Chervenkov, V. Delchev, and H. J. Neusser. High-Resolution Mass-Selective UV Spectroscopy of Pseudoephedrine: Evidence for Conformer-Specific Fragmentation. 115:9704–9713, 2011.

[87] J. L. Alonso, M. E. Sanz, J. C. López, and V. Cortijo. Conformational Behavior of Norephedrine, Ephedrine, and Pseudoephedrine. *J. Am. Chem. Soc.*, 131:4320–4326, 2009.

[88] A. O. Patil, W. T. Pennington, I. C. Paul, D. Y. Curtin, and C. E. Dykstra. Reactions of Crystalline (*R*)-(−)- and (*S*)-(+)-Mandelic Acid with Amines. Crystal Structure and Dipole Moment of (*S*)-Mandelic Acid. A Method of Determining Absolute Configuration of Chiral Crystals. *J. Am. Chem. Soc.*, 109:1529–1535, 1987.

[89] B. P. Mukhopadhyay, J. K. Dattagupta, and G. H. Evrard. Crystal and molecular structure of (±)-1-phenyl-2-amino-1-propanol, $C_9H_{13}NO$. *J. Crystallogr. Spectrosc. Res.*, 21:507–510, 1991.

[90] J. A. Groeper, S. R. Hitchcock, and G. M. Ferrence. A scalable and expedient method of preparing diastereomerically and enantiomerically enriched pseudonorephedrine from norephedrine. 17:2884–2889, 2006.

[91] E. A. Collier, R. J. Davey, S. N. Black, and R. J. Roberts. 17 salts of ephedrine: crystal structures and packing analysis. *Acta Cryst., Sect. B*, B62:498–505, 2006.

[92] M. Mathew and G. J. Palenik. The Crystal and Molecular Structures of (+)-Pseudoephedrine and (+)-Pseudoephedrine Hydrochloride. *Acta Cryst., Sect. B*, B33:1016–1022, 1977.

[93] M. J. Frisch, G. W. Trucks, H. B. Schlegel, G. E. Scuseria, M. A. Robb, J. R. Cheeseman, J. A. Montgomery, Jr., T. Vreven, K. N. Kudin, J. C. Burant, J. M. Millam, S. S. Iyengar, J. Tomasi, V. Barone, B. Mennucci, M. Cossi, G. Scalmani, N. Rega, G. A. Petersson, H. Nakatsuji, M. Hada, M. Ehara, K. Toyota, R. Fukuda, J. Hasegawa, M. Ishida, T. Nakajima, Y. Honda, O. Kitao, H. Nakai, M. Klene, X. Li, J. E. Knox, H. P. Hratchian, J. B. Cross, C. Adamo, J. Jaramillo, R. Gomperts, R. E. Stratmann, O. Yazyev, A. J. Austin, R. Cammi, C. Pomelli, J. W. Ochterski, P. Y. Ayala, K. Morokuma, G. A. Voth, P. Salvador, J. J. Dannenberg, V. G. Zakrzewski, S. Dapprich, A. D. Daniels, M. C. Strain, O. Farkas, D. K. Malick, A. D. Rabuck, K. Raghavachari, J. B. Foresman, J. V. Ortiz, Q. Cui, A. G. Baboul, S. Clifford, J. Cioslowski, B. B. Stefanov, G. Liu, A. Liashenko, P. Piskorz, I. Komaromi, R. L. Martin, D. J. Fox, T. Keith, M. A. Al-Laham, C. Y. Peng, A. Nanayakkara, M. Challacombe, P. M. W. Gill, B. Johnson, W. Chen, M. W. Wong, C. Gonzalez, and J. A. Pople. Gaussian 03, Revisions B.04 and C.02. Gaussian Inc., Pittsburgh PA, 2003.

[94] J. W. Moskowitz, Z. Bačić, A. Sarsa, and K. E. Schmidt. Relative stabilities of the two isomers of the methanol-water dimer: The effects of the internal rotations of the hydroxyl and methyl groups of methanol. *J. Chem. Phys.*, 114:10294–10299, 2001.

[95] P.-G. Jönsson. Hydrogen Bond Studies. CXIII. The Crystal Structure of Ethanol at 78 K. *Acta Cryst., Sect. B*, 32:232–235, 1976.

[96] F. Franks and D. J. G. Ives. The structural properties of alcohol-water mixtures. *Q. Rev. Chem. Soc.*, 20:1–44, 1966.

[97] J.-P. E. Grolier. Excess Volumes and Excess Heat Capacities of Water + Ethanol at 298.15 K. *Fluid Phase Equilibria*, 6:283–287, 1981.

[98] G. C. Benson and O. Kiyohara. Thermodynamics of Aqueous Mixtures of Nonelectrolytes. I. Excess Volumes of Water - n-Alcohol Mixtures at Several Temperatures. *J. Solution Chem.*, 9:791–804, 1980.

[99] G. L. Bertrand, F. J. Millero, C.-H. Wu, and L. G. Hepler. Thermochemical Investigations of the Water-Ethanol and Water-Methanol Solvent Systems. I. Heats of Mixing, Heats of Solution, and Heats of Ionization of Water. *J. Phys. Chem.*, 70:699–705, 1966.

[100] J. A. Larkin. Thermodynamic properties of aqueous non-electrolyte mixtures I. Excess enthalpy for water + ethanol at 298.15 to 383.15 K. *J. Chem. Thermodynamics.*, 7:137–148, 1975.

[101] M. A. Suhm. Hydrogen Bond Dynamics in Alcohol Clusters. *Adv. Chem. Phys.*, 142:1–57, 2009.

[102] P. A. Stockmann, G. A. Blake, F. J. Lovas, and R. D. Suenram. Microwave rotation-tunneling spectroscopy of the water-methanol dimer: Direct structural proof for the strongest bound conformation. *J. Chem. Phys.*, 107:3782–3790, 1997.

[103] S. Coussan, P. Roubin, and J. P. Perchard. Hydrogen Bonding in ROH:R'OH (R, R' = H, CH_3, C_2H_5) Heterodimers: Matrix-Dependent Structure and Infrared-Induced Isomerization. *J. Phys. Chem. A*, 108:7331–7338, 2004.

[104] Y. Matsuda, A. Yamada, K. Hanaue, N. Mikami, and A. Fujii. Catalytic Action of a Single Water Molecule in a Proton-Migration Reaction. *Angew. Chem. Int. Ed.*, 49:4898–4901, 2010.

[105] Y. J. Hu, H. B. Fu, and E. R. Bernstein. Infrared plus vacuum ultraviolet spectroscopy of neutral and ionic ethanol monomers and clusters. *J. Chem. Phys.*, 125:154305, 2006.

[106] F. N. Keutsch and R. J. Saykally. Water clusters: Untangling the mysteries of the liquid, one molecule at a time. *Proc. Natl. Acad. Sci.*, 98:10533–10540, 2001.

[107] M. Masella and J. P. Flament. Relation between cooperative effects in cyclic water, methanol/water, and methanol trimers and hydrogen bonds in methanol/water, ethanol/water, and dimethylether/water. *J. Chem. Phys.*, 109:7141–7151, 1998.

[108] E. E. Fileti, P. Chaudhuri, and S. Canuto. Relative strength of hydrogen bond interaction in alcohol-water complexes. *Chem. Phys. Lett.*, 400:494–499, 2004.

[109] E. E. Fileti and S. Canuto. Calculated Infrared Spectra of Hydrogen-Bonded Methanol-Water, Water-Methanol, and Methanol-Methanol Complexes. *Int. J. Quantum Chem.*, 104:808–815, 2005.

[110] L. González, O. Mó, and M. Yáñez. High level *ab initio* and density functional theory studies on methanol-water dimers and cyclic methanol(water)$_2$ trimer. *J. Chem. Phys.*, 109:139–150, 1998.

[111] A. Mandal, M. Prakash, R. M. Kumar, R. Parthasarathi, and V. Subramanian. Ab Initio and DFT Studies on Methanol–Water Clusters. *J. Phys. Chem. A*, 114:2250–2258, 2010.

[112] E. E. Fileti, M. A. Castro, and S. Canuto. Calculations of vibrational frequencies, Raman activities and degrees of depolarization for complexes involving water, methanol and ethanol. *Chem. Phys. Lett.*, 452:54–58, 2008.

[113] J. L. Iosue, D. M. Benoit, and D. C. Clary. Diffusion Monte Carlo simulations of methanol–water clusters. *Chem. Phys. Lett.*, 301:275–280, 1999.

[114] R. K. Campen and J. D. Kubicki. Interaction Energy and the Shift in OH Stretch Frequency on Hydrogen Bonding for the $H_2O \rightarrow H_2O$, $CH_3OH \rightarrow H_2O$ and $H_2O \rightarrow CH_3OH$ dimers. *J. Comput. Chem.*, 31:963–972, 2009.

[115] A. Galano, M. Narciso-Lopez, and M. Francisco-Marquez. Water Complexes of Important Air Pollutants: Geometries, Complexation Energies, Concentrations, Infrared Spectra, and Intrinsic Reactivity. *J. Phys. Chem. A*, 114:5796–5809, 2010.

[116] S. M. Mejía, J. F. Espinal, and F. Mondragón. Cooperative effects on the structure and stability of (ethanol)$_3$-water, (methanol)$_3$-water heterotetramers and (ethanol)$_4$, (methanol)$_4$ tetramers. *J. Mol. Struct. (Theochem)*, 901:186–193, 2009.

[117] M. Ferrario, M. Haughney, I. R. McDonald, and M. L. Klein. Molecular-dynamics simulation of aqueous mixtures: Methanol, acetone, and ammonia. *J. Chem. Phys.*, 93:5156–5166, 1990.

[118] D. González-Salgado and I. Nezbeda. Excess properties of aqueous mixtures of methanol: Simulation versus experiment. *Fluid Phase Equilibria*, 240:161–166, 2006.

[119] B. G. Oliveira and M. L. A. A. Vasconcellos. Hydrogen bonds in alcohol:water complexes: A theoretical study about new intramolecular interactions via CHELPG and AIM calculations. *J. Mol. Struct. (Theochem)*, 774:83–88, 2006.

[120] D. Peeters and G. Leroy. Small clusters between water and alcohols. *J. Mol. Struct. (Theochem)*, 314:39–47, 1994.

[121] Y. Katrib, P. Mirabel, S. Le Calvé, G. Weck, and E. Kochanski. Experimental Uptake Study of Ethanol by Water Droplets and Its Theoretical Modeling of Cluster Formation at the Interface. *J. Phys. Chem. B*, 106:7237–7245, 2002.

[122] S. M. Mejía, J. F. Espinal, A. Restrepo, and F. Mondragón. Molecular Interaction of (Ethanol)$_2$–Water Heterotrimers. *J. Phys. Chem. A*, 111:8250–8256, 2007.

[123] S. M. Mejía, J. F. Orrego, J. F. Espinal, P. Fuentealba, and F. Mondragón. Exploration of the (Ethanol)$_4$-Water Heteropentamers Potential Energy Surface by Simulated Annealing and Ab Initio Molecular Dynamics. *Int. J. Quantum Chem.*, 111:3080–3096, 2011.

[124] D. Nesbitt, T. Häber, and M. A. Suhm. On the spectroscopy of argon-coated water and deuterium oxide clusters. *Faraday Discuss.*, 118:305–309, 2001.

[125] C. J. Gruenloh, F. C. Hagemeister, J. R. Carney, and T. S. Zwier. Resonant Ion-Dip Infrared Spectroscopy of Ternary Benzene–(Water)$_n$(Methanol)$_m$ Hydrogen-Bonded Clusters. *J. Phys. Chem. A*, 103:503–513, 1999.

[126] N. Bakkas, Y. Bouteiller, A. Louteiller, J. P. Perchard, and S. Racine. The water–methanol complexes. Matrix induced structural conversion of the 1–1 species. *Chem. Phys. Lett.*, 232:90–98, 1995.

[127] D. Peeters and P. Huyskens. Endothermicity or exothermicity of water/alcohol mixtures. *J. Mol. Struct.*, 300:539–550, 1993.

[128] N. Bakkas, Y. Bouteiller, A. Louteiller, J. P. Perchard, and S. Racine. The water–methanol complexes. I. A matrix isolation study and an *ab initio* calculation on the 1-1 species. *J. Chem. Phys.*, 99:3335–3342, 1993.

[129] R. Wugt Larsen, P. Zielke, and M. A. Suhm. Hydrogen-bonded OH stretching modes of methanol clusters: A combined IR and Raman isotopomer study. *J. Chem. Phys.*, 126:194307, 2007.

[130] U. Buck and F. Huisken. Infrared Spectroscopy of Size-Selected Water and Methanol Clusters. *Chem. Rev.*, 100:3863–3890, 2000.

[131] S. Melandri. "Union is strength": how weak hydrogen bonds become stronger. *Phys. Chem. Chem. Phys.*, 13:13901–13911, 2011.

[132] T. N. Wassermann, P. Zielke, J. J. Lee, C. Cézard, and M. A. Suhm. Structural Preferences, Argon Nanocoating, and Dimerization of *n*-Alkanols As Revealed by OH Stretching Spectroscopy in Supersonic Jets. *J. Phys. Chem. A*, 111:7437–7448, 2007.

[133] T. Scharge, T. N. Wassermann, and M. A. Suhm. Weak Hydrogen Bonds Make a Difference: Dimers of Jet-Cooled Halogenated Ethanols. *Z. Phys. Chem.*, 222:1407–1452, 2008.

[134] R. Karaminkov, S. Chervenkov, and H. J. Neusser. Water binding sites in 2-*para*- and 2-*ortho*-fluorophenylethanol: A high-resolution UV experiment and *ab initio* calculations. *J. Chem. Phys.*, 133:194301, 2010.

[135] E. C. Lee, D. Kim, P. Jurečka, P. Tarakeshwar, P. Hobza, and K. S. Kim. Understanding of Assembly Phenomena by Aromatic–Aromatic Interactions: Benzene Dimer and the Substituted Systems. *J. Phys. Chem. A*, 111:3446–3457, 2007.

[136] K. Le Barbu-Debus, M. Broquier, A. Mahjoub, and A. Zehnacker-Rentien. Chiral recognition in jet-cooled complexes of (1*R*,2*S*)-(+)-*cis*-1-amino-2-indanol and methyl lactate: on the importance of the CH···π interaction. *Phys. Chem. Chem. Phys.*, 11:7589–7598, 2009.

[137] M. Albrecht. *Biologisch relevante Wasserstoffbrückensysteme im Überschallstrahl: Steuerung der Aggregation durch Substitution.* PhD Thesis, Universität Göttingen, 2009.

[138] K. Le Barbu-Debus, M. Broquier, A. Mahjoub, and A. Zehnacker-Rentien. Chiral Recognition between α-Hydroxylesters: A Double-Resonance IR/UV Study of the Complexes of Methyl Mandelate with Methyl Glycolate and Methyl Lactate. *J. Phys. Chem. A*, 112:9731–9741, 2008.

[139] N. Mori, Y. Tanaka, and Y. Tsuzuki. Intramolecular Hydrogen Bonds. VII. Methyl Mandelates and Related Compounds. *Bull. Chem. Soc. Jpn.*, 39:1490–1495, 1966.

[140] N. Mori, Y. Asano, T. Irie, and Y. Tsuzuki. Intramolecular Hydrogen Bonds. XIII. The Preferable Conformation of α-Hydroxy-carboxylic and *o*-Hydroxybenzoic Acids. *Bull. Chem. Soc. Jpn.*, 42:482–487, 1969.

[141] D. M. P. Gigante, F. Long, L. A. Bodack, J. M. Evans, J. Kallmerten, L. A. Nafie, and T. B. Freedman. Hydrogen Stretching Vibrational Circular Dichroism in Methyl Lactate and Related Molecules. *J. Phys. Chem. A*, 103:1523–1537, 1999.

[142] L. Schrader. *Relative Dampfdruckmessungen an chiralen Verbindungen und ihren Racematen*. Bachelor Thesis, Universität Göttingen, 2008.

[143] J. Zischang. *Vergleich enantiomerenreiner und racemischer Verbindungen mittels ATR-FTIR-Spektroskopie und EI-Massenspektrometrie.* Internship Report, Universität Göttingen, 2009.

[144] H. E. Gallis, P. J. van Ekeren, J. C. van Miltenburg, and H. A. J. Oonk. Mixtures of *d*- and *l*-carvone IV. Transformation from a solid solution to a racemic compound. *Thermochim. Acta*, 326:83–90, 1999.

[145] J. Jacques, A. Collet, and S. H. Wilen. *Enantiomers, Racemates, and Resolutions*. Krieger Publishing Company, Malabar, 1994.

[146] G. Müller and M. Lutz. A Curious Case of Partial Spontaneous Resolution on Crystallization of a Racemate. The Crystal and Molecular Structures of *N*-Acetyl-DL-alanine Methylester and *N*-Acetyl-L-alanine Methylester. *Z. Naturforsch.*, 56b:871–880, 2001.

[147] D. W. Mayo, F. A. Miller, and R. W. Hannah. *Course Notes on the Interpretation of Infrared and Raman Spectra*. Wiley, Hoboken, 2004.

[148] H. J. Hediger. *Infrarotspektroskopie. Grundlagen, Anwendungen, Interpretation*. Akademische Verlagsgesellschaft, Frankfurt am Main, 1971.

[149] T. Breuer and G. Witte. Epitaxial growth of perfluoropentacene films with predefined molecular orientation: A route for single-crystal optical studies. *Phys. Rev. B*, 83:155428, 2011.

[150] R. Signorell. Infrared spectroscopy of particulate matter: between molecular clusters and bulk. *Mol. Phys.*, 101:3385–3399, 2003.

[151] F. Ziegler. *Infrarotspektroskopie von Resublimationsprozessen*. Bachelor Thesis, Universität Göttingen, 2011.

[152] J. Wallbaum and T. Nack. *Infrarotspektroskopie von Resublimationsprozessen*. Internship Report, Universität Göttingen, 2012.

[153] G. D. Yadav, A. D. Sajgure, and S. B. Dhoot. Insight into microwave irradiation and enzyme catalysis in enantioselective resolution of RS-($\pm$)-methyl mandelate. *J. Chem. Technol. Biotechnol.*, 83:1145–1153, 2008.

[154] M. Acs, E. Novotny-Bregger, K. Simon, and G. Argay. Structural Aspects of Optical Resolutions. Optical Resolution of (R,S)-Mandelic Acid. DSC and X-ray Studies of the Diasteroisomeric Salts. *J. Chem. Soc., Perkin Trans. 2*, 11:2011–2017, 1992.

[155] E. J. Valente, J. Zubkowski, and D. S. Eggleston. Discrimination in Resolving Systems: Ephedrine-Mandelic Acid. *Chirality*, 4:494–504, 1992.

[156] E. J. Valente, C. W. Miller, J. Zubkowski, D. S. Eggleston, and X. Shui. Discrimination in Resolving Systems II: Ephedrine-Substituted Mandelic Acids. *Chirality*, 7:652–676, 1995.

[157] S. K. Tulashie, H. Lorenz, C. R. Malwade, and A. Seidel-Morgenstern. Ternary Solubility Phase Diagrams of Mandelic Acid and *N*-Methylephedrine in Chiral Solvents with Different Carbon Chain Lengths. *Cryst. Growth Des.*, 10:4023–4029, 2010.

[158] S. K. Tulashie, H. Kaemmerer, H. Lorenz, and A. Seidel-Morgenstern. Solid–Liquid Equilibria of Mandelic Acid Enantiomers in Two Chiral Solvents: Experimental Determination and Model Correlation. *J. Chem. Eng. Data*, 55:333–340, 2010.

[159] P. Horváth, A. Gergely, and B. Noszál. Determination of enantiomeric purity by simultaneous dual circular dichroism and ultraviolet spectroscopy. *Talanta*, 44:1479–1485, 1997.

[160] S. Mao, Y. Zhang, S. Rohani, and A. K. Ray. Kinetics of (R,S)- and (R)-mandelic acid in an unseeded cooling batch crystallizer. *J. Cryst. Growth*, 312:3340–3348, 2010.

[161] Y. Zhang, S. Mao, A. K. Ray, and S. Rohani. Nucleation and Growth Kinetics of (R)-Mandelic Acid from Aqueous Solution in the Presence of the Opposite Enantiomer. *Cryst. Growth Des.*, 10:2879–2887, 2010.

[162] V. M. Profir and Å. C. Rasmuson. Influence of Solvent and the Operating Conditions on the Crystallization of Racemic Mandelic Acid. *Cryst. Growth Des.*, 4:315–323, 2004.

[163] V. M. Profir, E. Furusjö, L.-G. Danielsson, and Å. C. Rasmuson. Study of the Crystallization of Mandelic Acid in Water Using in Situ ATR-IR Spectroscopy. *Cryst. Growth Des.*, 2:273–279, 2002.

[164] M. Kuhnert-Brandstätter and R. Ulmer. Beitrag zur thermischen Analyse optischer Antipoden: Mandelsäure. *Mikrochim. Acta*, 5:927–935, 1974.

[165] F. Toda, K. Tanaka, H. Miyamoto, H. Koshima, I. Miyahara, and K. Hirotsu. Formation of racemic compound crystals by mixing of two enantiomeric crystals in the solid state. Liquid transport of molecules from crystal to crystal. *J. Chem. Soc., Perkin Trans. 2*, 9:1877–1885, 1997.

[166] A. Fischer and V. M. Profir. A metastable modification of (*RS*)-mandelic acid. *Acta Cryst., Sect. E*, 59:o1113–o1116, 2003.

[167] R. K. Mughal, R. J. Davey, and N. Blagden. Application of Crystallization Inhibitors to Chiral Separations. 1. Design of Additives to Discriminate between the Racemic Compound and the Pure Enantiomer of Mandelic Acid. *Cryst. Growth Des.*, 7:218–224, 2007.

[168] K.-T. Wei and D. L. Ward. α-Hydroxyphenylacetic Acid: A Redetermination. *Acta Cryst., Sect. B*, 33:797–800, 1977.

[169] H. A. Rose. *dl*-Mandelic Acid. *Anal. Chem.*, 24:1680–1681, 1952.

[170] P. Cintas. Comment on "Enantiomer Resolution by Pressure Increase: Inferences from Experimental and Topological Results for the Binary Enantiomer System (*R*)- and (*S*)-Mandelic Acid". *J. Phys. Chem. B*, 115:14698–14703, 2012.

[171] E. A. Abourashed, A. T. El-Alfy, I. A. Khan, and L. Walker. Ephedra in Perspective - a Current Review. *Phytother. Res.*, 17:703–712, 2003.

[172] J. F. Malone and M. Parvez. The Crystal Structures of the Ephedrine Free Bases. *Acta Cryst., Sect. A*, A34:S76, 1978.

[173] S. P. Duddu, A. Khin-Khin, D. J. W. Grant, and R. Suryanarayanan. A Novel X-ray Powder Diffractometric Method for Studying the Reaction between Pseudoephedrine Enantiomers. *J. Pharm. Sci.*, 86:340–345, 1997.

[174] F. H. Allen. The Cambridge Structural Database: a quarter of a million crystal structures and rising. *Acta Cryst., Sect. B*, B58:380–388, 2002.

[175] T. M. R. Maria, R. A. E. Castro, S. S. Bebiano, M. R. Silva, A. M. Beja, J. Canotilho, and M. E. S. Eusébio. Polymorphism of *trans*-1,4-Cyclohexanediol: Conformational Isomorphism. *Cryst. Growth Des.*, 10:1194–1200, 2010.

[176] C. H. Stam and C. H. MacGillavry. The Crystal Structure of the Triclinic Modification of Vitamin-*A* Acid. *Acta Cryst.*, 16, 1963.

[177] C. H. Stam. The Crystal Structure of a Monoclinic Modification and the Refinement of a Triclinic Modification of Vitamin A Acid (Retinoic Acid), $C_{20}H_{28}O_2$. *Acta Cryst., Sect. B*, 28, 1972.

[178] J. Bernstein. *Polymorphism in Molecular Crystals*. Oxford University Press, Oxford, 2002.

[179] P. Müller, R. Herbst-Irmer, A. L. Spek, T. R. Schneider, and M. R. Sawaya. *Crystal Structure Refinement. A Crystallographer's Guide to SHELXL*, chapter Crystal structure refinement. IUCr Texts on Crystallography. Oxford University Press, Oxford, 2011.

[180] S. Chervenkov, O. Q. Wang, J. E. Braun, and H. J. Neusser. Fragmentation and conformation study of ephedrine by low- and high-resolution mass selective UV spectroscopy. *J. Chem. Phys.*, 121:7169–7174, 2004.

[181] J. J. Lee. *Adaptive Aggregation über starke Wasserstoffbrücken in der Gasphase*. PhD Thesis, Universität Göttingen, 2012.

[182] Y. Liu, C. A. Rice, and M. A. Suhm. Torsional isomers in methylated aminoethanols — A jet–FT-IR study. *Can. J. Chem.*, 82:1006–1012, 2004.

[183] K. E. Otto, S. Hesse, T. N. Wassermann, C. A. Rice, M. A. Suhm, T. Stafforst, and U. Diederichsen. Temperature-dependent intensity anomalies in amino acid esters: weak hydrogen bonds in protected glycine, alanine and valine. *Phys. Chem. Chem. Phys.*, 13:14119–14130, 2011.

[184] S. Hesse, T. N. Wassermann, and M. A. Suhm. Brightening and Locking a Weak and Floppy N–H Chromophore: The Case of Pyrrolidine. *J. Phys. Chem. A*, 114:10492–10499, 2010.

[185] L. Du and H. G. Kjaergaard. Fourier Transform Infrared Spectroscopy and Theoretical Study of Dimethylamine Dimer in the Gas Phase. *J. Phys. Chem. A*, 115:12097–12104, 2011.

[186] Y. Nibu, R. Marui, and H. Shimada. IR Spectroscopy of Hydrogen-Bonded 2-Fluoropyridine–Methanol Clusters. *J. Phys. Chem. A*, 110:12597–12602, 2006.

[187] C. Steinbach, U. Buck, and T. A. Beu. Infrared spectroscopy of large ammonia clusters as a function of size. *J. Chem. Phys.*, 125:133403, 2006.

[188] M. N. Slipchenko, B. G. Sartakov, and A. F. Vilesov. Evolution of the vibrational spectrum of ammonia from single molecule to bulk. *J. Chem. Phys.*, 128:134509, 2008.

[189] Z. Jane Li, William H. Ojala, and David J. W. Grant. Molecular Modeling Study of Chiral Drug Crystals: Lattice Energy Calculations. *J. Pharm. Sci.*, 90:1523–1539, 2001.

[190] F. C. Krebs, M. Jørgensen, B. Lebech, and K. Frydenvang. A perdeuterated cryoprotectant for neutron studies and a demonstration of its use for neutron powder diffraction on L-(−)-ephedrine hemihydrate. *J. Appl. Cryst.*, 34:203–207, 2001.

[191] B. Ivanova, T. Kolev, M. Lamshöft, H. Mayer-Figge, R. Seidel, W. S. Sheldrick, and M. Spiteller. Structural, spectroscopic and theoretical study of novel ephedrinum salt. *J. Mol. Struct.*, 971:8–11, 2010.

[192] U. Buck, I. Dauster, B. Gao, and Z. Liu. Infrared Spectroscopy of Small Sodium-Doped Water Clusters: Interaction with the Solvated Electron. *J. Phys. Chem. A*, 111:12355–12362, 2007.

[193] R. Bartlome, J. M. Rey, and M. W. Sigrist. Vapor-Phase Infrared Laser Spectroscopy: From Gas Sensing to Forensic Urinalysis. *Anal. Chem.*, 80:5334–5341, 2008.

[194] S. Krimm and A. M. Dwivedi. Vibrational Analysis of Peptides, Polypeptides and Proteins. XII–Fermi Resonance Analysis of the Unperturbed ND Stretching Fundamental in Polypeptides. *J. Raman Spectrosc.*, 12:133–137, 1982.

[195] J. R. Durig, C. Zheng, T. K. Gounev, W. A. Herrebout, and B. J. van der Veken. Conformational Stability From Temperature-Dependent Fourier

Transform Infrared Spectra of Noble Gas Solutions, r_0 Structural Parameters, and Barriers To Internal Rotation for Ethylamine. *J. Phys. Chem. A*, 110:5674–5684, 2006.

[196] S. J. Daunt and H. F. Shurvell. The Gas Phase Infrared Band Contours of *s*-Triazine and *s*-Triazine-*d*$_3$. The Fundamentals of $C_3N_3H_3$ and $C_3N_3D_3$ and Some Overtone and Combination Bands of $C_3N_3H_3$. *J. Mol. Spectrosc.*, 62:373–395, 1976.

[197] J. J. Lee, S. Höfener, W. Klopper, T. N. Wassermann, and M. A. Suhm. Origin of the Argon Nanocoating Shift in the OH Stretching Fundamental of *n*-Propanol: A Combined Experimental and Quantum Chemical Study. *J. Phys. Chem. C*, 113:10929–10938, 2009.

[198] T. Scharge, D. Luckhaus, and M. A. Suhm. Observation and quantification of the hydrogen bond effect on O-H overtone intensities in an alcohol dimer. *Chem. Phys.*, 346:167–175, 2008.

[199] C. Sándorfy. Hydrogen bonding: How much anharmonicity? *J. Mol. Struct.*, 790:50–54, 2006.

[200] F. M. Kollipost. *Nah- und Ferninfrarotausbau der gepulsten Überschallstrahl-FTIR-Spektroskopie*. PhD Thesis, Universität Göttingen, in preparation.

[201] C. Emmeluth, V. Dyczmons, and M. A. Suhm. Tuning the Hydrogen Bond Donor/Acceptor Isomerism in Jet-Cooled Mixed Dimers of Aliphatic Alcohols. *J. Phys. Chem. A*, 110:2906–2915, 2006.

[202] Y. Liu, M. Weimann, and M. A. Suhm. Extension of panoramic cluster jet spectroscopy into the far infrared: Low frequency modes of methanol and water clusters. *Phys. Chem. Chem. Phys.*, 6:3315–3319, 2004.

[203] N. O. B. Lüttschwager, T. N. Wassermann, R. A. Mata, and M. A. Suhm. The last globally stable extended alkane. *unpublished manuscript*.

[204] N. O. B. Lüttschwager. *Ramanspektroskopie von Konformationsumlagerungen bei tiefen Temperaturen*. PhD Thesis, Universität Göttingen, in preparation.

[205] L. Carlucci and A. Gavezzotti. Molecular Recognition and Crystal Energy Landscapes: An X-ray and Computational Study of Caffeine and Other Methylxanthines. *Chem. Eur. J.*, 11:271–279, 2005.

[206] M. Habgood. Form II Caffeine: A Case Study for Confirming and Predicting Disorder in Organic Crystals. *Cryst. Growth Des.*, 11:3600–3608, 2011.

[207] N. Pérez-Hernández, M. Febles, C. Pérez, J. Spandl, J. D. Martín, and H.-H. Limbach. IR Studies of H/D Exchange of Water, Hydroxyl, and Carboxylic Groups Reveal Slowly Diffusing Lattice Defects in Sub-Nanometer Pores. *J. Phys. Chem. C*, 115:9393–9402, 2011.

[208] A. Cesàro and G. Starec. Thermodynamic Properties of Caffeine Crystal Forms. *J. Phys. Chem.*, 84:1345–1346, 1980.

[209] P. Derollez, N. T. Correia, F. Danède, F. Capet, F. Affouard, J. Lefebvre, and M. Descamps. *Ab initio* structure determination of the high-temperature phase of anhydrous caffeine by X-ray powder diffraction. 61:329–334, 2005.

[210] C. W. Lehmann and F. Stowasser. The Crystal Structure of Anhydrous β-Caffeine as Determined from X-ray Powder-Diffraction Data. *Chem. Eur. J.*, 13:2908–2911, 2007.

[211] E. Suzuki, K. Shimomura, and K. Sekiguchi. Thermochemical Study of Theophylline and Its Hydrate. 37:493–497, 1989.

[212] L. Seton, D. Khamar, I. J. Bradshaw, and G. A. Hutcheon. Solid State Forms of Theophylline: Presenting a New Anhydrous Polymorph. *Cryst. Growth Des.*, 10:3879–3886, 2010.

[213] Y. Ebisuzaki, P. D. Boyle, and J. A. Smith. Methylxanthines. I. Anhydrous Theophylline. *Acta Cryst., Sect. C*, 53:777–779, 1997.

[214] J. Sutor. The Structures of the Pyrimidines and Purines. VII. The Crystal Structure of Caffeine. *Angew. Chem.*, 11:453, 1958.

[215] J. Pirttimäki, E. Laine, J. Ketolainen, and P. Paronen. Effects of grinding and compression on crystal structure of anhydrous caffeine. *Int. J. Pharm.*, 95:93–99, 1993.

[216] C. Sun, D. Zhou, D. J. W. Grant, and V. G. Young Jr. Theophylline monohydrate. *Acta Cryst., Sect. E*, 58:o368–o370, 2002.

[217] J. Zischang. *Infrarotspektroskopische Bildgebung von Überschallexpansionen und Kryoreaktionen*. PhD Thesis, Universität Göttingen, in preparation.

Curriculum Vitae

Personal Information

Name	Marija Nedić
Date of Birth	04th of August 1982
Place of Birth	Hamburg

Academic Education

Since Feb 2009	Ph.D. thesis at the Institute of Physical Chemistry, Georg-August-Universität Göttingen under the supervision of Prof. Dr. Martin A. Suhm
	Title of thesis: Adaptive Aggregation and Chirality Recognition of Neuroactive Substances and their Building Blocks: A Vibrational Spectroscopic and Microscopic Study
Dec 2008	1. Staatsexamen für das Lehramt an Gymnasien with the subjects Chemistry and Philosophy
	Title of thesis: „Der kleinste Schnaps der Welt"– Experimentell und theoretische Untersuchungen zu kleinen Alkohol-Wasser-Clustern
Oct 2003 – Dec 2008	Studies of Lehramt an Gymnasien with the subjects Chemistry and Philosphy, Georg-August-Universität Göttingen
Apr 2003 – Sep 2003	Studies of Lehramt an Gymnasien with the subjects Chemistry and German, Christian-Albrechts-Universität zu Kiel

School Education

2002	Allgemeine Hochschulreife (Abitur)
1993–2002	Gymnasium Hummelsbüttel in Hamburg
1989–1993	Grundschule Flughafenstraße in Hamburg